



**Long wavelength Type-II InAs/GaSb
Superlattice Infrared Photodetectors**

Dominic Chee Min Kwan

A thesis submitted as partial fulfilment for the degree
of Doctor of Philosophy

School of Physics and Astronomy

October 2022

Summary

Type-II superlattices (T2SLs) have demonstrated great potential for long-wavelength infrared (LWIR) photodetectors but have yet to achieve their theoretical performance levels.

In this research project, the capability at Cardiff University for simulation, fabrication, and characterisation of LWIR T2SLs is established and improved with the ultimate aim of improving the current performance levels of LWIR T2SL detectors. The strategies for improving performance, described herein, include improving the design of the superlattice (SL) period, optimisation of the fabrication process, and monolithic integration on GaAs substrates.

8 band k-p simulations are used for band structure modelling, which enables device design optimisation and informs analysis of experimental results. Molecular beam epitaxy (MBE) is used for growth of experimental T2SL reference wafers/samples, which employ novel SL period designs, GaAs substrates, or both. The material quality of these wafers is then investigated by x-ray diffraction (XRD), atomic force microscopy (AFM), and transmission electron microscopy (TEM). Band structure information is obtained through photoluminescence (PL) measurements. Diodes were fabricated using a standard photolithography process which was later modified to incorporate experimental improvements. The diode performance of the T2SLs was then tested in a cryogenic probe station.

Various strategies for improving device performance were tested and evaluated. By comparing different combinations of superlattice layer thicknesses, it was observed that the novel 12 ML InAs/4 ML GaSb superlattice structure was better suited to high-temperature operation than conventional designs. A comparison of the structural, optical, and device characteristics of LWIR T2SLs on GaSb and GaAs substrates was made to investigate the feasibility of LWIR T2SLs on a low-cost GaAs platform. It was observed that, despite using an interfacial misfit (IMF) array between the GaSb buffer and GaAs substrate, a material degradation due to the heteroepitaxial growth led to a corresponding degradation in optical and device performance. However, the reported work in this thesis is mere preliminary demonstration. There is a scope for improvement by involving different buffer layers, dislocation filters, and interfacial schemes of heteroepitaxy. The reasons for and nature of

this material degradation were studied in detail using TEM. This thesis also reports intermediate results from the development of a dry etching process for T2SLs are reported. Scanning electron micrographs show this process significantly improves the sidewall verticality and fill factor compared to wet etching. I-V measurements indicate the performance of dry-etched devices is degraded by roughly two orders of magnitude at low temperatures compared to wet etched reference samples but is comparable at high temperatures.

Acknowledgements

I would firstly like to thank my PhD supervisors, Manoj Kesaria and Diana Huffaker for their continuous support. For this research work, much credit goes to my entire supervisory team - Primary supervisors Diana Huffaker (October 2018 to July 2020) and Manoj Kesaria (July 2020 onward), co-supervisors Peter Hargrave (internal) and Mark Furlong (external from IQE) and additional co-supervisors Marie Delmas (October 2018- March 2019), Ezekiel Anyebe (March 2020 onward). Marie's knowledge, kindness, and patience for silly questions made the opening months of my PhD easier and brighter. Following Marie's departure in April 2019, I was hugely reassured by Manoj's willingness to join my supervisory team. It was thanks to his direction that I was able to complete the research work included in this thesis and have managed to publish three journal papers as a first author. I have also benefitted greatly from Diana's supervision: if, over the course of my PhD, I have grown from a student to a scientist, it is due, in large part, to her rigour and investment. I am also grateful to Ezekiel Anyebe who has read every word of this thesis and provided valuable feedback. I would also like to thank all the colleagues, researchers, engineers, and technicians who have cheerfully invested in my development with no apparent benefit to themselves, I hope to imitate their kindness throughout my career.

I am, as ever, indebted to my family for the love, encouragement, and entertainment they have given me – it is truly a family of which I count myself blessed to be a part. I would also like to express my heartfelt gratitude to my friends, church, and colleagues who, in various ways, have been a source of joy to me throughout my time at Cardiff University.

Funding

The author is grateful for funding from:

EPSRC National Productivity Investment Fund: EP/R512503/1

Ser Cymru National Research Network in Advanced Engineering and Materials: 509722

HEFCW: 50976

Significant Contributions

The work described herein results from a collaborative effort, with contributions from both internal and external researchers, as described below.

Marie Delmas, formerly a postdoctoral researcher at Cardiff University, designed the samples in this project. The samples were then grown by Baolai Liang of the California Nanosystems Institute (CNSI), who also assisted in the design.

XRD and AFM measurements were also performed by Baolai Liang and his colleagues at CNSI but analysed by the author at Cardiff. Marie Delmas designed, acquired, and assembled the PL (Figure 3.28) and probe station (Figure 3.29) set-ups. Some data collection, shown in Figures 4.6, 4.19, 4.20, and 4.21 was led by Marie Delmas but conducted mainly by the author. However, the author did the data analysis, interpretation, and creation of plots. TEM measurements, shown in Chapter 5, were performed and analysed by J.J. Jimenez and F.M. Morales from Universidad de Cádiz.

The standard fabrication process, described in Section 3.3, was developed by Marie Delmas, who fabricated the samples in Chapter 4. Fabrication work was done in the Institute for Compound Semiconductors (ICS) cleanroom with the help of ICS process engineers. Stuart Thomas greatly assisted the author in developing the dry etching processes described in Chapter 6.

The simulation tool, described in Chapters 3, and 4, was developed in Nextnano³ software with the help of Stefan Birner, managing director and founder of Nextnano Holding GmbH.

Having noted the above exceptions, the work done in this project was carried out and analysed by the author with valuable support from my supervisory team. I am also grateful for the help of my fellow students Dhafer Alshahrani and Paradeisa O'Dowd Phanis.

Publications

The four publications listed below are directly relevant to Chapters 1, 2, 4, and 5 of this thesis.

[1] **D. C. M. Kwan**, M. Kesaria, J. J. Jiménez, V. Srivastava, M. Delmas, B. L. Liang, & D. L. Huffaker, Monolithic integration of a 10 μm cut-off wavelength InAs/GaSb type-II superlattice diode on GaAs platform. *Sci. Rep.* **12**, 11616 (2022).

In this article, I carried out PL characterisation and device characterisation and fabrication with help from others in my group at Cardiff. External research collaborators performed epitaxy and TEM characterisations. Excluding the section on TEM characterisation, all of the paper was written by me.

[2] **D. C. M. Kwan**, M. Kesaria, E. A. Anyebe, & D. Huffaker, Recent trends in 8–14 μm type-II superlattice infrared detectors. *Infrared Phys. Technol.* **116**, 103756 (2021).

I planned, structured, and wrote all of this review paper with feedback from other group members.

[3] **D. C. M. Kwan**, M. Kesaria, E. A. Anyebe, D. O. Alshahrani, M. Delmas, B. L. Liang, & D. L. Huffaker, Optical and structural investigation of a 10 μm InAs/GaSb type-II superlattice on GaAs. *Appl. Phys. Lett.* **118**, 203102 (2021).

I performed all PL and Nomarski characterisations for this article. External research collaborators performed the growth and XRD characterisation and I analysed the data. I wrote all of the paper with feedback from colleagues.

[4] M. Delmas, **D. C. M. Kwan**, M. C. Debnath, B. L. Liang, & D. L. Huffaker, Flexibility of Ga-containing Type-II superlattice for long-wavelength infrared detection. *J. Phys. D* **52**, 475102 (2019).

I assisted in the PL and device characterisation and analysis for this article. I also provided my feedback on the manuscript.

The two publications listed below are other research works done by the author and are not directly relevant to this thesis.

[5] M. Kesaria, D. O. Alshahrani, **D. C. M. Kwan**, E. A. Anyebe, & V. Srivastava, Optical and electrical performance of 5 μm InAs/GaSb Type-II superlattice for NO_x sensing application. *Mater. Res. Bull.* **142**, 111424 (2021).

I performed the band structure simulation and device performance modelling described in this article and wrote the corresponding sections. I also gave feedback on the writing and structure of the article.

[6] J. Huang, C. Zhao, B. Nie, S. Xie, **D. C. M. Kwan**, X. Meng, Y. Meng, D. L. Huffaker, & W. Ma, High-performance mid-wavelength InAs avalanche photodiode using $\text{AlAs}_{0.13}\text{Sb}_{0.87}$ as the multiplication layer. *Photonics Res.* **8**, 755 (2020).

I performed some electrical characterisation for this paper.

Papers presented in conferences:

D. C. M. Kwan, M. Kesaria, Emerging Type-II Superlattices (T2SL) for Infrared Detectors. *Photon 2022* (2022). [Scheduled for 31/08/22]

D. C. M. Kwan, M. Kesaria, J. J. Jiménez, V. Srivastava, M. Delmas, B. L. Liang, F. M. Morales, D. L. Huffaker, Influence of the Interfacial Misfit Array for 10 μm InAs/GaSb Type-II Superlattice Diodes on GaAs Substrates. *Semiconductor Integrated Optoelectronics (SIOE)* (2022).

D. C. M. Kwan, D. O. Alshahrani, E. A. Anyebe, D. L. Huffaker, & M. Kesaria, Type-II InAs/GaSb superlattices on GaAs for 10 μm infrared detection. Mid-Infrared Optoelectronic Materials and Devices (MIOMD) (2021).

D. C. M. Kwan, M. Kesaria, D. L. Huffaker, Optical and structural characterisations of a long-wavelength infrared InAs/GaSb superlattice on GaAs. *Semiconductor Integrated Optoelectronics (SIOE)* (2021).

D. C. M. Kwan, M. Delmas, B. Liang, & D. Huffaker, A comparative study of period composition and thickness of type-II InAs/GaSb superlattices for long-wavelength infrared detectors. UK Semiconductors (2019).

D. C. M. Kwan, M. Delmas, B. Liang, & D. Huffaker, Growth and characterisation of long-wavelength Type-II InAs/GaSb superlattice infrared detectors. *Semiconductor Integrated Optoelectronics (SIOE)* (2019).

Contents

0. Introduction.....	1
0.1. Infrared detectors.....	1
0.2. Mercury cadmium telluride and type-II superlattices.....	1
0.3. Thesis overview.....	2
1. Background.....	4
1.1. Long-wavelength infrared radiation.....	4
1.2. Infrared detectors.....	6
1.3. Type-II superlattice detectors.....	8
1.4. Figures of merit.....	12
1.4.1. Quantum efficiency.....	12
1.4.2. Responsivity.....	13
1.4.3. Noise equivalent power.....	13
1.4.4. Specific detectivity.....	14
1.5. Sources of dark current.....	14
1.6. Background-limited infrared photodetection.....	15
1.7. Linear and focal plane arrays.....	16
1.7.1. Modulation transfer function.....	16
1.7.2. Noise equivalent temperature difference.....	17
2. Motivation.....	19
2.1. Performance comparison of MCT and T2SLs.....	19
2.1.1. Dark current.....	19
2.1.2. Diffusion length in LWIR T2SLs.....	20
2.1.3. Minority carrier lifetime.....	23
2.2. Aims and objectives of current work.....	26
2.2.1. Growth on GaAs substrates.....	26
2.2.2. Simulations and band-structure engineering.....	31
2.2.3. Fabrication developments.....	33
3. Research tools.....	37
3.1. Simulation.....	37
3.1.1. k.p. theory.....	37

3.1.2. Spurious solutions.....	39
3.1.3. Numerical realisation.....	39
3.1.4. Implementation in Nextnano ³	40
3.1.5. Validation of the simulation tool.....	42
3.2. MBE Growth.....	54
3.2.1. The MBE reactor.....	54
3.2.2. <i>In-situ</i> characterisation.....	57
3.3. Fabrication.....	59
3.4. Characterisation.....	64
3.4.1. Nomarski microscopy.....	64
3.4.2. X-ray diffraction.....	65
3.4.3. Scanning electron microscopy.....	67
3.4.4. Transmission electron microscopy.....	68
3.4.5. Energy dispersive X-ray spectroscopy.....	69
3.4.6. Photoluminescence.....	70
3.4.7. Electrical characterisation.....	72
Appendix to Chapter 3: The NEWPIN mask.....	73
4. Flexibility of LWIR InAs/GaSb Type-II Superlattices.....	78
4.1. InAs/GaSb reference samples.....	78
4.1.1. Design and Growth.....	78
4.1.2. X-ray Diffraction.....	83
4.1.3. Photoluminescence.....	86
4.1.4. Band structure simulations.....	92
4.2. InAs/GaSb devices.....	98
4.2.1. Design and growth.....	98
4.2.2. X-ray diffraction.....	99
4.2.3. Photoluminescence.....	101
4.2.4. Device fabrication.....	102
4.2.5. Electrical characterisation.....	104
4.3. Summary.....	111
5. LWIR InAs/GaSb T2SLs on GaAs substrates.....	113
5.1. Introduction.....	113

5.2 Samples.....	113
5.3. X-ray diffraction.....	114
5.4. Nomarski microscopy.....	116
5.5. Transmission electron microscopy.....	117
5.6. Photoluminescence.....	124
5.7. A T2SL PIN diode on GaAs.....	134
5.8. Comparison of 12/4 and 14/7 T2SLs on GaAs.....	141
5.9. Summary.....	150
6. Fabrication.....	152
6.1. Dry etching.....	152
6.1.1. Process and recipe development.....	153
6.1.2. Device fabrication.....	168
6.2. Passivation.....	175
6.3. Summary.....	176
7. Conclusion.....	177
7.1. T2SL layer thicknesses.....	177
7.2. InAs/GaSb T2SLs on GaAs.....	179
7.3. Dry etching and passivation.....	181
7.4. Future work.....	181
References.....	184

List of abbreviations

A7	Auger 7
AES	Auger electron spectroscopy
AIM	AIM Infrarot Module GmbH
ALD	Atomic layer deposition
APT	Atom probe tomography
AR	Anti-reflection
ARL	U.S. Army Research Laboratory
ASU	Arizona State University
BLIP	Background-limited infrared photodetection
CAR	Continuous azimuthal rotation
CQD	Centre for Quantum Devices
DIC	Differential interface contrast
DRS	DRS Infrared Technologies
EBIC	Electron-beam induced current
EBR	Edge bead removal
EM	Electromagnetic
EQE	External quantum efficiency
ETBM	Empirical tight-binding model
FIB	Focused ion beam
FPA	Focal plane array
FTIR	Fourier transform infrared spectrometer

FWHM	Full width at half maximum
G-R	Generation-recombination
HOT	High operating temperature
HR(S)TEM	High-resolution (scanning) transmission electron microscopy
HRTEM	High-resolution transmission electron microscopy
IF	Interface
IMF	Interfacial misfit
IPA	Isopropanol alcohol
IR	Infrared
JPL	Jet Propulsion Laboratory (USA)
LDA	Linear detector arrays
LHe	Liquid helium
LN2	Liquid nitrogen
LWIR	Long-wavelength infrared
MBE	Molecular beam epitaxy
MCT	Mercury Cadmium Telluride
MEE	Migration enhanced epitaxy
MIS	Metal-insulator-semiconductor
MO	Metalorganic
MOCVD	Metalorganic chemical vapour deposition
MTF	Modulation transfer function
MWIR	Mid-wavelength infrared
n.i.d.	non-intentionally doped

NASA	National Aeronautics and Space Administration (USA)
NEI	Noise equivalent irradiance
NEP	Noise equivalent power
NETD	Noise equivalent difference temperature
$NE\Delta\Phi$	Noise equivalent flux
NIR	Near infrared
NVESD	U.S. Army Night Vision and Electronic Sensors Directorate
PC	Photoconductive
PECVD	Plasma enhanced chemical vapour deposition
PL	Photoluminescence
PV	Photovoltaic
QD	Quantum dots
QE	Quantum efficiency
QW	Quantum well
RHEED	Reflection high-energy electron diffraction
RSEMI	Reticulated shallow etch mesa isolation
SBU	Stony Brook University (USA)
SCD	Semiconductor devices (Israel)
SNL	Sandia National Laboratories
SNR	Signal-to-noise ratio
SPM	Scanning probe microscopy
SRH	Shockley-Read-Hall
STIP	Shanghai Institute of Technical Physics

STM	Scanning tunnelling microscopy
StP	St. Petersburg State Polytechnical University (Russia)
SWaP	Size, weight, and power
SWIR	Short-wavelength infrared
T2SL	Type-II superlattice
TAT	Trap-assisted tunnelling
TE	Thermoelectric
TEM	Transmission electron microscopy
TMR	Time-resolved-microwave-reflectance
Ulowa	University of Iowa
VLWIR	Very long-wavelength infrared
XRD	X-ray diffraction

List of Figures

Figure 1.1: Planck's curves for black bodies of various temperatures.

Figure 1.2: Transmission of IR radiation through the atmosphere.

Figure 1.3: Schematic of a photoconductive detector.

Figure 1.4: Schematic of a photovoltaic detector.

Figure 1.5: (a) Heterostructure band alignment types (b) The band alignment of the 6.1 Å family of compound semiconductors.

Figure 2.1: Collected values of the dark current density at 77 K for long-wavelength infrared type-II superlattice detectors compared with 'Rule 07' for HgCdTe Detectors.

Figure 2.2: Collected values of external quantum efficiency vs active region thickness for recent (2018-2020) superlattice-based and MCT-based long-wavelength infrared detectors.

Figure 2.3: Collected minority carrier lifetimes vs cut of wavelength for Ga-free and Ga-containing type-II superlattices and HgCdTe.

Figure 2.4: Schematic of an optically immersed T2SL detector.

Figure 2.5: Schematic of an interfacial misfit array at a GaSb-on-GaAs interface.

Figure 2.6: Schematic of the LWIR T2SL on GaAs reported by Müller et al.

Figure 2.7: The (a) forward graded, (b) overshoot graded, (c) jump graded, and (d) reverse graded approaches to the linearly graded metamorphic buffer layer.

Figure 3.1: (a) The band structure, (b) electron and hole wavefunctions, and (c) E-k diagram for an example SL.

Figure 3.2: Comparison of band gap energies for four samples of different Sb content as measured by PL at Lancaster, simulations at Lancaster, and simulations performed in this work.

Figure 3.3: Schematic diagram of the M structure SL as proposed by Nguyen et al. Coloured regions show the forbidden energy gap.

Figure 3.4: Comparison of simulated and measured band gaps for various T2SL M-structures. Structures have A ML InAs/ B ML GaSb/ C ML AlSb/ D ML GaSb.

Figure 3.5: Simulated band diagrams for a (a) 13/2.5/1/2.5 SL, (b) 13/5 SL, and (c) 13/17 SL.

Figure 3.6: The electron effective masses for various M-structure SLs as calculated by (a) 8 band k·p theory and (b) the empirical tight binding model.

Figure 3.7: 8 band k·p simulation for a 19 ML InAs/ 16 ML GaSb/ 2 ML AlSb SL for (a) the effect of the position on the AlSb barrier on the conduction and valence bands and (b) the effect of the AlSb position on the energy gap and wavelength.

Figure 3.8: 8 band k·p simulations of the band structure for (a) WSL-A and (b) WSL-B.

Figure 3.9: A comparison of the band structure simulation results of this work and that of Aifer et al. for W-structure SLs with 5 ML AlSb/ N ML InAs/9 ML $\text{In}_x\text{Ga}_{1-x}\text{Sb}$ / N ML InAs.

Figure 3.10: 8 band k·p simulations of the band structure for a) a 13 ML InAs/7 ML GaSb SL and b) a 13 ML $\text{InAs}_{0.91}\text{Sb}_{0.09}$ /7 ML $\text{In}_{0.5}\text{Ga}_{0.5}\text{As}_{0.46}\text{Sb}_{0.54}$ SL.

Figure 3.11: Schematic of a typical MBE reactor.

Figure 3.12: RHEED intensity oscillations during the growth of one monolayer.

Figure 3.13: Schematic of a typical ellipsometry unit.

Figure 3.14: Schematic of a typical PIN diode before fabrication.

Figure 3.15: (a) Schematic and (b) optical image of a sample after Step 3 of fabrication. The green circle highlights the photoresist undercut.

Figure 3.16: (a) Schematic and (b) optical image of a sample after Step 4 of fabrication.

Figure 3.17: (a) Schematic and (b) optical image of a sample after Step 5. Of fabrication.

Figure 3.18: (a) Schematic and (b) optical image of a sample after Step 6. Of fabrication.

Figure 3.19: (a) Schematic, (b) optical image, and (c) SEM micrograph of a sample after Step 7 of fabrication.

Figure 3.20: Schematic diagram of a Nomarski microscope.

Figure 3.21: Schematic of XRD in a crystal lattice, taken from.

Figure 3.22: The schematic arrangement of an X-ray diffractometer.

Figure 3.23: Schematic of a typical SEM unit.

Figure 3.24: Schematic of a typical TEM unit.

Figure 3.25: Schematic diagram of the PL process.

Figure 3.26: Schematic of the experimental set up used for PL experiments.

Figure 3.27: Schematic representation of the cryogenic probe station experimental set-up.

Figure 3.28: Optical micrograph of the Top Contact panel of the NEWPIN mask. The red circle highlights alignment markers.

Figure 3.29: Optical micrograph of the Mesa panel of the NEWPIN mask. The red circle highlights alignment markers.

Figure 3.30: Optical micrograph of the SU8 panel of the NEWPIN mask. The red circle highlights alignment markers.

Figure 3.31: Optical micrograph of the Lower Contact panel of the NEWPIN mask. The red circle highlights alignment markers.

Figure 3.32: Optical micrograph of the SINX panel of the NEWPIN mask. The red circle highlights alignment markers.

Figure 3.33: Optical micrograph of the AR Coating panel of the NEWPIN mask.

Figure 4.1: The Energy gap and lattice constant for selected III-V semiconductors. The lattice mismatch of InAs and InSb to GaSb is also shown.

Figure 4.2: The shutter sequences used for the samples in this study. The duration of the In-Soak was determined from the SL period.

Figure 4.3: The structural schematic for the LWIR InAs/GaSb T2SLs.

Figure 4.4: XRD rocking curves, taken around the GaSb (004) reflection for (a) Sample A, (b) Sample B, (c) Sample C, and (d) Sample D.

Figure 4.5: $2\sin(\theta_n)/\lambda$ of each SL satellite peak as a function of the satellite order.

Figure 4.6: PL profiles for $T = 77 - 180$ K for (a) Sample A, (b) Sample B, (c) Sample C, (d) Sample D.

Figure 4.7: The temperature dependant band gap energy of each T2SL sample and Varshni equation fits.

Figure 4.8: (a) Integrated PL and (b) FWHM as a function of temperature for each SL sample.

Figure 4.9: Schematic showing the non-radiative recombination process present in the SL structures. Coloured regions represent forbidden gaps, taken from Reference ¹⁷¹.

Figure 4.10: Measured and simulated cut-off wavelengths for different SL structures.

Figure 4.11: Simulated $E(k)$ diagrams for a (a) 10/4, (b) 12/4, (c) 14/4, and (d) 14/7 SL structure for the in-plane direction along $[1\ 0\ 0]$ in the Brillouin zone.

Figure 4.12: Band structure simulations in real space for (a) Sample A, (b) Sample B, (c) Sample C, and (d) Sample D.

Figure 4.13: The wavefunction overlaps for the 10/4, 12/4, and 14/4 SL structures.

Figure 4.14: Structural Schematic for the PIN diode structures described in this chapter.

Figure 4.15: XRD rocking curves, taken around the GaSb (004) reflection for (a) 14/7 SL, and (b) 12/4 SL PIN diodes.

Figure 4.16: PL profiles as a function of temperature for (a) 14/7 SL and (b) 12/4 SL.

Figure 4.17: The PL peak as a function of temperature fitted to Equation 4.2.

Figure 4.18: (a) Optical microscopy image of fabricated diodes, (b) SEM image of a mesa sidewall, (c) structural schematic of a fabricated diode.

Figure 4.19: Dark current density as a function of applied bias for samples with etching depths of 760 nm and 1130 nm.

Figure 4.20: Dark current density vs applied bias for every fabricated diode on (a) Sample E and (b) Sample F.

Figure 4.21: Dark current density as a function of applied bias for (a) $\phi = 140 \mu\text{m}$, Sample E (b) $\phi = 140 \mu\text{m}$, Sample F, (c) $\phi = 240 \mu\text{m}$, Sample E, (d) $\phi = 240 \mu\text{m}$, Sample F.

Figure 4.22: Dark current density measured at -50 mV as an inverse function of temperature for (a) Sample E and (b) Sample F diodes. Diffusion and G-R currents are plotted by the blue dashed and red dotted lines respectively.

Figure 4.23: (a) capacitance vs voltage and (b) $1/C^2$ vs voltage for each SL diode.

Figure 4.24: I-V profiles and fitting for (a) Sample E and (b) Sample F for a 140 μm diameter diode at 77 K.

Figure 4.25: Measured and simulated current density profiles for the temperature range 77 K – 200 K for (a) Sample E and (b) Sample F.

Figure 4.26: The minority carrier lifetimes extracted from Figure 4.25 for (a) Sample E and (b) Sample F.

Figure 5.1: (a) XRD rocking curves and (b) an enhanced view of the SL_0 peak for both Samples B and G.

Figure 5.2: $2 \cdot \sin(\theta_n) / \lambda$ of each SL satellite peak as a function of the satellite order.

Figure 5.3: Representative Nomarski micrographs from (a) Sample B and (b) Sample G.

Figure 5.4: CTEM micrographs from a) the T2SL layer of Sample A, (b) the GaSb substrate of Sample B, and (c) the whole heterostructure of Sample G.

Figure 5.5: Two-beam, bright-field diffraction contrast TEM micrograph of the whole structure of Sample G.

Figure 5.6: HRTEM micrographs of the T2SL layers of (a) Sample B and (b) Sample G.

Figure 5.7: The GaSb-on-GaAs IF of Sample G as observed by (a) CTEM and (b) HRTEM.

Figure 5.8: (a) FFT filtered image of Figure 5.7b and (b) – (e)enlarged images of the indicated areas.

Figure 5.9: For (a) – (f) Samples B and (g) – (l) G and from left to right: STEM-HAADF image from a region around the middle layers of the T2SL, spectrum image combining atomic percentage maps by In, As, Ga, and Sb and individual maps for each element, including some thickness measurements. EDX integrated atomic percentage spectrum profiles registered from the bottom to the top of the mapped areas shown after filtering them, in (m) Sample B and (n) Sample G.

Figure 5.10: Normalised PL profiles at 77 K for Samples B and G.

Figure 5.11: PL profiles at 77 K with fitted Gaussians and the envelope functions thereof for (a) Sample B and (b) Sample G.

Figure 5.12: The normalised PL spectra for (a) Sample B and (b) Sample G from 77 K – 240 K.

Figure 5.13: Measured energy band gap as a function of temperature and fitted Varshni equation for both samples.

Figure 5.14: Integrated PL intensity as a function of temperature for Samples B and G.

Figure 5.15: PL FWHM vs temperature for Samples B and G as determined by (a) no fitting and (b) Voigt fitting.

Figure 5.16: Integrated PL intensity as a function of the power of the pump laser for Samples B and G.

Figure 5.17: PL mapping for selected spots on (a) Sample B and (b) Sample G.

Figure 5.18: (a) XRD rocking curves and (b) an enhanced view of the SL_0 peak for both Samples F and H.

Figure 5.19: Normalised PL signal for Samples F and H.

Figure 5.20: The I-V profiles for the temperature range 77 K – 150 K of a 140 μm diameter diode for (a) Sample F and (b) Sample H. (c) The corresponding Arrhenius for Samples F and H.

Figure 5.21: I-V profiles and fitting for a (a) Sample F and (b) Sample H for a 140 μm diameter diode at 77 K.

Figure 5.22: The forward bias and fitted diode equation for (a) Sample F and (b) Sample H.

Figure 5.23: SEM micrographs of the mesa sidewalls of (a) Sample F and (b) Sample H.

Figure 5.24: XRD rocking curves for Samples H and I.

Figure 5.25: PL spectra at 77 K for Samples D and E.

Figure 5.26: The I-V profile over the temperature range 77 K – 150 K for (a) a 440 μm 12/4 T2SL diode, (b) a 440 μm 14/7 T2SL diode, (d) a 240 μm 12/4 T2SL diode, (e) a 240 μm 14/7 T2SL diode, (g) a 140 μm 12/4 T2SL diode, and (h) a 140 μm 14/7 T2SL diode. Figures (c), (f), and (i) show the Arrhenius plots of 440 μm , 240 μm , and 140 μm diameter diodes respectively.

Figure 5.27: Dark current density at -50 mV as a function of device diameter for Samples H and I.

Figure 5.28: The measured current density at -50 mV at 77 K as a function of the Perimeter/Area for (a) Sample H and (b) Sample I.

Figure 5.29: I-V profiles and fitting for a (a), (c), and (e) Sample H and (b), (d), and (f) Sample I for a 140 μm diameter diode at 77 K.

Figure 5.30: The (a) shunt and (b) TAT currents at -50 mV as a function of perimeter/area extracted from Figure 5.22 for Samples H and I.

Figure 6.1: Schematic of the Ni etch mask process (Process 1).

Figure 6.2: SEM micrographs of mesa sidewalls etched using Etch 1.

Figure 6.3: SEM micrographs of mesa sidewalls etched using Etch 2. The red oval highlights suspected micromasking and the blue oval highlights a shelf.

Figure 6.4: Schematic of an SiO₂ etch mask process (Process 2).

Figure 6.5: Optical micrographs of the Sample fabricated under Process 2 (a) after the RIE etch of SiO₂ (Step 5) and (b) after the removal of the Ni mask (Step 6).

Figure 6.6: Schematic of an updated SiO₂ etch mask process (Process 3a).

Figure 6.7: Optical micrographs of the Si test sample undergoing Process 3a following photolithography (Step 3). (a) shows a stitched image of the whole sample and (b) shows a close-up of one stripe.

Figure 6.8: Optical micrographs of the Si test sample undergoing Process 3b following photolithography (Step 3). (a) shows a stitched image of the whole sample and (b) shows a close-up of one stripe.

Figure 6.9: Optical micrographs of the Si test sample undergoing Process 3c following photolithography (Step 3). (a) shows a stitched image of the whole sample and (b) shows a close-up of one stripe.

Figure 6.10: SiO₂ strips on Si, fabricated using Process 3c, measured by (a) SEM, (b) optical microscopy, and (c) DEKTAK profilometry.

Figure 6.11: Representative SEM micrographs of the sidewalls and profiles of a T2SL sample processed using Process 3c and etched using Recipe 1.

Figure 6.12: Representative SEM micrographs of the sidewalls and profiles of a T2SL sample processed using Process 3c and etched using Recipe 3.

Figure 6.13: Representative SEM micrographs of the sidewalls and profiles of a T2SL sample processed using Process 3c and etched using Recipe 4.

Figure 6.14: Representative SEM micrographs of the sidewalls and profiles of a T2SL sample processed using Process 3c and etched using Recipe 5.

Figure 6.15: An (a) optical and (b) SEM micrograph of the SiN etch mask deposited on a T2SL sample using Process 3d.

Figure 6.16: Representative SEM micrographs of the sidewalls and profiles of a T2SL sample processed using Process 3d and etched using Recipe 5.

Figure 6.17: Optical micrograph of a LWIR T2SL fabricated using the dry etch.

Figure 6.18: I-V profiles at 77 K for a 140 μm diameter device fabricated using the wet etch and dry etch approaches.

Figure 6.19: The measured I-V profile and diode equation fit for the dry etched sample (a) before and (b) after cleaning of photoresist protection.

Figure 6.20: Temperature dependant I-V profiles for (a) the wet etched reference sample, (b) the dry etched sample before cleaning, and (c) the dry etched sample after cleaning and photoresist protection.

Figure 6.21: The Arrhenius plot for the wet etched reference sample, the dry etched sample before cleaning, and the dry etched sample after cleaning and photoresist protection.

Figure 6.22: I-V fitting at 77 K for (a) the wet etched reference sample, (b) the dry etched sample before cleaning, and (c) the dry etched sample after cleaning and photoresist protection.

Figure 6.23: Dark current density at -50 mV as a function of the perimeter/area ratio for (a) the wet etched sample and (b) the dry etched sample after cleaning and photoresist protection.

Figure 7.1: The dark current density of the diodes reported in Chapter 4 of this work compared with T2SLs and Rule 07 as reported in Figure 2.1.

List of Tables

Table 2.1: Summary of the key objects of this project.

Table 3.1: Material parameters of InAs, GaSb, and InSb binaries used in Nextnano³ for the k·p band structure calculation. All values used can be found in Refs. ¹⁴⁶, ¹⁴⁷, ¹⁴⁸, and ¹⁴⁹.

Table 3.2: Summary of InAs/InAsSb T2SL sample structures.

Table 3.3: Parameters extracted from 8 band k·p simulations for WSL-A and -B.

Table 3.4: Parameters extracted from 8 band k·p simulations for the structures in Figure 3.10.

Table 4.1: The shutter sequence used for the absorber region of each superlattice structure.

Table 4.2: The lattice mismatch, FWHM, and period thickness for each SL sample as determined by XRD measurements.

Table 4.3: Parameters extracted from PL vs T measurements for each SL sample.

Table 4.4: Parameters extracted from band structure simulations of different SL structures.

Table 4.5: Parameters extracted from XRD rocking curves for each SL diode.

Table 4.6: Parameters extracted from PL measurements of the SL diodes.

Table 5.1: Parameters extracted from XRD measurements of Samples B and G.

Table 5.2: Parameters for peaks fitted to the PL profiles of Samples A and B.

Table 5.3: Parameters extracted from PL FWHM analysis for both samples.

Table 5.4: Parameters extracted from XRD measurements for Samples A, B, C, and D.

Table 5.5: Parameters extracted from XRD measurements for Samples H and I.

Table 6.1: Summary of dry etching processes, recipes, and results.

List of Samples

The following table provides an overview of the samples used throughout this work. The sample names presented are kept consistent throughout the thesis.

Sample name	T2SL Period	Substrate	Design	First occurrence
Sample A	10/4	GaSb	Reference	Section 4.1.1
Sample B	12/4	GaSb	Reference	Section 4.1.1
Sample C	14/4	GaSb	Reference	Section 4.1.1
Sample D	14/7	GaSb	Reference	Section 4.1.1
Sample E	14/7	GaSb	PIN Diode	Section 4.2.1
Sample F	12/4	GaSb	PIN Diode	Section 4.2.1
Sample G	12/4	GaAs	Reference	Section 5.2
Sample H	12/4	GaAs	PIN Diode	Section 5.2
Sample I	14/7	GaAs	PIN Diode	Section 5.2

0. Introduction

0.1. Infrared detectors

Infrared (IR) detectors enable observation of electromagnetic (EM) radiation invisible to both the naked eye and conventional cameras. As a result, IR detectors have become vital for both military and civilian applications, leading to a predicted market value of over USD 6.8 billion per year by 2023¹. Long-wavelength infrared (LWIR) detectors are among the most pursued types of IR detectors due to their unmatched suitability to thermal imaging applications.

The range of military applications for LWIR detectors is broad, with devices installed in joint strike fighters, missile defence systems, warships, surface to air missiles, attack helicopters and many more². LWIR detectors therefore enable users to see, acquire, and target opposing forces in any light and under adverse battlefield conditions, detect explosive hazards, and protect troops and installations from enemy intrusion³. LWIR detectors are also used for satellite-mounted earth-observation applications such as environmental modelling, meteorology, and surveillance. Access to the LWIR wavelength range is also important for scientific and industrial applications such as gas sensing, medical imaging, and spectroscopy.

Each of these applications requires high performance, low cost, high yield, high uniformity, high operability, and high stability operation. Furthermore, the prevalence of space and defence applications for LWIR detectors make reduced size, weight, and power (SWaP) hugely important. This can be achieved through fabrication of detector elements that do not require bulky cooling systems for high performance operation.

0.2. Mercury cadmium telluride and type-II superlattices

The state-of-the-art material system for LWIR detectors is Mercury Cadmium Telluride (HgCdTe or MCT). This is due to its low dark current, easily tuneable band gap energy, high

quantum efficiency (QE), and mature fabrication technology. Unfortunately, MCT suffers from high costs, fabrication difficulties, low uniformity, and increasing restrictive regulations, which motivate the search for an alternative material system for LWIR detectors⁴. Furthermore, MCT is unlikely to achieve the high operating temperature (HOT) performance required for low SWaP applications. The InAs/GaSb type-II superlattice (T2SL), first proposed by Sai-Halasz and Esaki⁵, is an alternative material system which many believe can challenge MCT for supremacy in the LWIR detector market. These hopes are buoyed by high theoretical performance limits, good wavelength tuneability, lower costs, easier fabrication, greater uniformity, and less restrictive regulations^{6,7}. Unfortunately, however, the performance levels of T2SLs still lag behind those of MCT. There is therefore a great deal of research effort aimed towards enabling T2SLs to achieve their theoretically predicted performance levels and thereby surpass MCT to become the basis for the next generation of HOT LWIR detectors.

The work described herein therefore explores various novel techniques for improving the performance of LWIR T2SL detectors. Optimisation of the T2SL period, growth on GaAs substrates, optimisation of the fabrication process, and simulations of experimental designs are all examined and appraised.

0.3. Thesis overview

This thesis is organised as follows:

Chapter 1 provides an introduction to the fundamental physics behind LWIR T2SL-based detectors. This includes an introduction to IR radiation, a description of different detector types, and the operation and history of the T2SL. The figures of merit and major sources of dark current for IR detectors are also described. Finally, the principles of focal plane array operation, including appropriate figures of merit, are provided.

Chapter 2 compares the performance levels of state-of-the-art MCT- and T2SL-based LWIR detectors. A review of the literature covering the fundamental properties of T2SLs is performed to explain the present dominance of MCT. A sampling of techniques aimed at

improving the performance of T2SLs is then provided. Based on this review, the aims and objectives of the present work are described.

Chapter 3 provides the technical details of the techniques and processes employed to pursue the aims and objectives described in Chapter 2. This includes simulation, growth, fabrication, and characterisation.

Chapter 4 reports on optimisation of the T2SL period for high performance, high operating temperature LWIR applications. Novel T2SL designs were grown by molecular beam epitaxy and compared to a conventional design in a structural and optical characterisation study. Selected designs were then used for growth of T2SL PIN diodes for a comparative device characterisation study. The results of this study are used to develop a simulation tool capable of accurately predicting the band parameters of any given InAs/GaSb T2SL structure. Finally, a novel T2SL PIN diode is grown, fabricated, characterised and compared to a conventional design.

Chapter 5 reports on the growth of a LWIR T2SL on a GaAs substrate using an interfacial misfit (IMF) array. Following growth of a reference sample on a GaSb substrate, a comparative material, optical, and device characterisation was performed enabling a detailed appraisal of the efficacy of the IMF array for achieving heteroepitaxial growth.

Chapter 6 outlines the development of a dry etching process capable of replacing the wet etch process used for the devices in Chapters 4 and 5. A comparative characterisation study is performed to determine the advantages and disadvantages of this approach.

Finally, Chapter 7 recounts the key conclusions of the current work, and pointers for future work.

1. Background

This chapter introduces the basic principles of LWIR radiation and detection. The working principles of different detector types are outlined with reference to their suitability for various applications. The T2SL is introduced and its underlying physical principles, history of development from the 1970's, and notable variations are all outlined. Dark current contributions, figures of merit, and performance limits for IR detectors are also described.

1.1. Long-wavelength infrared radiation

All objects with a temperature above absolute zero emit electromagnetic radiation known as blackbody radiation. A blackbody is a hypothetical concept of an entity which absorbs and reemits all energy with perfect efficiency. There are three main laws for describing the black body radiation emitted from such an entity:

- Planck's law⁸

This law describes the probability distribution of the wavelengths of the photons emitted from the body. The distribution varies with temperature and is written as:

$$W(\lambda, T) = \frac{2\pi hc^2}{\lambda^5} \cdot \frac{1}{e^{\frac{hc}{\lambda k_B T}} - 1}, \quad (1.1)$$

where W is the spectral radiance of a body, T is the temperature, h is the Planck's constant, k_B is the Boltzmann constant, c is the speed of light, and λ is the wavelength of the photons. Its units are (W/m²/μm). Figure 1.1 shows the Planck's curves for radiation emitted from blackbodies of various temperature.

- Wien's law⁸

Wien's law gives the relationship between the temperature of a black body and its peak wavelength, λ_{max} , given by:

$$\lambda_{max} = \frac{2898}{T}. \quad (1.2)$$

Wien's law is shown, superimposed on top of Planck's law, in Figure 1.1.

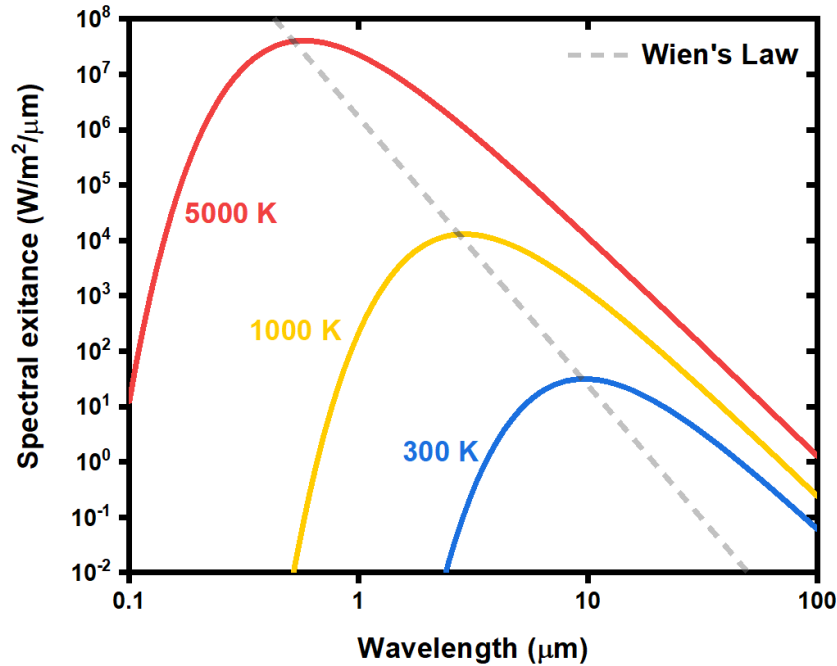


Figure 1.1: Planck's curves for black bodies of various temperatures.

- Stefan-Boltzmann law⁸

The Stefan-Boltzmann law provides an estimate of the total energy radiated per unit area per unit time by a black body of temperature T and is given by:

$$M = \sigma \cdot T^4, \quad (1.3)$$

where σ is the Stefan-Boltzmann constant equal to $5.67 \times 10^{-12} \text{ W}\cdot\text{cm}^{-2}\cdot\text{K}^{-4}$.

As shown in Figure 1.1, black body objects around room temperature (300 K) emit electromagnetic radiation with a peak wavelength of around $10 \mu\text{m}$. This wavelength is therefore of special interest in a variety of imaging applications. However, as practical applications require detection of EM radiation through the atmosphere, it is also important to consider the absorption of the atmospheric media through which this radiation propagates. Figure 1.2 shows the transmission of IR radiation through the atmospheric media which gives rise to the different atmospheric windows of transmission. These include near infrared (NIR)

radiation corresponding to 0.7 μm – 1.5 μm , short-wavelength infrared (SWIR) radiation corresponding to 1.5 μm – 2.5 μm , mid-wavelength infrared (MWIR) radiation corresponding to 3 μm – 5 μm , LWIR radiation corresponding to 8 μm – 12 μm , and very long-wavelength infrared (VLWIR) radiation corresponding to 12 μm – 32 μm .

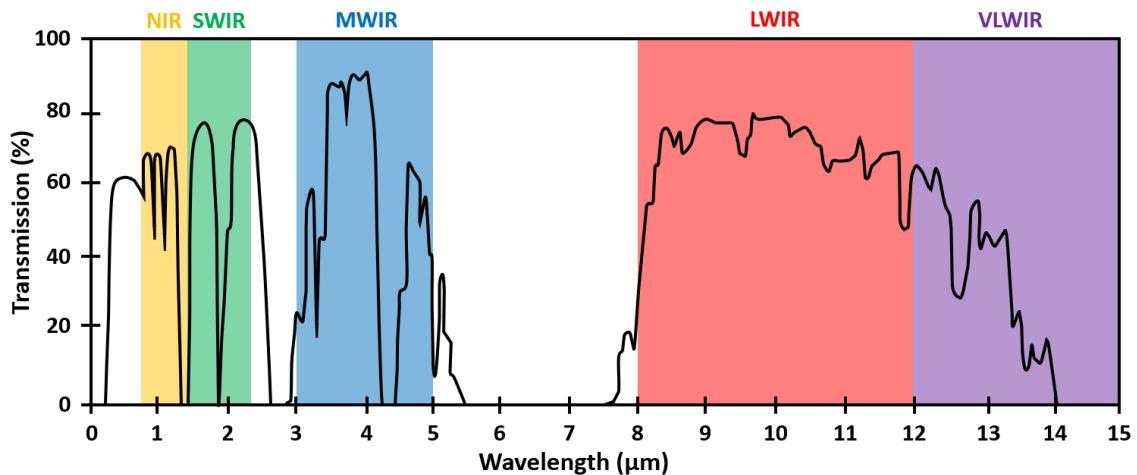


Figure 1.2: Transmission of IR radiation through the atmosphere.

It can therefore be seen that radiation around 10 μm in wavelength has excellent atmospheric transmission and is therefore ideal for thermal imaging.

1.2. Infrared detectors

A LWIR detector is a device which transduces energy from incident LWIR radiation into another form, usually electrical. This can be achieved using two classes of detectors: thermal detectors and photon detectors (or photodetectors). Thermal detectors, such as micro bolometers or pyroelectric detectors, rely on the increase in temperature of the detector brought about by the absorption of radiation. This then gives rise to a measurable change in the physical or electrical properties of the detector, such as resistance or capacitance. Photodetectors operate on the principle of photoexcitation, whereby an interaction between an incident photon of sufficient energy and a bound electron results in the generation of a free electrical carrier which can be detected using electrical circuitry. As operation of a photodetector does not require the heating of the detector by the absorbed radiation, these devices are preferred for any application in which a fast time response is necessary and are the focus of the present thesis.

Photodetectors can be classified into two distinct classes: photoconductive (PC) and photovoltaic (PV). In PC detectors, the conductivity of the detector is increased by the creation of photogenerated carriers. As shown in Figure 1.3, these carriers are then collected by electrical contacts. Here, E_C , E_V , and E_F , represent the energy levels of the conduction band, valance band, and fermi level respectively.

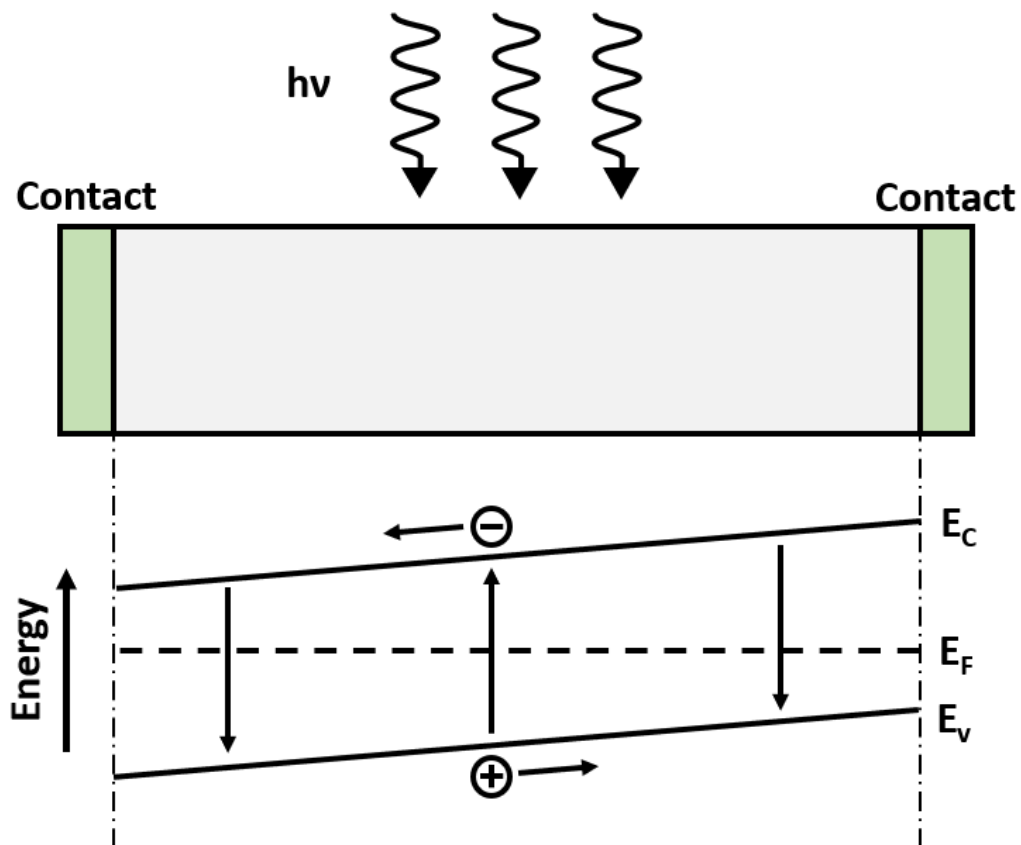


Figure 1.3: Schematic of a photoconductive detector.

A schematic of a PV detector is shown in Figure 1.4. Here, the doping of the device produces an electric field which gives rise to an electromotive force which drives the photogenerated carriers to the contacts.

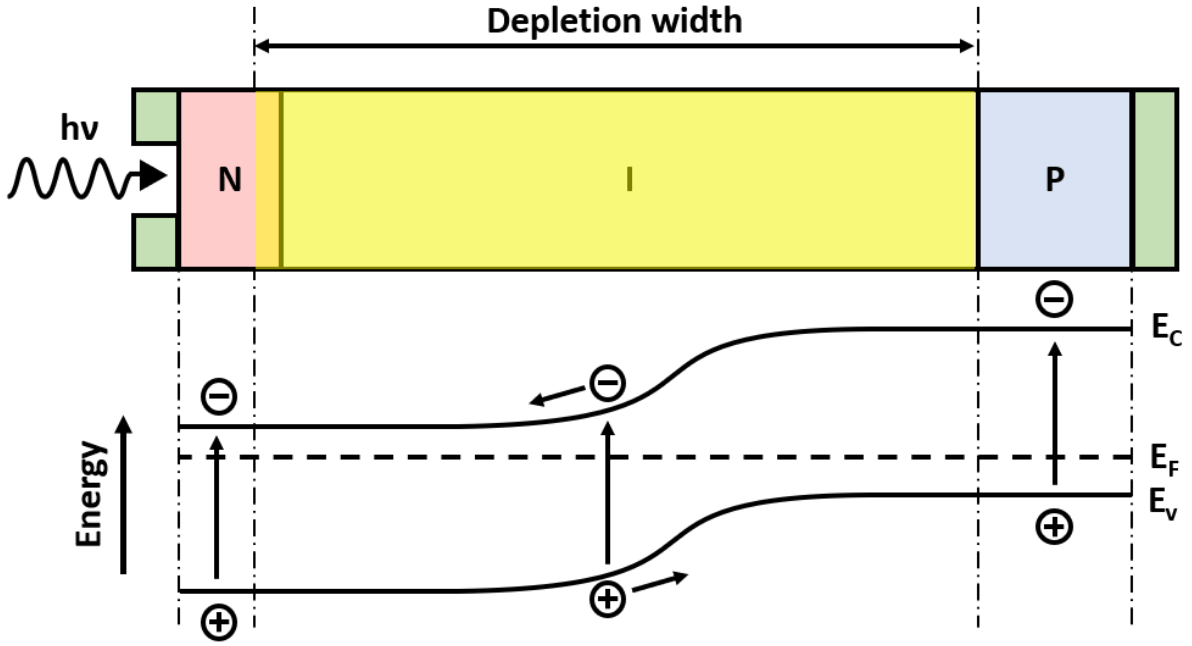


Figure 1.4: Schematic of a photovoltaic detector under an applied bias.

The dominant noise mechanisms in PV and PC detectors are shot noise and generation-recombination (G-R) noise respectively. These can be modelled according to Equations 1.4 and 1.5 respectively,

$$i_s = \sqrt{2qi\Delta f}, \quad (1.4)$$

$$i_{G-R} = 2\sqrt{qiG\Delta f}, \quad (1.5)$$

where Δf is the electrical bandwidth, q is the electron charge, i is the dark current and G is the photoconductive gain⁹.

1.3. Type-II superlattice detectors

For several decades MCT has been the material of choice for LWIR photodetection with well-established technology, high performance, and wavelength tunability. However, MCT-based LWIR detectors require cryogenic cooling which, in combination with various fabrication difficulties, has resulted in the quest for alternative material systems. The industry-driven desire for reduced SWaP has led manufactures to pursue HOT devices which negate the need for bulky cooling systems.

The InAs/GaSb T2SL structure, comprised of a periodic sequence of alternating InAs and GaSb layers, which was first developed by Sai-Halasz and Esaki⁵ in 1977, has emerged as a highly promising alternative to MCT. This is as a result of its exceptional properties including the characteristic type-II broken gap (or type-III) alignment, illustrated in Figure 1.5, which leads to the formation of spatially separated electrons and holes in the InAs and GaSb quantum wells (QWs), respectively. The interactions between adjacent QWs forms a periodic potential which results in the formation of minibands analogous to the band structure of bulk crystals. The charge transfer, caused by the spatial separation of electrons and holes, gives rise to a local electric field and interlayer tunnelling of carriers which does not need to be externally induced by an applied bias or doping¹⁰.

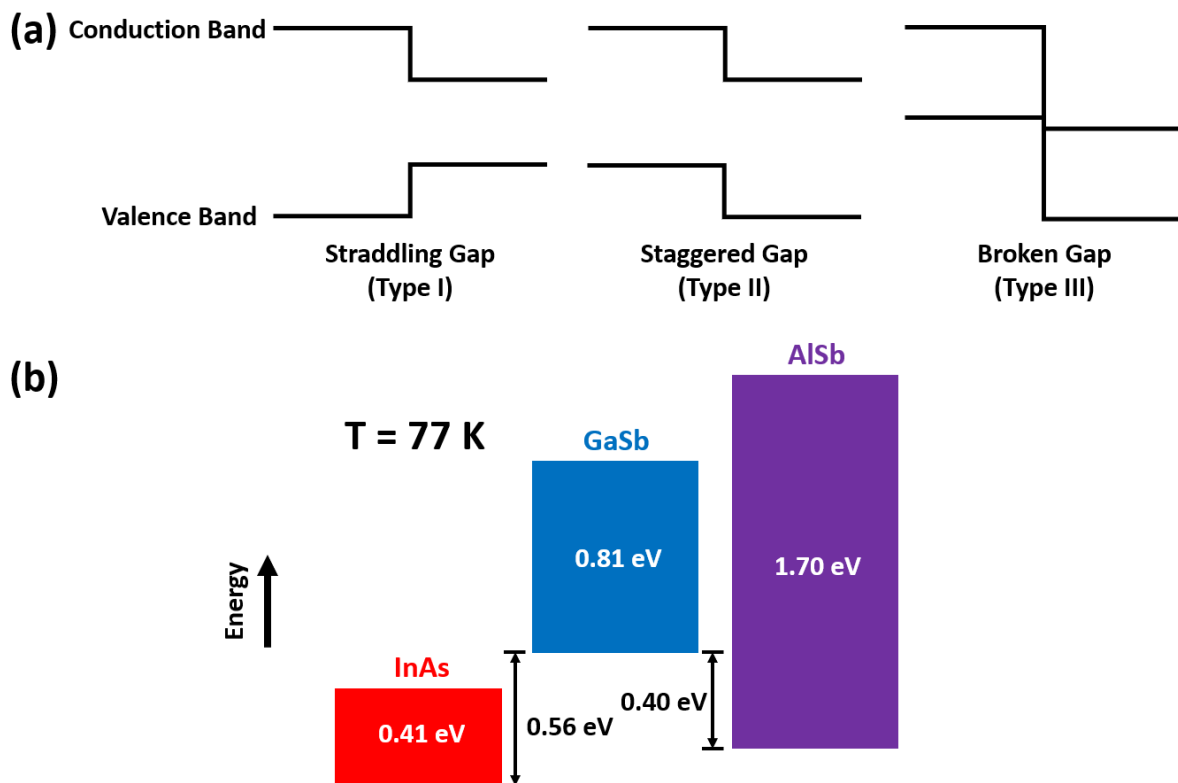


Figure 1.5: (a) Heterostructure band alignment types (b) The band alignment of the 6.1 Å family of semiconductors.

The SL bandgap is determined by the well widths and the interaction strength between adjacent QWs. Thus, by careful choice of the SL layer thicknesses, the T2SL material system becomes a narrow-gap semiconductor with a tuneable bandgap. It was proposed by Smith

and Mailhiot¹¹ in 1987, that these properties could be exploited for the manufacture of T2SLs for IR detector applications. Furthermore, owing to the small lattice mismatch between the materials of the 6.1 Å family (III-V materials with lattice constants close to 6.1 Å), the T2SL structure provides the needed flexibility for combining different material systems enabling device designs tailored for optimal performance in optoelectronic applications. Thus, any combination of InAs, GaSb and AlSb binaries (or alloys thereof) that make up the 6.1 Å family could be utilised for an ideal superlattice application. The unique properties of T2SLs have led to several suggested theoretical advances over the current state-of-the-art MCT LWIR detectors. Grein et al.^{12,13} demonstrated the suppression of Auger recombination by several orders of magnitude in T2SLs in comparison to MCT. The flexibility provided by the 6.1 Å family has also been used for the design and growth of innovative barrier architectures capable of mitigating G-R current.

The material advantages of III-V compounds, compared to MCT, which is a II-VI compound, include lower defect density and greater robustness and suppression of tunnelling currents due to larger effective masses. T2SLs also hold production advantages over MCT including the “-ilities”: operability, uniformity, stability, producibility, and affordability for FPA applications while lattice-matched GaSb substrates are now available in 2”, 3”, 4” and 6” diameters. High yield for wafer growth and FPA fabrication in addition to the presence of a III-V compound commercial industry is also advantageous.

The increased interest in the development of the T2SL was largely stimulated by impressive results of pioneering theoretical studies in the 1970’s. In 1978, Sai-Halasz et al.¹⁴ demonstrated that InAs/GaSb superlattices can exhibit semiconducting properties in the thinner InAs and GaSb layers. In the same year, Nucho and Madhukar¹⁵ showed that by increasing the magnitude of the discontinuity, the SL bandgap changes from direct gap to indirect gap or semimetal. However, despite promising theoretical proposals, high-quality T2SL detectors were not realized experimentally until notable advancements in molecular beam epitaxy (MBE) technology occurred. The first experimental demonstration of an InAs/Ga_{0.64}In_{0.36}Sb (38/16 Å) T2SL detector was performed by Johnson et al.¹⁶ in 1996 with a photoresponse up to 10.6 μm. A year later, Mohseni et al,¹⁷ demonstrated the MBE growth and characterization of InAs/GaSb T2SLs for LWIR detectors. In the same year, LWIR photodetection was demonstrated by Fuchs et al.¹⁸ using an InAs/GaInSb T2SL with significant

suppression of band-to-band tunnelling currents coupled with improvement in material quality. A significant milestone was reached in 2004¹⁹ with the first development of a high performance T2SL focal plane array (FPA) which confirmed the aptitude of the T2SL material system for IR photodetection.

The past decade has seen the development of Ga-free (usually InAs/InAsSb) T2SL detectors as a possible alternative to the more well-established Ga-containing (usually InAs/GaSb) variant. The Ga-free T2SL was first proposed as an $\text{InAs}_{0.4}\text{Sb}_{0.6}/\text{InAs}_{1-x}\text{Sb}_x$ strained-layer superlattice, with $x > 0.6$ for LWIR detector applications, by Osbourn in 1984²⁰, who used the strain and type-II band alignment of the InAsSb/InAsSb material system to reduce the bandgap below what was achievable at the time through bulk semiconductors. Growth and fabrication of Ga-free T2SLs were demonstrated throughout the 1990's with notable developments including the InAsSb/InSb SLS LWIR detector grown by Metalorganic Chemical Vapor Deposition (MOCVD)²¹, InAs/InAsSb T2SL LEDs on GaAs substrates²²⁻²⁴ and InAs/InAsSb T2SL lasers on InAs substrates²⁵⁻²⁷. However, interest in LWIR Ga-free T2SLs then waned until around 2011²⁷ when it was reported they exhibit significantly longer minority carrier lifetimes in comparison to their Ga-based counterpart²⁸ coupled with renewed interest from several research groups, notably Arizona State University (ASU),²⁸⁻³³ the Centre for Quantum Devices at Northwestern University (CQD)³⁴⁻³⁶ and NASA Jet Propulsion Lab³⁷⁻³⁹. Both Ga-containing and Ga-free T2SLs continue to be pursued for LWIR detectors with both material systems exhibiting clear advantages and disadvantages.

In addition to longer minority carrier lifetimes, a notable advantage of the Ga-free material system for LWIR detectors is its tolerance to defects. This arises from the very low-lying defect states in resonance with the conduction band instead of the bandgap^{32,40}. This defect tolerance is particularly advantageous for the heteroepitaxy on lattice-matched substrates such as GaAs⁴¹. The surface of the Ga-free T2SL is inherently n-type which is advantageous for n-type absorber regions in which surface band bending will repel minority carriers and reduce surface current. However, this same effect will be problematic for p-type absorbers⁴². The growth of Ga-free T2SLs is also thought to be more straight forward due to the availability of a simple shutter sequence in which only the Sb shutter is switched on and off. This contrasts with Ga-containing T2SLs in which 4 shutters must be carefully controlled and the problem of interfaces and strain balancing addressed. However, some groups have employed more

complex shutter sequences for the growth of Ga-free T2SLs using 2 Sb shutters for better control of Sb content⁴³. Nevertheless, the Ga-containing T2SL holds two major advantages over the Ga-free in the LWIR spectral range. Firstly, the Ga-containing T2SL requires a significantly shorter period thickness compared to the Ga-free to reach the same cut-off wavelength. The shorter period of the Ga-containing T2SL results in stronger oscillator strength and thus stronger absorption, particularly in the LWIR spectral range. Secondly, while both material systems have comparable electron effective masses, the hole effective mass of the Ga-free T2SL is notably larger than the Ga-containing resulting in unfavourable hole transport properties⁴⁴. This issue also worsens for longer wavelength and lower Sb content, making it particularly problematic for LWIR detectors. By contrast, due to the position of the heavy hole mini band in the broken gap, the hole transport properties of the Ga-containing T2SL have a very weak dependence on the cut-off wavelength. Considering these findings, no one material system has demonstrated an overall advantage over the other and so both are widely pursued LWIR detectors.

The majority of LWIR detectors are designed for space and defence applications meaning the reduction of SWaP is a foremost consideration. Unfortunately, the SWaP of modern LWIR detector modules is undermined by the bulky cooling systems required for low-temperature and high-performance operation. The theoretical advantages of the LWIR T2SL detectors have led to much expectation that this material could form the basis for the next generation of HOT, low SWaP LWIR detectors.

1.4. Figures of merit

As reductions in SWaP are largely driven by increases in performance, it is informative to detail the figures of merit used for appraising detector performance. The figures of merit, described below, are powerful tools for accurately appraising and comparing the performance of LWIR detectors⁴⁵.

1.4.1. Quantum efficiency

The External quantum efficiency (EQE, η) of a photodetector is defined as the number of carriers

measured at the detector output divided by the flux of incident photons and is given by:

$$\eta = \frac{I_{ph}}{q\Phi A_d}, \quad (1.6)$$

where I_{ph} is the photocurrent, q is the electron charge, Φ is the photon incidence and A_d is the effective optical area of the detector. Thus, the QE is less than 1 but is usually given as a percentage.

1.4.2. Responsivity

The external quantum efficiency, η , defined above is closely related to the responsivity which relates the output signal of a detector (in Amps or Volts) to the radiant input that produced that signal (in Watts) and is given by:

$$R = \frac{\eta q}{h\nu}, \quad (1.7)$$

where $h\nu$ is the energy of incident photons. The spectral responsivity, R , gives the responsivity in terms of wavelength while the blackbody responsivity gives the peak responsivity.

1.4.3. Noise equivalent power

The signal-to-noise ratio (SNR) is described by the following equation:

$$SNR = \frac{R\varphi_e}{i_n}, \quad (1.8)$$

where φ_e is the radiant power and i_n is the noise expressed as a current. The noise equivalent power (NEP) is a measure of the incident radiant power that produces an SNR of unity given by:

$$NEP = \frac{i_n}{R} = \frac{\varphi_e}{i_{signal}/i_{noise}}, \quad (1.9)$$

The lower the NEP, the more sensitive the device, although it does not allow direct comparison between different detector configurations.

1.4.4. Specific detectivity

To compare detectors in any given configuration, the specific detectivity, D^* , is the inverse of the NEP which take into accounts both the active area and the signal bandwidth of the detector. It represents the primary figure of merit for comparing single-pixel IR detectors and is given by:

$$D^* = \frac{\sqrt{A_d \Delta f}}{NEP}, \quad (1.10)$$

where Δf is the signal bandwidth. It can thus be seen that the major figures of merit for IR detectors are determined by the signal-to-noise ratio, where the signal is related to the QE, and the noise, which is related to the dark current.

1.5. Sources of dark current

Dark current is the current flowing through the detector in the absence of any incident photon flux. Through the use of modelling based on experimental data, Gopal et al.⁴⁶⁻⁴⁸ have identified that the diffusion current, generation-recombination current, trap-assisted tunnelling (TAT) current and ohmic shunt current are the main sources of dark current in a T2SL. The diffusion current, I_{diff} , caused by the diffusion of minority carriers from high to low concentrations, is modelled as:

$$I_{diff} = \frac{qAn_i^2}{N_d} \left\{ \frac{kT}{q} \frac{\mu_h}{\tau_h} \right\}^{1/2} \tanh \frac{d}{L_h} \left[\exp \left(\frac{qV}{kT} \right) - 1 \right], \quad (1.11)$$

where A is the junction area, n_i is the intrinsic carrier concentration, N_d is the donor concentration, μ_h is the hole mobility, τ_h is the hole lifetime, V is the diode bias voltage, d is the thickness of the n region, and L_h is the hole diffusion length.

G-R current is generated due to depletion region defects which act as Shockley-Read-Hall (SRH) recombination centres. For reverse bias, considered above, the G-R current can be given by:

$$I_{G-R} = \frac{qAn_iW_{dep}V}{V_t\tau_{G-R}}, \quad (1.12)$$

$$A_{G-R} = \frac{qn_t A}{2\tau_{G-R}} \left[\frac{2\varepsilon_0 \varepsilon_s (N_a + N_d)}{qN_a N_d} \right]^{1/2}, \quad (1.13)$$

where τ_{G-R} is the G-R lifetime, N_a is the acceptor concentration and W_{dep} is the depletion region width. The TAT current originates from mid-gap trap states which carriers can use to tunnel between bands, usually under a high electric field, and is expressed as:

$$I_{TAT} = \frac{\pi^2 q^2 A m_e V_t M^2 N_T}{h^3 (E_g - E_t)} \times \exp \left\{ -\frac{8\pi (2m_e)^{1/2} (E_g - E_t)^{3/2}}{[3qhF(V)]} \right\}, \quad (1.14)$$

where m_e is the effective mass related to the tunnelling, E_g is the T2SL bandgap, E_t is the trap energy level below the conduction band edge, M is the matrix element of the trap potential, N_T is the trap density, $F(V)$ is electric field strength across the depletion region which is dependent on voltage.

Ohmic shunt currents are usually caused by native oxides, formed on the mesa sidewalls during and after etching, which act as good conductors. This component can simply be described using Ohm's law:

$$I_{sh} = \frac{V}{R_{sh}}, \quad (1.15)$$

where R_{sh} is the diode shunt resistance. An understanding of which dark current mechanism is dominant for a given voltage or temperature is essential for improving device performance.

1.6. Background-limited infrared photodetection

For IR detectors, the point at which the noise associated with the detector and amplifier is negligible compared to the photon noise is considered a key performance benchmark. This is because the origin of the photon noise is associated with the detection process itself, resulting from the discrete nature of the radiation field, rather than any imperfection in the detector. As the radiation incident on the detector is from both the target and background, the photon noise is technically the sum of fluctuations in signal and background radiation. However, practically speaking, the operating limit for most IR detectors arises only from the fluctuation in background radiation and is therefore known as the background-limited infrared photodetection (BLIP) limit. The detectivity at the BLIP limit, derived from the shot noise, is defined as,

$$D_{BLIP}^*(\lambda, T) = \frac{\lambda}{hc} k \left(\frac{\eta}{2\Phi_B} \right)^{1/2}, \quad (1.16)$$

where Φ_B is the total background photon flux density reaching the detector, denoted as,

$$\Phi_B = \sin^2(\theta/2) \int_0^{\lambda_c} \Phi(\lambda, T_B) d\lambda, \quad (1.17)$$

where θ is the detector field of view angle and λ_c is the wavelength of the peak response.

1.7. Linear and focal plane arrays

The discussion thus far is primarily applicable to single-pixel detectors. These, however, are insufficient for imaging applications which require assemblies of multiple pixels known as arrays. The two varieties of arrays are linear detector arrays (LDAs) and FPAs. LDAs consist of a one-dimensional row of connected detector elements. A two-dimensional image is obtained by moving the measurand object, relative to the array, in a direction perpendicular to the length of the array. FPAs are two-dimensional arrays of detectors placed on the focal plane of an imaging system and, as a result, no scanning is required to obtain a two-dimensional image, though this can be performed to obtain a high-resolution image using a low-resolution array. In addition to increased efficiency, subtraction of background radiation can be performed with much greater ease in arrays compared to single-pixel systems. Unlike single-pixel detectors, the primary figures of merit for arrays is not the detectivity but the modulation transfer function (MTF) and the noise equivalent difference temperature (NEDT).

1.7.1. Modulation transfer function

The MTF is a measure of the spatial resolution of the array by quantifying the ability of the system to resolve or transfer spatial frequencies⁴⁹. Consider a detector set up attempting to measure a bar pattern in which the cross-section of each bar is a sine wave. The detector set-up will accurately reproduce the bar pattern provided it is sufficiently sparsely spaced. However, as the spacing of the bar pattern decreases, the detector set-up will approach its limit. The modulation, M , at the point of this limit is defined as

$$M = \frac{E_{max} - E_{min}}{E_{max} + E_{min}}, \quad (1.18)$$

where E is the irradiance. The modulation is then used to calculate the MTF of the imaging system using

$$MTF = \frac{M_{image}}{M_{object}}. \quad (1.19)$$

The MTF of the detector set-up is defined for a particular operating wavelength and determined by the size of the detector and the aperture of the optics.

1.7.2. Noise equivalent temperature difference

The NEDT is a measure of the temperature sensitivity of the detector and is the most commonly used figure of merit for arrays. It defines the temperature change that will produce a signal equal in magnitude to the rms noise of the detector set-up and is defined as

$$NEDT = \frac{V_n(\partial T/\partial \Phi)}{(\partial V_s/\partial \Phi)} = V_n \frac{\Delta T}{\Delta V_s}, \quad (1.20)$$

where V_n is the rms noise, Φ is the spectral photon flux density (photons/cm²s) incident on a focal plane, and ΔV_s is the signal measured for the temperature difference ΔT . To gain a deeper understanding of the NEDT and related concepts, it is informative to follow the derivations of Kinch et al.⁵⁰ discussed below.

When the current signal current in an IR FPA is generated, it is sent to a capacitive node with a carrier well with capacity N_w . Assuming there is no excess noise, the performance limit of the node occurs at the point at which the minimum detectable signal flux, $\Delta\Phi$, produces an output signal equal to the shot noise of the node:

$$\Delta\Phi\eta A_d\tau_{int} = \sqrt{N_w} = \sqrt{\frac{(J_{dark} + J_\Phi)A_d\tau_{int}}{q}}, \quad (1.21)$$

where η is the detector collection efficiency, A_d is the detector area, τ_{int} is the integration time, J_{dark} is the detector dark current, and J_Φ is the flux current.

A related parameter, the noise equivalent flux (NE $\Delta\Phi$), is determined by equating the minimum detectable signal to the integrated current noise, thus

$$\eta\Phi_s A_d \tau_{int} = \sqrt{\frac{(J_{dark} + J_\Phi) A_d \tau_{int}}{q}}, \quad (1.22)$$

giving

$$NE\Delta\Phi = \frac{1}{\eta} \sqrt{\frac{J_{dark} + J_\Phi}{q A_d \tau_{int}}}. \quad (1.23)$$

The $NE\Delta\Phi$ can be converted to a noise equivalent irradiance (NEI), defined as the minimum observable flux power incident on the system aperture. This is achieved by renormalising the incident flux density on the detector to the system aperture area, A_{opt} . The NEI is then defined as

$$NEI = NE\Delta\Phi \frac{A_d h\nu}{A_{opt}}, \quad (1.24)$$

assuming monochromatic radiation with energy $h\nu$. Further, by assuming high background flux, the signal flux is given by

$$\Delta\Phi = \Delta T (d\Phi_B / dT). \quad (1.25)$$

By combining Equations 1.21 and 1.25 we get the following expression for shot noise,

$$\eta\Delta T \frac{d\Phi_B}{dT} = \sqrt{\frac{J_{dark} + J_\Phi}{q A_d \tau_{int}}}. \quad (1.26)$$

By rearranging Equation 1.26, we get the following expression for the NEDT,

$$NEDT = \frac{1 + (J_{dark} / J_\Phi)}{\sqrt{N_w C}}, \quad (1.27)$$

where $C = (d\Phi_B / dT) / \Phi_B$ is the scene contrast through the optics. Equation 1.27 assumes perfect transmission through the optics and no flux contribution from the cold shield of the detector. It can thusly be seen how the dark current expressions, defined in Section 1.5, contribute to the NEDT, the most universal figure of merit for detector performance.

2. Motivation for the T2SL

This chapter provides a comparison of the current performance levels of MCT- and T2SL-based LWIR detectors. Experimental and theoretical studies are discussed to determine the factors that give rise to the present disparity between the two material systems. Techniques for bridging this disparity and then described. Finally, a summary of the author's research in developing these techniques is described.

2.1. Performance comparison of MCT and T2SLs

2.1.1. Dark current

The theoretical advantages of T2SL detectors over MCT is yet to be experimentally demonstrated in superior device performance. Figure 2.1 shows that the state-of-the-art T2SL LWIR detectors have dark currents within one order of magnitude proximity to Rule 07 (which provides a heuristic predictor for the state-of-the-art performance of an MCT photodiode⁵¹). The Rule 07 "rule of thumb" was developed based on I-V data collected from 26 MBE-grown MCT devices with various cut-off wavelengths. These devices were all diffusion limited and had a donor doping concentrations of $0.5 \times 10^{15} \text{ cm}^3$ to $2.0 \times 10^{15} \text{ cm}^3$. Accordingly, an exponential variation, modified by fitting parameters, of the equilibrium minority carrier concentration with the product of the temperature and cut-off wavelength was assumed. The values of these fitting parameters were then determined by a trial and error fit of the exponential to the measured data. The dark current of devices fabricated by various research groups including the CQD at Northwestern University, USA^{43,52}, Semiconductor devices (SCD) Israel⁵³, Jet propulsion Laboratory (JPL) at the National Aeronautics and Space Administration (NASA), USA^{54,55}, Shanghai Institute of Technical Physics (SITP) of the Chinese Academy of Sciences, China⁵⁶, Arizona State University (ASU), USA³³, Institut d'Électronique et des Systèmes, France^{57,58}, and IRnova AB, Sweden^{59,60} have been compared. In Chapter 7, these values will be compared to those of the present work which can also be found in Ref. ⁶¹. As Figure 2.1

shows, the performance of T2SLs only becomes competitive with MCT when cooled to lower temperatures.

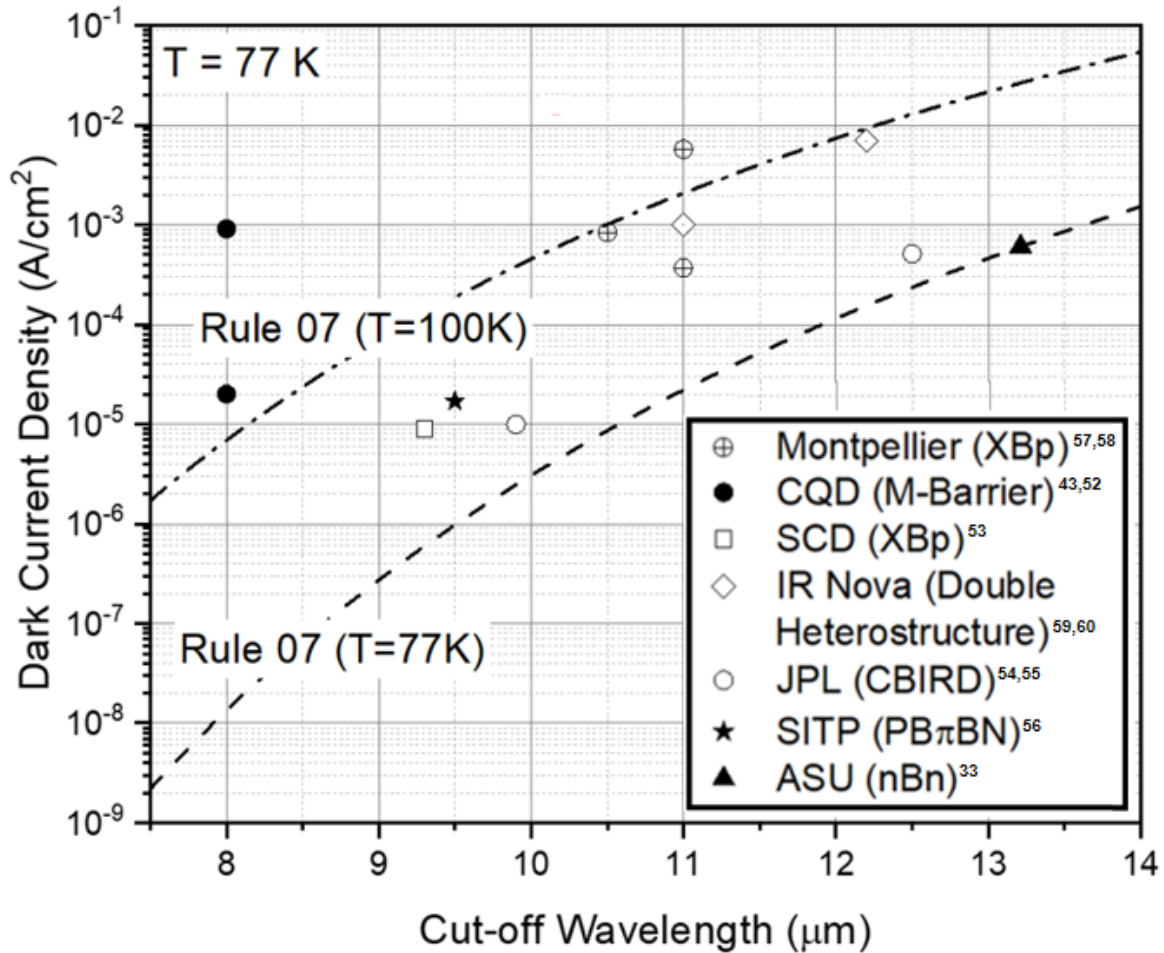


Figure 2.1: Collected values of the dark current density at 77 K for long-wavelength infrared type-II superlattice detectors compared with 'Rule 07' for HgCdTe Detectors.

For standard devices, the dark current at low reverse bias is limited by the G-R current at low temperatures and the diffusion current at higher temperatures. By examining Equations 1.11 and 1.12, it can be seen that the disparity in dark current between T2SLs and MCT likely arises from short minority carrier lifetime and diffusion length of the former.

2.1.2. Diffusion length in LWIR T2SLs

In addition to its contribution to the dark current (see Section 1.5), the minority carrier diffusion length also affects the performance of LWIR T2SLs through the collection efficiency.

It is generally understood that to achieve high quantum efficiencies, the active region thickness of a detector should be equal to, if not greater than, the target cut-off wavelength. However, increasing the active region thickness larger than the diffusion length might not yield the desired increase in device performance. This is because carriers generated within the region larger than the diffusion length and farther from the contact are unlikely to be collected. Klipstein et al.⁶² have reported minority carrier diffusion lengths for T2SLs in the range of 3 – 7 μm at 78 K for T2SLs, using k.p simulations fit to experimental data. As a result, T2SL active region thicknesses have been limited to around 6 μm to maintain high collection efficiencies of around 90%. To extend the active region thickness into the range desirable for LWIR applications ($\sim 10 \mu\text{m}$) and increase absorption would significantly affect the collection efficiency. Furthermore, critical thickness issues arising from the internal strain of the superlattice can cause a degradation of material quality with an increase in the thickness of the constituent layers of the superlattice. This issue arises from the slight lattice mismatch between InAs and GaSb (or $\text{InAs}_x\text{Sb}_{1-x}$). As more layers of a non-lattice matched material are deposited on another, the internal strain energy in the structure increases. This energy will continue to increase until a certain critical thickness is reached beyond which the formation of dislocations becomes energetically favourable. The Matthews Blakeslee model⁶³ provides a generalised formula for the critical thickness of a given two materials. The diffusion length for MCT has been reported to be around 20 μm meaning there is no trade-off between absorption and collection efficiency. As a result, as Figure 2.2 highlights, MCT detectors can capitalise on longer diffusion lengths and achieve higher QEs using thicker active regions in addition to the reduced dark current, according to Equation 1.11.

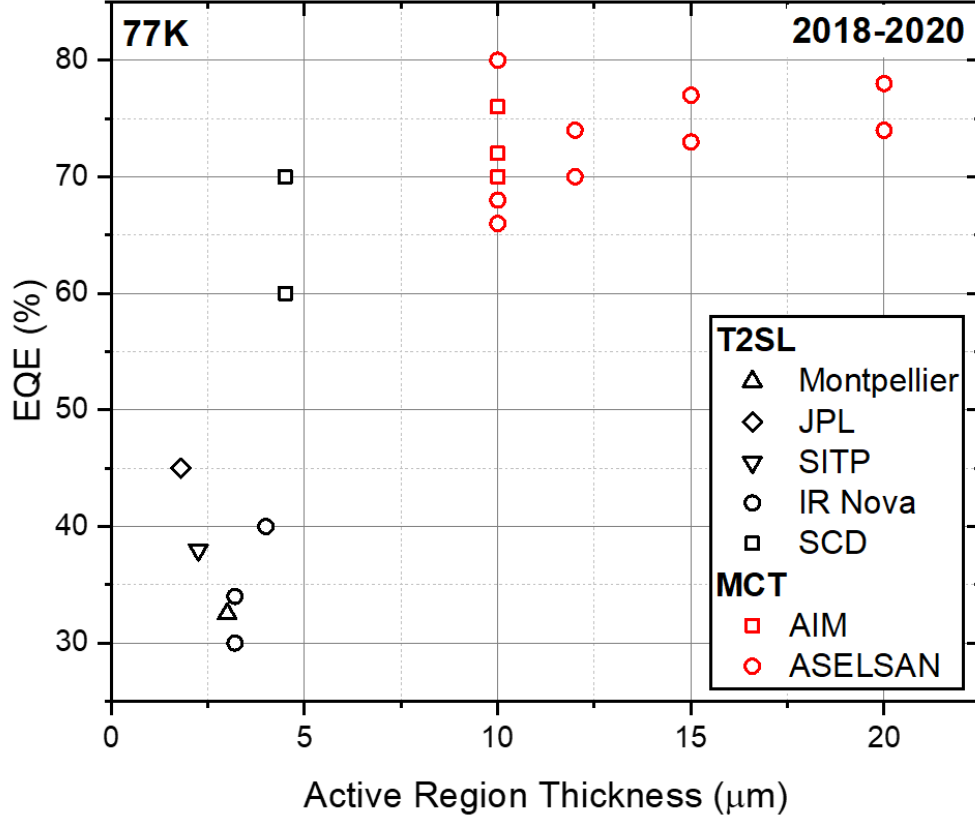


Figure 2.2: Collected values of external quantum efficiency vs active region thickness for recent (2018-2020) superlattice-based and MCT-based long-wavelength infrared detectors.

The EQE of devices from Montpellier^{57,58}, JPL⁵⁵, SITP⁵⁶, IR Nova AB^{60,64}, SCD⁶⁵, Aim Infrarot-Module (AIM) GmbH⁶⁶⁻⁶⁸, Germany and ASELSAN AS⁶⁹, Turkey is compared in Figure 2.2. The clear advantage of MCT, arising from the diffusion length, is not necessarily maintained as the temperature increases above 77 K. The literature contains somewhat conflicting arguments regarding the temperature dependence of the minority carrier diffusion length. Some have assumed that the diffusion length decreases at higher temperatures⁷⁰, possibly due to the reduction in minority carrier lifetime suggested by the known $T^{-1/2}$ dependence of SRH lifetimes (this will be discussed in more detail in Section 2.1.3). However, recent reports suggest otherwise. Klipstein et al.⁶² reported that in T2SLs over the temperature range 70 – 130 K, the lateral diffusion length varies linearly with an increase in temperature from 6.3 μm (78 K) to 11 μm (130 K). These findings are also in agreement with diffusion coefficient dependence on the temperature which is described by:

$$D = \frac{k_B T}{e} \mu, \quad (2.1)$$

where D is the diffusion coefficient, T is the temperature and μ is the mobility. Note, however, that it is the vertical diffusion length, not the lateral, that limits detector performance and it is not possible to measure the vertical diffusion length in this way. Furthermore, Taghipour et al.⁷¹ directly measured the vertical diffusion length of InAs/GaSb T2SLs at temperatures from 80 – 170 K using the Electron-beam induced current (EBIC) method. The preponderance of the findings suggest that the vertical diffusion length stays constant at around 1.5 μm in the temperature range 80 – 140 K and thereafter increases roughly linearly to 4.5 μm at 170 K. However, data from low e-beam energy (~ 10 keV) shows a linear relationship from 80 K. These studies suggest that the diffusion length of T2SLs increases with temperature even up to ~ 11 μm at 130 K. If this is the case, the advantage of MCT, whereby thicker active regions are used to obtain higher quantum efficiencies, will be eroded at higher temperatures. With a diffusion length comparable to the intended cut-off wavelength, HOT LWIR T2SL detectors could employ sufficiently thick active regions with no loss of collection efficiency, provided issues related to critical thickness can be overcome. Furthermore, the critical thickness issues that inhibit the growth of thick, high-quality T2SL material may not be as detrimental as first thought. This is because Klipstein et al. have reported that the vertical diffusion length, which contributes to device performance, may be less affected by degradations in material quality than lateral diffusion lengths.

2.1.3. Minority carrier lifetime

The minority carrier lifetime contributes to the dark current of T2SL detectors as expressed by Equations 1.12 and 1.13 as well as the detectivity and operating temperature. It is linked to the diffusion length by:

$$L = \sqrt{D\tau}, \quad (2.1)$$

where L is the minority carrier diffusion length and τ is the minority carrier lifetime. As shown in Figure 2.3, the typical lifetimes for LWIR SLs are in the range of 10-30 ns for Ga-containing and 100-400 ns for Ga-free T2SLs. This increases to around 100 ns and 2-10 μs respectively for the MWIR spectral range.

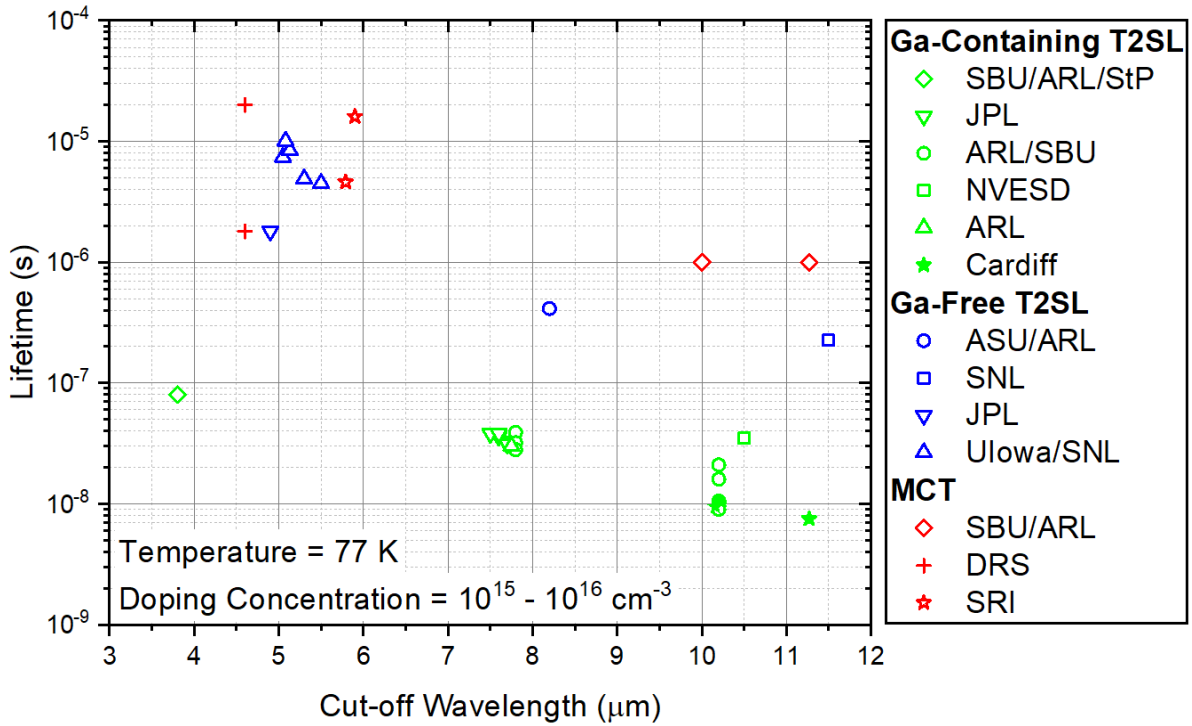


Figure 2.3: Collected minority carrier lifetimes vs cut of wavelength for Ga-free and Ga-containing type-II superlattices and MCT.

The minority carrier lifetimes of T2SLs and MCT, as reported by selected research groups including Stony Brook University (SBU) and U.S. Army Research Laboratory (ARL)⁷²⁻⁷⁶, St. Petersburg State Polytechnical University (StP)⁷³, JPL^{77,78}, ASU^{28,33}, Sadia National Laboratories (SNL)^{79,80}, University of Iowa (Ulowa)⁸⁰, Cardiff University⁶¹, U.S. Army Night Vision and Electronic Sensors Directorate (NVESD)⁸¹, DRS Infrared Technologies [now Leonardo DRS] (DRS)⁸², and SRI International⁸³ are compared in Figure 2.3 which also shows a near-linear decrease in carrier lifetime with increasing wavelength for both Ga-containing and Ga-free. It also highlights the limitation posed by minority carrier lifetime in LWIR T2SLs. However, Ga-free T2SLs have lifetimes comparable to MCT in the MWIR range and the LWIR lifetimes are in the proximity of an order of magnitude to that of MCT. As the lifetime directly affects the diffusion current of T2SL devices according to $I_{diff} \sim \tau^{-1}$, the performance of diffusion-limited Ga-free T2SL devices is expected to greatly exceed that of Ga-containing detectors, however, this has not yet been realized. For a detailed analysis of T2SL lifetimes and their effect on device performance, the reader is directed to the reviews in Refs. ^{4,170}.

The minority carrier lifetime in a T2SL is a combination of SRH, radiative, and Auger recombination processes where:

$$\tau^{-1} = \tau_{SRH}^{-1} + \tau_{Rad}^{-1} + \tau_{Auger}^{-1}, \quad (2.2)$$

Grein et al.^{13,84} have argued that the Auger contribution can be neglected in p-type T2SLs since the degeneracy split occurs in the light hole and the heavy hole by the strain in the minibands. This degeneracy, brought about by the lattice mismatch between the SL constituent materials, introduces sub bandgaps in the band structure which reduce the available phase space for Auger processes. Though this is not the case for n-type T2SLs, suppression of Auger processes can still be achieved by increasing the (In)GaSb thickness, thus flattening the lowest conduction band. However, the performance expectations set by Auger suppression is yet to be realized in T2SL devices. Since the publication of Rogalski's reviews in Refs. ^{4,85}, new research has been conducted that challenges the widely accepted physics affecting carrier lifetimes in T2SLs. Contrary to Grein's assertions, 8 band k.p modelling recently performed by Klipstein et al.⁸⁶ for an LWIR InAs/GaSb T2SL suggests that the Auger 7 (A7) process should be quite effective. The apparent dominance of the SRH process, despite the presence of an effective A7 process, suggests the physics of this area requires further study. While this may simply be explained by an unusually high concentration of Ga-related defects acting as SRH centres, Klipstein et al. propose SRH recombination and the suppression of A7 processes occurs due to donor-like traps concentration. The latter theory is consistent with experimental data suggesting Auger rates are significantly stronger in Ga-free T2SLs compared to Ga-containing⁸⁷.

The complex physics surrounding the recombination processes and their relative prominence in T2SLs are directly relevant for HOT device performance as they determine the minority carrier lifetime and its temperature dependence. Aytac et al.⁸⁷ have performed temperature-dependent measurements of recombination rates in InAs/InAsSb T2SLs and fitted the data to the theoretical behaviour of SRH, radiative, and Auger recombination processes. It was found that for unintentionally doped T2SLs, the SRH process dominates for the temperature range 77 – 200 K, during which the lifetime is roughly constant with temperature, and Auger processes dominate between 200 K to room temperature, in which the lifetime decreases with temperature. It was observed that SRH lifetimes could be increased by increasing Sb

content while reducing SL period thickness, thereby reducing the number of available SRH recombination centres. Increasing Sb content was also found to reduce Auger coefficients, possibly due to conduction band flattening, though these remain much larger than for the equivalent Ga-containing T2SLs⁷². Using a similar approach, Taghipour et al.⁷¹ measured the temperature dependence of recombination mechanisms in InAs/GaSb T2SLs and found that the lifetime is SRH limited from 80 – 150 K and Auger limited above 150 K. The prevalence of Auger recombination over SRH is likely due to the relatively high ($\sim 5.0 \times 10^{16} \text{ cm}^{-3}$) doping concentration. Unlike the Ga-free T2SLs reported previously, the minority carrier lifetime of the Ga-containing T2SLs appears roughly constant with temperature over a range of 80 K to room temperature. More experimental studies are required to understand the recombination mechanisms in T2SLs, it can be concluded based on the current research that the minority carrier lifetime remains roughly constant as the temperature is increased.

These results suggest that the material limitations of the T2SL, namely the minority carrier diffusion length and lifetime, does not deteriorate with an increase in the operating temperature from 77 K to around 150 K for both Ga-containing and Ga-free T2SLs.

2.2. Aims and objectives of current work

In light of the current disparity between the presently achievable performance levels of LWIR T2SLs and MCT, the aim of this project is to develop techniques to improve the performance of LWIR T2SLs towards their theoretically achievable levels. A key aim in the furtherance of this goal will be to establish and improve the simulation, fabrication, and characterization capabilities for T2SL detectors. As discussed below, one of the most promising routes to improving the performance of LWIR T2SLs beyond that of MCT is to grow T2SLs on GaAs substrates, thereby enabling the fabrication of backside illuminated and optically immersed detectors. The final aim of this project is therefore to develop a high performance LWIR T2SL on a GaAs substrate.

2.2.1. Growth on GaAs substrates

Many of the initial demonstrations of LWIR T2SLs in the 1990's were grown on GaAs substrates⁸⁸⁻⁹⁰. However, when GaSb substrates became widely available they were preferred for most T2SLs due to better lattice matching between substrate and SL. In recent years, there

has been renewed interest in the GaAs substrate due to reduced costs and the availability of larger wafers⁹¹. Furthermore, some notable advantages have been observed from the use of GaAs substrates for LWIR T2SLs. Pour et al.⁹² have reported that T2SLs on GaAs have an increased QE stemming from the refractive index difference between the GaAs and GaSb. This allows the formation of a Fabry-Perot cavity between the GaAs substrate/ GaSb buffer interface (IF) and T2SL/ air IF which enhances the intensity of light in the device active region. Also advantageous is the high transmission of LWIR radiation through GaAs which allows the device to access backside reflections which further increases the QE. This property has more recently been utilized to fabricate optically immersed T2SL-based detectors with detectivities comparable to equivalent MCT-based detectors^{41,93–96} under thermoelectric (TE) cooling. The technique, shown in Figure 2.4, makes use of hemispherical immersion lenses that concentrate the impinging IR radiation onto the detector element. This has the effect of increasing the apparent optical size of the detector without increasing its actual size, thereby improving detectivity. In optically immersed T2SLs, the immersion lens is fabricated from the GaAs substrate itself using micromachining techniques and the device is then backside illuminated. This approach is not possible with conventional GaSb substrates as LWIR transmission through GaSb is very weak.

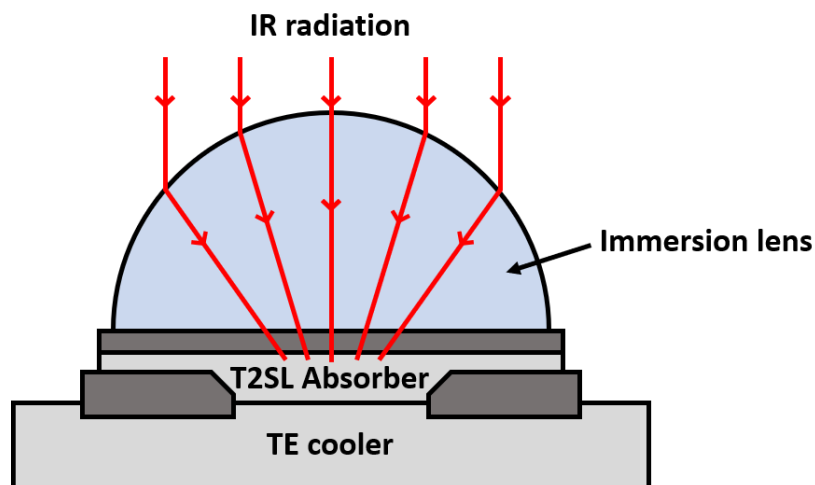


Figure 2.4: Schematic of an optically immersed T2SL detector.

The major drawback of the GaAs substrates for T2SLs is the considerable 7.8% lattice mismatch between the GaSb and GaAs. This means the critical thickness of the 6.1 Å family epilayers will be limited to a few monolayers before the generation of threading dislocations

occurs⁹⁷ which have been shown to have a detrimental effect on device performance⁹⁸. Two principal solutions to this problem have been proposed and are detailed below.

The first approach, the IMF array, was developed by Huang et al.^{99,100} in 2006 and uses a periodic array of 90° misfit dislocations at the GaSb-on-GaAs IF to prevent the propagation of threading dislocations into the device active region. For the case of GaSb-on-GaAs, these misfits occur at every 14th lattice site, as shown in Figure 2.5. These 90° misfits propagate laterally and are believed to be the predominant mechanism for strain relief. The formation of threading dislocations in GaSb epilayers on GaAs is associated with the presence 60° misfits at the GaSb-on-GaAs IF¹⁰¹. It is therefore essential to tailor the growth conditions of the IMF array to favour the formation of 90° over 60° misfits^{102,103}. In this way, a reduction of the density of threading dislocations in GaSb epilayers on GaSb from $10^8 - 10^9 \text{ cm}^{-2}$ down to 10^5 cm^{-2} has been achieved¹⁰⁴. The initial demonstrations of the IMF array simply involved the growth of GaSb epilayers on GaAs substrates, but the IMF array has been utilised for the growth of T2SLs on GaAs^{41,91,105-108}. The preponderance of these studies suggests that T2SLs grown on GaAs substrates continue to have issues with material quality albeit somewhat relieved by the presence of IMF array, possibly due to the formation of some 60° misfits at the GaSb-on-GaAs IF. As discussed above, these issues with material quality are likely to reduce device performance.

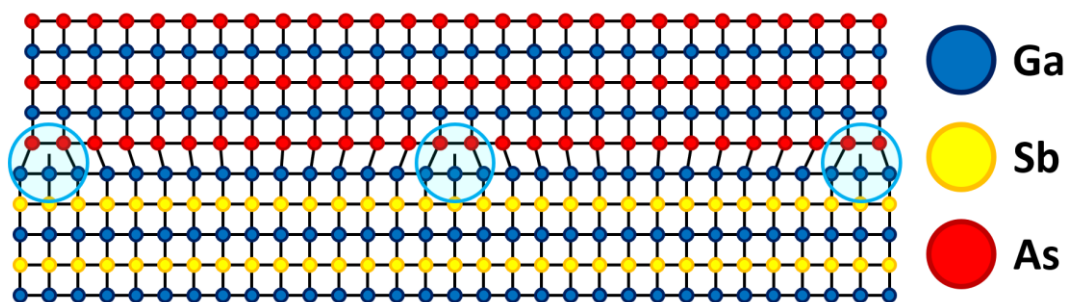


Figure 2.5: Schematic of an interfacial misfit array at a GaSb-on-GaAs interface.

The second approach, the metamorphic buffer layer, seeks to partially relax the structure through the introduction of misfit dislocations. The most commonly used strategy employs compositional grading¹⁰⁹ but low-temperature growth¹¹⁰⁻¹¹⁴ and temperature grading¹¹⁵⁻¹¹⁷ approaches are becoming increasingly popular. In the compositional grading approach, the overall change in lattice constant is divided into several uniform layers which can be equal, as

in linear step grading, or varied, as in non-linear step grading. For example, GaSb is grown on a GaAs substrate through sequential layers of $\text{GaAs}_x\text{Sb}_{1-x}$, where x is reduced from 1 to 0. This approach was adopted by Müller et al.⁹⁴ for a LWIR T2SL on GaAs, shown schematically in Figure 2.6.

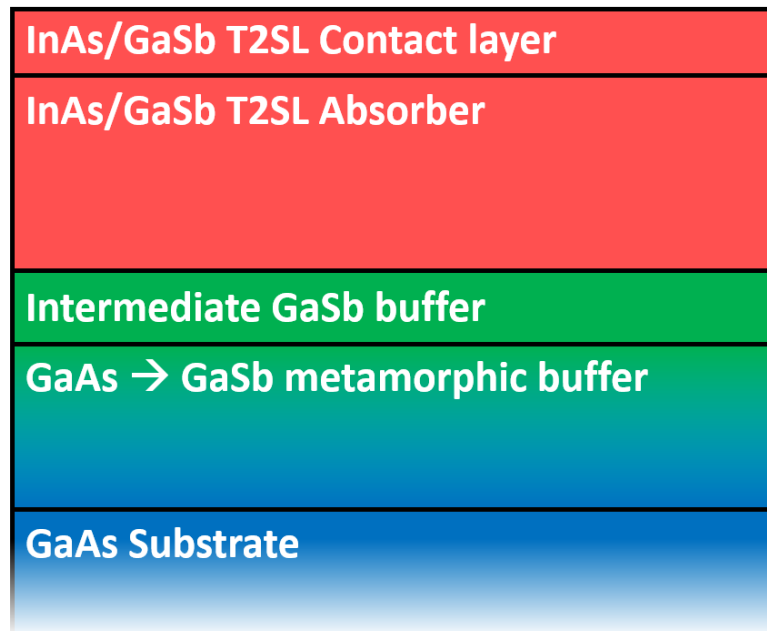


Figure 2.6: Schematic of the LWIR T2SL on GaAs reported by Müller et al.

There exist several approaches to the linear compositional grading metamorphic buffer layer. The “forward-graded” buffer (Figure 2.7a), employed by Müller et al. above, ensures the lattice mismatch is zero at the substrate-buffer IF and increases linearly until the lattice constant matches that of the device or intermediate buffer. For the “overshoot-graded” layer, shown in Figure 2.7b, the lattice mismatch is increased beyond that of the device with the aim of compensating for incomplete relaxation by allowing in-plane lattice matching between the strained buffer and relaxed device. The “jump-graded” buffer, shown in Figure 2.7c, ensures a non-zero lattice mismatch at the substrate-buffer IF. This buffer will contain interfacial misfit dislocations and can quickly reach a steady-state threading dislocation density. In the “reverse-graded” buffer, shown in Figure 2.7d, the lattice mismatch has the opposite sign to the device. Wong et al.¹¹⁸ have reported the reverse grading of this type allows the bending over of threading dislocations which results in low dislocation densities. With the exception of the “reverse-graded” buffer, all these approaches require a thick buffer

layer (often several microns) to achieve acceptable dislocation densities. This is not only expensive but also undesirable for backside illuminated devices due to the low transmission of LWIR radiation in GaSb.

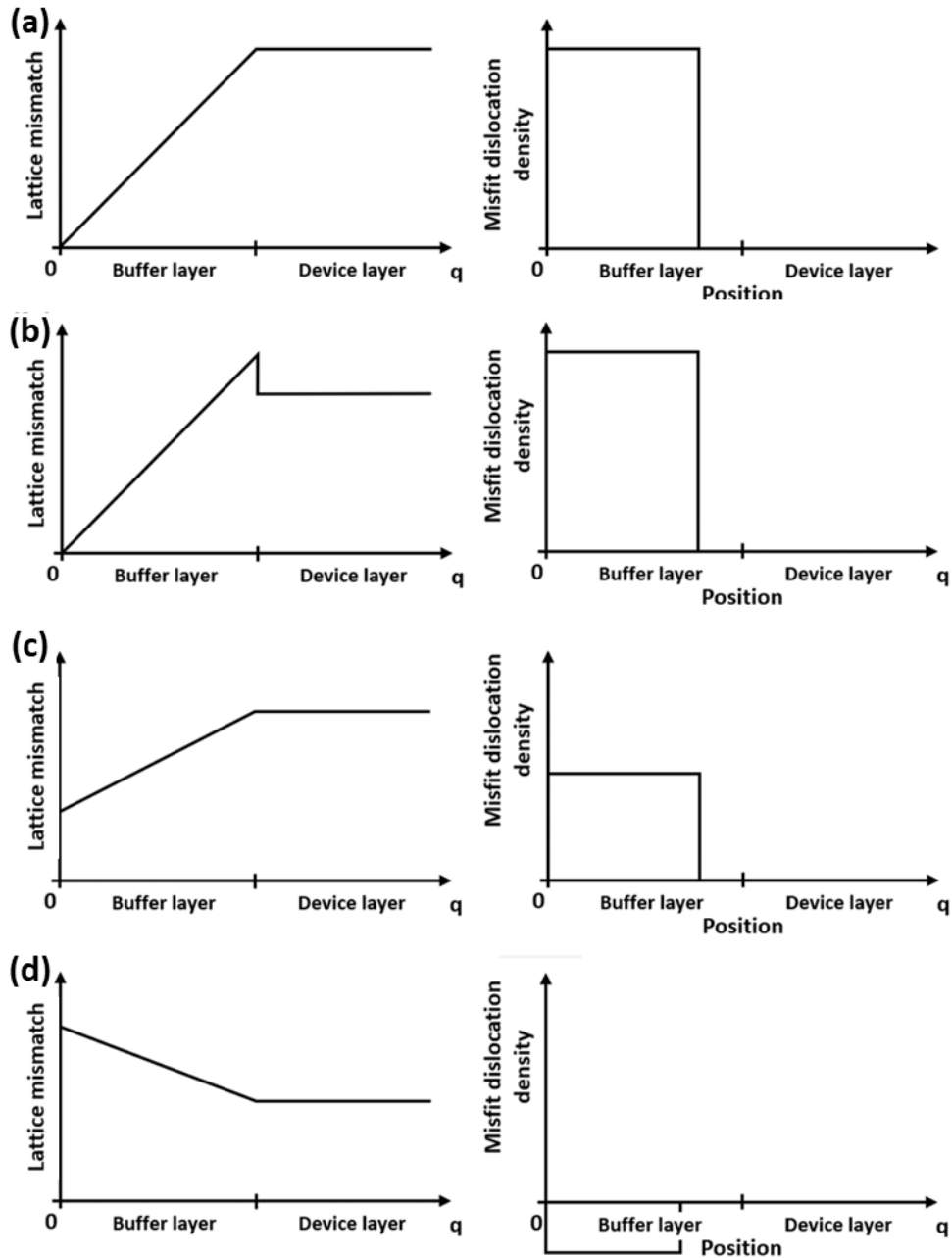


Figure 2.7: The (a) forward graded, (b) overshoot graded, (c) jump graded, and (d) reverse graded approaches to the linearly graded metamorphic buffer layer.

It is therefore argued that one of the most promising routes for T2SLs to overtake the performance levels of MCT is through the fabrication of HOT optically immersed detectors on

GaAs substrates using the IMF. This is because the material degradation introduced by the non-native GaAs substrate is less detrimental at high temperature where diffusion current, not G-R current, is most prevalent. Indeed, optically immersed LWIR T2SLs on GaAs have already been shown to have superior detectivity to equivalent MCT detectors at high temperatures^{41,94,96}. Therefore, a major objective of this project is the development of a LWIR T2SL on a GaAs substrate using the IMF array. The IMF array is here preferred to the metamorphic buffer layer for the reduced thickness of the required GaSb buffer layer which is more conducive to LWIR transmission. However, results from Korkmaz et al.²² suggest that some performance degradation persists in T2SLs on GaAs despite the presence of the IMF array. Unfortunately, characterisation of the IMF array itself has, so far, been relatively limited. Therefore, in the process of achieving the above objective, this project aims to perform a detailed characterisation study to determine the origins of this performance degradation. It is thought that this study can then be used to optimise future device designs.

2.2.2. Simulations and band-structure engineering

As mentioned above, the 6.1 Å family of materials provides great flexibility for the design of high performance T2SLs. The minimal lattice mismatch between InAs ($a = 6.0583$ Å), GaSb ($a = 6.0959$ Å), and AlSb ($a = 6.1335$ Å) ensures a large critical thickness for heterostructures comprised of these materials. This affords device designers a great deal of flexibility in choosing different combinations of 6.1 Å materials to tailor the band-structure and other band parameters of the resulting T2SL for a specific application.

The InAs layer in the T2SL period acts as a QW in which the electrons are confined. In a manner analogous to the analytical solution of the well-known “particle in a 2D box” problem, the energy level of a particle is closely inversely proportional to the product of its effective mass and the square of the well width. Therefore, the lower edge of the conduction band will decrease as the InAs thickness increases. If the InAs thickness is increased such that the conduction band edge decreases below the GaSb valence band edge, the superlattice becomes a semi-metal.

The GaSb layer acts as a QW in which the holes of the T2SL are confined but also acts as the barrier confining the electrons in the adjacent InAs QWs. The effective mass of holes in the

valence band is approximately 1 order of magnitude larger than that of electrons in the conduction band so that the dependence of the energy level on the GaSb well width is comparatively weak. This means the valence band of the T2SL stays roughly constant, close to the valence band of GaSb, regardless of GaSb thickness. However, the conduction band edge of the T2SL is strongly dependant on the GaSb thickness. In a manner analogous to the formation of energy bands from multiple atoms in bulk semiconductors, the conduction band of the T2SL is formed by the interaction between the electrons in the InAs wells. The strength of this interaction is determined by the separation between wells and the height of the blocking barrier. When the thickness of the GaSb layer is increased the interaction between the electrons in the InAs wells decreases. This narrows the conduction band of the T2SL, thereby increasing the conduction band edge. If the GaSb thickness is increased to the point where no interaction occurs between adjacent InAs wells, the “superlattice” simply becomes a multi QW structure.

While variations of the simple InAs/GaSb T2SL can reach cut-off wavelengths of around 3 – 30 μm , a further degree of flexibility can be achieved through incorporation of an AlSb barrier into the period of the T2SL. In addition to various performance enhancements discussed throughout Chapter 7.2, this addition enables the band engineering of the previously immobile T2SL valence band. The AlSb layer can be inserted in to the InAs layer (W-structure SL)^{119–122}, the GaSb layer (M-structure SL)¹²³, or between the InAs and GaSb layers (N-structure SL)^{124–126}. The effect of the AlSb barrier on the T2SL band structure depends on the design in which it is implemented, and this is discussed in more detail in Section 3.1.5. However, the general principle, whereby the barrier manipulates the wavefunction of the holes to push down the valence band edge, is common to most designs.

It can therefore be seen that with careful choice of the InAs, GaSb, and, if desirable, AlSb layer thicknesses, the T2SL can be designed to target any wavelength in the LWIR spectral range and beyond. Furthermore, multiple different combinations of SL structures can access the same target wavelength. This means that, if sufficiently well-informed, the device designer can choose a design with favourable parameters such as wavefunction overlap, effective masses, density of states, absorption coefficient etc.

Therefore, a key objective of this project is to develop a simulation that can accurately predict the band parameters of a given SL structure. This firstly allows for identification of a range of candidate SL designs to target the 10 μm cut-off wavelength. It is then possible to choose from the identified structures the SL that is best suited to a predetermined set of performance criteria that can be based on the intended application. Therefore, one objective of this project is to develop a simulation tool capable of accurately determining the band parameters of several feasible T2SLs. Following verification against both existing literature and our own experimental results, the parameters extracted from band structure simulations will then be used to inform further simulations on the device performance. Finally, these tools will be used to design new structures that are better optimised to their intended applications.

2.2.3. Fabrication developments

The fabrication of SL materials into devices is an active area of research with no standardised processes achieving universal adoption. As detailed below, the main areas of development needed are etching and passivation.

The functionality of a detector element requires that the signals from the different pixels are distinguishable from one another. Though some research has been undertaken to achieve this through diffusion doping^{127–130}, the vast majority of processes employ some kind of etching to define mesas. The two approaches to etching are wet etching, which uses chemical solutions, and dry etching, which uses plasmas. Wet etching usually involves submersing the sample in a solution containing an acidic etchant, such as citric or phosphoric acid for T2SLs, and an oxidising agent such as hydrogen peroxide. The main advantage of this approach is the availability and low cost of the necessary equipment and ingredients. However, the resulting etch will be either isotropic (Figure 2.9a), crystallographic (Figure 2.9c), meaning the etch follows the crystal planes of the semiconductor, or some combination of the two. This firstly means that the fill factor of the pixels will be very low and therefore unsuitable for the closely packed pixels of FPAs. Secondly, due to the isotropic or crystallographic nature of this etching process, the homogeneity of the resulting etch profiles is likely to be low with different pixels or planes etching with different rates.

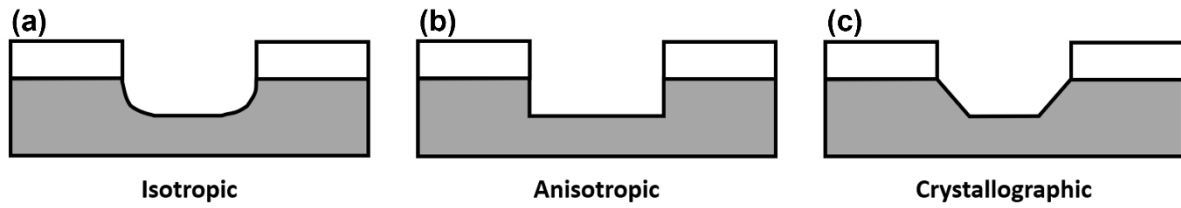


Figure 2.9: Schematic of an a) isotropic, b) anisotropic, and c) crystallographic.

This has led researchers to pursue dry etching for high performance detectors. The dry etching process uses high energy plasmas that are accelerated towards the sample surface. The etchant gasses used can be chemical (such as BCl_3), which evaporates the semiconductor material through a chemical process, physical (such as Ar), which physically dislodges the desired material, or as is most often the case, a combination of the two. The resulting etch will be anisotropic which allows development of very high fill-factor etches. Furthermore, dry etching, when properly optimised, is a very controllable process and very homogeneous across the wafer. Dry etching is therefore preferred for most high-performance applications and is considered a necessity for FPA fabrication due to the fill factor it provides. Also common in T2SLs is a combined approach in which the mesas are defined using a dry etch but some etch damage is removed using a wet etch.

Following the etching process, oxygen diffuses to the surface of the exposed sidewalls and forms native oxides through the following processes:



Not only do these oxidation processes occur readily but the resulting native oxides are good conductors, leading to a problematic surface dark current. This problem is particularly challenging for (V)LWIR detectors due to their reduced bandgap. A common solution is to physically shield the mesa sidewalls from ambient air using polyimide passivation such as $\text{SUG}^{131,132}$. The primary advantage of this technique is its accessibility rather than its efficacy as it is widely agreed that chemical passivation is a more effective solution than physical protection from ambient air. Recently, Al_2O_3 , deposited by Atomic layer deposition (ALD), has

been proposed as an effective form of passivation due to its favourable Gibbs free energy leading to the preferential formation of Al_2O_3 over In, Ga, As and Sb oxides. Specht et al.¹³³ have demonstrated that Al_2O_3 passivation reduces the dark current by an order of magnitude in p-type InAs/GaSb LWIR T2SLs. Perimeter/area analysis indicates the reduction in the surface-related component of the dark current. Furthermore, Salihoglu et al.^{124,134} have demonstrated that Al_2O_3 passivation is more effective for MWIR InAs/GaSb T2SLs than conventional approaches including SiO_2 , TiO_2 , HfO_2 , ZnO, and Si_3N_4 , by several orders of magnitude in some cases. Epitaxial overgrowth of a wide-bandgap material has also been proven to be an effective method of suppressing surface leakage current^{135,136}. The efficacy of this technique in T2SLs arises from the large band offset between the absorber and wide-bandgap semiconductor leading to a depletion of carriers in the vicinity of the IF. An advantage of this technique over dielectric deposition is that, by doping the wide-bandgap region, the common Fermi level between the two materials can be tuned. Sulphur-based passivation, in which a covalently bonded sulphur layer passivates the outer group-III and group-V atoms, has also been proven as an effective means of passivation and is often used in combination with a dielectric layer^{136,137}. Reticulated shallow etch mesa Isolation (RSEMI) and heterostructure designs are being exploited as an alternative to the chemical passivation to suppress the surface leakage current^{119,138}. This approach takes advantage of the barrier architectures such as the nBn in which only the n-top contact is etched. Etching through the barrier layer of such a device would be sufficient for pixel isolation. In this way, the unetched absorber region does not contribute to the surface current. Thus far, the best passivation results for LWIR T2SLs have been achieved using the gating technique in which a metal-insulator-semiconductor (MIS) structure is deposited on the mesa sidewalls. By applying a known bias to the MIS, the surface leakage current can be effectively controlled¹³⁹. Chen et al.¹⁴⁰ pioneered in reporting a two orders of magnitude reduction in the dark current using the gating technique in LWIR T2SLs by utilising a SiO_2 passivation layer. The gating technique has now been demonstrated for LWIR T2SLs using Y_2O_3 ¹⁴¹, hybrid SiO_2 - Y_2O_3 ¹⁴², and Si_3N_4 ¹⁴³ passivation layers. The major drawback of this technique is the high gate bias required for effective leakage suppression which is problematic for small-pixel FPAs although, a gated bias as low as -4.5 V has been achieved. It is theoretically possible to combine many of these techniques, such as dielectric deposition, sulphur-based passivation, the gating technique etc., into a single device.

The established process at Cardiff university for fabrication of single pixel T2SLs has been a standard photolithography process in which mesas were defined using a citric acid based wet etch and a hard-baked photoresist was used to physically protect the mesa sidewalls from ambient air. It is therefore an objective of this project to optimise this fabrication process through development of an effective passivation scheme and dry or combined etching process. Table 2.1 summarises these objectives and provides the chapter in which each is pursued.

Table 2.1: Summary of the key objects of this project.

Objective	Approach	Thesis chapter
Optimise the period of the T2SL	Grow and characterise T2SLs with different periods then use simulation tools to analyse results.	Chapter 4
Determine mechanisms by which performance degradation occurs in T2SLs on GaAs grown using the IMF	Grow and characterise a T2SL on GaAs using the IMF array. Compare results to a reference T2SL on GaSb.	Chapter 5
Optimise fabrication process	Develop and test dry etch and fabrication processes then compare device performance to wet etched and unpassivated samples.	Chapter 6

3. Research tools

To pursue the objectives described in Chapter 2 requires a range of experimental techniques which are described here. Design and analysis of samples is aided through the simulation tool described in Section 3.1. Samples were then grown using the technique described in Section 3.2. Devices were then fabricated from these samples using the process and techniques outlined in Section 3.3. Finally, both fabricated and unfabricated samples were characterised using the techniques described in Section 3.4.

3.1. Simulation

Determining the electronic properties of a T2SL is, fundamentally, a quantum mechanical problem. It is therefore necessary to solve the Schrödinger equation for the entire device to compute its global electronic structure. Previous studies have employed microscopic electronic structure methods such as the pseudopotential^{144,145} or empirical tight-binding model (ETBM)¹⁴⁶ which approach the problem on an atomic scale. However, as these methods are computationally expensive and the structures involved extend over tens of nanometres, an 8-band k·p method, detailed below, was used here.

3.1.1. k·p theory

The electronic structure of a bulk semiconductor is, in general, determined by a many-particle Hamiltonian that includes all electrons and nuclei of a crystal. By assuming the atomic cores to be stationary and by applying a mean field approximation for all multi-particle interactions, the problem can be described by a single-particle Schrödinger equation for an electron in a perfectly periodic crystal,

$$\hat{H}\psi_n(x) = \left[\frac{\hat{p}^2}{2m_0} + V(x) \right] \psi_n(x) = E_n \psi_n(x), \quad (3.1)$$

Where \hat{p} is the momentum operator, $V(x)$ is the resulting band edge profile that includes band offsets, band shifts due to strain, and the electrostatic potential. Due to the periodicity

of the crystal, the eigenfunctions, $\psi_n(x)$, obey Bloch's theorem, i.e. they are the same time eigenfunctions of the translation operator, $\hat{T}_{\mathbf{R}}$, such that,

$$\hat{T}_{\mathbf{R}}\psi_{n,\mathbf{k}}(x) = \exp(i\mathbf{k} \cdot \mathbf{R})\psi_{n,\mathbf{k}}(x). \quad (3.2)$$

Inserting these Bloch functions into the Schrödinger equation in Equation (3.1) yields,

$$\hat{H}(k)u_{n,\mathbf{k}}(x) = \left[\frac{(\hat{p} + \hbar\mathbf{k})^2}{2m_0} + V(x) \right] u_{n,\mathbf{k}}(x) = E_n(\mathbf{k})u_{n,\mathbf{k}}(x). \quad (3.3)$$

To solve above equation for the calculation of the band structure $E_n(\mathbf{k})$, the k·p method assumes that the majority of the carriers occupy regions close to the conduction band minima or valence band maxima. Thus, the k·p method takes a certain extremum, k_0 , for which the energies, $E_n(k_0)$, and Bloch factors, $u_{n,k_0}(x)$, are assumed to be known. By splitting the Hamiltonian in Equation (3.3) into a constant extremum part and a k-dependant part and assuming only wave vectors in the vicinity of the extrema of a few bands are relevant, the following Hamiltonian can be obtained,

$$\hat{H}'_{v\mu} = \hat{H}_{v\mu}(\mathbf{k}) + \sum_{\beta \in B} \frac{\hat{H}_{v\beta}(\mathbf{k})\hat{H}_{v\mu}(\mathbf{k})}{E_v(\mathbf{k}_0) - E_v(\mathbf{k}_0)}. \quad (3.4)$$

The Hamiltonian in Equation (3.4) can be solved using a single-band or multi-band approach. The single-band model, also called the effective mass approximation, is simplest but multi-band models are more accurate. Various k·p models have been reported in the literature, differing mainly in the number of bands considered and approach to strain and spin-orbit interaction¹⁴⁷⁻¹⁵⁰. In the present work, an 8-band k·p model was identified as an optimum compromise between accuracy and computational cost. One conduction and three valence bands were therefore considered. In a multi-band Schrödinger equation, an addition term, H_{SO} , must be added to take into account the relativistic effect of spin,

$$H_{SO} = \frac{\hbar^2}{4m_0^2c^2} (\nabla V \times \hat{p}) \cdot \sigma, \quad (3.5)$$

where σ is the vector of the Pauli matrices. Following the derivation of Andlauer¹⁵¹, the 8-band Hamiltonian can then be shown to be,

$$\hat{H}^{8 \times 8}(k) = \begin{pmatrix} \hat{H}_{ee}^{2 \times 2}(k) & \hat{H}_{ev}^{2 \times 6}(k) \\ \hat{H}_{ve}^{6 \times 2}(k) & \hat{H}_{vv}^{6 \times 6}(k) \end{pmatrix}, \quad (3.6)$$

with

$$\hat{H}_{ee}^{2 \times 2}(k) = (E_c + \sum_{i=1}^3 k_i A_c k_i) \otimes 1^{2 \times 2}, \quad (3.7)$$

and

$$\hat{H}_{ve}^{6 \times 2}(k) = \begin{pmatrix} -ik_1 P + k_3 B k_2 \\ -ik_2 P + k_1 B k_3 \\ -ik_3 P + k_2 B k_1 \end{pmatrix} \otimes 1^{2 \times 2}, \quad (3.8)$$

where the parameter B, related to the inversion symmetry of the crystal, can be considered to be zero for III/V materials. A detailed summary defining the relevant k·p parameters is provided in Ref. ¹⁵².

3.1.2. Spurious solutions

Spurious solutions, taking the form of ghost states, incorrect bound states at interfaces, and artificial oscillatory wave functions, lead to an undesirable ambiguity in the approach detailed above. In the present approach, these problems are eliminated by careful treatment of “remote-band contributions” to the bulk k·p Hamiltonians by defining an operator ordering that leads to self-adjoint Hamiltonians and employing an unwinding scheme for the discretisation of derivatives. For simplicity, a 2-band Hamiltonian, which has sufficient complexity to include all problems that may occur, is considered for the present discussion,

$$\hat{H}^{2 \times 2}(k) = \begin{pmatrix} E_c + A_c k^2 & iPk \\ -iPk & E_v + A_v k^2 \end{pmatrix}, \quad (3.9)$$

where A_c and A_v are parameters describing the free-electron and remote-band contributions to the effective masses. Solving the Hamiltonian in Equation 3.9 exhibits two solutions of k^2 for any given value of E , only one of which will be physical given the non-overlapping conduction- and valence-bands in semiconductor materials. In this case, the spurious solution of k^2 can form oscillatory nodes that lead to spurious ghost states. In the present work, following Ref. ¹⁵³, this problem is avoided by setting $A_c = 0$ and rescaling certain valence band parameters accordingly. The problematic k^4 term is thereby removed from the dispersion. Additional mitigations to spurious solutions are given in more detail in Ref. ¹⁵¹.

3.1.3. Numerical realisation

The numerical solution of the physical relations is achieved by mapping the partial differential equations on a discrete lattice by discretisation of the differential operators and, therefore,

transformed into linear algebra problems. A box integration finite difference approach is here employed for discretisation. In this approach, the simulation domain is split into regular, non-overlapping boxes, each covering the area closest to one grid node. The partial differential equations are now integrated over these box volumes, obtaining an integral equation that is discretised using the finite difference scheme detailed in Ref. ¹⁵¹. Following discretisation, the partial differential equations become a large system of linear or non-linear equations. These systems are solved iteratively using the conjugate gradient method¹⁵⁴, composite step conjugate gradient method¹⁵⁵, or biconjugate gradient method¹⁵⁶.

3.1.4. Implementation in Nextnano³

The 8-band k·p method described above has been implemented in the Nextnano³ software¹⁵⁷. The structures considered in this work contain the compounds InAs, GaSb, InSb, AlSb, and alloys thereof. The parameters used for these binaries, along with the accompanying references, are given in Table 3.1.

Table 3.1: Material parameters of InAs, GaSb, and InSb binaries used in Nextnano³ for the k·p band structure calculation. All values used can be found in Refs. ^{158, 159, 160, 161} and ¹⁶².

Parameter	InAs	GaSb	InSb	AlSb
Lattice constant a_0 (Å)	6.0583 ¹⁵⁹	6.0959 ¹⁵⁹	6.4794 ¹⁵⁹	6.1355 ¹⁵⁹
Energy band gap at 0K (eV)	0.410 ¹⁵⁹	0.812 ¹⁵⁹	0.240 ¹⁵⁹	2.386 ¹⁵⁹
Varshni parameter α (meV/K)	0.276 ¹⁵⁹	0.417 ¹⁵⁹	0.320 ¹⁵⁹	0.42 ¹⁵⁹
Varshni parameter β (K)	93 ¹⁵⁹	140 ¹⁵⁹	170 ¹⁵⁹	140 ¹⁵⁹
Conduction band mass m_c ($/m_0$)	0.022 ¹⁵⁸	0.042 ¹⁵⁸	0.135 ¹⁵⁹	0.14 ¹⁵⁹
Luttinger parameter γ_1	19.77 ¹⁵⁸	11.74 ¹⁵⁸	34.8 ¹⁵⁹	5.18 ¹⁵⁹
Luttinger parameter γ_2	9.43 ¹⁵⁸	5.28 ¹⁵⁸	16.5 ¹⁵⁹	1.19 ¹⁵⁹
Luttinger parameter γ_3	22.2 ¹⁵⁸	22.4 ¹⁵⁸	23.3 ¹⁵⁹	1.97 ¹⁵⁹
Interband matrix element E_p (eV)	0.38 ¹⁶⁰	0.752 ¹⁶⁰	0.81 ¹⁵⁹	18.7 ¹⁵⁹
Spin orbit splitting Δ_0 (eV)	832.9 ¹⁶⁰	884.2 ¹⁶⁰	684.7 ¹⁵⁹	0.676 ¹⁵⁹
Elastic constant c_{11} (GPa)	832.9 ¹⁵⁹	884.2 ¹⁵⁹	684.7 ¹⁵⁹	87.69 ¹⁵⁹
Elastic constant c_{12} (GPa)	452.6 ¹⁵⁹	402.6 ¹⁵⁹	373.5 ¹⁵⁹	43.41 ¹⁵⁹
Elastic constant c_{44} (GPa)	395.9 ¹⁵⁹	432.2 ¹⁵⁹	311.1 ¹⁵⁹	40.76 ¹⁵⁹
Deformation potential CB a_c (eV)	-6.66 ¹⁶¹	-9.33 ¹⁶¹	-6.94 ¹⁵⁹	-8.12 ¹⁶²
Deformation potential VB a_v (eV)	-1 ¹⁶¹	-1.32 ¹⁶¹	-0.36 ¹⁵⁹	0.73 ¹⁶²
Uniaxial deformation potential b (eV)	-1.8 ¹⁵⁹	-2 ¹⁵⁹	-2 ¹⁵⁹	-1.35 ¹⁵⁹
Uniaxial deformation potential d (eV)	-3.6 ¹⁵⁹	-4.7 ¹⁵⁹	-4.7 ¹⁵⁹	-4.3 ¹⁵⁹
Valence band offset VBO (eV)	-0.56 ¹⁵⁹	0 ¹⁵⁹	0.03 ¹⁵⁹	-1.81 ¹⁵⁹

The IF matrix, H_{IF} , described by Klipstein¹⁶³, was implemented inside the software framework.

For the case of the no-atom-in-common SL, e.g. the InAs/GaSb T2SL, the matrix is defined as:

$$H_{IF} = \sum_i \delta(z-z_i) \begin{bmatrix} D_S & 0 & 0 & \pi_i \beta \\ 0 & D_X & \pi_i & 0 \\ 0 & \pi_i \alpha & D_X & 0 \\ \pi_i \beta & 0 & 0 & D_Z \end{bmatrix}, \quad (3.10)$$

where i is the index of the IF at the position z_i and π_i is either -1 or 1. The IF parameters, α and β , have been set to $0.2 \text{ eV}\cdot\text{\AA}$ according to Ref.¹⁶³. The diagonal IF parameters, D_S , D_X , and D_Z should be determined through comparison with experimental results. Due to the sparsity of optical data available in the literature, this could not be done for the InAs/GaSb T2SL until our own data was collected, as discussed in Section 4.1.4. However, as discussed in the following section, the accuracy of this simulation tool can be verified through comparison with the literature of other SL structures.

3.1.5. Validation of the simulation tool

The first superlattice structure considered for validation purposes was the InAs/InAsSb T2SL, discussed in Section 1.3. The 8 band k-p simulation implemented in Nextnano3 discussed previously was modified for simulation of InAs/InAsSb T2SLs. The IF matrix (Equation 3.7) was implemented but the diagonal IF parameters (D_S , D_X , D_Z) were set to zero as the InAs/InAsSb T2SL is a *common-atom* SL¹⁶³. No interfacial layer was added between the InAs and InAsSb layers on the assumption that the commonality between the two SL layers will result in abrupt IFs. However, this assumption can be challenged on the basis of more recent characterisation papers reporting significant Sb segregation and interfacial intermixing at the SL IFs^{164,165}. The effect of these phenomena could be incorporated in future simulations although it is difficult to determine the extent to which they occur. Furthermore, characterisation techniques, such as Atom probe tomography (APT), are both destructive and very localised which raises questions of whether the results are representative of the whole sample.

The InAs layers were simulated using the parameters given in Table 3.1. The parameters for InAsSb were defined as a weighted average of the parameters for InAs and InSb. For some parameters, a bowing parameter, b , was inserted according to Vegard's law:

$$\alpha_{InAsSb} = x\alpha_{InAs} + (1 - x)\alpha_{InSb} - bx(1 - x), \quad (3.11)$$

where α is a given material parameter, x is the InAsSb alloy constant, and b is the bowing parameter. The bowing parameters for the conduction and valence band energies were +0.65 eV and -0.98 eV respectively in accordance with Keen et al.¹⁶⁶ A bowing parameter of -0.8 eV was also added to the band shift of the InAsSb layer as an approximate accommodation of the 40:60 bowing split between the CB and VB as suggested by Liu et al.¹⁶⁷.

Figure 3.1a shows an example 14 nm InAs/14 nm InAsSb SL with 13.8% Sb content. As Figure 3.1b shows, the electron wavefunction has a maximum in the InAs layer which acts as a well for electrons and decays exponentially in the InAsSb layer which acts as a barrier. As this is reversed for holes, the hole wavefunction has a maximum in the InAsSb well and decays exponentially in the InAs barrier as predicted. Figure 3.1c shows the E(k) diagram from which the electron and hole effective masses can be extracted.

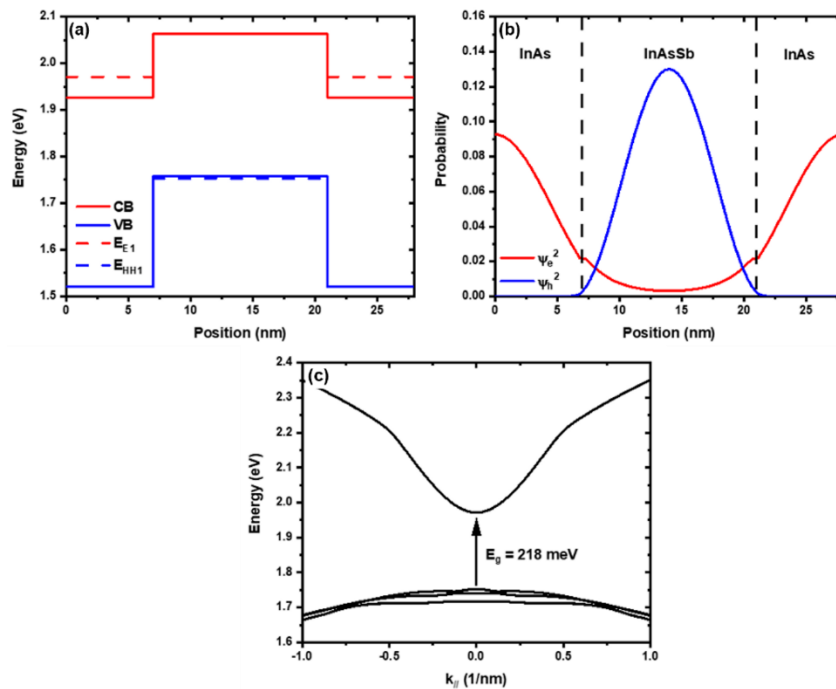


Figure 3.1: (a) The band structure, (b) electron and hole wavefunctions, and (c) E-k diagram for an example SL.

The results of the simulation were compared to those of Keen et al.¹⁶⁶, who demonstrated the growth of a set of InAs/InAsSb T2SL samples by MBE and used both PL measurements and simulation to determine the band gap energies of each design. Table 3.2 provides an overview of sample designs and Figure 3.2 provides a comparison of results.

Table 3.2: Summary of InAs/InAsSb T2SL sample structures.

Sample	InAs layer thickness (nm)	InAsSb layer thickness (nm)	No. of periods	Sb content, x (%)
Ga-free 1	14.0	14.0	50	3.8
Ga-free 2	14.0	14.0	50	6.2
Ga-free 3	14.0	14.0	50	9.5
Ga-free 4	14.0	14.0	50	13.5

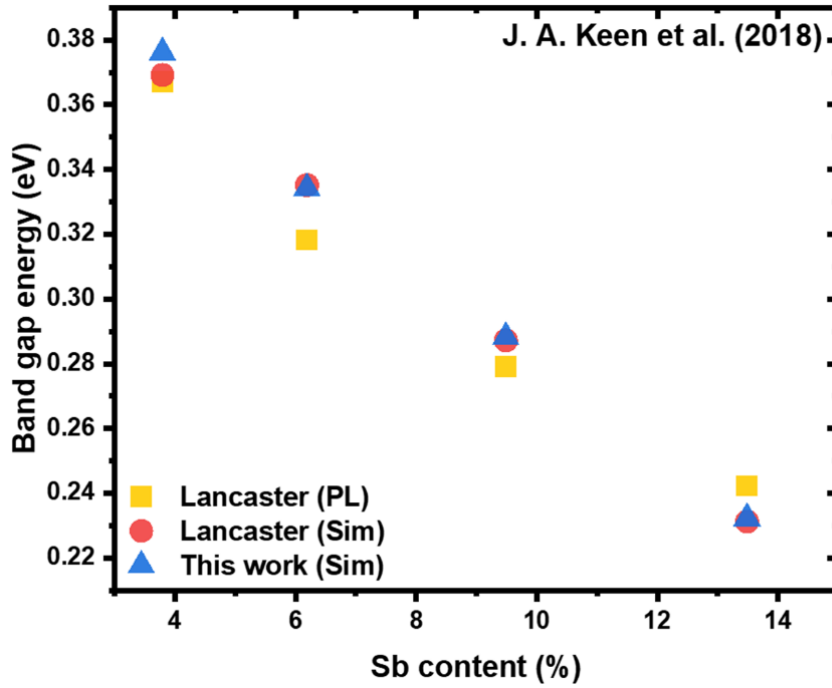


Figure 3.2: Comparison of band gap energies for four samples of different Sb content as measured by PL at Lancaster, simulations at Lancaster, and simulations performed in this work.

Figure 3.2 shows that the simulation results reported in the present work match very closely to those of Keen et al.¹⁶⁶ which both reported a linear decrease in the band gap energy with increasing Sb content. Interestingly, the band gap energy as measured by PL shows a concave, rather than linear, dependence on the Sb content which is not predicted by either simulation. However, this could be attributed to either an uncertainty in the growth of these samples through Sb content in the InAsSb layer, Sb segregation in the InAs layer, or interfacial intermixing or an oversimplification in the simulations. Unfortunately, Keen et al.¹⁶⁶ provide only limited details on their simulation which makes it difficult to determine which explanation is most plausible.

It is also useful to consider T2SLs that incorporate AlSb barriers for band structure engineering purposes as there is an abundance of literature with which simulation results can be compared. The “M-structure” SL, in which a thin AlSb layer is inserted into GaSb layer of a conventional InAs/GaSb SL, was first proposed by Nguyen et al.¹⁶⁸. The structure is shown schematically in Figure 3.3 which highlights the eponymous “M” shape.

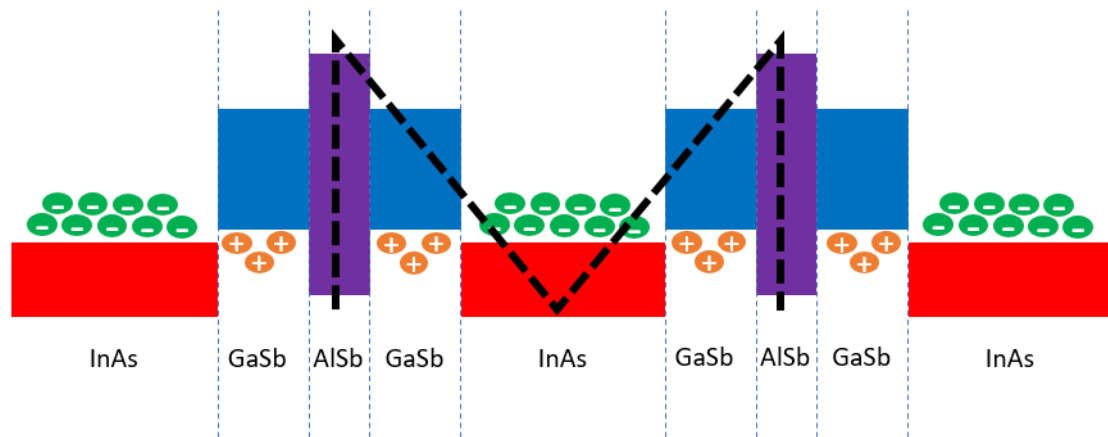


Figure 3.3: Schematic diagram of the M structure SL as proposed by Nguyen et al. Coloured regions show the forbidden energy gap.

The authors explicated several advantages of the M-structure over the conventional SL designs. Firstly, the M-structure preserves the type-II band alignment of the SL and the accompanying suppression of Auger recombination. Furthermore, unlike the structures below, the M-structure only uses lattice-matched binary materials and is therefore easier to realise. Ease of growth is also enhanced by the common Sb atom at the GaSb/AlSb IFs. However, the primary advantages are related to performance and band engineering. The

insertion of an AlSb barrier in the GaSb layer has the effect of increasing the electron effective mass and decreasing electron mobility as the AlSb blocks the electron transport. This blocking effect is advantageous as it reduces the thickness of GaSb required to reach a given wavelength. The AlSb barrier creates a double quantum well which pushes the holes to the edges of the GaSb layer which increases their interaction with the electrons in the InAs layer. The overall effect of the increased interaction between electrons and holes is to improve the optical properties of the superlattice. Nguyen et al.¹⁶⁹ have also demonstrated suppression of dark current with an M-structure barrier photodiode. Here the higher effective masses of the M-structure suppress the transport of tunnelling and diffusion currents at the depletion region which results in favourable performance.

The M-structure SL was simulated within the Nextnano3 framework described in Section 3.1.2 using the material parameters in Table 3.1. These results were then compared with measured PL results and ETBM simulations reported by Nguyen et al.¹⁶⁸. As Figure 3.4 shows, there is a good agreement between the simulated and experimental results.

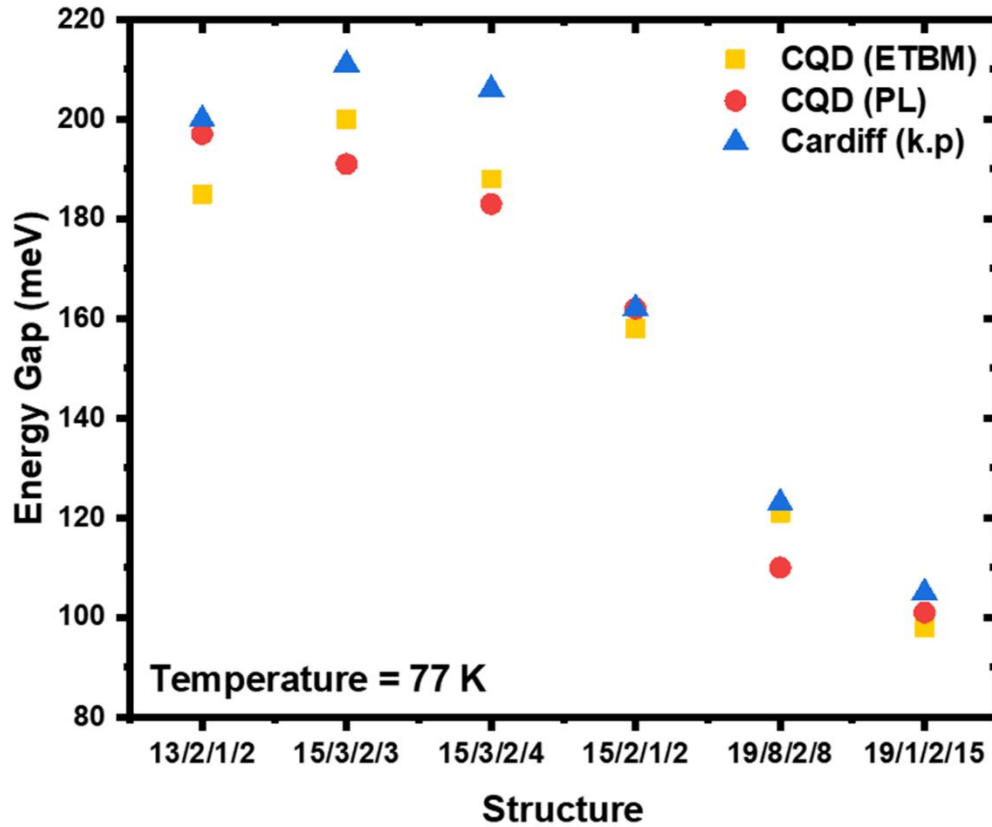


Figure 3.4: Comparison of simulated and measured band gaps for various T2SL M-structures. Structures have A ML InAs/ B ML GaSb/ C ML ALSb/ D ML GaSb.

To verify the hypothesis that the ALSb barrier improves optical performance of the T2SL by pushing the holes to the edges of the GaSb layer, an M-structure with 13 ML InAs/ 2.5 ML GaSb/ 1 ML ALSb/ 2.5 ML GaSb was compared to a 13/5 SL (the same structure with the ALSb layer removed) and a 13/17 SL (the conventional SL structure with comparable band gap energy). The simulated band diagrams for each SL structure are shown in Figure 3.5.

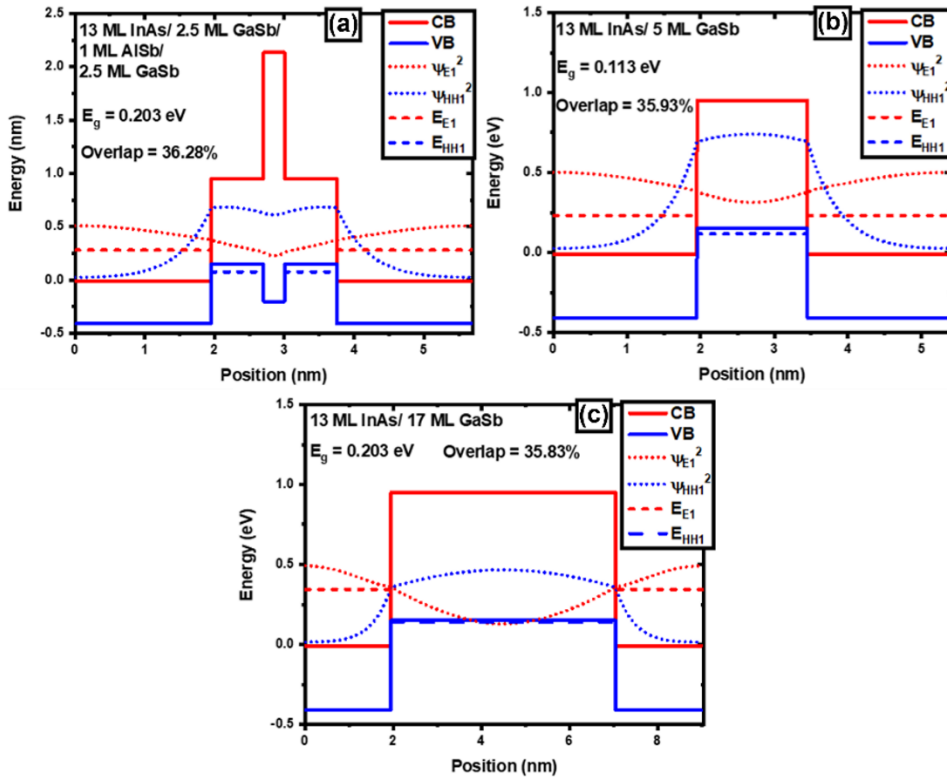


Figure 3.5: Simulated band diagrams for a (a) 13/2.5/1/2.5 SL, (b) 13/5 SL, and (c) 13/17 SL.

By comparing Figure 3.5a with b and c, it is clear that the insertion of a 1 ML AISb barrier has the desired effect of pushing the holes to the edges of the InAs layer which is why the hole wavefunction is larger in these areas. As Figure 3.5 shows, this increases the overall wavefunction overlap of the M-structure SL compared to both the same structure without the AISb barrier (Figure 3.5b) and a similar structure of comparable wavelength (Figure 3.5c), but in each case by less than 1%. By comparing Figure 3.5a and c it is also clear that the AISb barrier reduces the required thickness of the GaSb layer to reach a given energy gap.

The electron effective masses for multiple M-structure T2SLs were simulated and compared to those of Nguyen et al.¹⁶⁸. Figure 3.6 shows that both the 8 band k-p model and ETBM predict the electron effective mass to increase with increasing AISb layer thickness. Furthermore, the magnitudes of the electron effective masses of SL structures with 0 and 1 ML of AISb are approximately comparable in magnitude when calculated by 8 band k-p theory and ETBM. However, according to the curves for SLs with 3 and 5 ML of AISb, the ETBM predicts a more significant increase in the electron effective mass with increasing AISb barrier thickness compared to the model based on 8 band k-p theory. Perhaps more notably, the

ETBM predicts an apparently exponential increase of the electron effective mass with GaSb layer thickness whereas the 8 band k-p model predicts an apparently logarithmic increase. Nguyen et al. claim that the exponential increase in electron effective mass arises from the exponential dependence of the tunnelling probability on the thickness of the barrier. It follows that, as the GaSb layer acts as a barrier for electrons, the electron effective mass should increase exponentially with the GaSb thickness. It should therefore be noted that the model reported here may be of limited use for predicting effective masses.

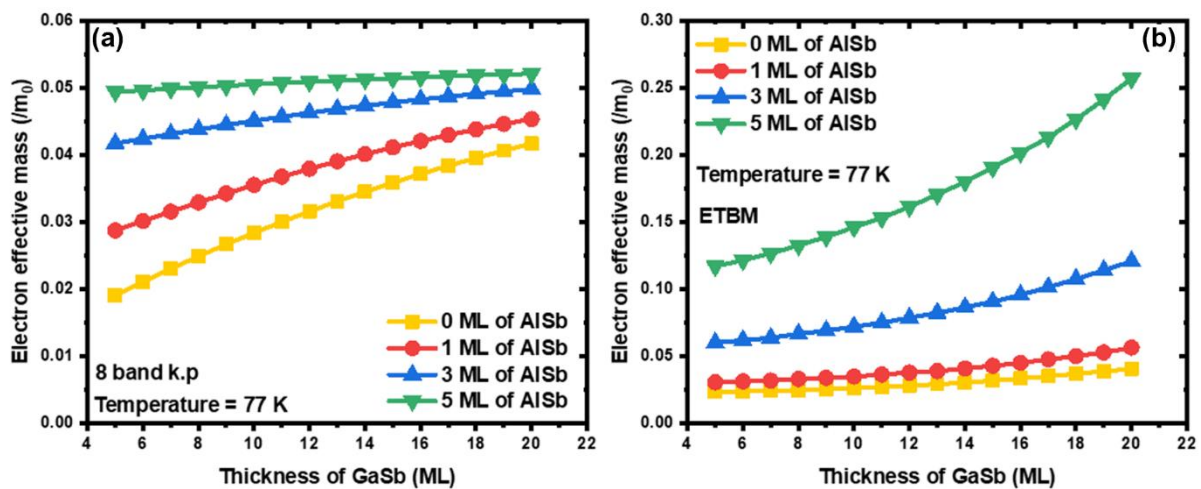


Figure 3.6: The electron effective masses for various M-structure SLs as calculated by (a) 8 band k-p theory and (b) the empirical tight binding model.

Finally, the effect of the position of the AISb barrier layer on the band structure of the SL was investigated. Figure 3.7 shows the band structure of an 18 ML InAs/ 16 ML GaSb/ 2 ML AISb M-structure SL in which the AISb barrier is displaced from the center of the GaSb well. Figure 3.7 is in very strong agreement with Figure 6 from Ref.¹⁶⁸. This confirms the 8 band k-p model is capable of accurately predicting the band gap of the any given M-structure T2SL, irrespective of layer thicknesses and positions.

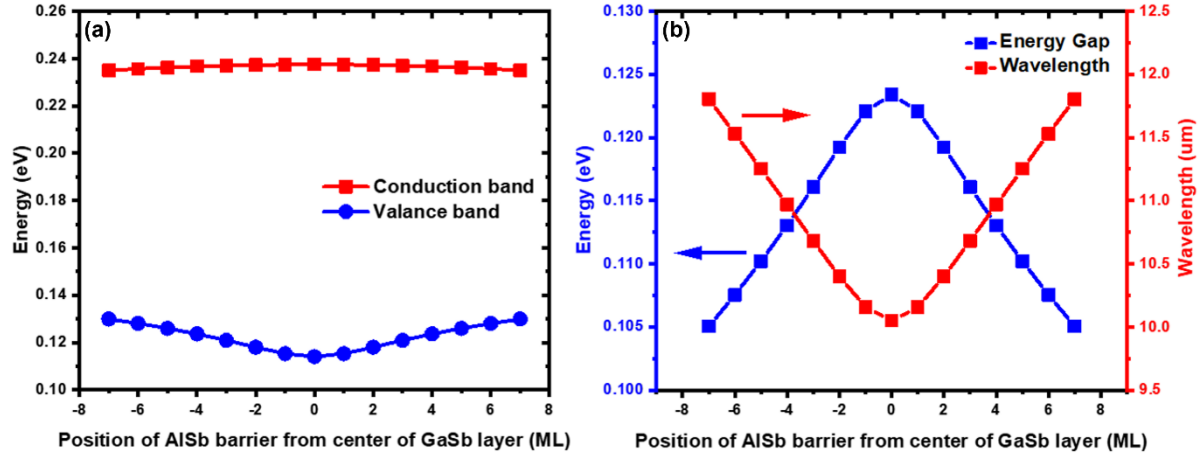


Figure 3.7: 8 band k-p simulation for a 19 ML InAs/ 16 ML GaSb/ 2 ML AISb SL for (a) the effect of the position on the AISb barrier on the conduction and valence bands and (b) the effect of the AISb position on the energy gap and wavelength.

The W-structure SL, which inserts a thin AISb barrier into the InAs well of a conventional InAs/GaSb T2SL, was also considered for validation purposes. This structure differs from the M-structure SL in that the AISb layer is inserted into the InAs, rather than GaSb, layer. The strong confinement generated by the AISb barrier gives the W-structure SL a nearly 2-dimensional density of states which gives rise to a much sharper absorption edge than conventional T2SLs. This results in a higher peak quantum efficiency at higher wavelengths. Furthermore, the effect mentioned above for M-structure SLs, whereby the AISb barrier pushes the carriers to the edges of the well and increasing wavefunction overlap, is present in W-structure SLs. The overall effect is that W-structure SLs have greatly improved the optical properties compared to conventional T2SLs^{129–132}. The W-structure SL was simulated using the same methodology as the M-structure SL described above. Linear interpolation was used to determine the material parameters of all ternary alloys unless stated otherwise. A bowing parameter of 0.415 eV was used for the bandgap energy of GaInSb in accordance with Vurgaftman et al.¹⁵⁹. The band parameters of the quaternary alloy $\text{Al}_{0.4}\text{Ga}_{0.49}\text{In}_{0.11}\text{Sb}$ were selected to be in good agreement with Ref. ¹³¹.

Figure 3.8 shows two examples of W-structure SLs (Table 3.3) described by Aifer et al.¹³¹. Both structures replace the conventional GaSb layer with a $\text{Ga}_{0.81}\text{In}_{0.19}\text{Sb}$ alternative for lattice matching reasons discussed in the section below. Figure 3.8a shows a conventional W-

structure (WSL-A) with AISb barriers while Figure 3.8b shows a modified W-structure (WSL-B) with $\text{Al}_{0.4}\text{Ga}_{0.49}\text{In}_{0.11}\text{Sb}$ barriers. Figure 3.8 matches closely with Figure 1 in Ref.¹³¹.

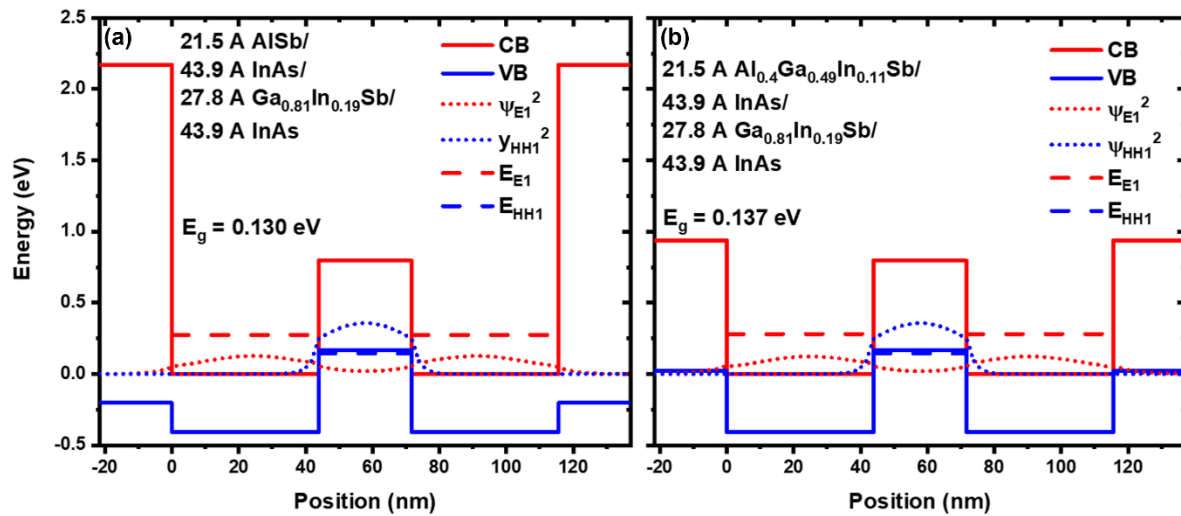


Figure 3.8: 8 band k-p simulations of the band structure for (a) WSL-A and (b) WSL-B.

Table 3.3: Parameters extracted from 8 band k-p simulations for WSL-A and -B.

Sample	Barrier	Band gap (eV)	Wavefunction overlap (%)	Electron effective mass ($/m_0$)	Hole effective mass ($/m_0$)
WSL-A	AISb	0.130	8.6%	0.0285	0.0373
WSL-B	$\text{Al}_{0.4}\text{Ga}_{0.49}\text{In}_{0.11}\text{Sb}$	0.137	8.6%	0.0284	0.0372

Figure 3.9 shows the calculated band energy of various W-structure SLs as calculated by this work and compared to that of Aifer et al.¹³⁰. The structures considered are of 5 ML AISb/ N ML InAs/9 ML $\text{In}_x\text{Ga}_{1-x}\text{Sb}$ / N ML InAs where the In content, x, is chosen for lattice matching and given next to the relevant data point. The model presented here shows a very good agreement with the 16 band k-p simulation reported by Aifer et al.¹³⁰ Table 3.3 shows the band parameters extracted from the simulations for WSL-A and -B. The results confirm the assertion of Aifer et al. that the incorporation of the $\text{Al}_{0.4}\text{Ga}_{0.49}\text{In}_{0.11}\text{Sb}$ barrier, in place of the conventional AISb, reduces the effective masses in the SL although Table 3.3 suggests this

effect is very minor. Results also show that the wavefunction overlap remains unchanged, but the band gap increases slightly with the $\text{Al}_{0.4}\text{Ga}_{0.49}\text{In}_{0.11}\text{Sb}$ barrier.

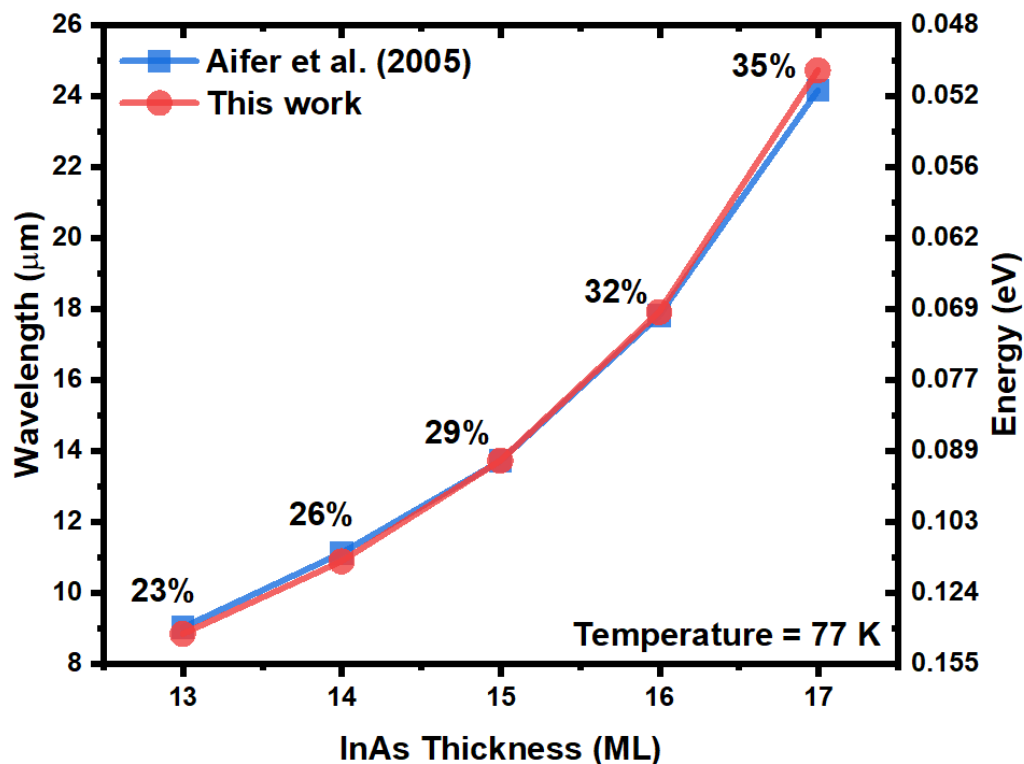


Figure 3.9: A comparison of the band structure simulation results of this work and that of Aifer et al. for W-structure SLs with 5 ML AlSb/ N ML InAs/9 ML $\text{In}_x\text{Ga}_{1-x}\text{Sb}$ / N ML InAs.

Finally, a variant of the InAs/GaSb T2SL which incorporates ternary and quaternary layers in place of the conventional binaries was considered. This principle has been used for multiple structures but only the 13 ML $\text{InAs}_{0.91}\text{Sb}_{0.09}$ /7 ML $\text{In}_{0.5}\text{Ga}_{0.5}\text{As}_{0.46}\text{Sb}_{0.54}$ T2SL, reported by Du et al.^{170,171}, is considered here. The input parameters for the InAsSb layer were determined using the method described for the InAs/InAsSb T2SLs described above. The band gap and alignment of the $\text{In}_{0.5}\text{Ga}_{0.5}\text{As}_{0.46}\text{Sb}_{0.54}$ was chosen for best agreement with the structure shown by Du et al.^{170,171}. However, it was also ensured that these values were consistent with the band energies and bowing parameters for InGaAs and InGaSb given by Vurgaftman et al.¹⁵⁹. All other parameters were determined as a weighted average of the values for InGaAs and InGaSb. The results are shown in Figure 3.10 and the extracted parameters are shown in Table 3.4.

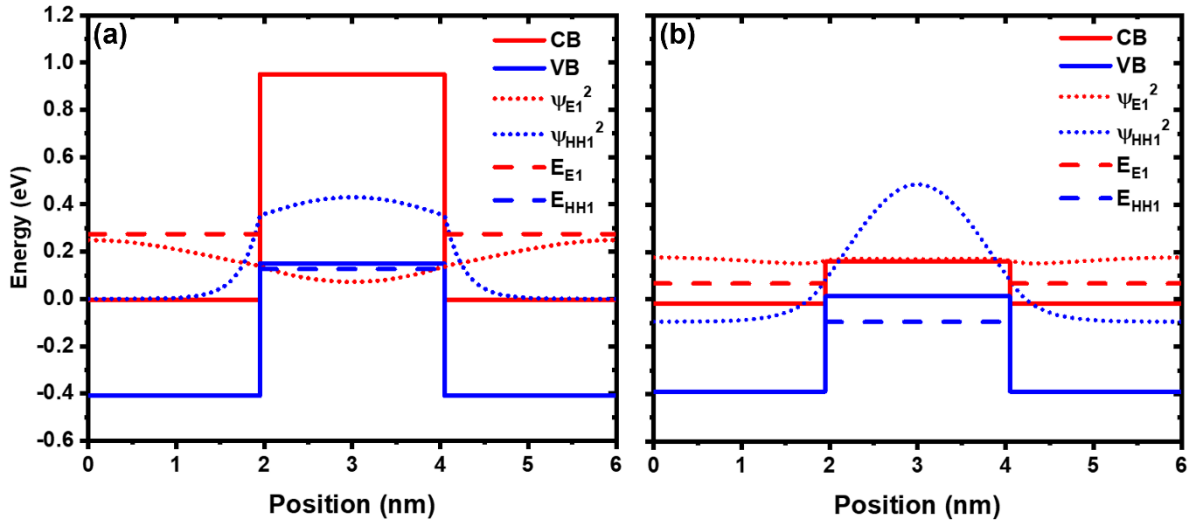


Figure 3.10: 8 band k·p simulations of the band structure for a) a 13 ML InAs/7 ML GaSb SL and b) a 13 ML InAs_{0.91}Sb_{0.09}/7 ML In_{0.5}Ga_{0.5}As_{0.46}Sb_{0.54} SL.

Table 3.4: Parameters extracted from 8 band k·p simulations for the structures in Figure 3.10.

Structure	Band structure (eV)			Wavefunction overlap (%)
	CB	VB	E_g	
InAs/GaSb	0.275	0.126	0.150	33.2
InAsSb/InGaAsSb	0.0668	-0.095	0.162	45.6

Du et al. claim that, when compared to a conventional 13 ML InAs/7 ML GaSb T2SL using PL measurements at 77 K, the quaternary SL showed a similar peak wavelength but a sevenfold higher peak intensity. This was attributed to an increase in the wavefunction overlap, brought about by the delocalisation of conduction band electrons. This explanation corroborates the shape of the electron wavefunction shown in Figure 3.10b and the wavefunction overlaps shown in Table 3.4. Table 3.4 also shows the simulated peak wavelength of the InAsSb/InGaAsSb SL (7.7 μm) is very close to that measured using PL by Du et al. (7.7 μm). However, the simulated peak wavelength of the InAs/GaSb SL (8.3 μm) deviates notably from

that measured by Du (7.7 μm). This discrepancy can be attributed to uncertainty regarding the interfacial scheme Du et al. used in the growth of the T2SLs. Table 3.4 also shows the InAsSb/InGaAsSb SL has a notably larger wavefunction overlap than the conventional InAs/GaSb SL. Figure 3.10 shows that this is due to the decreased barrier height of the $\text{In}_{0.5}\text{Ga}_{0.5}\text{As}_{0.46}\text{Sb}_{0.54}$ barrier layer which causes a delocalization of electrons in the conduction band, shown by the flattening of the electron wavefunction in Figure 3.10b. It can therefore be seen that our 8 band k.p simulations confirm the findings of Du et al.

The accuracy with which the simulation tool has replicated the results of the literature suggests its suitability for simulation of InAs/GaSb. While some discrepancies have been noted in the simulation of the effective masses, the simulation tool has repeatedly demonstrated accurate reproduction of both measured and simulated band gap energy values.

3.2. MBE Growth

3.2.1. The MBE reactor

MBE is a versatile technique for the growth of high-quality compound semiconductor films as well as other materials. The process involved the crystallisation of thin epitaxial films via reactions of thermal-energy molecular or atomic beams of the constituent elements and a substrate maintained at a high temperature (a few hundred Kelvin) in an ultrahigh vacuum-chamber. The composition of the epilayer can be controlled through careful choice of the evaporation or sublimation rates of the appropriate sources which determines the relative arrival rates of the constituent elements. Provided the growth rate is sufficiently low, the impinging species will migrate along the surface to ensure an even film deposition. More complex structures, including T2SLs, are grown by opening and closing mechanical shutters for periodically stopping and starting the deposition.

The in situ monitoring and precise control of the MBE growth process is required to achieve the monolayer precision needed to accurately and consistently define the QWs of the T2SL. In the last decade, various groups have reported the growth of T2SLs using MOCVD which has the advantage of lower costs and higher throughput^{29,172}. However, most of these reports concern the Ga-free variant due to the low melting InSb and low equilibrium vapour pressure

of Sb MO-sources which are required for the InSb interfaces commonly employed in Ga-containing T2SLs. Huang et al.¹⁷³ have successfully grown InAs/GaSb T2SLs by MOCVD using GaAs-like interfacial layers, but this technique has not been widely studied or replicated. It can therefore be concluded that, in the present scenario, MBE is the only technique suitable for growth of high-performance T2SLs.

Figure 3.11 shows a schematic diagram of a typical MBE chamber during growth. As shown in Figure 3.11, the reactor consists of several key components which are detailed below:

- Load lock

The load lock is used to bring samples in and out of the main chambers without breaking the vacuum of these chambers. The load lock chamber is designed with a small volume to allow the backing pump to quickly achieve the correct pressure ($\sim 10^{-8}$ Torr).

- Preparation chamber

The initial outgassing occurs in the preparation chamber. The samples are then transferred to the growth chamber via the preparation chamber. The chamber is equipped with an ion pump that allows it to achieve a pressure comparable to the growth chamber ($\sim 10^{-10}$ Torr).

- Growth chamber

The growth chamber is main chamber of the MBE reactor in which epitaxial growth takes place. There is therefore a need for ultrahigh vacuum operation ($\sim 10^{-11}$ Torr) which, due to the size of the chamber, requires a turbopump, ion pump, working together with a cryopump.

- Continuous azimuthal rotation assembly

The substrate heater is equipped with a continuous azimuthal rotation (CAR) assembly which has the capability for rotation rates of up to around 150 rotations per minute. This increases the surface uniformity of the epitaxial film.

- Effusion cells

The effusion cells house the source materials in a condensed phase inside an inert crucible. To generate the molecular beams, a resistance heated source is used to heat the crucible to the necessary temperature for evaporation/sublimation. The temperature is controlled using a thermocouple. Many modern designs use a “dual-filament” configuration in which separate thermocouples are used to heat the base and tip of the cell which improves the uniformity of the epitaxial layer.

- Cracker cells

Cracker cells are an alternative to conventional effusion cells used in solid source epitaxy. They produce dimeric molecules, such as As_2 or Sb_2 , from elemental sources, this case As_4 and Sb_4 . For high vapour pressure materials such as As, Te and Sb, the cracker cell is used to thermally dissociate larger molecules (such as As_4 and Sb_4) to smaller, more reactive species dimeric molecules, such as As_2 or Sb_2 .

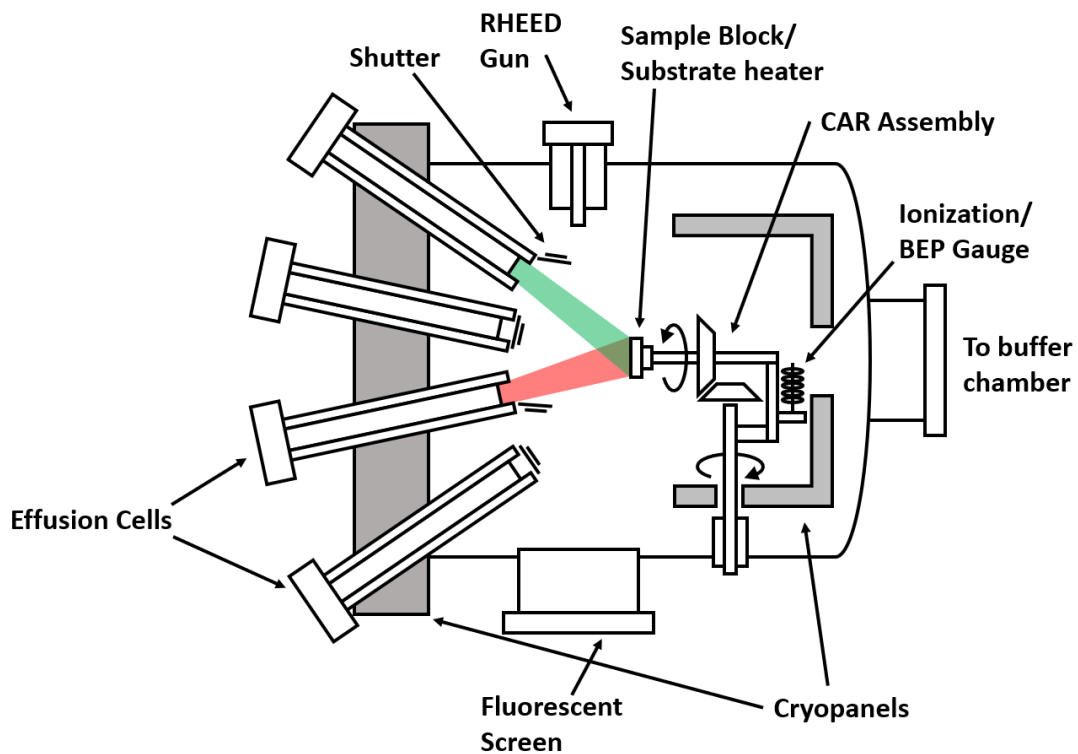


Figure 3.11: Schematic of a typical MBE reactor.

3.2.2. *In-situ* characterisation

A significant advantage of MBE compared to other epitaxial growth techniques arises from the fact that it is realised in an ultrahigh vacuum environment. This enables the use of surface sensitive *in-situ* characterisation techniques such as reflection high-energy electron diffraction (RHEED), Auger electron spectroscopy (AES), and ellipsometry. These techniques facilitate a high degree of control over the epitaxial deposition by eliminating much of the guesswork. This advantage, as mentioned above, facilitates the growth of complex structures such as T2SLs. These techniques are detailed below:

- Reflection high-energy electron diffraction

RHEED is the most important of the *in-situ* analysis techniques and allows for observation of the dynamics of the MBE growth process. As shown in Figure 3.12, a high energy beam of electrons with energy 3 – 10 keV is directed towards the sample surface at a grazing angle of around $1^\circ - 3^\circ$. This ensures the penetration of the beam is limited to the outermost atomic layers. These electrons are then diffracted by the crystal structure of the sample surface and impinge on a phosphor screen mounted on the opposite side of the chamber. As shown in Figure 3.12, the intensity of the RHEED signal depends on the roughness and atomic arrangement of the sample surface. If the surface is rough, many electrons will be scattered and not detected by the phosphor screen. Conversely, if the sample surface is atomically smooth the RHEED signal will be very strong. It is therefore possible to measure the layer-by-layer deposition of the epitaxial film from the oscillations of the RHEED signal.

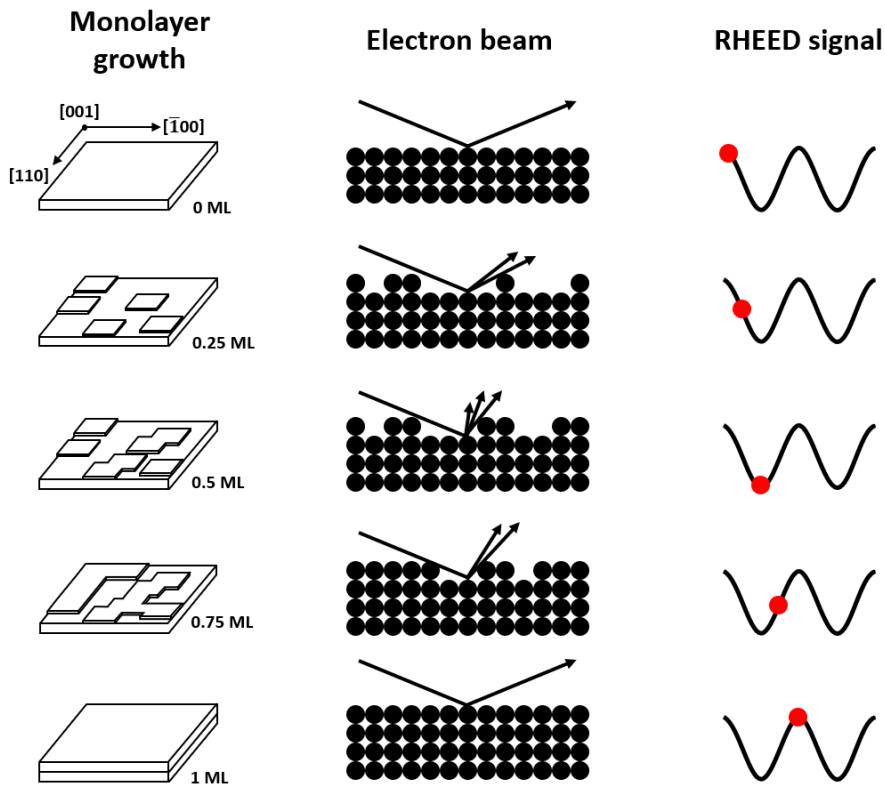


Figure 3.12: RHEED intensity oscillations during the growth of one monolayer.

- Ellipsometry

In ellipsometry, polarised light is incident on the sample and reflected off the sample into a polarisation sensitive detector. The ellipsometer then detects the change in polarisation caused by the reflection off the sample. In most configurations, monochromatic linearly polarised light is incident on the sample and is measured to be elliptically polarised after reflection off the sample. Providing the parameters of the substrate and light beam are known, the changes in polarisation of the reflected light can be used to measure the changing in characteristics of the epitaxial film during MBE growth. A schematic of a typical ellipsometry unit is shown in Figure 3.13.

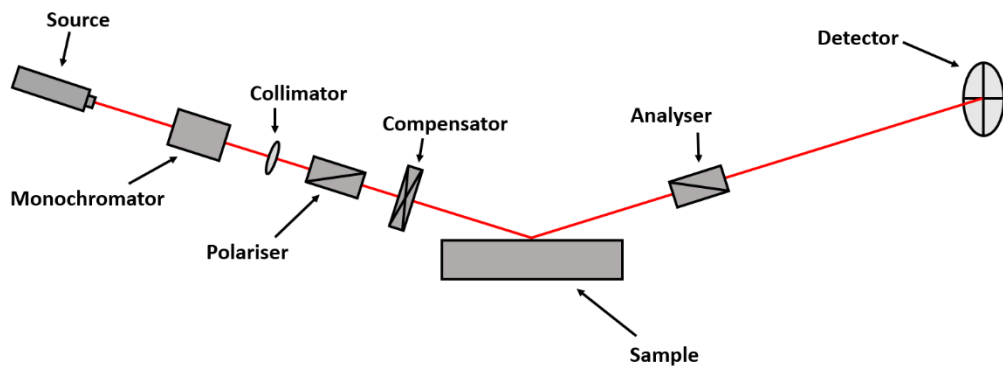


Figure 3.13: Schematic of a typical ellipsometry unit.

- Auger electron spectroscopy

AES is a surface sensitive technique which utilises the emission of low energy electrons in the Auger process. In the Auger process, shown in Figure 3.14, a core hole is created in the K-shell using a beam of high energy electrons (typically 2 – 10 keV). An electron from the L1 level then recombines to fill the K-shell and, in the process, emits an Auger electron. The composition of the surface layers can thus be determined from the kinetic energy of these Auger electrons.

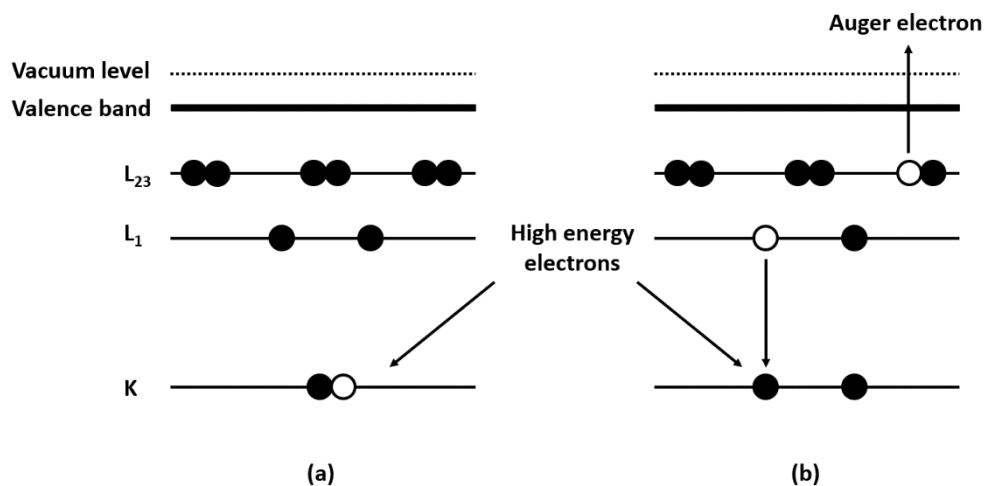


Figure 3.14: (a) Creation of a K-shell hole through impact ionisation and (b) emission of an Auger electron.

3.3. Fabrication

This section outlines the standard fabrication process for single pixel diodes (performed in the ICS cleanroom at Cardiff University) in seven steps. As discussed in Section 2.2.3, this

process would benefit from optimisations such as dry etching and passivation which are detailed in Chapter 6.

1. Figure 3.15 shows a typical PIN diode sample used throughout this work. The pink, grey, and blue regions represent the n-doped, non-intentionally doped, and p-doped regions respectively.

InAs cap $N^+ \sim 1 \times 10^{18} \text{ cm}^{-3}$ $t \sim 20 \text{ nm}$
LW T2SL $N^+ \sim 1 \times 10^{18} \text{ cm}^{-3}$ $t \sim 60 \text{ nm}$
LW T2SL 12 ML InAs/ 4 ML GaSb n.i.d $t \sim 1 \mu\text{m}$
LW T2SL $P^+ \sim 1 \times 10^{18} \text{ cm}^{-3}$ $t \sim 60 \text{ nm}$
GaSb buffer $P^+ \sim 1 \times 10^{18} \text{ cm}^{-3}$ $t \sim 100 \text{ nm}$
GaSb P-type substrate

Figure 3.15: Schematic of a typical PIN diode before fabrication.

2. The solvents, methanol, acetone, and isopropanol alcohol (IPA), were heated to 80°C using a hotplate. The sample was then successively rinsed in methanol, acetone, and IPA and dried with a nitrogen spray gun. Here, the solvents methanol and acetone are used to remove oils and organic residue from the surface of the sample. However, acetone can leave its own residue on the sample, so it is important to quickly remove this residue using IPA. Nitrogen is appropriate for drying because it is inert and would not react unfavourably with the sample.

3. The photoresist PMGI SF11 was spun and baked onto the sample followed by a second resist, S1813 SP15, which was deposited in the same way. The sample was then exposed under the 'NEWPIN – Top Contact' mask (see the appendix to Chapter 3 for overview of the NEWPIN mask) and developed in MF319. This step is shown completed in Figure 3.16, both schematically and as an optical micrograph. An undercut, indicated by the green circle in Figure 3.16a, was achieved through use of the two resists, S1813 and PMGI, and is desirable

to aid the lift-off in the following step. This undercut can also be achieved using a negative resist put the bilayer process was chosen as the NEWPIN mask is designed for positive resists. It was also decided that there would be very limited benefit to developing an alternative process for the minor simplification this provides.

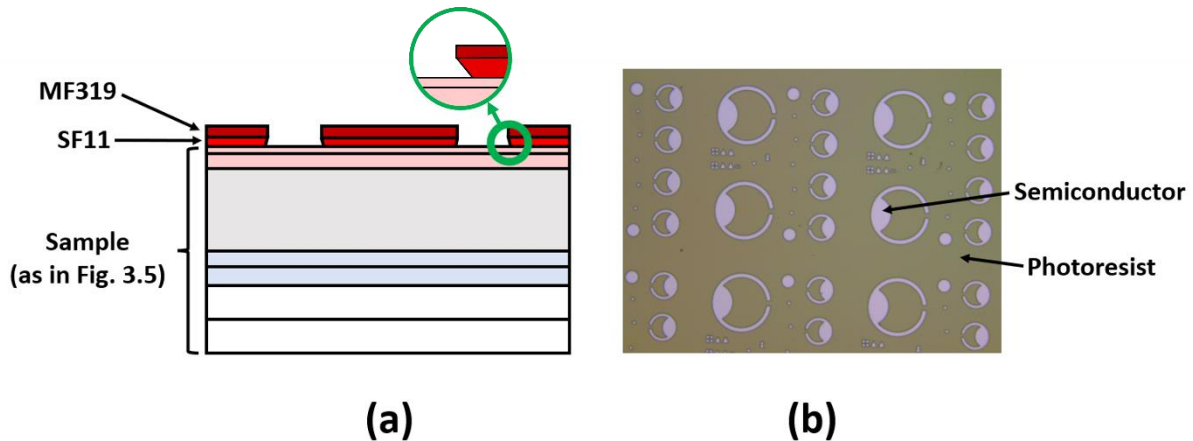


Figure 3.16: (a) Schematic and (b) optical image of a sample after Step 3 of fabrication. The green circle highlights the photoresist undercut.

4. Thermal evaporation was used to deposit Cr and Au contacts. A lift-off was performed using acetone and NPM1165 in an ultrasound bath. The sample was then cleaned in IPA and dried with a nitrogen spray gun, see Figure 3.17. The deposition of top contacts can be done before or after mesa definition. Top contacts are here deposited before mesa definition for two reasons. Firstly, the alignment markers of the NEWPIN mask are specifically designed for this process flow. This makes sense because it is much easier to produce effective alignment markers with metal deposition than with etching. Secondly, it is undesirable to place the top contact deposition step between mesa definition and sidewall protection as this would maximise the time for detrimental oxidation of sidewall surfaces. This second disadvantage could be mitigated by immediate protection with photoresist but this would also be problematic for alignment.

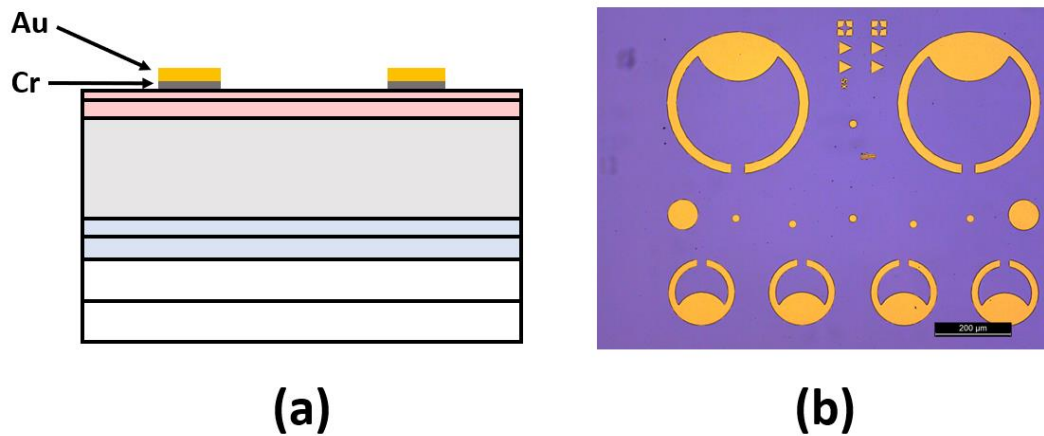


Figure 3.17: (a) Schematic and (b) optical image of a sample after Step 4 of fabrication.

5. Using the method described in Step 3, a layer of S1813 resist was deposited and patterned using the 'NEWPIN – Mesa'. A citric acid based wet etch was then performed to an etch depth of $\sim 1 \mu\text{m}$ as shown in Figure 3.18 (note the etch appears totally anisotropic in the schematic but is isotropic in reality). Once made, the etch recipe was left to settle for around 5 minutes, during which time no stirring was used. Based on previous calibrations, each sample was etched for exactly 5 minutes. The etch depth was only checked when the etch was completed and was therefore completely uninterrupted. Based on previous calibrations, this etch depth was achieved using a duration of exactly 5.00 minutes. A two stage DI water rinse was used to stop the reaction. The sample was then cleaned with acetone and IPA as in Step 2. As shown in Figure 3.20c, the resulting etch is isotropic which motivates the development of an anisotropic dry etching process discussed in Chapter 6.

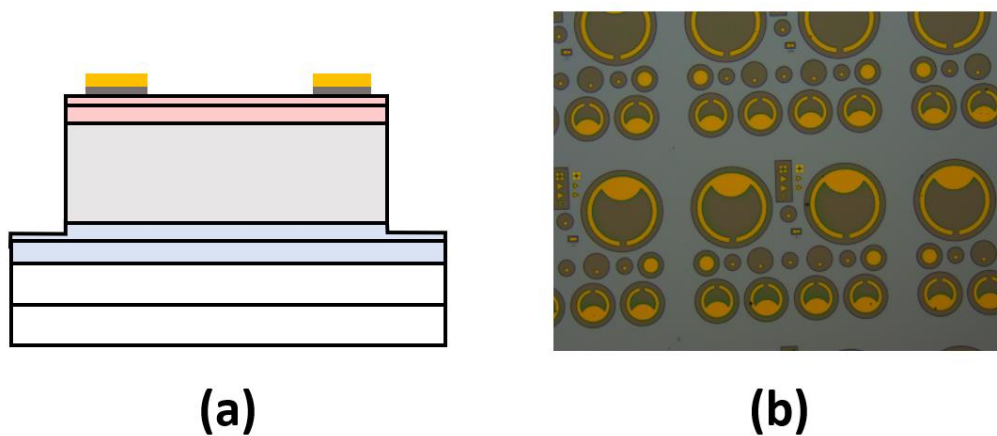


Figure 3.18: (a) Schematic and (b) optical image of a sample after Step 5. Of fabrication.

6. A layer of S1813 was patterned onto the sample using the 'SU8' section of the mask described in the Appendix to Chapter 3 and shown in Figure 3.19. This layer was then hard baked for 2 hours at 200°C. The baking process is not expected to damage the sample because annealing studies of SL are usually conducted above 400 °C^{174,175}. It is well understood that the physical protection of mesa sidewalls employed here is not as effective as chemical passivation.

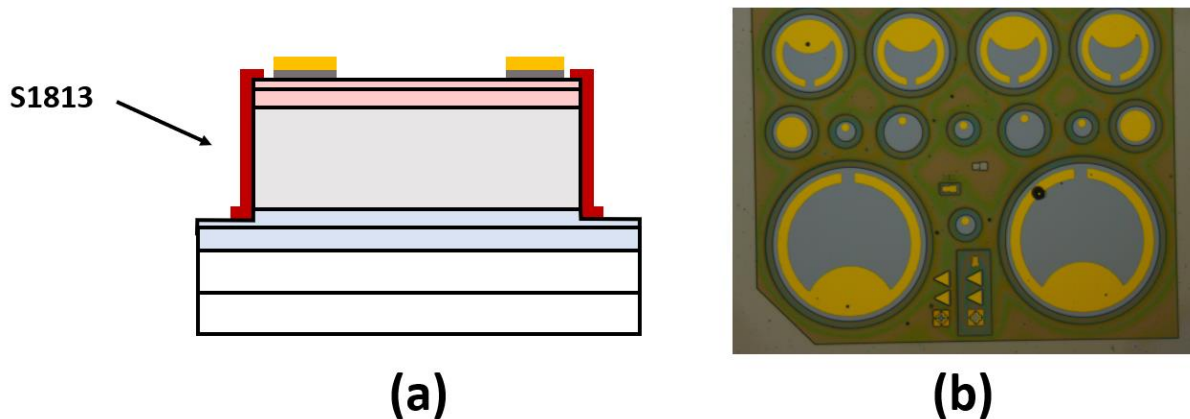


Figure 3.19: (a) Schematic and (b) optical image of a sample after Step 6. Of fabrication.

7. The lower contacts were deposited by repeating Steps 3. And 4. Using the 'NEWPIN – Lower contact'. See Figure 3.20. The lower contacts can either be deposited at the base of the mesas, as shown in Figure 3.20a), or on the underside of the sample. The former is necessary for T2SLs on GaAs substrates as in this case the semi-insulating substrate will block the path of the current.

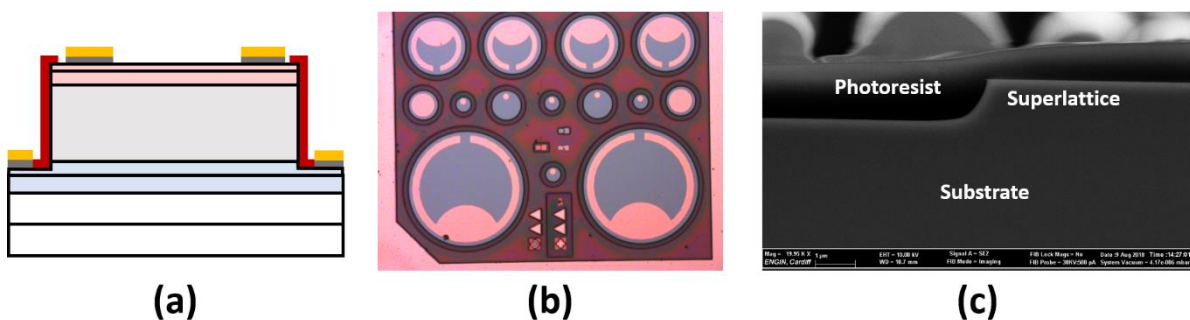


Figure 3.20: (a) Schematic, (b) optical image, and (c) SEM micrograph of a sample after Step 7 of fabrication.

3.4. Characterisation

3.4.1. Nomarski microscopy

The Nomarski microscope, sometimes called the differential interference contrast (DIC) microscope, is used to provide high contrast images of a sample surface. The basic operation is shown in Figure 3.22.

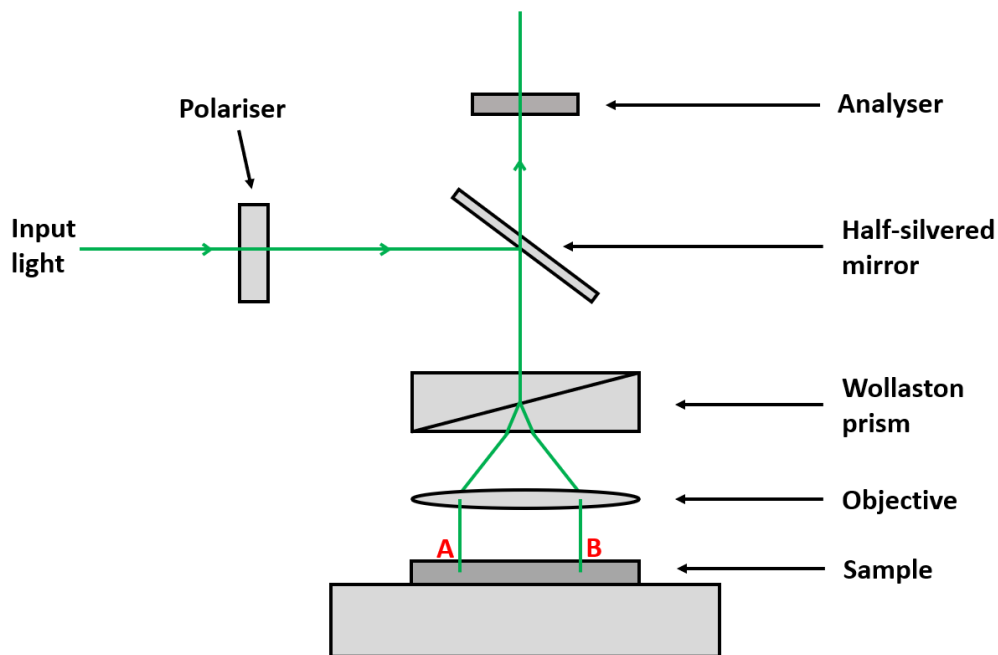


Figure 3.21: Schematic diagram of a Nomarski microscope.

A white light source is shone through a polariser and diverted onto a Wollaston prism. The Wollaston prism splits the light into two separate beams with orthogonal polarisation. An objective then directs the two beams onto the sample surface which then reflect back into the Wollaston prism and recombine. An analyser, placed above the Wollaston Prism, collects the beams and generates an interference pattern. The resulting image represents the difference between two points, A and B, on the samples surface. The colour changes in the image therefore correspond to the changes in slope on the samples surface. In this way Nomarski provides more information on the surface roughness of a sample than is typically available through conventional optical techniques.

The primary of Nomarski microscopy advantage is its accessibility and ease of use. Unlike AFM, it can scan large areas of the sample very quickly and the resolution of the set-up is sufficient to determine the number of surface defects. However, as with AFM, this technique provides little information about the bulk of the sample and should only be used as a corollary to other methods.

3.4.2. X-ray diffraction

X-Ray Diffraction (XRD) is a non-destructive method for investigating the structure of a crystal material. Other uses include evaluation of composition in ternary and quaternary compounds and the strain in heteroepitaxial structures. The process of XRD, shown in Figure 3.23, starts by firing X-rays at the sample whereupon they interact with electrons in the crystal lattice and are scattered. The wavelength of the X-rays is chosen to be comparable to the distances separating atoms in the lattice, usually $\lambda = 1.5 \text{ nm}$, to ensure interference occurs between the scattered X-rays. The resulting scattering peaks and troughs provide information on the crystal structure.

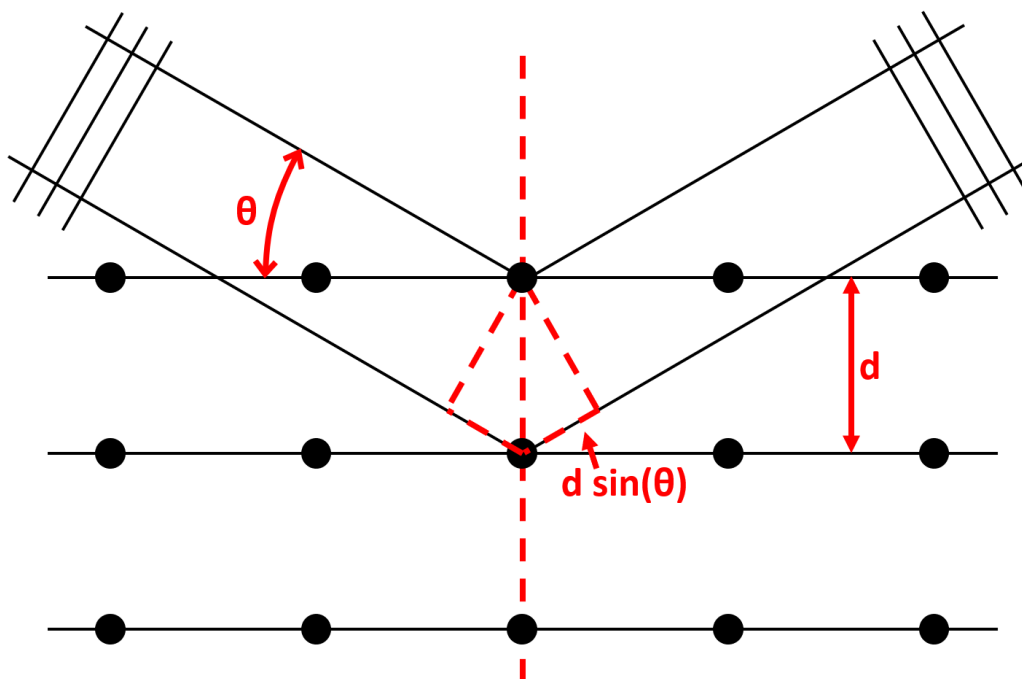


Figure 3.22: Schematic of XRD in a crystal lattice.

The Bragg Condition, shown in Equation 3.45, is met when the scattered x-rays from the crystal lattice are in phase with each other and are therefore constructively interfering.

$$n\lambda = 2t_p \sin(\theta), \quad (3.12)$$

where t_p is the period thickness and θ is the angle of incident x-rays. A typical XRD configuration is shown in Figure 3.24. An X-ray tube and detector are mounted onto a goniometer which moves each component simultaneously as shown. An alternative configuration in which the detector and sample holder are rotated in unison is also commonly used but this does not alter the operating principle.

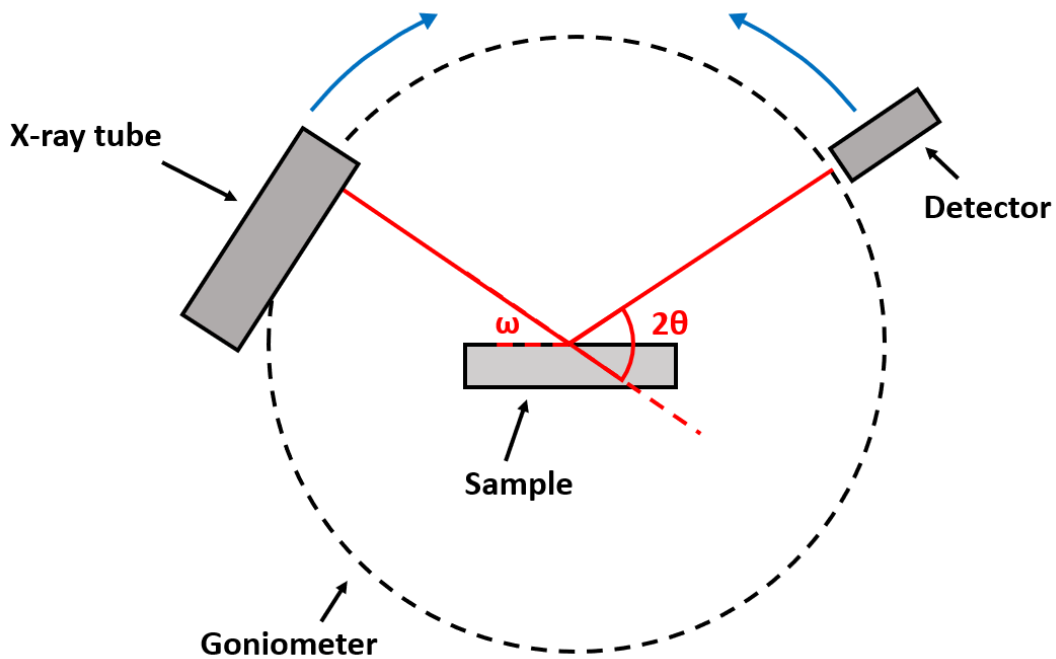


Figure 3.23: The schematic arrangement of an X-ray diffractometer.

Unlike AFM and Nomarski microscopy, XRD provides information about the bulk of the sample. It is therefore very useful for providing a relatively quick method of measuring the material quality of a whole sample. Furthermore, the principles of XRD can be expanded to produce reciprocal space maps, measure strain/relaxation, and determine defect density, provided the set-up is sufficiently sophisticated. However, even the most sophisticated XRD measurement can only be considered as an average of the whole sample and cannot give specific structure of the lattice at any given point. This, as described below, requires electron microscopy.

3.4.3. Scanning electron microscopy

Scanning electron microscopy produces 2D images of sample surfaces with a typical resolution of a few tens of nanometres. As shown in Figure 3.25, the SEM operates by using an electron source to fire a high energy beam of electrons towards the sample surface. This beam is focussed through a series of lenses and apertures, the exact configuration of which can vary depending on the model. This electron beam is directed to scan the sample in a raster pattern. When these electrons interact with the sample surface, backscattered and secondary electrons are generated which are picked up by detectors in the chamber. As a result, it is very difficult to produce a high-quality SEM micrograph of a non-conducting sample due to the effects of charge build up.

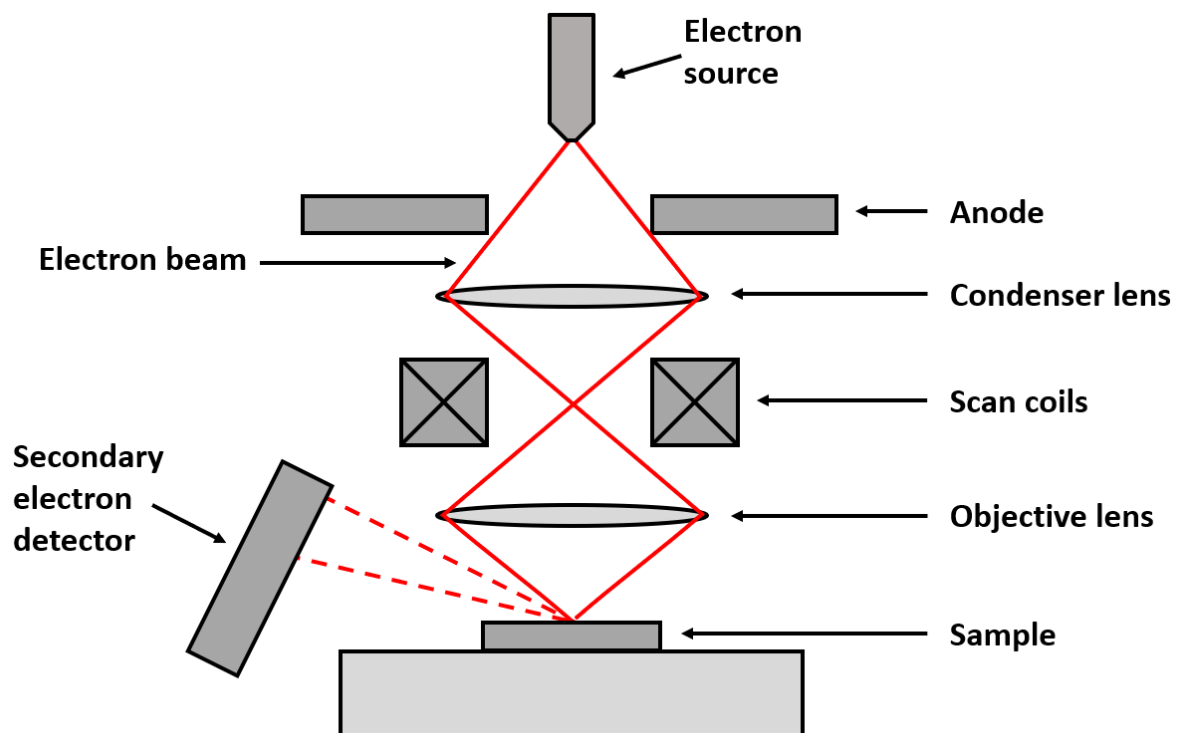


Figure 3.24: Schematic of a typical SEM unit.

However, SEM is extremely useful for characterising the outcome of fabrication processes. For example, SEM is ideal for determining the sidewall roughness and verticality of a certain etch process. However, SEM is only suitable for surface measurements and therefore not used for characterising the material quality of T2SL samples. This is because it provides less information than AFM and is less quick to use than Nomarski microscopy. It is possible to

cleave the sample and use SEM to observe the sideview of the SL epitaxial layers, but destruction to the sample does not usually justify the limited information this approach provides. Therefore, in order to apply the advantages of electron microscopy to the measure the bulk of a sample, transmission measurements are necessary.

3.4.4. Transmission electron microscopy (TEM)

Transmission electron microscopy, shown schematically in Figure 3.28, is similar to SEM. However, it relies on detecting electrons transmitted through a very thin sample rather than scattered from it. In this case, a high energy beam of electrons is shone through the sample. Due to the interactions between the electron beam and the crystal lattice, the crystal structure of the sample can be determined from the transmitted electrons. These transmitted electrons are then focused by an objective lens onto a fluorescent screen which then forms an image of the crystal structure of the lattice. In this way, 2D images with atomic scale resolution can be obtained.

TEM is commonly operated in bright field mode in which the aperture selects the transmitted electrons for detection, while the scattered electrons are blocked. In dark field mode, the opposite is the case as scattered electrons are selected by the aperture while transmitted electrons are excluded. The optimal mode of operation depends on the sample and desired information. The principal advantage of bright field TEM is the better contrast it provides, making it the most widely used technique. However, this technique can also suffer when measuring very small crystal lattices. Therefore, dark field TEM is often preferable for measuring features such as crystal defects and dislocations. Both bright and dark field TEM are used throughout his project.

As TEM is both very high resolution and a bulk technique, it is considered one of the few ways to determine the true structure of a crystal lattice. It is therefore crucial for characterisation of structures like T2SLs since, unlike the aforementioned techniques, TEM can directly verify the existence of the intended QWs. TEM can also be used to determine the presence of phenomena like intermixing, segregation, sub-monolayer features such as quantum dots, and extended lattice defects. It is therefore extremely useful for determining and comparing the quality of SL samples and for identifying the phenomena by which any degradation occurs.

Unfortunately, TEM is a destructive technique for semiconductor samples as it requires the sample to be milled into layers thin enough for electrons to pass through, using techniques like focused ion beam (FIB) milling.

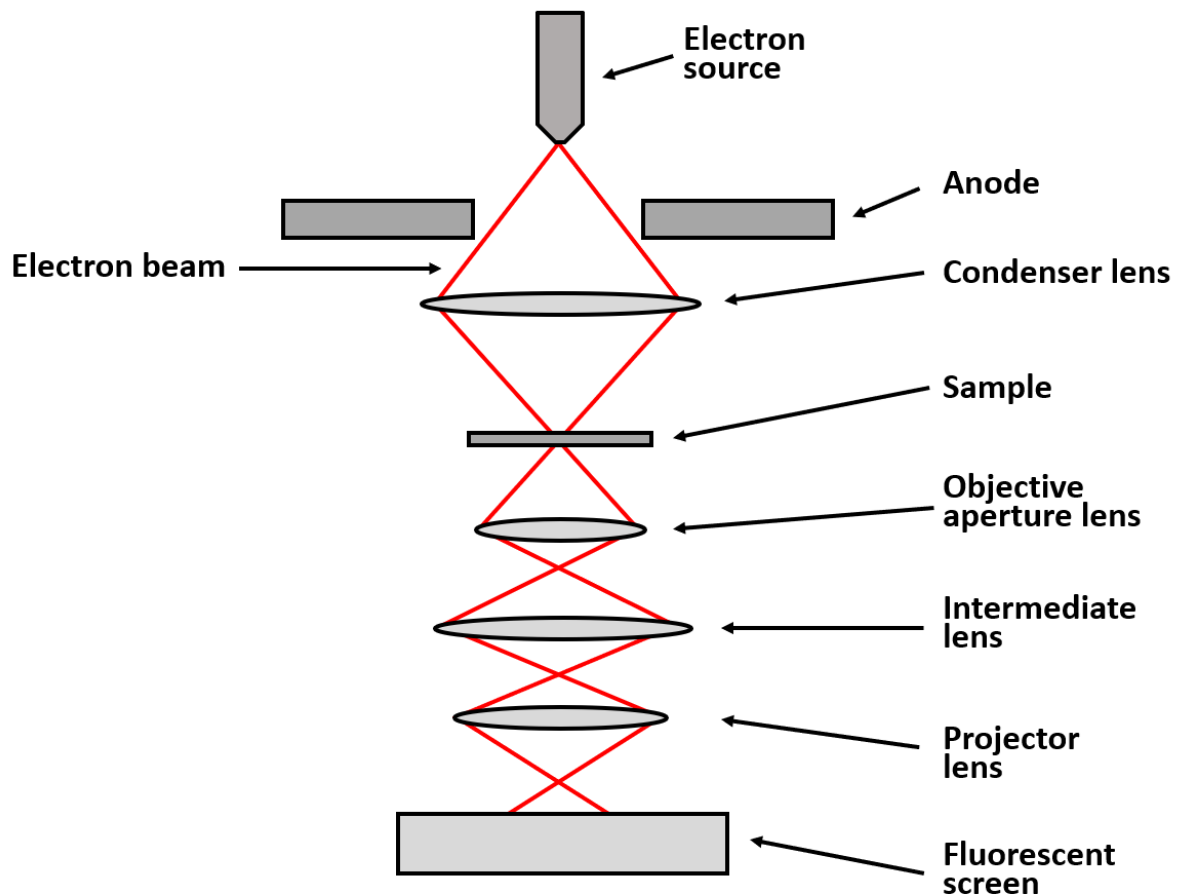


Figure 3.25: Schematic of a typical TEM unit.

3.4.5. Energy dispersive x-ray spectroscopy

Energy dispersive x-ray spectroscopy is a non-destructive technique for determining the elemental composition of materials. It can be implemented within SEM and TEM for analysis of the surface and bulk of the sample respectively. Here, the atoms of the sample are excited by the electron beam of the SEM or TEM to thereby emit x-rays, the wavelength of which will be characteristic of the atomic structure of the elements in the sample. An energy dispersive detector can then be used to analyse the X-ray emissions and identify the elemental composition of the sample.

3.4.6. Photoluminescence

Photoluminescence (PL) spectroscopy is a powerful tool and widely used for studying the band structure of semiconductor materials. PL is the process by which an incident photon of energy greater than the bandgap excites an electron from the valence band to the conduction band which subsequently recombines with the emission of a photon. Due to excess energy in the incident photon, this process, shown in Figure 3.27, generally excites an electron from the valence band to the upper levels of the conduction band. This electron then relaxes to near the conduction band minimum where it has a finite probability of radiatively recombining.

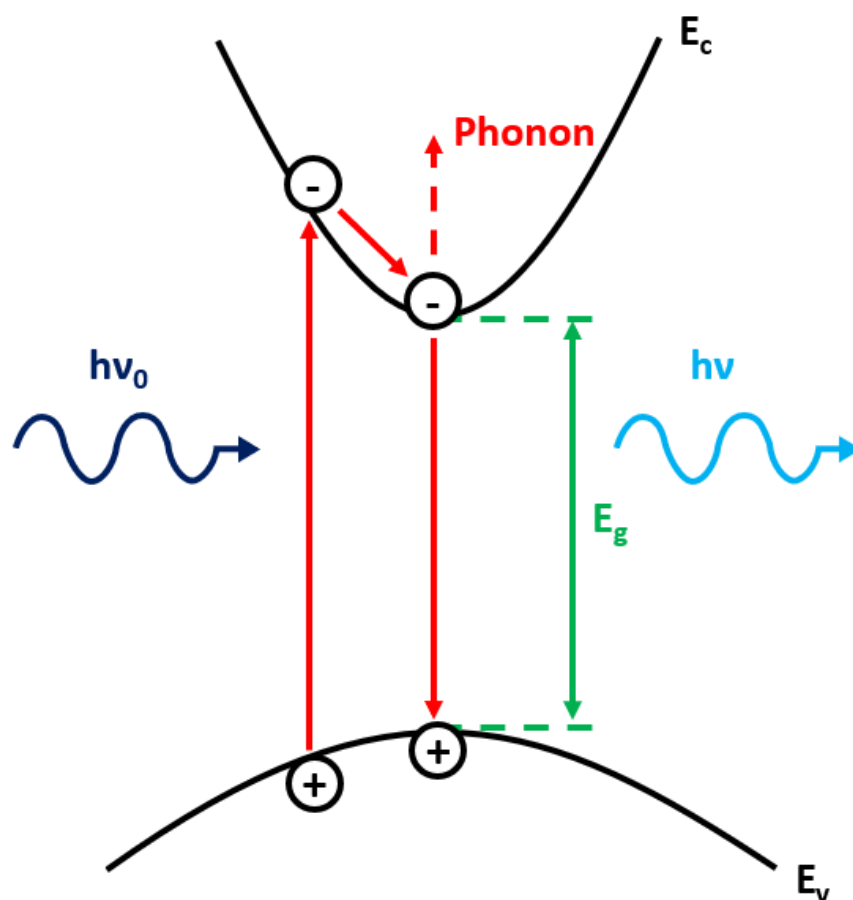


Figure 3.26: Schematic diagram of the PL process.

The resultant PL profile provides information about the radiative and non-radiative recombination channels. As the non-radiative channels of recombination are often related to defects or other material phenomena, this can also provide useful information on material

quality. PL intensity, peak position, integrated PL, and FWHM are all useful avenues of analysis.

For the present work, PL measurements were performed using an arrangement schematically shown in Figure 3.28. Samples were loaded into a liquid nitrogen (LN₂) cooled cryostat equipped with CaF₂ windows. As background blackbody radiation has a peak at around 10 μm it was necessary to subtract this from the PL profiles. This was achieved using a pattern generator to modulate the excitation source, a 735 nm diode laser, at a frequency of 20 kHz. A lock-in amplifier was then used to subtract the background signal. A Nicolet iS50-R Fourier Transform Infrared Spectrometer (FTIR) equipped with a KBr beamsplitter and liquid nitrogen cooled MCT-A detector was used to collect the signal.

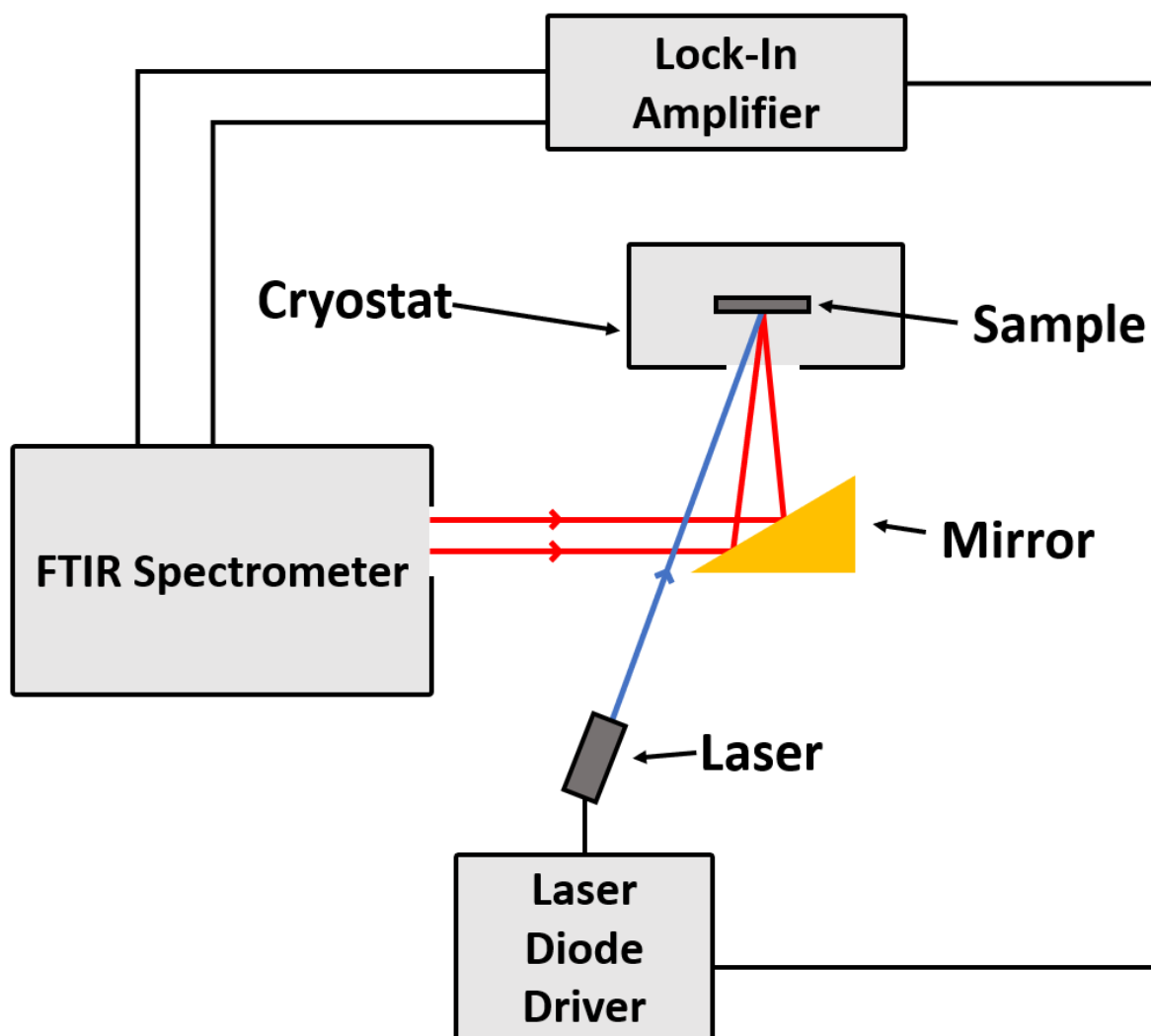


Figure 3.27: Schematic of the experimental set up used for PL experiments.

The 735 nm diode laser excitation source was chosen for cost, availability, and easy interfacing with the pattern generator. The disadvantage of this excitation source is that it pumps the sample with a photon energy (~ 1.6 eV) much greater than the band gap of a typical SL sample (~ 0.12 eV). This means that photoexcited electrons will be excited high into the conduction band of the superlattice. Relaxation to the conduction band edge is therefore a high energy transition and will be accompanied by a significant emission of phonons, quantum mechanical quasiparticles corresponding to vibrational modes in the crystal lattice. These phonons can cause undesirable effects such as linewidth broadening of the PL profile. However, these effects did not prove excessively detrimental as the current experiments were limited to measurement of the PL peaks, integrated intensity, and shape of the PL profile rather than detailed fitting analyses. A higher wavelength excitation source could be considered for FWHM measurements though it should be noted that phonon induced broadening can be resolved in analysis and should not lead to spurious results.

Throughout this project, PL measurements were performed at a temperature of 77 K and above using a continuous-flow cryostat connected to an LN2 dewar. As the LN2 in the dewar evaporates and expands, the vapour flows through the cryostat, cooling the sample. A vacuum pump maintains a constant high vacuum of around 1×10^{-5} mbar and a PID heater is used to control the temperature of the sample. The advantage of this system is that it is simple, convenient, and inexpensive. With the addition of a pumping manifold, this set up is also capable of interfacing with liquid helium (LHe) dewars for operation below 77 K. However, as the excess vapour of the system is vented into the atmosphere, the set up would prove very wasteful for expensive LHe operation without some kind of helium recapture system.

3.4.7. Electrical characterisation

Electronic measurements were performed in a cryogenic probe station using a set-up shown schematically in Figure 3.29. The sample is placed on the sample holder and cooled to 77 K using LN2. Probes are contacted to the top and lower contacts respectively. For devices with a bottom contact the sample holder itself can also serve as a probe. A voltage is applied between the probes and the device analyser measures the corresponding current or

capacitance depending on the experiment. A temperature controller is used to vary the temperature from 77 K to room temperature.

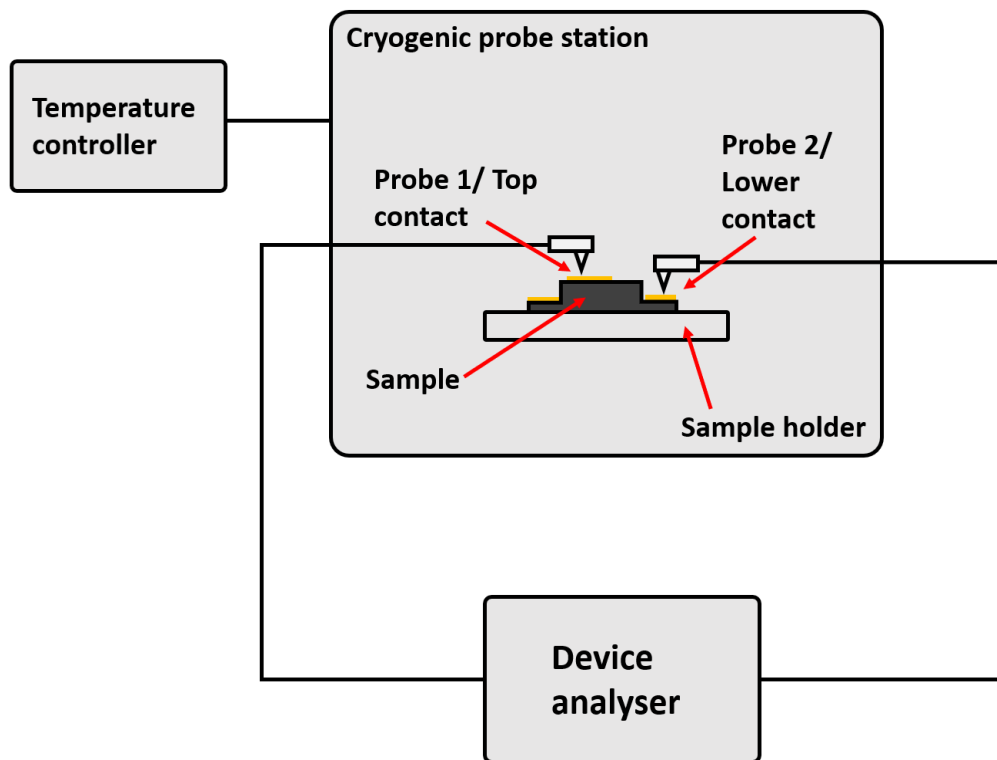


Figure 3.28: Schematic representation of the cryogenic probe station experimental set-up.

Appendix to Chapter 3: The NEWPIN Mask

The so-called NEWPIN mask was used for all fabrication in this project. The design and intended use of this mask is detailed here. A discussion of how this mask can be improved is discussed in Chapter 6. The NEWPIN mask has six panels described below:

- Top Contact

This panel, shown in Figure 3.30, is designed for the deposition of top contacts. The gold areas block the photolithographic light while black areas let it through. This is designed for top contact deposition with a positive resist and lift-off technique. Cross and triangular alignment markers are also patterned onto the sample as shown.

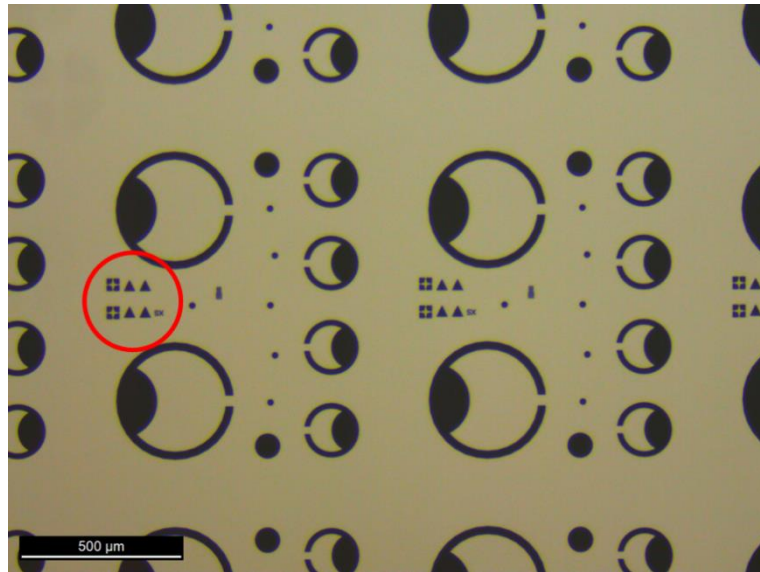


Figure 3.29: Optical micrograph of the Top Contact panel of the NEWPIN mask. The red circle highlights alignment markers.

- Mesa

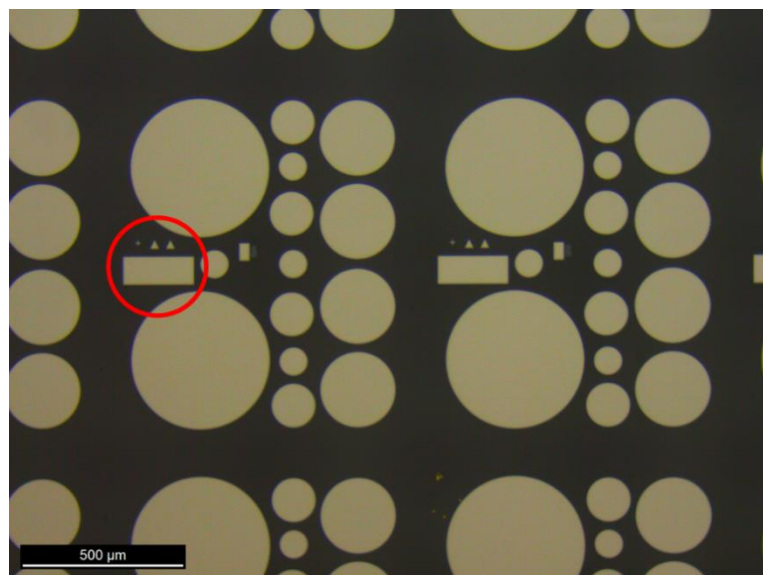


Figure 3.30: Optical micrograph of the Mesa panel of the NEWPIN mask. The red circle highlights alignment markers.

This panel, shown in Figure 3.31, is designed for definition of mesas using a positive resist and etching technique. Here, one set of alignment markers is used to align the mesas with the deposited top contacts while the other set is protected by the mask for use in the following steps.

- SU8

This panel, shown in Figure 3.32, is designed for deposition of a positive photoresist to protect the mesa sidewalls from ambient air. The lower alignment markers are used to align the mask to the mesas.

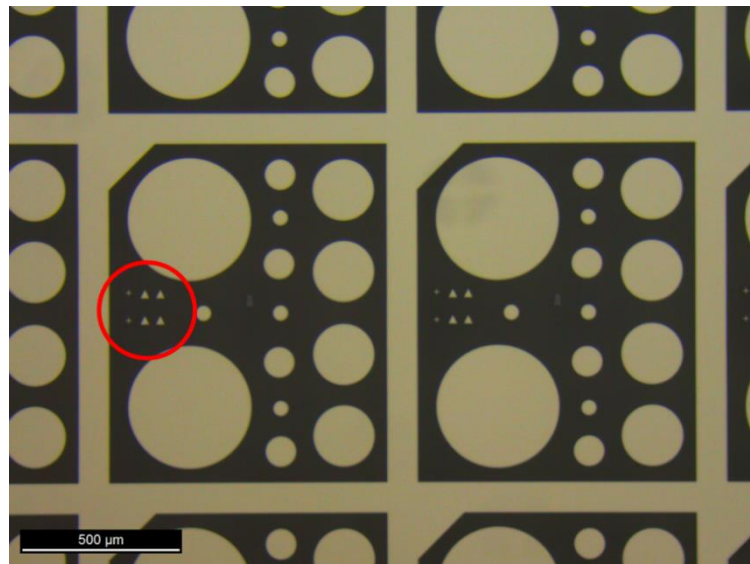


Figure 3.31: Optical micrograph of the SU8 panel of the NEWPIN mask. The red circle highlights alignment markers.

- Lower contact

This panel, shown in Figure 3.33, is designed for deposition of bottom contacts through use of a positive resist and lift-off technique. Both alignment markers are used to align the mask to the mesas.

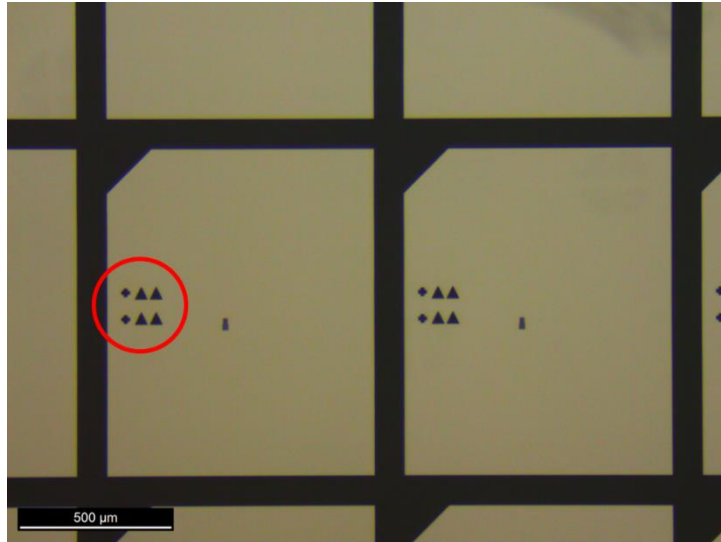


Figure 3.32: Optical micrograph of the Lower Contact panel of the NEWPIN mask.
The red circle highlights alignment markers.

- SINX

This panel is designed for deposition of a dielectric passivation. The intended process is to deposit the passivation layer over the whole sample surface, spin and expose a positive resist over the desired areas, and etch away the undesired dielectric. Both alignment markers are used to align the mask to the mesas.

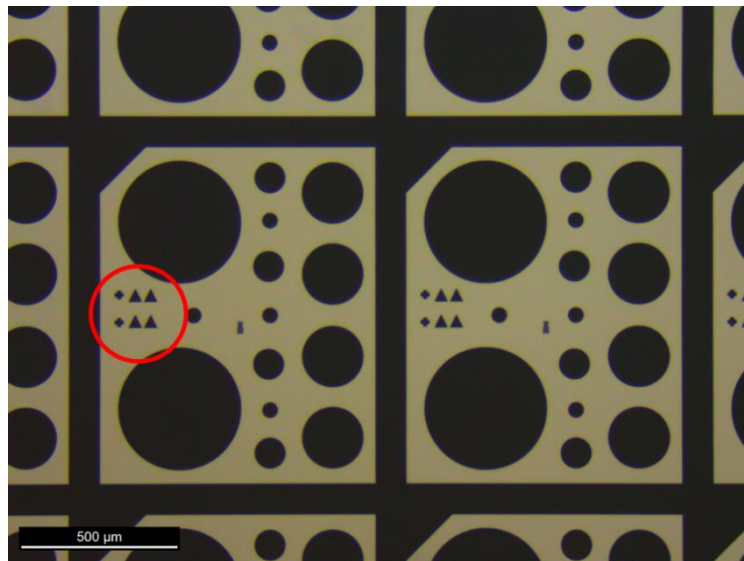


Figure 3.33: Optical micrograph of the SINX panel of the NEWPIN mask. The red circle highlights alignment markers.

- AR Coating

This panel, shown in Figure 3.35, is designed for deposition of an anti-reflection (AR) coating but was not eventually used in this project.

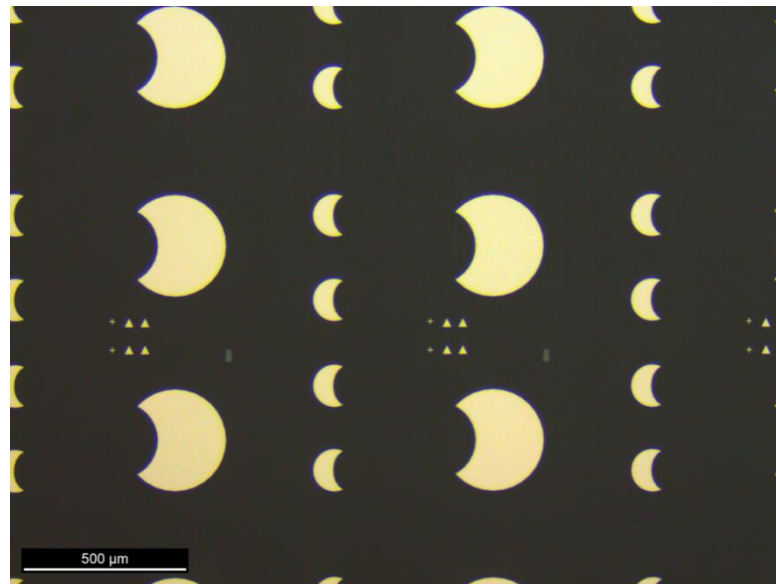


Figure 3.34: Optical micrograph of the AR Coating panel of the NEWPIN mask.

4. Flexibility of LWIR

InAs/GaSb Type-II

Superlattices

The flexibility of the 6.1 Å family of materials has allowed growth and fabrication of high-quality heterostructures for optoelectronic devices. The small lattice mismatch between the constituent materials of the family, which includes InAs ($a = 6.0584 \text{ \AA}$), GaSb ($a = 6.0959 \text{ \AA}$) and AlSb ($a = 6.1355 \text{ \AA}$), allows good control of layer thicknesses while maintaining low defect densities. This mismatch advantage has allowed bandgap engineering of InAs/AlSb/GaSb superlattice detectors with cut off wavelengths ranging from the short wave to (very) long-wave infrared spectral ranges. As a consequence of the above flexibility, multiple different combinations of SL layer thicknesses can be simulated to achieve the same cut-off wavelength. This chapter will provide a comparative study of InAs/GaSb T2SLs of different layer thicknesses, with a cut-off wavelength in the LWIR spectral range. Material and device characterisation were performed to appraise the advantages of each T2SL structure.

4.1. InAs/GaSb reference samples

This section describes growth and structural and optical characterisation of reference (i.e. not device) T2SL samples of different layer thicknesses. The development of a band structure simulation tool, based on optical measurements, is also described.

4.1.1. Design and Growth

The structures presented in this chapter were all grown on a quarter of two-inch p-type (001)-oriented GaSb substrate. The solid source Veeco Gen 930 MBE reactor was equipped with

dual filament SUMO Knudsen effusion cells for Ga and In and Mark V valved cracker effusion cells for As and Sb. The In and Ga growth rates were set to 0.3 and 0.5 ML s⁻¹ respectively. InAs and GaSb layers were grown using a V/III flux ratio of 1.2 and 2 respectively. RHEED oscillations were used to optimise these values. The growth temperature was monitored by a pyrometer and thermocouple and calibrated with the (1 x 3) to (2 x 5) reconstruction transition of the GaSb substrate and buffer layer. Before growth, the native oxide on the GaSb was thermally desorbed at a temperature of 540 °C. The growth temperature was then lowered to 490 °C and 410 °C for the buffer layer and superlattice layers respectively.

The slight lattice mismatch of 0.6% between InAs and GaSb is enough to introduce a tensile strain when InAs is grown on GaSb. This small tensile strain is still large enough to limit the thickness and material quality of the SL layers. This limitation is more significant for LWIR structures due to the larger SL periods required. Furthermore, an InAs-rich period, which will further increase the strain on GaSb, is desirable for LWIR T2SLs due to the increased optical absorption¹⁷⁶. To address this issue, the structures described in this chapter contain a layer of InSb intentionally grown at each the IF of both GaSb-on-InAs and InAs-on-GaSb, that is to say, both the GaSb-on-InAs and InAs-on-GaSb IFs. As shown in Figure 4.1, InSb has a lattice mismatch of 6.3% when grown on GaSb which will corresponds to a compressive strain.

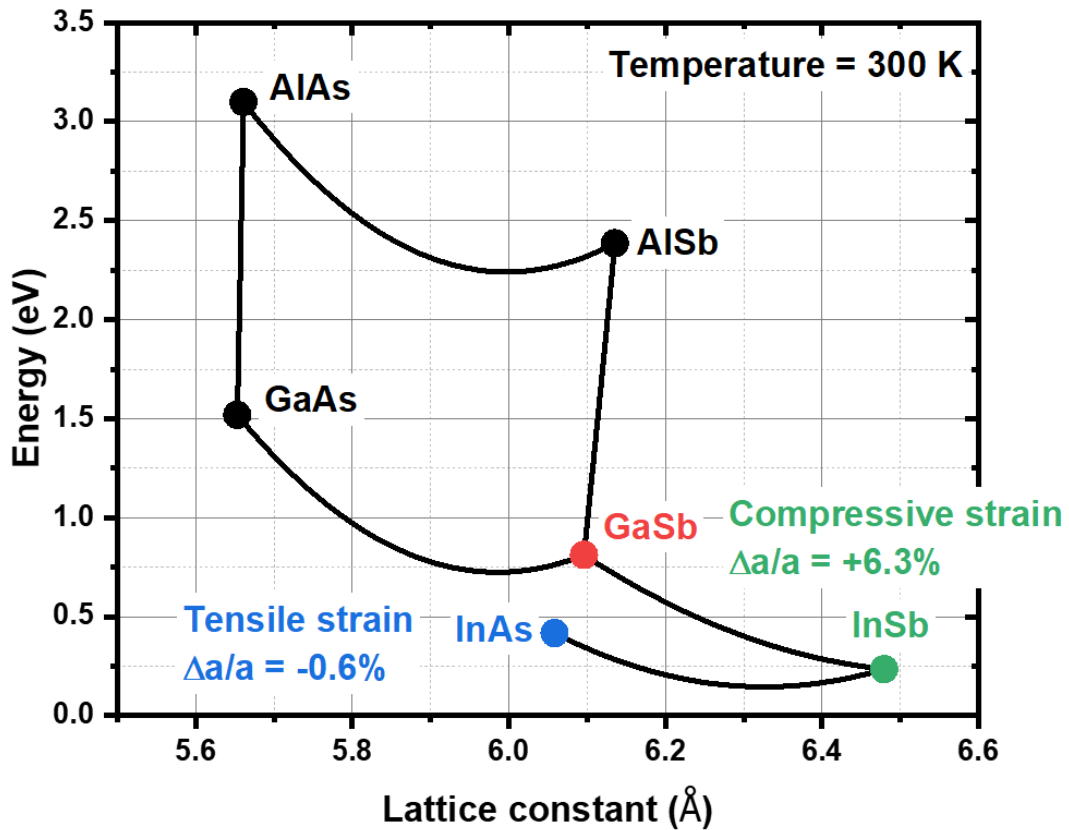


Figure 4.1: The Energy gap and lattice constant for selected III-V semiconductors. The lattice mismatch of InAs and InSb to GaSb is also shown.

By careful choice of growth parameters, the layer thickness can be tuned such that the compressive strain of the InSb compensates for the tensile strain of the InAs. As the lattice mismatch to of GaSb of to InSb is approximately 10× larger than InAs, the InSb thickness should, correspondingly, be approximately 10× smaller than the InAs thickness. The strain compensating InSb layer was grown by migration enhanced epitaxy (MEE) in which, in contrast to conventional MBE growth, the asynchronous opening of both the group III and group V shutters enhances the surface migration of the surface adatoms¹⁷⁷. MEE has previously been demonstrated to achieve abrupt SL interfaces^{178,179} and favourable optical performance¹⁸⁰. Figure 4.2 shows the shutter sequences that were used for the structures in this chapter. After growth of the InAs layer, the In shutter was left open for a period of time determined by the SL period thickness while the As shutter was immediately closed. This formed the InSb layer at the GaSb-on-InAs IF. Likewise, the InSb layer at the InAs-on-GaSb IF

was formed by immediately closing the Ga shutter after growth of the GaSb layer but leaving the Sb shutter open for an additional 6 seconds. The In shutter was then opened for the same period as used previously. This process is repeated until the desired number of SL periods were grown, in this case 100. All fluxes were kept constant during SL growth.

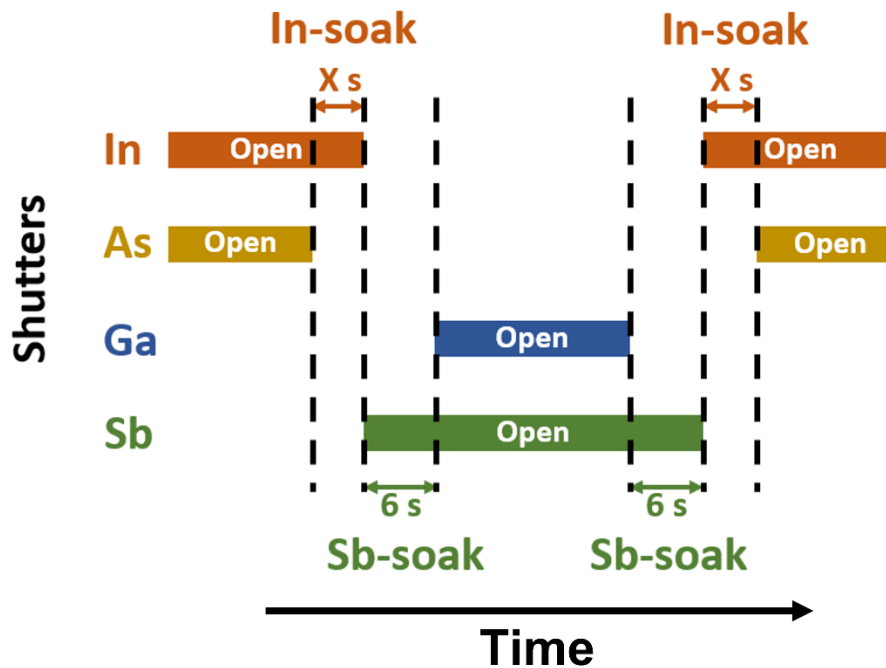


Figure 4.2: The shutter sequences used for the samples in this study. The duration of the In-Soak was determined from the SL period.

The reference samples presented in this chapter are shown in Figure 4.3. Each sample consisted of a 45 nm GaSb buffer layer, a 20 nm AlSb barrier, a 100 period SL absorber layer, a second 20 nm AlSb barrier and a 4 ML GaSb cap. Four structures were grown as SL absorber layer period of X ML of InAs/ Y ML of GaSb where $X/Y = 10/4, 12/4, 14/7$ and $14/7$. The purpose of the AlSb barrier layer is to confine the carriers in the absorber region. AlSb is chosen for the barrier layer due to its wide, indirect band gap of 1.58 eV and closely matched lattice constant of 6.1355 Å.

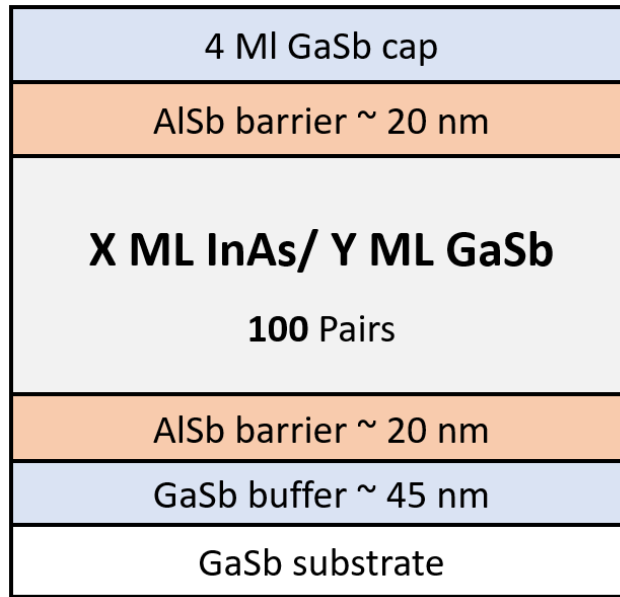


Figure 4.3: The structural schematic for the LWIR InAs/GaSb T2SLs.

The shutter sequences, shown in Table 4.1, were chosen to ensure the thickness of the InSb layer was around 10% of the InAs thickness. Where one ML of InAs, InSb and GaSb has a thickness of 3.03 nm, 3.07 nm, 3.05 nm respectively.

Table 4.1: The shutter sequence used for the absorber region of each superlattice structure.

Sample name	InAs/ GaSb SL (MLs)	In Shutter opening time (s)	Sb Shutter opening time (s)
Sample A	10/4	1	6
Sample B	12/4	1.5	6
Sample C	14/4	2	6
Sample D	14/7	2	6

4.1.2. X-Ray Diffraction

The material quality of each sample was appraised using a Bede D1 x-ray diffractometer. The X-ray diffraction (XRD) rocking curves for an $\omega/2\theta$ scan taken around the GaSb (004) reflection for each sample is shown in Figure 4.4.

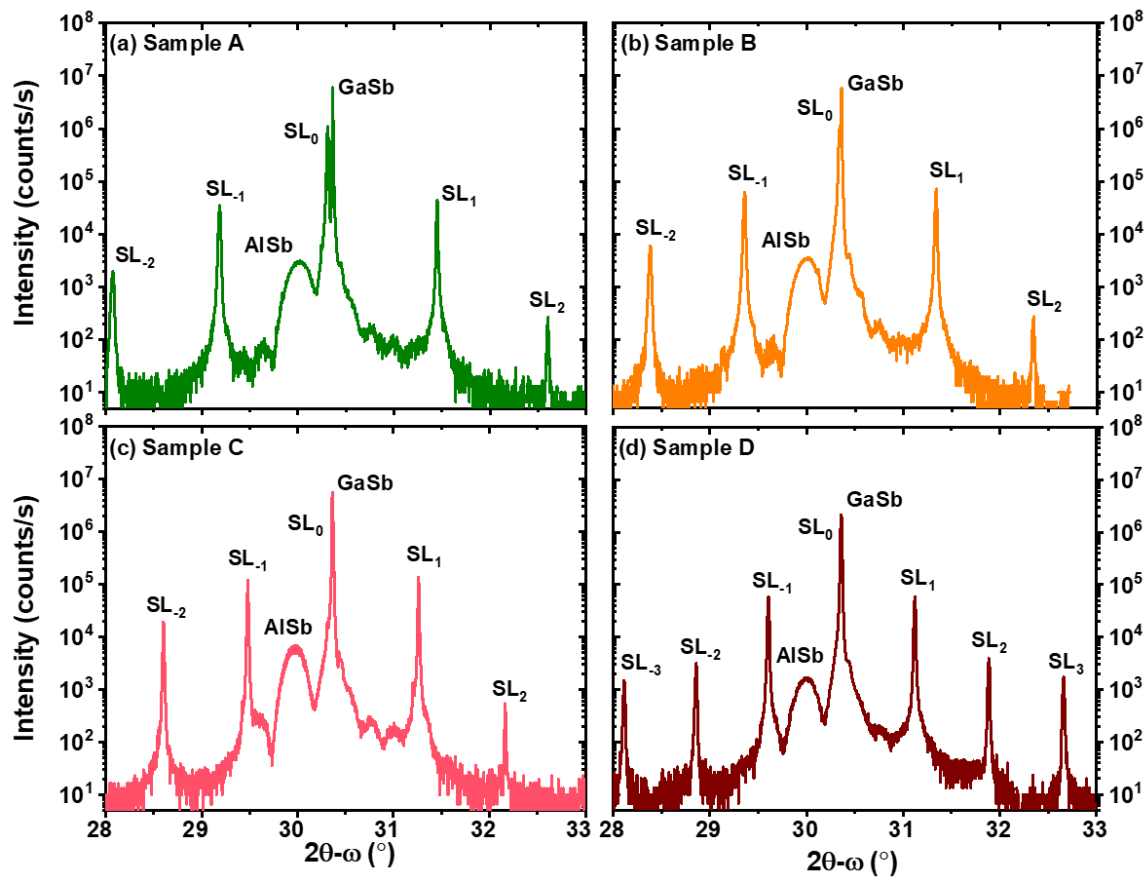


Figure 4.4: XRD rocking curves, taken around the GaSb (004) reflection for (a) Sample A, (b) Sample B, (c) Sample C, and (d) Sample D.

The presence of sharp, well-defined satellite peaks for each sample is an indication of good material quality. The lattice mismatch between the SL and substrate was extracted from the difference between the substrate peak and the zeroth-order superlattice peak according to:

$$\frac{\Delta a}{a}_{SL} = \frac{a_{SL} - a_{GaSb}}{a_{GaSb}} = \frac{\sin(\theta_{GaSb}) - \sin(\theta_{SL_0})}{\sin(\theta_{SL_0})}, \quad (4.1)$$

where Δa is the difference in lattice constant between substrate and superlattice, a is the lattice constant and θ is the diffraction angle of the XRD peak. In this way, the efficacy of MEE

for growth of strain compensated SLs was appraised. The SL period thickness of each sample was determined by measuring the distance between successive SL satellite peaks. Bragg's law Equation 3.45 was then used to extract the period thickness from the slope of the fit in Figure 4.5.

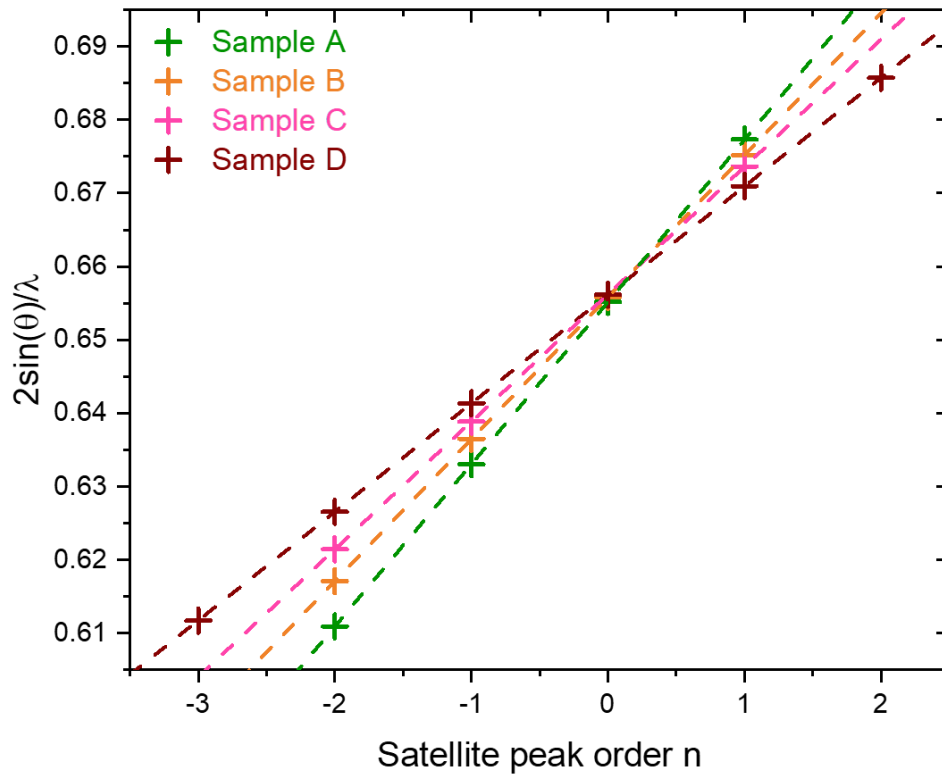


Figure 4.5: $2\sin(\theta_n)/\lambda$ of each SL satellite peak as a function of the satellite order.

The full width at half maximum (FWHM), a measure of material quality, of the SL_{-1} peak, was measured for each sample. The results of the XRD characterisation are shown in Table 4.2.

Table 4.2: The lattice mismatch, FWHM, and period thickness for each SL sample as determined by XRD measurements.

Sample	InAs/ GaSb SL (ML)	$\Delta a/a$ (%)	FWHM SL ₁ (arcsec)	Period Thickness (nm)		
				Expected	Measured	Error
Sample A	10/4	+0.149	63	4.25	4.52	0.27
Sample B	12/4	+0.06	64	4.85	5.17	0.32
Sample C	14/4	~0	38	5.46	5.75	0.29
Sample D	14/7	~0	58	6.37	6.76	0.39

$\Delta a/a$ in Table 4.2 shows that the Sample A was significantly lattice mismatched to the GaSb substrate, indicating the presence of a large compressive strain. This suggests that the thickness of the InSb interfacial layer is too large in comparison to the InAs thickness. The Samples C and D both showed a lattice mismatch lower than the sensitivity of the set up while the 12/4 SL showed only a small lattice mismatch of 0.06%. The two strain balanced samples, the 14/4 and 14/7 SLs, also showed the smallest FWHM. The FWHM of the Sample C is significantly lower than any other sample which, in addition to the smallest lattice mismatch, suggests this sample has the highest material quality. The expected period thickness was calculated by assuming the thickness of 1 ML of semiconductor to be half its lattice constant for the zinc blende structure of InAs and GaSb. Table 4.2 shows that the thickness measured by XRD is always larger than the expected thickness by around 0.3 nm. This could be attributed to the interfacial layer of InSb. It should be noted, however, that reliable characterisation for determining the exact nature of the IFs has not been performed for these samples. Such an analysis would require a method like High-Resolution Transmission Electron Microscopy (HRTEM) though other methods are available¹⁸¹.

4.1.3. Photoluminescence

The PL profiles for each sample performed at temperatures from 77 – 150 K are shown in Figure 4.6. The parameters extracted from the PL profiles are presented in Table 4.3. The measurement temperatures were chosen based on the trade-off between the expected usefulness of the results and availability of the equipment and resources. Performing PL at higher temperatures would be informative but, due to the signal to noise ratio decreasing with increasing temperature, was not prioritised here. As the T2SLs samples are being excited by a relatively high energy pump laser (~ 1.8 eV) compared to the energy gap (~ 0.12 eV), it is possible that the PL profiles observed here are convolutions of carrier relaxation into the minibands and the recombination rates. This was deemed unlikely to be a major issue because, as discussed in Section 5.6., power dependant measurements indicate that our T2SL samples are dominated by radiative processes and minimally affected by non-radiative relaxation processes.

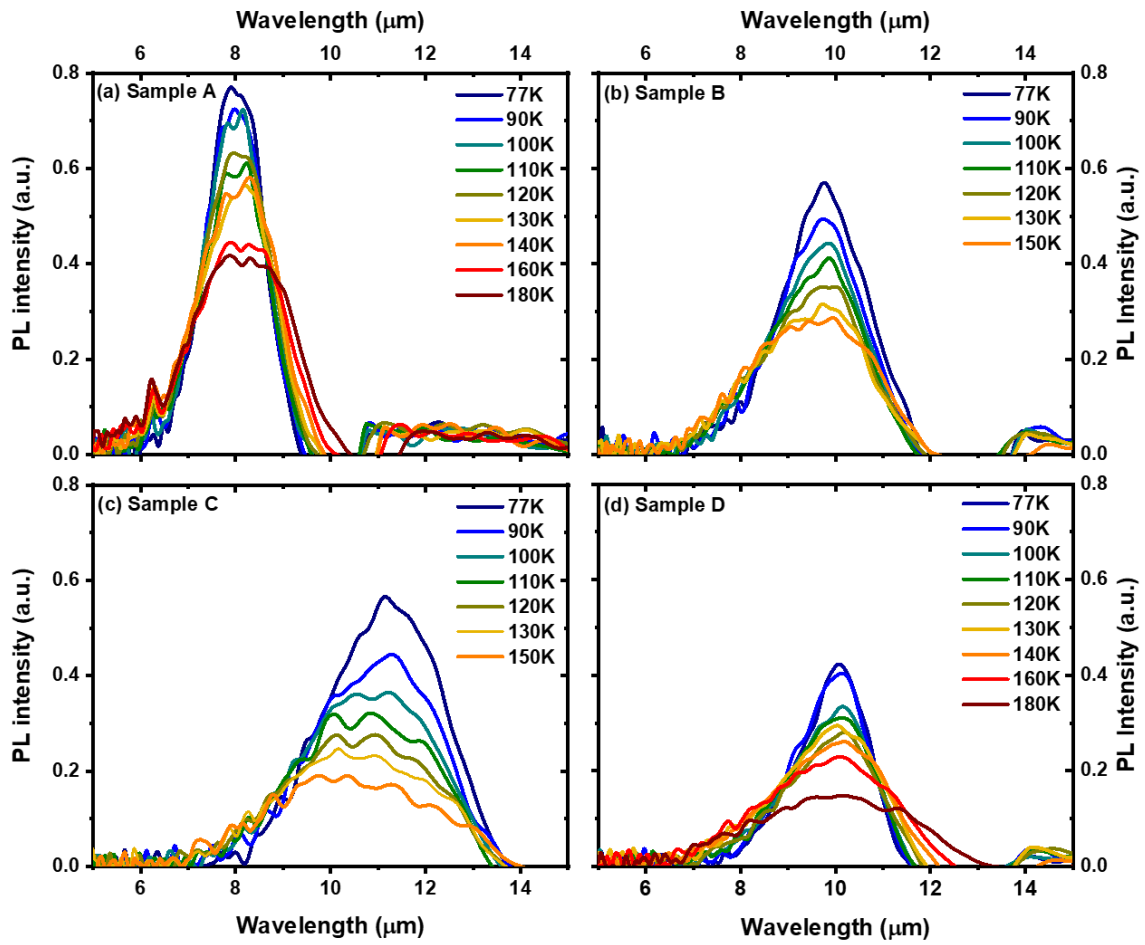


Figure 4.6: PL profiles for $T = 77 - 180$ K for (a) Sample A, (b) Sample B, (c) Sample C, (d) Sample D.

Table 4.3: Parameters extracted from PL vs T measurements for each SL sample.

Sample	Max PL Intensity (a.u.)	Varshni Parameters			FWHM			Integrated PL		
		$E_g(0K)$ (eV)	$\lambda_c(0K)$ (μm)	A (meV/K)	Γ_i	Γ_c	E_{lo} (meV)	I_{sat}	A	E_a (eV)
Sample A	0.754	0.154	8.05	0.168	0.025	0.102	25	1.329	0.6	0.033
Sample B	0.556	0.127	9.76	0.186	0.026	0.377	39	1.322	4.532	0.034
Sample C	0.535	0.103	11.04	-0.232	0.025	0.078	18	2.255	10.24	0.022
Sample D	0.424	0.121	10.25	0.119	0.018	0.192	29	0.758	14.72	0.035

Table 4.3 shows that the SL structures with the thinnest periods have the strongest PL intensity. This is in line with the theory for Type-II structures which states that due to the spatial separation of electrons and holes the recombination occurs at the interfaces where the wavefunction overlap is strongest¹⁰. As will be discussed below, thinner SL layers yield a larger wavefunction overlap and therefore a higher absorption coefficient resulting in stronger PL. The band-gap of each SL can be determined by subtracting the thermal contribution, that is, $k_B T/2$, from the peak of the PL profile. This corresponds to the 50% cut-off wavelength. Considering the case of the X/4 SLs, it is clear from Table 4.3 that by increasing the InAs thickness the band-gap of the SL is decreased corresponding to an increased cut-off wavelength. This occurs through changes in the confinement energy and interaction strength between adjacent wells, as discussed in Section 1.3.

The temperature dependence of the band gap is described by the Varshni equation:

$$E_g(T) = E_g(0K) - \frac{\alpha T^2}{\beta + T} \quad (4.1)$$

where α is a damping constant, β is the Debye Temperature (also constant) and T is the temperature. For this analysis, the value of β was fixed at 270 K¹⁸². The temperature dependant band gaps of each SL are shown in Figure 4.7 and the extracted parameters are shown in Table 4.3.

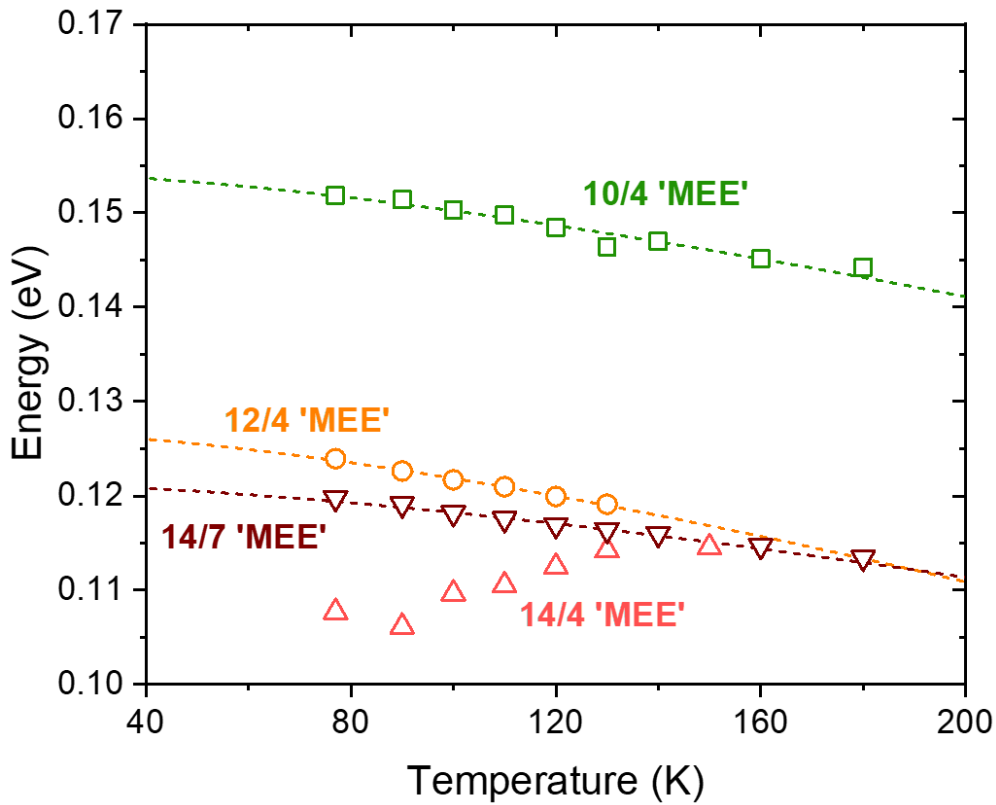


Figure 4.7: The temperature dependant band gap energy of each T2SL sample and Varshni equation fits.

Figure 4.7 shows that the bandgap of the Sample D is the least affected by changes in temperature which corresponds to a low α value in Table 4.3. Note that the Sample C does not follow the trend predicted by Equation 4.1. This, in combination with the wide FWHM, suggests that more than one transition is being measured meaning the PL profile shown in Figure 4.6 is a convolution of more than one transition. The way to confirm this hypothesis would be to perform PL at a lower temperature using liquid helium. In this way, it is possible to observe several distinct peaks, if they are present, rather than one convoluted peak. To examine the non-radiative recombination of the SL structures, the integrated PL profiles were examined as a function of temperature as shown in Figure 4.8a.

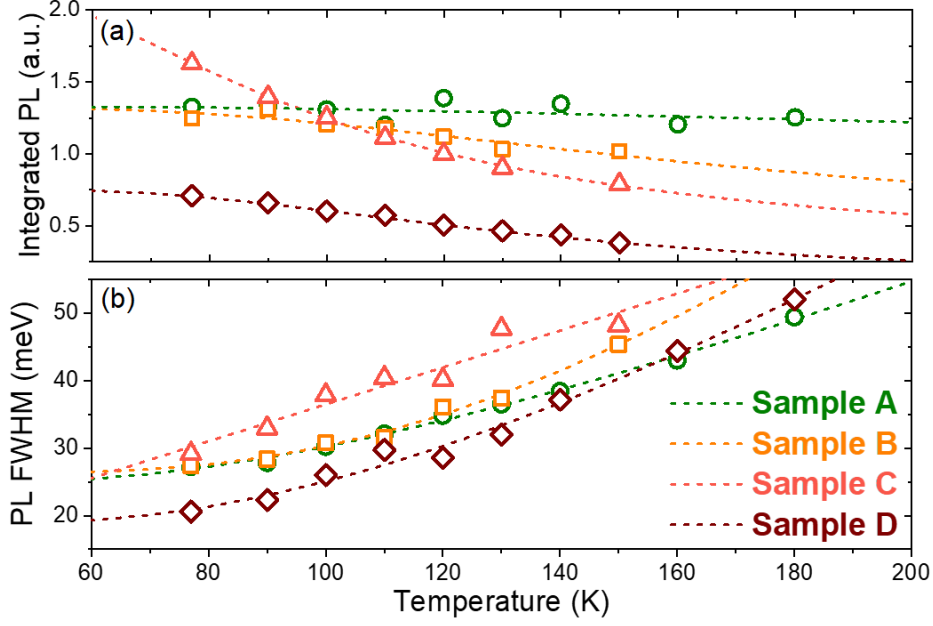


Figure 4.8: (a) Integrated PL and (b) FWHM as a function of temperature for each SL sample.

The integrated PL as a function of temperature can be modelled by the Arrhenius Equation for one non-radiative recombination mechanism:

$$I(T) = \frac{I(0K)}{1 + Ae^{-\frac{E_a}{kT}}} \quad (4.2)$$

where $I(T)$ is the integrated PL at temperature T , $I(0K)$ is the integrated PL at $T = 0K$, A is the ratio of non-radiative to radiative recombination probability and E_a is the activation energy of the non-radiative recombination process. As the temperature does not go below $\sim 60K$ it is safe to assume that only one non-radiative mechanism is present¹⁸³. This mechanism, shown in Figure 4.9, corresponds to the thermal escape of electrons in the conduction miniband to the conduction band of the interfacial InSb layer. These electrons are then likely to be trapped by defects and recombine non-radiatively. The activation energy of this process, E_a , and the relative probability of this process occurring compared to radiative recombination, A , is shown in Table 4.3. Once the Sample C has been discounted due to the potentially spurious results discussed previously, it can be seen that the remaining three SLs have very similar activation energies suggesting the non-radiative process is dominant in each case. The Sample A has the lowest probability of this process occurring, possibly because this sample has the thinnest layer of interfacial InSb which is associated with this process. This also corresponds to the strong PL from this sample discussed previously. This trend is also supported by the

Sample B and D. It should be noted, however, that the extreme difference between the measurements of this ratio for the different samples calls into question the legitimacy of this result. More tests at a lower temperature, and with less noise correspondingly, would be required to verify this result. In this case, it could no longer be assumed that only one recombination process is present, and an extra term must be added to the Arrhenius Equation as follows:

$$I(T) = \frac{I(0K)}{1 + A_1 e^{-\frac{E_{T1}}{kT}} + A_2 e^{-\frac{E_{T2}}{kT}}} \quad (4.3)$$

where $A_{1(2)}$ and $E_{T1(T2)}$ are the ratios of non-radiative to radiative recombination and activation energies for the high (low) temperature recombination processes respectively. It has been suggested that at low-temperature the non-radiative recombination process relates to defects in the SL material¹⁷¹.

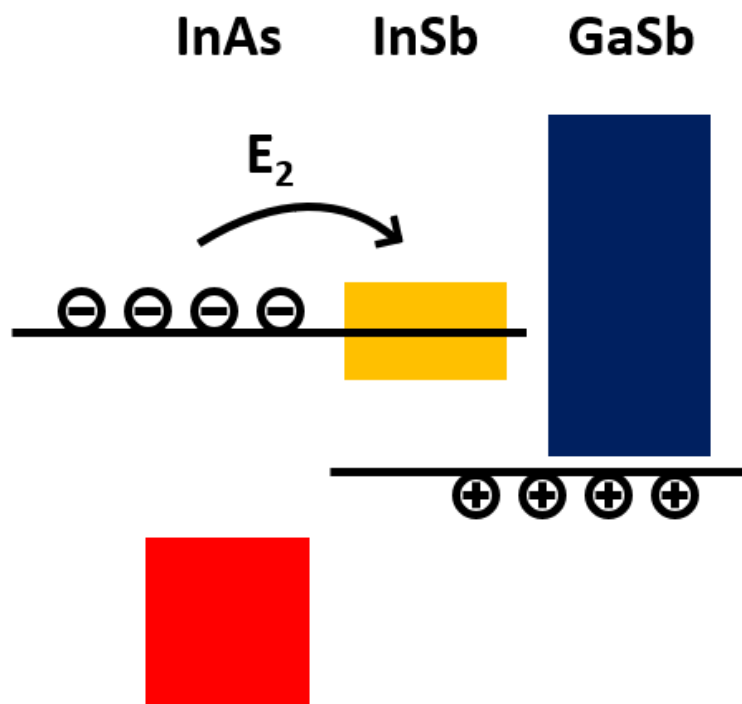


Figure 4.9: Schematic showing the non-radiative recombination process present in the SL structures. Coloured regions represent forbidden gaps, taken from Reference ¹⁷¹.

The FWHMs of each SL sample is shown, as a function of temperature, in Figure 4.8 b. The FWHM of each PL profile is composed of an inhomogeneous part and a temperature-dependent homogeneous part described by:

$$\Gamma(T) = \Gamma_i + \frac{\Gamma_c}{\exp\left(\frac{E_{LO}}{k_b T}\right) - 1}, \quad (4.4)$$

where $\Gamma(T)$ is the temperature dependant FWHM and Γ_i is the inhomogeneous broadening. The second term in Equation 4.4 is collectively the homogeneous broadening of the PL profile where Γ_c is the coupling strength of excitons and phonons and E_{LO} is the energy of the longitudinal optical phonons. The fitting of the data to Equation 4.4 is shown in Figure 4.8b, the extracted parameters are shown in Table 4.3. The E_{LO} for InAs, GaSb and InSb are 30 meV, 29 meV, and 24 meV respectively¹⁸⁴. The 10/4 and 14/7 SLs both have an E_{LO} in this region, but the E_{LO} of the 12/4 SL is much larger. A possible cause for this may be the presence of GaAs-like interfaces or intermixing as GaAs has an E_{LO} of 35 meV. The fact that the exciton phonon-coupling, Γ_c , is also much larger for the Sample B supports this theory as the exciton phonon interaction that affects PL is mainly located around the IFs. The Sample D shows the lowest component of inhomogeneous broadening suggesting this sample has the best structural quality. This is in agreement with the XRD results, presented in Table 4.2, which shows this sample to be the most strain compensated on the GaSb substrate and with the smallest FWHM, excluding the Sample C which is not considered here.

4.1.4. Band structure simulations

8 band k.p simulations, described in Section 3.1, were performed to determine the band structure and parameters of the SL structures described above. The method is described in detail in Section 3.1 and the scope of these simulations for device design is discussed further in Chapter 7. The interfacial InSb layer, described in Section 4.1.1, was also included in the model. To verify the accuracy of the simulation for InAs/GaSb T2SLs, the simulated cut-off wavelength is compared with that extracted from the PL measurements described above, shown in Figure 4.10. A MWIR 7/4 SL structure is also included to increase the sample size.

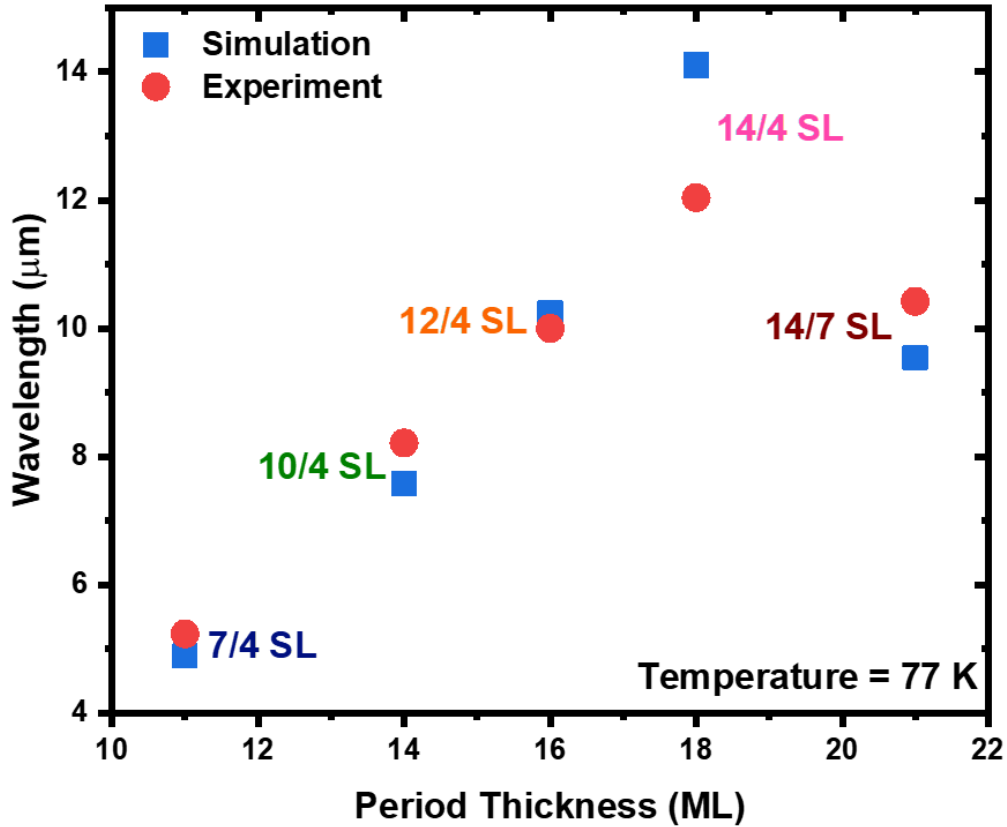


Figure 4.10: Measured and simulated cut-off wavelengths for different SL structures.

Figure 4.10 shows a good agreement between measured and simulated cut-off wavelength for SL structures with the exception of the Sample C. It is possible this arises from the same phenomena that give rise to the anomalous PL results of the Sample C discussed in Section 4.1.3. It should also be noted that minor changes in the MBE growth rate can lead to changes in the composition and layer thicknesses of the SL which can lead to a deviation in the design not considered in the simulation. However, the overall conclusion from Figure 4.10 is that the simulation is in good agreement with the experiment.

Once the accuracy of the simulation was verified, the $E(k)$ diagrams of the SL structures were calculated for the in-plane direction in the Brillouin zone $k_{//}$, as shown in Figure 4.11. The corresponding band structure diagrams are then shown in Figure 4.12 and the extracted parameters are given in Table 4.4.

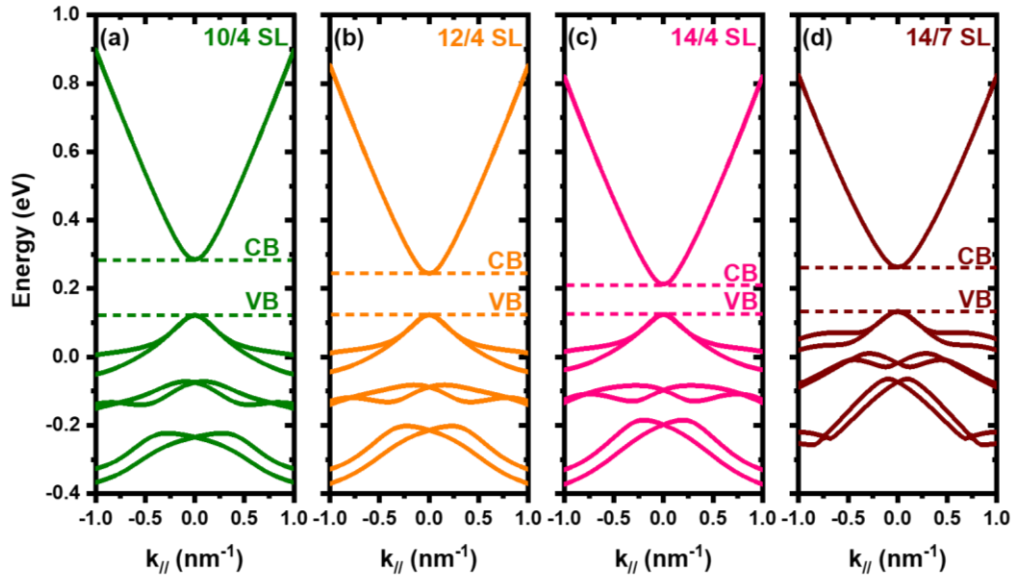


Figure 4.11: Simulated E(k) diagrams for a (a) 10/4, (b) 12/4, (c) 14/4, and (d) 14/7 SL structure for the in-plane direction along [1 0 0] in the Brillouin zone.

Table 4.4: Parameters extracted from band structure simulations of different SL structures.

Structure	Band structure (eV)				Wave-function overlap (%)	Effective mass (/m ₀)		Normalised effective density of states
	CB edge	VB edge	Band gap	HH-LH splitting		Electron	Hole (Ref. ⁶¹)	
10/4 SL	0.286	0.122	0.164	0.196	25.17	0.0193	-0.176	0.33
12/4 SL	0.245	0.123	0.121	0.211	21.06	0.0180	-0.277	0.59
14/4 SL	0.213	0.125	0.088	0.221	18.05	0.0168	-0.303	0.61
14/7 SL	0.263	0.133	0.130	0.150 93	18.22	0.0229	-0.309	1

Table 4.4 shows that as the InAs thickness in the SL structure increases from 10 ML to 14 ML, the conduction band edge decreases from 0.286 eV to 0.213 eV, a total decrease of 73 meV. As the InAs layer acts as a well for electrons in the conduction band, increasing its thickness decreases the confinement energy in the electron wells which results in the reduction in the conduction band edge noted above. However, as Table 4.4 shows, the increase in InAs layer

thickness has a negligible impact on the valence band edge. As theorised by Razeghi et al.¹⁰, this is because the effective masses of holes in the valence band is much heavier than those of electrons in the conduction band. By consideration of the formula for the energy levels in an infinite quantum well, it is clear that this makes the valence band edge more weakly dependant on the InAs thickness.

When the GaSb layer thickness is increased from 4 ML to 7 ML, the conduction band edge increases considerably from 0.213 eV to 0.263 eV. This occurs primarily because the GaSb layer acts as a barrier isolating electrons in the InAs wells. In a manner analogous to the formation of energy bands in bulk semiconductors, the minibands of a T2SL arise from the broadening of energy levels resulting from the interaction between adjacent quantum wells. When the GaSb layer thickness is increased, the interaction between adjacent InAs wells decreases, resulting in reduced broadening of the conduction band and an increased conduction band edge as observed above. The valence band edge shows only a minor increase which can be attributed to the reduction in confinement energy in the GaSb well. As noted above, the change in the valence band edge is comparatively minor because of the large hole effective mass.

The HH-LH splitting is extracted from the $E(k)$ diagrams shown in Figure 4.11 and given in Table 4.4. For every SL structure, the HH-LH splitting is larger than the band gap energy which is advantageous for suppressing Auger recombination and improving minority carrier lifetime. Table 4.4 suggests that increasing InAs thickness is favourable for increasing HH-LH splitting while increasing GaSb thickness is unfavourable. The reason for this is presently uncertain and requires further investigation.

The electron-hole wavefunction overlap, which relates to the optical matrix elements for type-II transition, was calculated for each SL structure. As the InAs layer thickness is increased from 10 ML to 14 ML, the wavefunction overlap decreases from 25% to 18% which has a detrimental effect on the optical performance of the SL. As Figure 4.12 shows, increasing the InAs layer thickness has the effect of lowering the electron wavefunction. This can be seen more clearly by comparing only the electron wavefunctions as in Figure 4.13. The heavy hole wavefunction appears relatively invariant of the InAs layer thickness which is attributed to the large heavy hole effective mass as argued above. However, when the GaSb layer thickness

is increased from 4 ML to 7 ML, the heavy hole wavefunction reduces significantly and appears to “flatten” in real space. As Table 4.4 shows, this only has a minor effect on the wavefunction overlap.

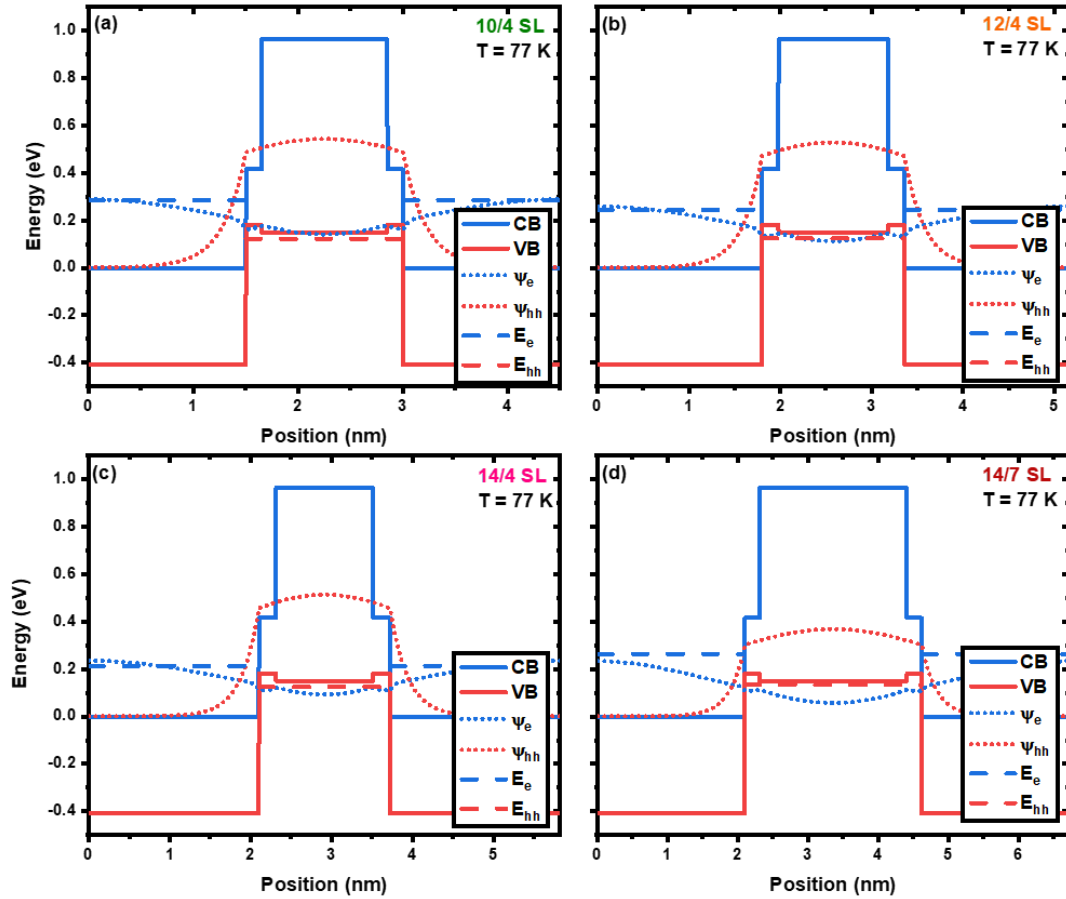


Figure 4.12: Band structure simulations in real space for (a) Sample A, (b) Sample B, (c) Sample C, and (d) Sample D.

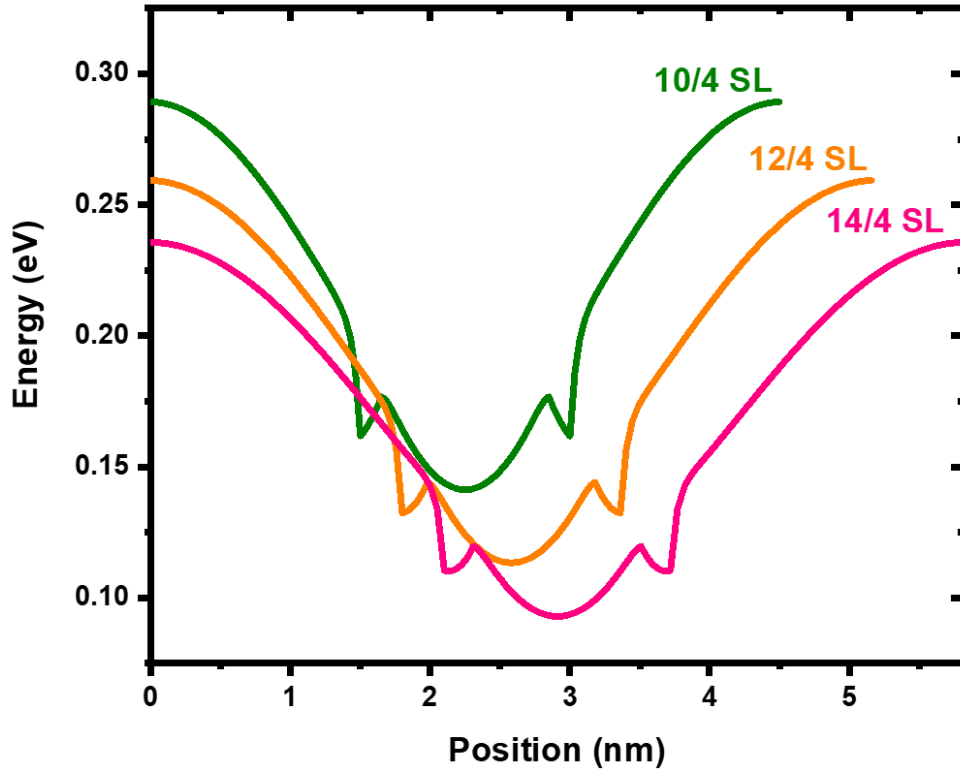


Figure 4.13: The electron wavefunction for the 10/4, 12/4, and 14/4 SL structures.

The extent of the lowering of the electron wavefunction with increasing the InAs layer thickness is shown more clearly in Figure 4.13. This is in contrast to the heavy hole wavefunction which, as argued above, appears relatively invariant of the InAs layer thickness which is attributed to the large heavy hole effective mass. The effective masses for each structure were extracted from the curvature of the $E(k)$ diagrams in Figure 4.11 and are shown in Table 4.4. For the case of electrons, the InAs layer is the well and the GaSb layer is the barrier. It is therefore intuitive to observe that increasing the InAs layer thickness (well width) decreases the electron effective mass while increasing the GaSb layer thickness (barrier width) increases the effective mass. The converse is true for the case of the hole effective mass. Once the effective masses are calculated, the effective density of states, $N_c N_v$, can be calculated using Equations 4.5 and 4.6:

$$N_C = 2 \cdot M_C \cdot \left(\frac{2 \cdot \pi \cdot m_n \cdot k_B}{h^2} \right)^{3/2}, \quad (4.5)$$

$$N_V = 2 \cdot \left(\frac{2 \cdot \pi \cdot m_p \cdot k_B}{h^2} \right)^{3/2}, \quad (4.6)$$

where M_c is the number of equivalent minima in the conduction band, m_n and m_p are the electron and hole effective masses respectively, and h is the Planck constant. The normalised effective density of states was calculated from the electron and hole effective masses and is given in Table 4.4. In general, it can be seen that the thicker the SL period the larger the effective density of states. Based on the dark current equations described in Section 1.5., it is clear that a lower electron effective mass is advantageous for lowering the trap-assisted tunnelling currents for which a larger InAs layer thickness is advantageous. However, a lower effective density of states, achieved through a lower InAs thickness, is advantageous for lower diffusion and generation-recombination currents. Increasing the GaSb layer thickness has the effect of increasing both the electron effective mass and effective density of states and is therefore favourable for tunnelling current. This trade trade-off is discussed in more detail in Section 4.2.

4.2. InAs/GaSb devices

The simulations and PL measurements presented above show that both the Samples B and D have a cut-off wavelength close to 10 μm . This section describes the growth, fabrication, and characterisation of PIN diodes which was carried out to determine which of these designs is most suited to high performance operation.

4.2.1. Design and growth

The 14/7 and 12/4 SLs designs described previously were selected to form the absorber regions of the PIN diode structures (Samples E and F), the schematics of which are shown in Figure 4.14. Both samples had a targeted i-layer thickness of 1 μm . Due to the differing period thicknesses of the 14/7 and 12/4 SLs, the two samples had 166 and 204 periods respectively.

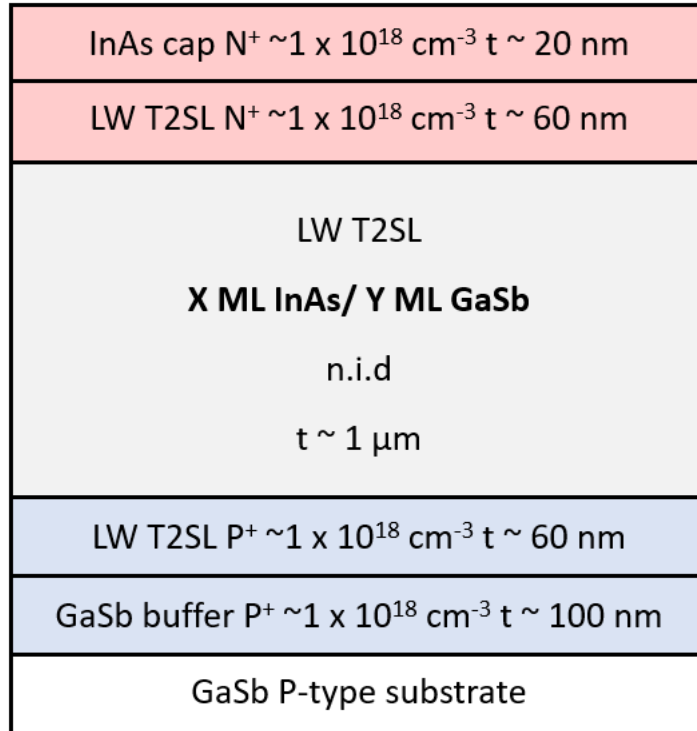


Figure 4.14: Structural Schematic for the PIN diode structures described in this chapter.

The same shutter sequences shown in Figure 4.2 for reference samples were used for the PIN diodes described in the present section. Each SL was grown on a p-type GaSb substrate and consisted of a 100 nm thick p-doped GaSb buffer layer, 60 nm of p-doped SL, a 1 μm thick non-intentionally doped (n.i.d.) SL active region, 60 nm of n-doped GaSb and a 20 nm thick n-doped InAs cap. The P⁺ and N⁺ regions both have a doping concentration of 1 x 10¹⁸ cm⁻³ and were doped using tellurium and beryllium respectively.

4.2.2. X-ray diffraction

XRD characterisation was performed using the setup described in Section 3.4.3 and the results are shown in Figure 4.15. Table 4.5 shows the parameters extracted from Figure 4.15.

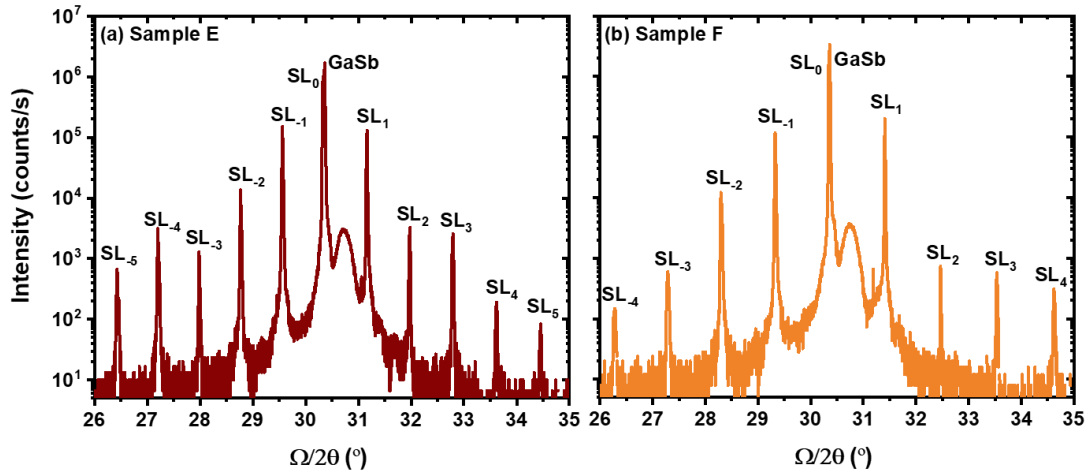


Figure 4.15: XRD rocking curves, taken around the GaSb (004) reflection for (a) 14/7 SL, and (b) 12/4 SL PIN diodes.

Table 4.5: Parameters extracted from XRD rocking curves for each SL diode and the data for the corresponding reference samples.

Sample	InAs/GaSb SL (ML)	$\Delta a/a$ (%)	FWHM ₋₁ (arcsec)	Period Thickness (nm)		
				Expected	Measured	Error
Sample B	12/4	+0.06	64	4.85	5.17	0.32
Sample D	14/7	~0	58	6.37	6.76	0.39
Sample E	14/7	+0.05	58	4.85	4.91	0.06
Sample F	12/4	+0.069	50	6.37	6.28	-0.09

The presence of many well defined satellite peaks is indicative of good material quality as described above. Table 4.5 shows that both SLs are under a slight compressive strain on the GaSb substrate. This deviation from the results of the reference sample, reported in Section 4.1.2, is most likely due to a change in growth rate which affected the layer thicknesses in the SL period. The FWHM of the SL₋₁ peak is also lower than that of the reference samples which suggests good material quality. The measured period of each SL is closer to the expected than previously observed, this too is likely due to fluctuations in growth rate.

4.2.3. Photoluminescence

PL measurements from 77 – 160 K were performed and results are shown in Figure 4.16. Varshni's equation, Equation 4.2, is once again used to fit the temperature dependence of the band gaps. The parameters extracted from the PL measurements are shown in Table 4.6.

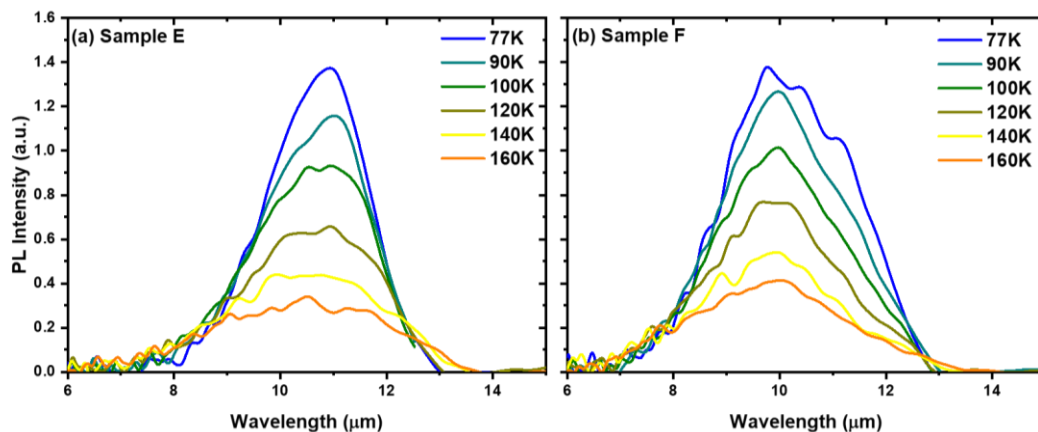


Figure 4.16: PL profiles as a function of temperature for (a) 14/7 SL and (b) 12/4 SL.

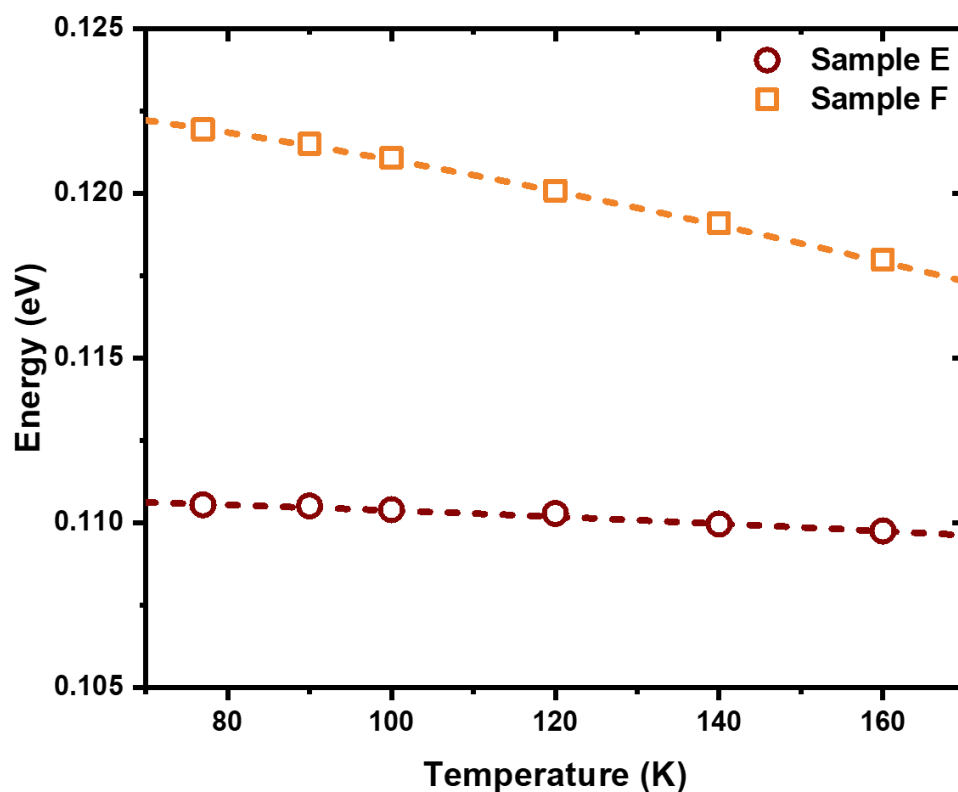


Figure 4.17: The PL peak as a function of temperature fitted to Equation 4.2.

Table 4.6: Parameters extracted from PL measurements of the SL diodes and the data for the corresponding reference samples. Note that a different normalisation was applied to the mas PL intensity of Samples B and D compared to Samples E and F.

Sample	InAs/GaSb SL (ML)	Max PL Intensity (a.u.)	Varshni Parameters		
			$E_g(0K)$ (eV)	$\lambda_c(0K)$ (μm)	α (meV/K)
Sample B	12/4	0.556	0.127	9.76	0.186
Sample D	14/7	0.424	0.121	10.25	0.119
Sample E	14/7	1.37	0.11	11.17	0.094
Sample F	12/4	1.38	0.124	10.00	0.019

Table 4.6 shows that the $E_g(0K)$ for the Sample F is close to that measured for the reference sample in Section 4.1.2 while the Sample E has shown a somewhat significant variation. This can, once again, be attributed to fluctuations in growth rate suggested by the XRD analysis. The measured value of α for the Sample E is close to that measured from the reference sample but α for the Sample F shows a much smaller value than the equivalent reference sample. It is possible that this can be attributed to the presence of doping related impurities.

4.2.4. Device Fabrication

The Devices, shown in Figure 4.18, were then fabricated from each diode sample using a standard photolithography process described in Section 3.3. Cr/Au was thermally evaporated onto the InAs cap of each sample to form the top contact. Mesas, with diameters ranging from 140 μm – 440 μm , were defined using a citric acid-based wet etch. Mesa sidewalls were then protected from ambient air using the photoresist SF1813 which was then hard-baked. Finally, Cr/Au was then thermally evaporated for the lower contact.

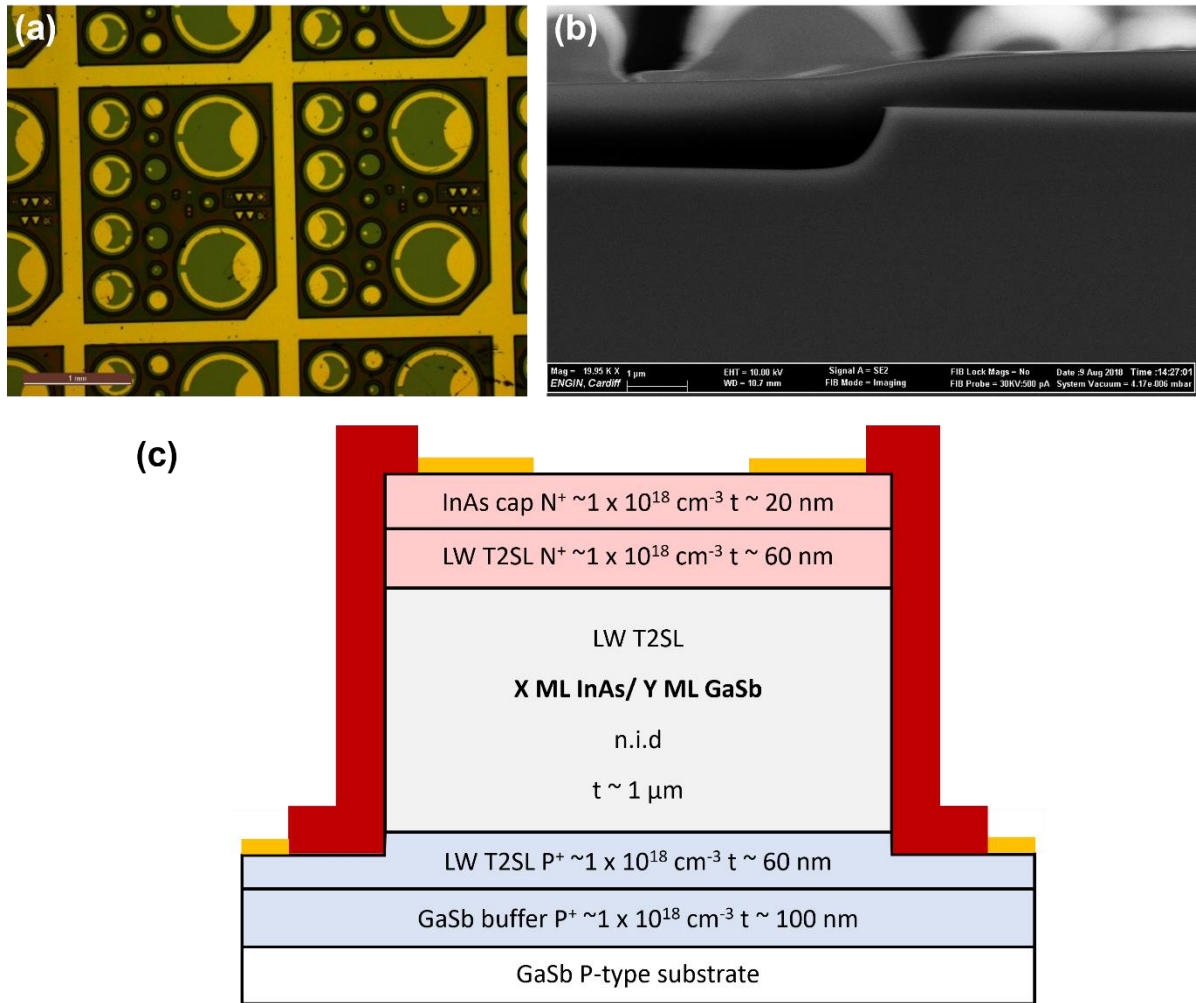


Figure 4.18: (a) Optical microscopy image of fabricated diodes, (b) SEM image of a mesa sidewall, (c) structural schematic of a fabricated diode.

The citric acid etch rate was calibrated and timed to target the T2SL P⁺ region. Electrical characterisation was performed using a cryogenic probe station for samples with different etch depths. As the samples were designed to be sensitive to blackbody radiation emitted from room temperature objects, blackbody radiation from the lab is likely to induce an unwanted photocurrent in these measurements. The induced photocurrent is likely to be orders of magnitude lower than the measured dark currents but was still minimised through cryogenic cooling of the sample environment and radiation shielding. Electrical characterisation for samples with different etch-depths, shown in Figure 4.19, shows that the best electrical performance is achieved when the etch depth is calibrated to this region.

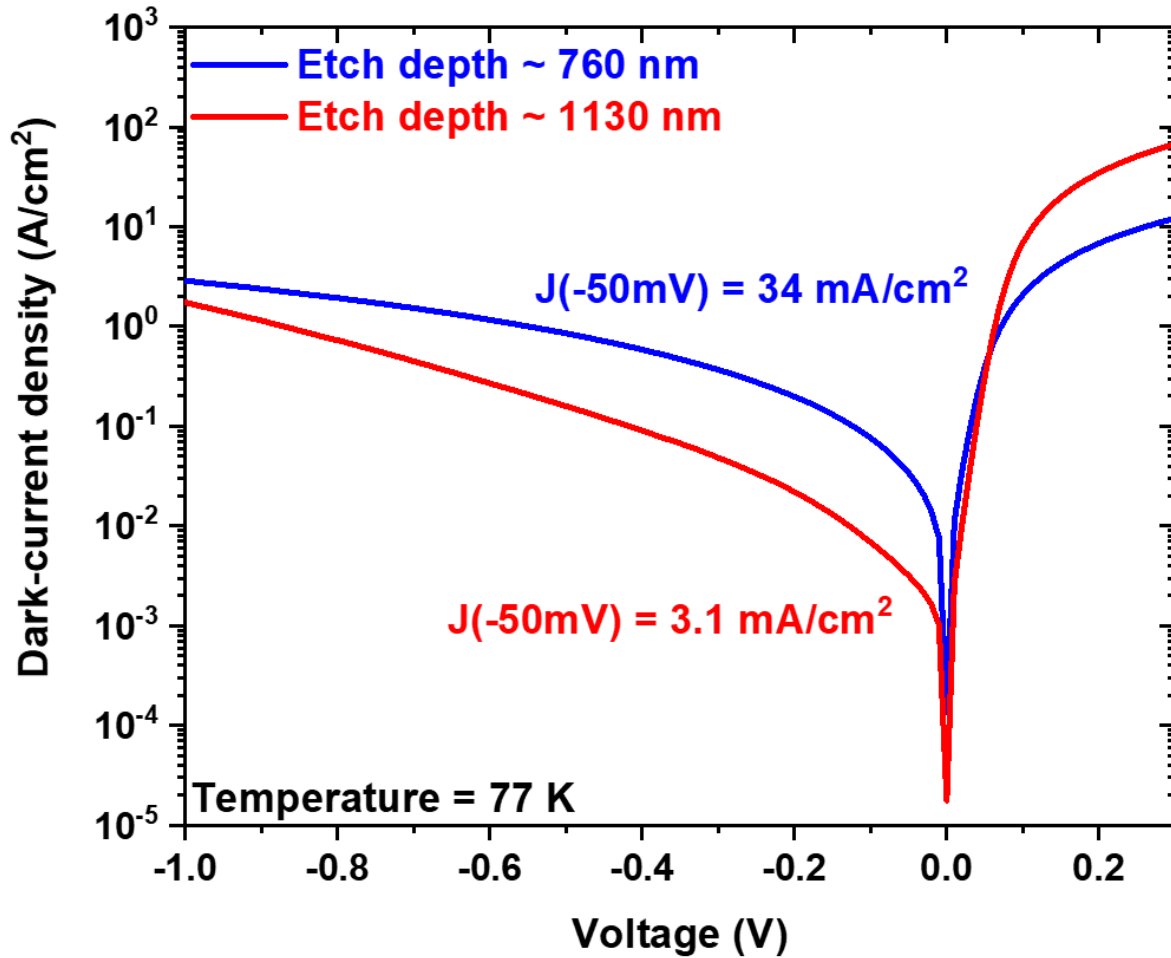


Figure 4.19: Dark current density as a function of applied bias for samples with etching depths of 760 nm and 1130 nm.

4.2.5. Electrical characterisation

A Lakeshore Cryogenic Probe Station was used to measure the electrical performance of each diode. The dark current density as a function of applied bias, shown in Figure 4.20, was measured at 77 K for every device on a 10 mm x 10 mm piece of each SL sample.

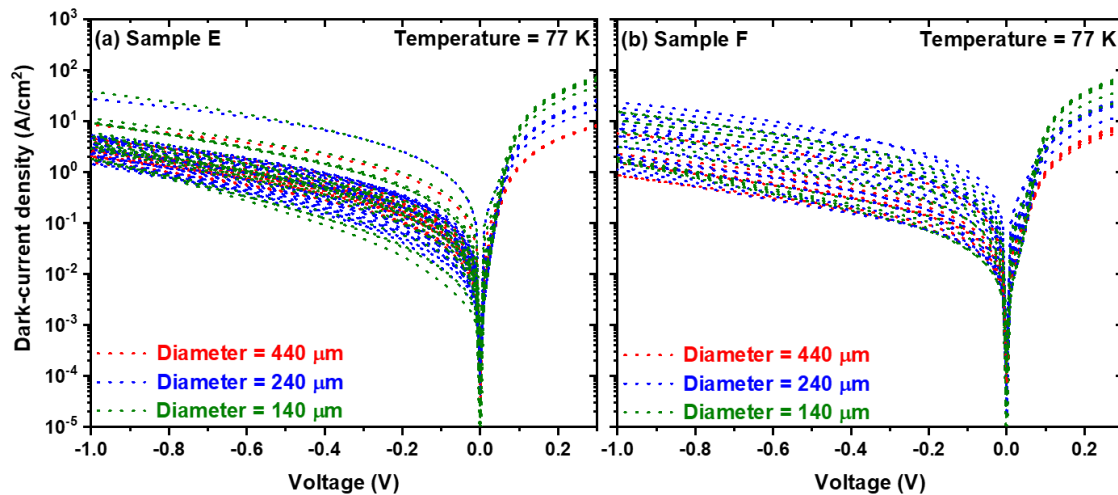


Figure 4.20: Dark current density vs applied bias for every fabricated diode on (a) Sample E and (b) Sample F.

Figure 4.20 shows that the dark current characteristics of different samples on the same chip can vary by almost two orders of magnitude. This presents a significant challenge to the scale-up to FPAs as these require a high degree of uniformity between diodes^{185–187}. A possible cause of this inhomogeneity is the lack of effective passivation. While photoresist was used to protect the mesa sidewalls from ambient air, this is not as effective as methods which make use of crystalline materials to chemically passivate the dangling bonds created during mesa etching. Another possibility is the uniformity of the etch. It is well known that acid-based wet etches can be both crystallographic as well as isotropic in nature¹⁸⁸. It is therefore difficult to predict the nature of the mesa sidewalls these etches will produce or have any guarantee of uniformity between mesas.

Temperature dependant $I - V$ measurements, shown in Figure 4.21, were performed for two different mesa sizes on each sample. The best devices for this study were chosen for their low dark current and diode-like characteristics i.e. low and flat under reverse bias and straight under forward bias with no kink. The dark current density at a reverse bias of -50 mV was measured as a function of temperature for each sample and shown in Figure 4.22.

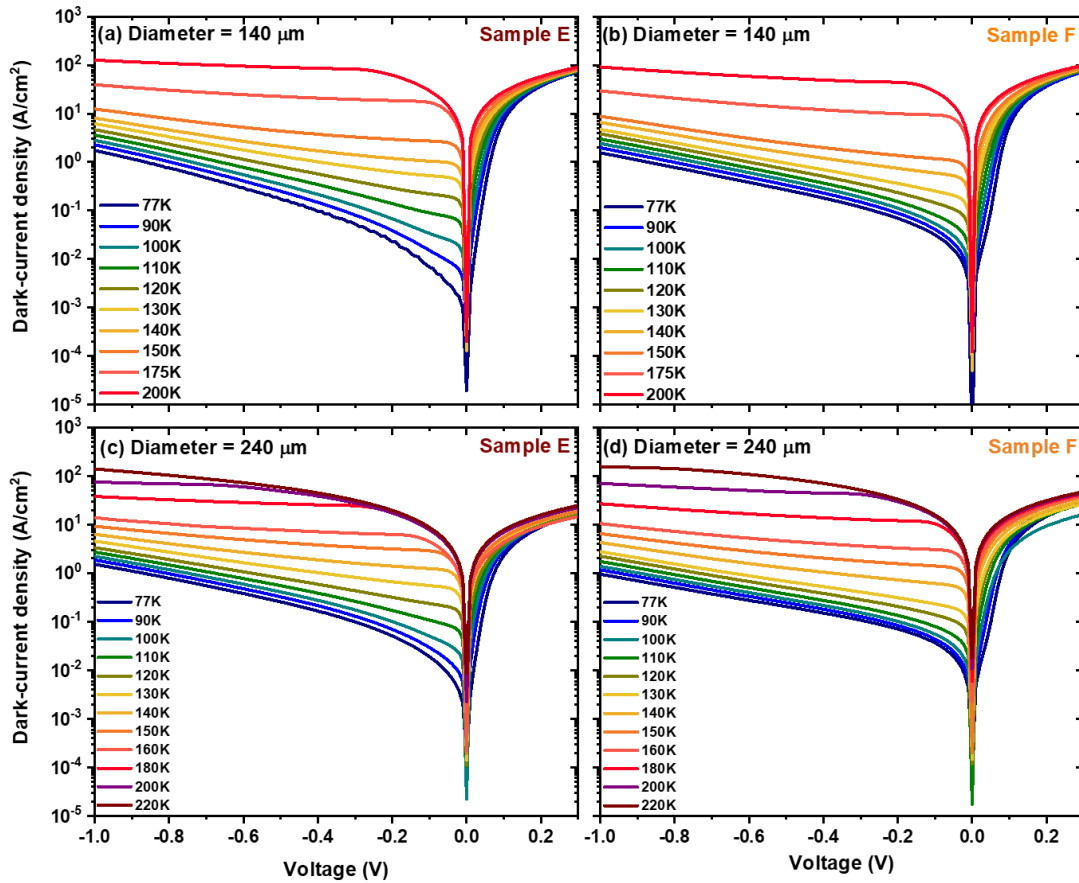


Figure 4.21: Dark current density as a function of applied bias for (a) $\phi = 140 \mu\text{m}$, Sample E (b) $\phi = 140 \mu\text{m}$, Sample F, (c) $\phi = 240 \mu\text{m}$, Sample E, (d) $\phi = 240 \mu\text{m}$, Sample F.

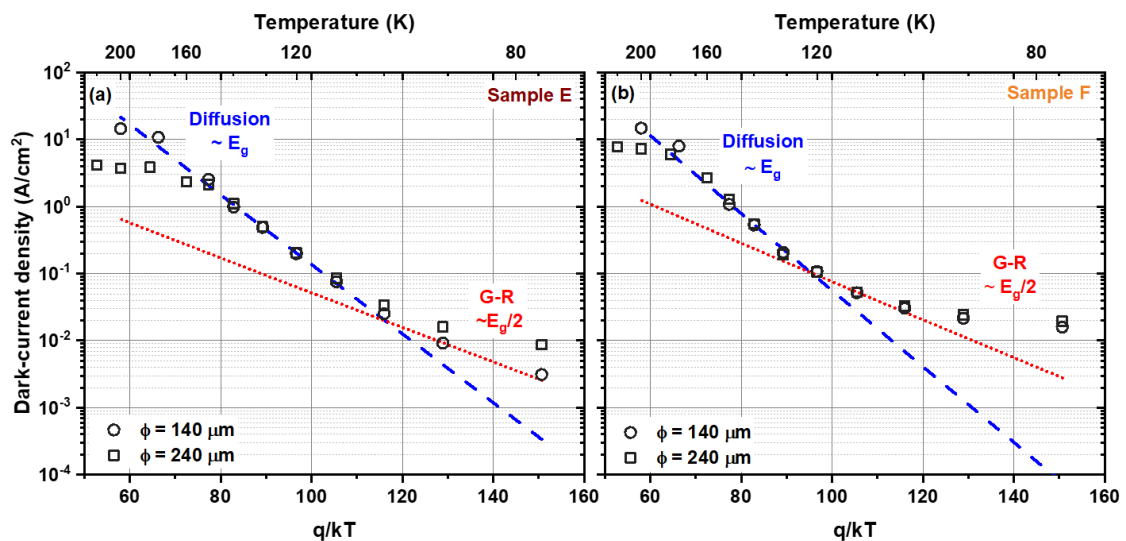


Figure 4.22: Dark current density measured at -50 mV as an inverse function of temperature for (a) Sample E and (b) Sample F diodes. Diffusion and G-R currents are plotted by the blue dashed and red dotted lines respectively.

By considering the equations for the diffusion (Equation 1.11) and G-R (Equations 1.12 and 1.13) current, it can be seen that:

$$I_{diff} \propto n_i^2 \propto \exp\left[-\frac{E_g}{k_B T}\right] \quad (4.7)$$

$$\text{and } I_{G-R} \propto n_i \propto \exp\left[-\frac{E_g}{2k_B T}\right]. \quad (4.8)$$

The relations derived in Equations 4.7 and 4.8 are fitted to the data shown in Figure 4.22. It is observed that both the Samples E and F are dominated by diffusion current above $T \sim 100$ K. A deviation is observed above $T \sim 160$ K possibly resulting from thermally induced G-R current. At temperatures below 100 K, the G-R current dominates in the case of the $\phi = 140$ μm , Sample E. A slight deviation is seen when the diameter is increased to $\phi = 240$ μm . This is likely due to a surface leakage current as the devices are not passivated and the effect increases with the surface area of the mesa sidewalls as discussed below. Both of the device diameters measured from the Sample F deviate from the G-R dominated behaviour observed in Sample E. By comparing the dark current density at 150 K, where diffusion current dominates for both samples, it can be seen that the Sample F (1.07 A cm^{-2}) has a notably lower diffusion current compared with the Sample E (2.52 A cm^{-2}). This remains the case even correcting for the difference in band gaps.

To understand why this was the case, the capacitance of each sample was measured as a function of applied bias, shown in Figure 4.23. The residual doping of each SL active region was measured to be $1.4 \times 10^{15} \text{ cm}^{-3}$ and $1.3 \times 10^{15} \text{ cm}^{-3}$ for Samples E and F respectively. These values were obtained from Figure 4.23b using the method described in Ref. ¹⁸⁹. It can thus be concluded that the residual doping concentration is unlikely to be the cause of the lower diffusion current in Sample F.

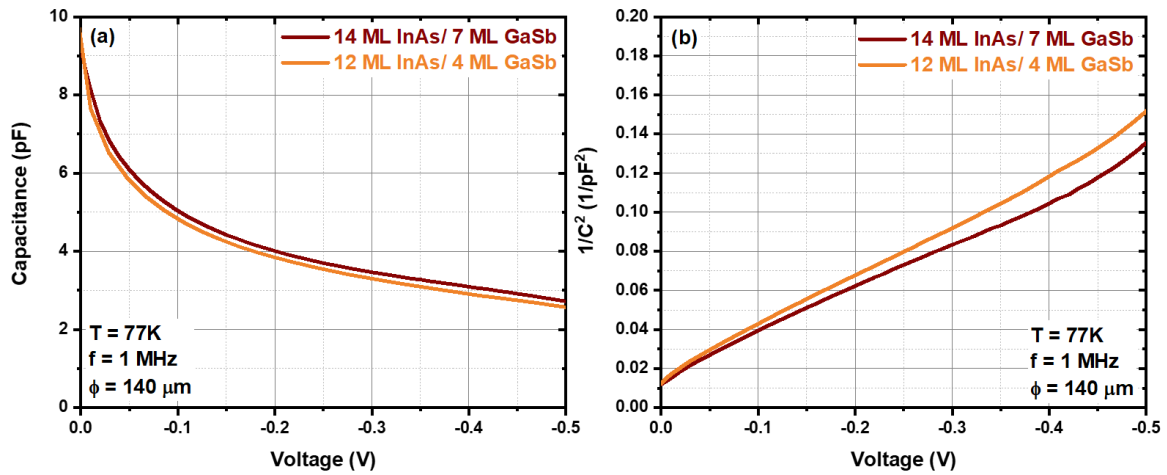


Figure 4.23: (a) capacitance vs voltage and (b) $1/C^2$ vs voltage for each SL diode.

To better understand the dark current mechanisms in each structure, the Mathematica software was used to fit the dark current equations described in Section 1.5 to the I-V profiles at 77 K. The results are shown in Figure 4.24. A good agreement between the measured and calculated dark current was achieved by manually adjusting certain fitting parameters in the dark current equations. These fitting parameters were the minority carrier lifetime and diffusion length, the G-R lifetime, the trap density, and the shunt resistance.

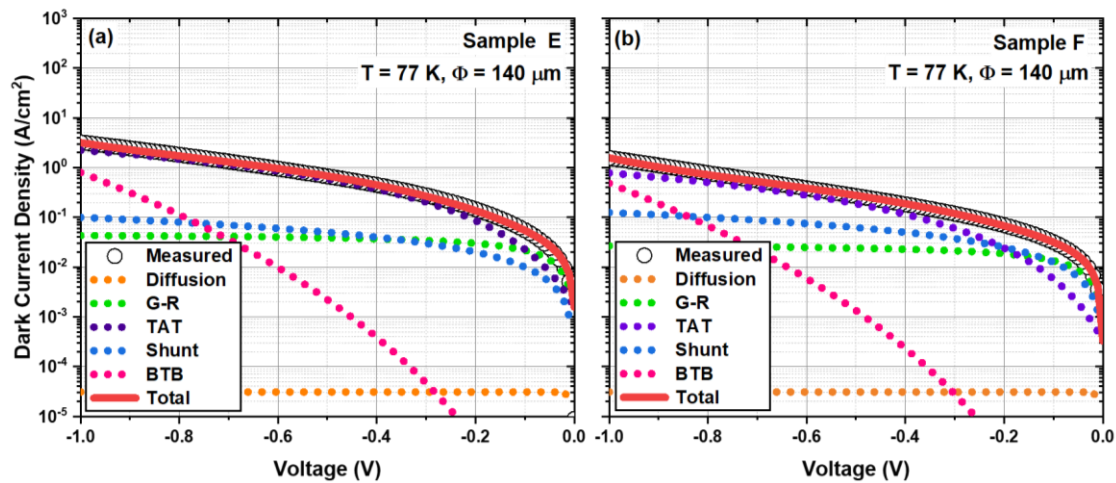


Figure 4.24: I-V profiles and fitting for (a) Sample E and (b) Sample F for a 140 μm diameter diode at 77 K.

Figure 4.24 shows that, as indicated by Figure 4.22, at 77 K both samples are largely dominated by G-R current at low reverse bias but become dominated by TAT currents and eventually BTB currents as the bias increases. The TAT current is larger in the Sample E which,

by considering Equations 4.9 and 4.10, is accounted for by the larger effective masses (see Table 4.4) in this sample. In the case of the Sample F, the deviation from purely G-R dominated behaviour appears to result from the considerable shunt current observed in Figure 4.24. The reason for the increased shunt current in the Sample F sample is not certain. One possibility is the different chemical composition of the sample results in a different response to the etch. Alternatively, it may be attributed to the inhomogeneity and unpredictability of the wet etching process, further highlighting the need for a dry etch alternative. This result also highlights the need for effective chemical passivation which can greatly suppress the contribution from shunt currents.

Using the method described in Section 3.1, Silvaco simulations for Samples E and F were performed across the temperature range 77 K – 200 K (Figure 4.25). The energy gaps and residual doping concentrations, determined by PL and C-V measurements above, were inputted into the simulation. A serial resistance of $1.5 \Omega \cdot \text{cm}^2$ was added to accommodate the sheet and contact resistances. As this resistance only affects the forward bias, the only fitting parameter for the reverse bias is the minority carrier lifetime, τ . It can be seen that the agreement between the measured and simulated I-V profiles is best for the temperature range 100 K – 150 K (175 K for the Sample F). This can be explained by the dominance of the well understood G-R and diffusion processes in this range, shown in Figure 4.22. The deviation from this behaviour outside this temperature range is attributed to tunnelling and contact resistance phenomena. The extracted minority carrier lifetimes at a temperature of 150 K for the two samples were compared as this temperature showed the best agreement between the measure data and the fit. The lower minority carrier lifetime of Sample F (12 ns) compared to Sample E (18 ns) corroborates the lower dark current of the sample at this temperature.

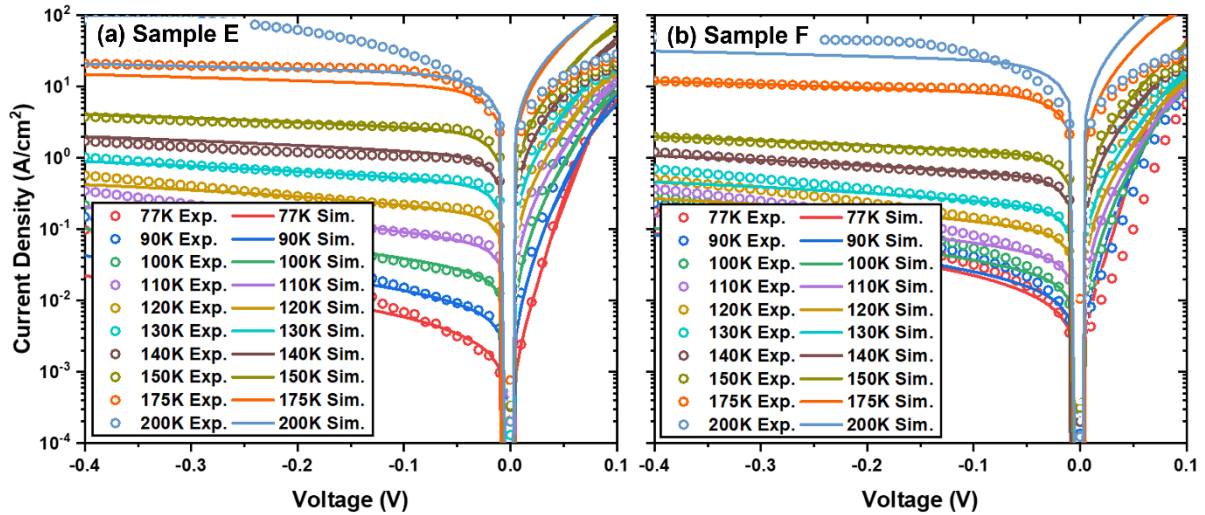


Figure 4.25: Measured and simulated current density profiles for the temperature range 77 K – 200 K for (a) Sample E and (b) Sample F.

Despite the limitations of the simulation tool outside of the optimal temperature range, the minority carrier lifetimes for each sample for the whole temperature range were extracted and are shown in Figure 4.26. Both samples show an initial increase in the minority carrier lifetime with temperature, a peak, and finally a decrease with temperature. The peak value is found at 90 K and 120 K for Samples E and F respectively. However, it should be noted that the peak value for Sample E appears somewhat anomalous and lies outside the 100 K – 150 K range of good agreement between measurement and simulation. The minority carrier lifetime peak at around 120 K, observed for Sample F, can be explained by considering the dominant recombination mechanisms in the SL. Taghipour et al.¹⁹⁰ have measured the minority carrier lifetime of a 10 ML InAs/10 ML GaSb SL over the temperature range 20 K – 260 K using time-resolved-microwave-reflectance (TMR) measurements. Results show that, though the minority carrier lifetime is roughly invariant of temperature, it is dominated by SRH processes below ~ 120 K and by Auger processes above. It is therefore plausible that the peak around 120 K, observed in Figure 4.26b, is due to a change in the dominant recombination mechanism from SRH to Auger. The deviation from this behaviour in the 14/7 SL, shown by Figure 4.26a, can be attributed to the lack of agreement between simulation and measurement at low temperature.

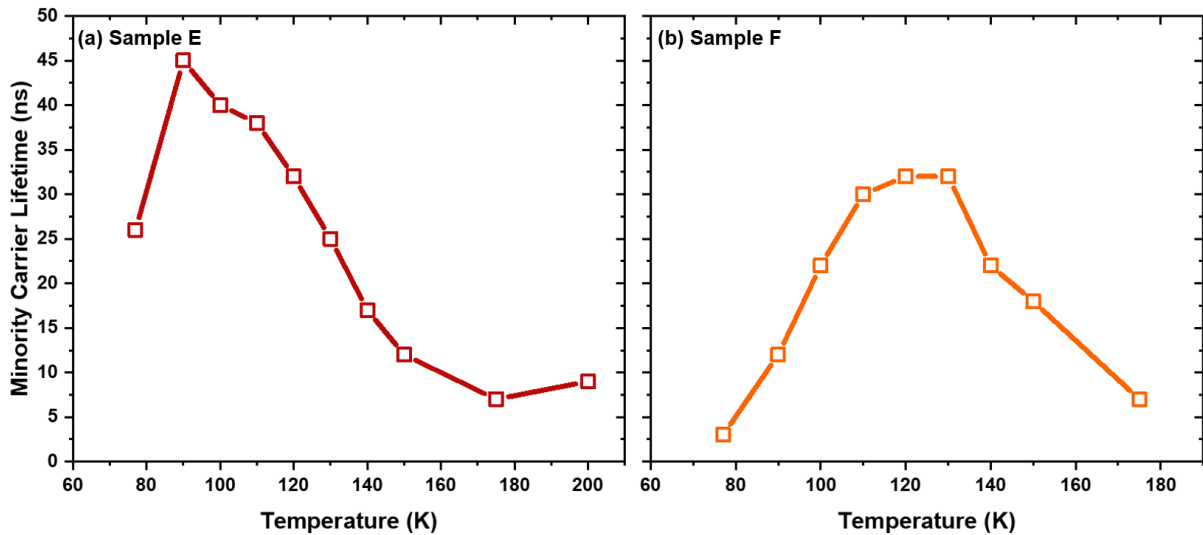


Figure 4.26: The minority carrier lifetimes extracted from Figure 4.25 for (a) Sample E and (b) Sample F.

4.3. Summary

In conclusion, the results reported here demonstrate the flexibility of the InAs/GaSb T2SL for LWIR applications. The material properties of four different LWIR T2SL structures were studied to conclude, through XRD, that good quality SLs can be obtained in each case. PL measurements have also demonstrated that all SL structures have a cut-off wavelength in the LWIR spectral range at 77 K. 8 band k.p simulations were used to study the band structure of each SL structure and corroborate other results. InAs/GaSb T2SL PIN diodes were also grown using the 14/7 and 12/4 SL structures and a standard photolithography process was used to fabricate single pixel-diodes. The dark current density at 150 K was measured to be 2.52 A cm^{-2} and 1.07 A cm^{-2} for the 14/7 and 12/4 SLs respectively. I – V measurements were taken at temperatures from 77 – 200 K and I-V modelling were used to identify the dominant dark current mechanisms.

These results show that a thinner SL period is advantageous for the optical properties of the SL due to the increased wavefunction overlap. Furthermore, a thinner period is likely to result in lower effective masses, provided the cut-off wavelength is relatively unchanged. This is advantageous for the reduction of diffusion, G-R, and TAT currents. However, when tested by comparing a 14/7 and 12/4 SL diodes, these advantages were only observed at higher temperature due to the shunt currents present in the 12/4 SL. The contribution from the

shunt current may be mitigated through use of a chemical passivation. However, due to the high demand for low SWaP detectors, it is the higher temperature (~ 150 K) operation of SL detectors that is most important.

5. LWIR InAs/GaSb T2SLs on GaAs Substrates

In Chapter 4, the 12/4 SL structure was proposed as a viable route to achieving high performance LWIR T2SLs. In this chapter, we aim to determine whether the 12/4 SL is a suitable structure for growth on GaAs substrates due to the cost, size, and potential performance enhancements it provides.

5.1. Introduction

Growth, fabrication, and characterisation of 12/4 SL reference samples and diodes on GaSb and GaAs substrates were performed. In the latter case, the strain from the 7.8% lattice mismatch was compensated through the use of IMF array described in Chapter 2. The material quality of the reference samples grown on GaSb and GaAs substrates were compared using XRD, Nomarski microscopy, and TEM measurements. PL measurements were then used to compare the optical quality and uniformity of each sample. Following device fabrication, the performance of the diodes was compared using I-V measurements.

Finally, following the work of the previous chapter, a 14/7 SL diode was grown on a GaAs substrate and compared to the 12/4 SL device. The above characterisations were performed in order to determine whether the advantages observed in Chapter 4 remained when the 14/7 SL was grown on a GaAs substrate.

5.2. Samples

The samples in the present work were grown under the same conditions detailed in Chapter 4. The reference sample grown on a GaSb substrate (Sample B) is from the same wafer as the 12/4 SL reference sample described in Chapter 4. The reference sample on GaAs (Sample G) was grown on a quarter of a two-inch semi-insulating GaAs (1 0 0) substrate. A 500 nm GaSb

buffer layer was grown with an IMF array at the GaSb-on-GaAs IF followed by 80 periods of 12/4 SL layer capped with 4 ML of GaSb. As with Sample B, a strain compensating interfacial InSb layer was intentionally grown at the interfaces for both samples using migration enhanced epitaxy. The pin diode sample on GaSb (Sample F) was taken from the same wafer as the 12/4 diode discussed in Chapter 4. The pin diode sample on GaAs (Sample H) was again grown on a quarter of a two-inch semi-insulating GaAs (1 0 0) substrate followed by a 500 nm GaSb buffer layer grown with an IMF array at the GaSb-on-GaAs IF. As with Sample F, the GaSb buffer layer was followed by the growth of a 60 nm 12/4 SL P-region, 1 μm non-intentionally doped 12/4 SL absorber region, 60 nm 12/4 SL N-region, and 20 nm N-doped InAs cap. The P- and N- regions of Samples F and H targeted a doping concentration of $1 \times 10^{18} \text{ cm}^{-3}$. A 14/7 diode on GaAs (Sample I) was grown using the exact same structure and growth parameters as Sample D but with the 12/4 SL replaced by the 14/7 SL structure. Mesa diodes were fabricated using the process described in Section 3.3.

5.3. X-ray diffraction

HRXRD measurements, ($\omega/2\theta$ scans in Figure 5.1a), were performed for both Samples B and G. Figure 5.1b shows an enhanced view of the SL zeroth order peak from each sample and the GaSb substrate peak of Sample B. These peaks were then used to calculate the lattice mismatch between the substrate and SL using Equation 3.45. Both Samples B and G show multiple satellite peaks which are indicative of good material quality. Using the method applied in Section 4.2.2, the period thickness of each sample was extracted from the gradients (Figure 5.2). Finally, the FWHM of the SL_{-1} peak was measured. The results are shown in Table 5.1, in which the rocking curve for the Sample G is offset by a factor of 10^3 for clarity.

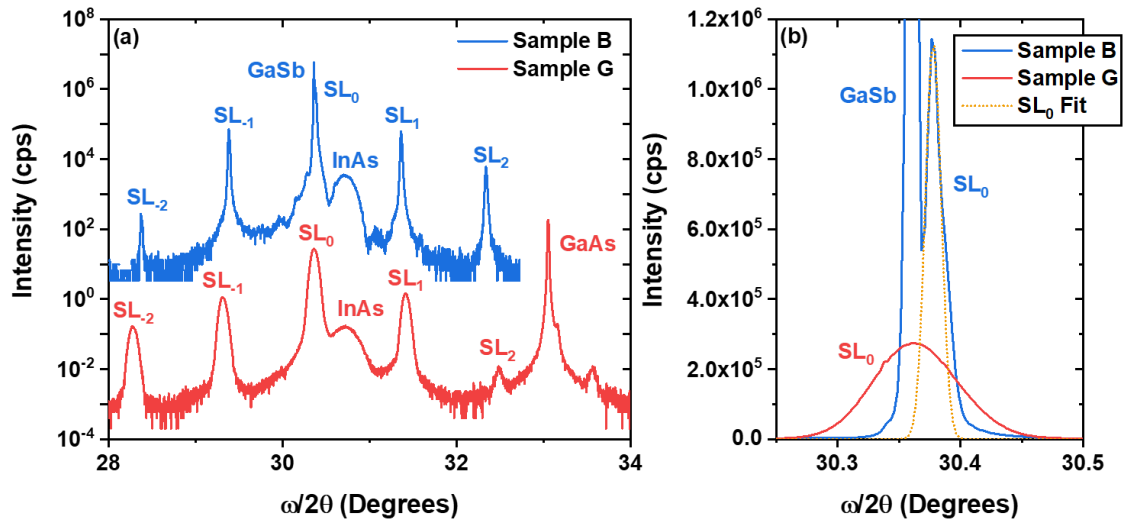


Figure 5.1: (a) XRD rocking curves and (b) an enhanced view of the SL_0 peak for both Samples B and G.

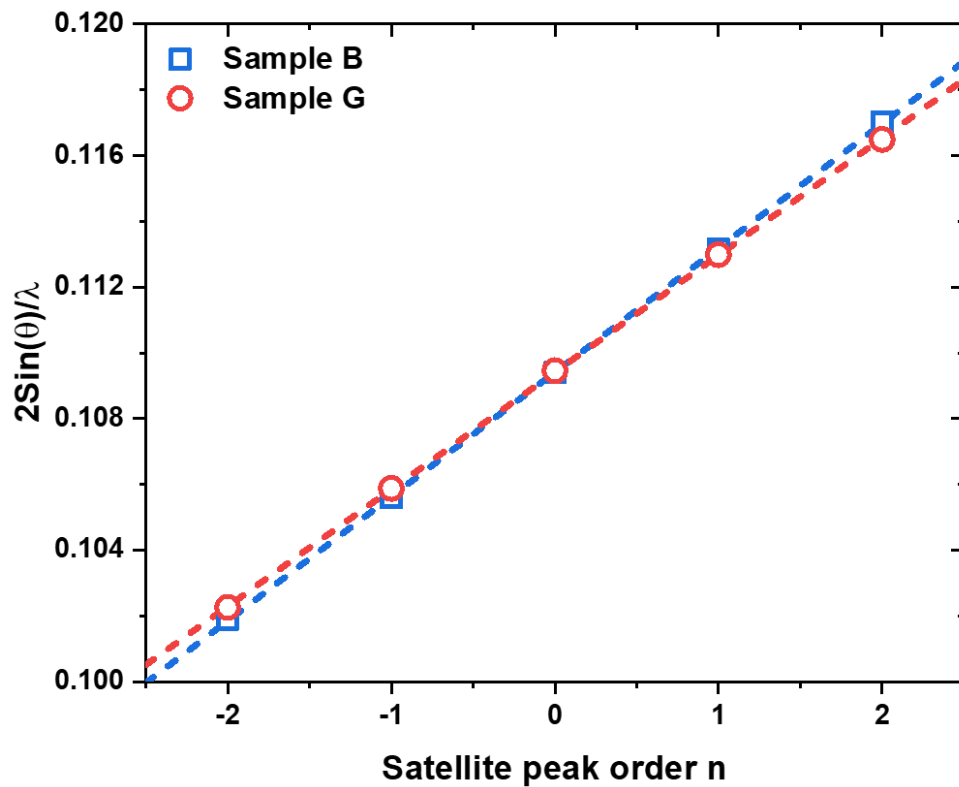


Figure 5.2: $2\sin(\theta_n)/\lambda$ of each SL satellite peak as a function of the satellite order.

Table 5.1: Parameters extracted from XRD measurements of Samples B and G.

Sample	Substrate	FWHM SL ₋₁ (arcsec)	Period Thickness (nm)	Lattice mismatch (%)
Sample B	GaSb	60	5.17	-0.05
Sample G	GaAs	301	4.86	7.90

Table 5.1 shows the FWHM of the SL₋₁ peak of Sample B is a factor of 5 smaller than that of Sample G. The larger FWHM is indicative of a decreased material homogeneity that may be attributed to the generation of threading dislocations as will be discussed in Section 5.4. The degradation of material quality despite the presence of the IMF array, indicated by the increased FWHM, has been well documented for GaSb epilayers grown on GaAs substrates using the IMF array^{191–194}. It is also clear that Sample B has a period thickness very close to that intended (5.16 nm). However, Sample G shows a notable but not substantial deviation from this value which could be attributed to a reduced material homogeneity induced by the GaAs substrate or simply a fluctuation in the growth rate. For the case of Sample B, there is a -0.05% lattice mismatch between the GaSb and SL₀ peaks, indicating the SL is almost lattice matched onto the substrate. The -0.05% lattice mismatch indicates the presence of a slight tensile strain which suggests the interfacial InSb layers are too thin for a fully strain compensated SL. The 7.9% lattice mismatch between substrate and SL for Sample G is close to the 7.8% lattice mismatch between GaSb and GaAs. This result simply highlights the absence of significant relaxation in the GaSb layer that alters its lattice constant and is therefore to be expected. The slight discrepancy between these values suggests the presence of a slight compressive strain between the SL and GaSb buffer layer.

5.4. Nomarski Microscopy

Nomarski microscopy was used to investigate the surface topology of each sample. Large regions of each sample were scanned such that the micrographs given in Figure 5.3 are representative of the whole of each sample. To highlight the presence of defects, the contrast of each micrograph is enhanced by the same factor. Figure 5.3 shows that a much greater density of surface defects in Sample G compared to Sample B, indicating an inferior material

quality in this sample despite the presence of the IMF array. The origin of these defects will be discussed in Section 5.5.

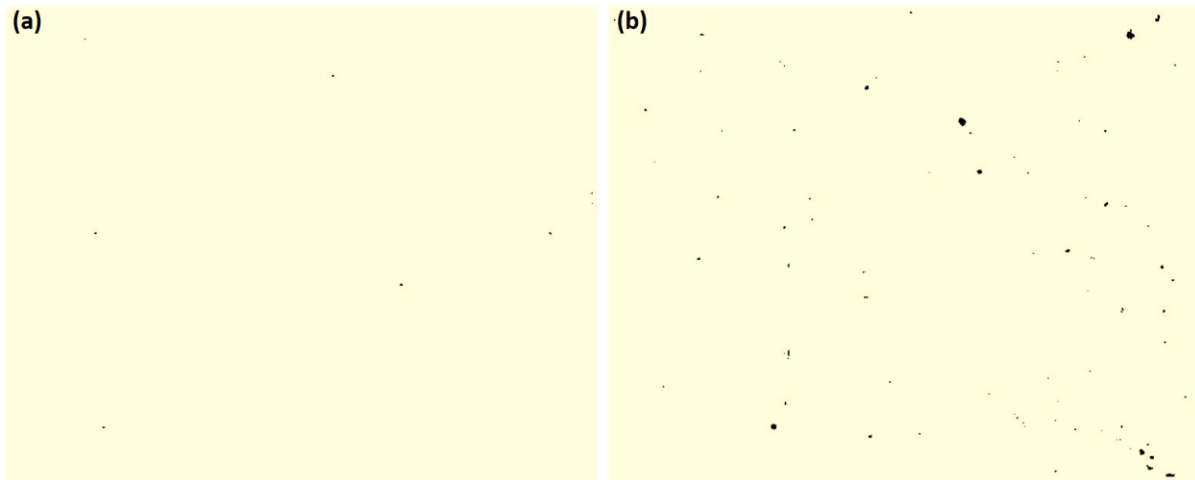


Figure 5.3: Representative Nomarski micrographs with enhanced contrast from (a) Sample B and (b) Sample G.

5.5. Transmission electron microscopy

To investigate the structural properties of the two samples, TEM characterisations were performed. Figure 5.4 shows low-magnification CTEM micrographs, taken from Samples B and G. The white arrow in Figure 5.4c highlights the IMF array in Sample G, which appears as a dark line at the GaSb-on-GaAs IF. Figure 5.4a indicates that Sample B has a very homogeneous contrast through the T2SL, meaning no extended lattice defects are present. However, Figure 5.4c shows the presence of some line-shaped, dark formations which will be analysed below.

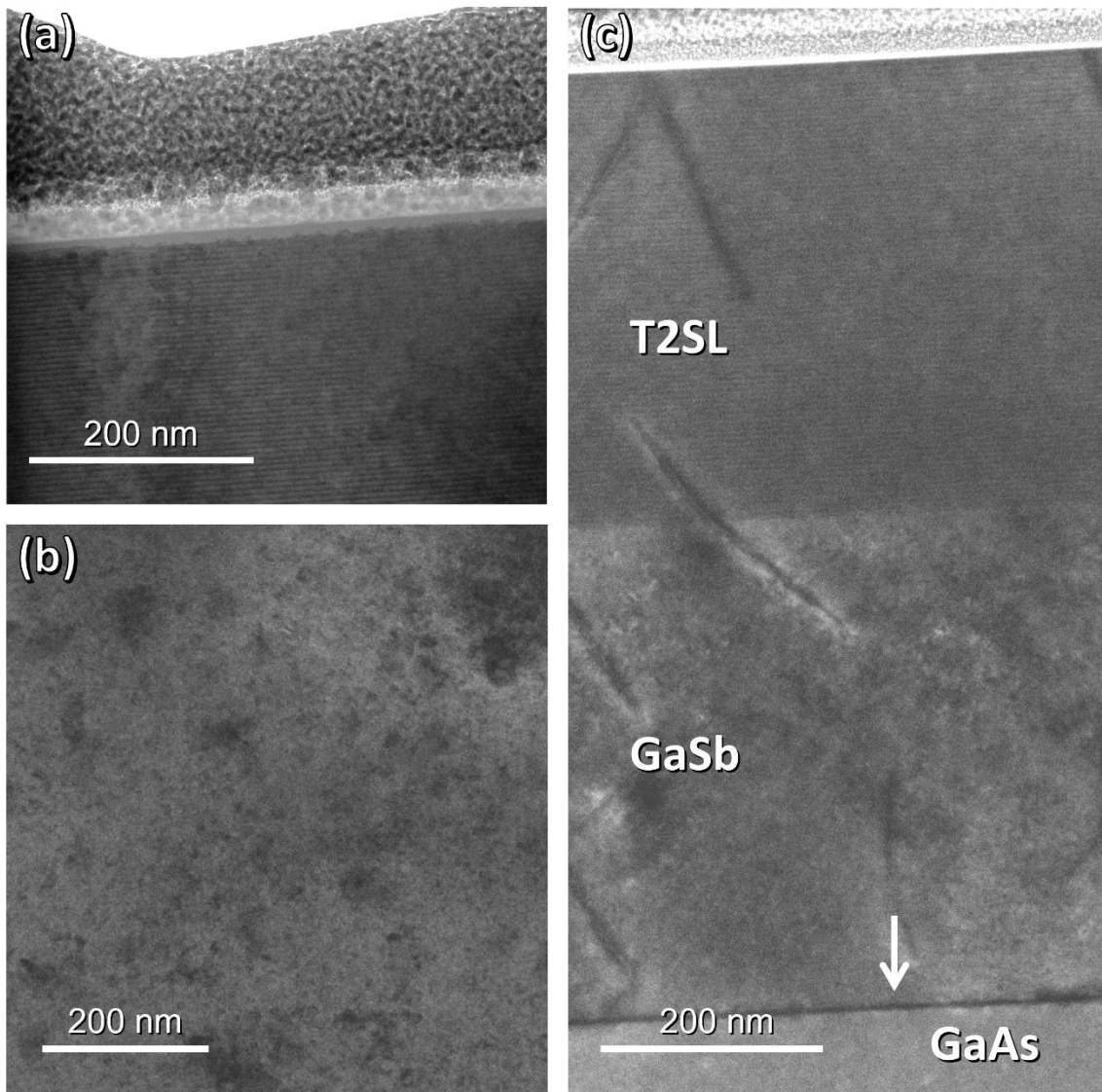


Figure 5.4: CTEM micrographs from a) the T2SL layer of Sample A, (b) the GaSb substrate of Sample B, and (c) the whole heterostructure of Sample G. The white arrow in Figure 5.4c highlights the IMF array of Sample G.

Representative SAED patterns from the regions (not shown) confirm the presence of single-crystalline, epitaxially related materials in both Samples B and G. This can be deduced from the fact the respective reflections are aligned and discrete and do not contain diffraction rings or diffuse signals.

A second CTEM micrograph of Sample G was taken under two-beam and bright-field diffraction contrast TEM conditions to enhance the visibility of the defects and is shown in Figure 5.5. This shows threading dislocations and stacking faults visible along specific glide

planes, some of which are highlighted with white arrows. The threading dislocations appear to be coming from random spots along the GaSb-on-GaSb IF. It is expected that these threading dislocations will terminate either at the surface of the heterostructure, possibly resulting in the defects observed in Figure 5.3, or annihilate by reaching other dislocations. The presence of threading dislocations is attributed to the formation of some 60° misfit dislocations in addition to the desirable 90° misfit dislocations at the GaSb-on-GaAs IF as the former have been shown to be the origin of threading dislocations in GaSb epilayers on GaAs^{193,194}. This could be mitigated through optimisation of the growth parameters. In particular, the prevalence of 60° misfits has been shown to be particularly sensitive to the growth temperature¹⁹⁵. It should also be noted that a fraction of these defects appears to terminate at the T2SL-on-GaSb IF, suggesting the GaSb layer itself acts as a kind of dislocation filter.

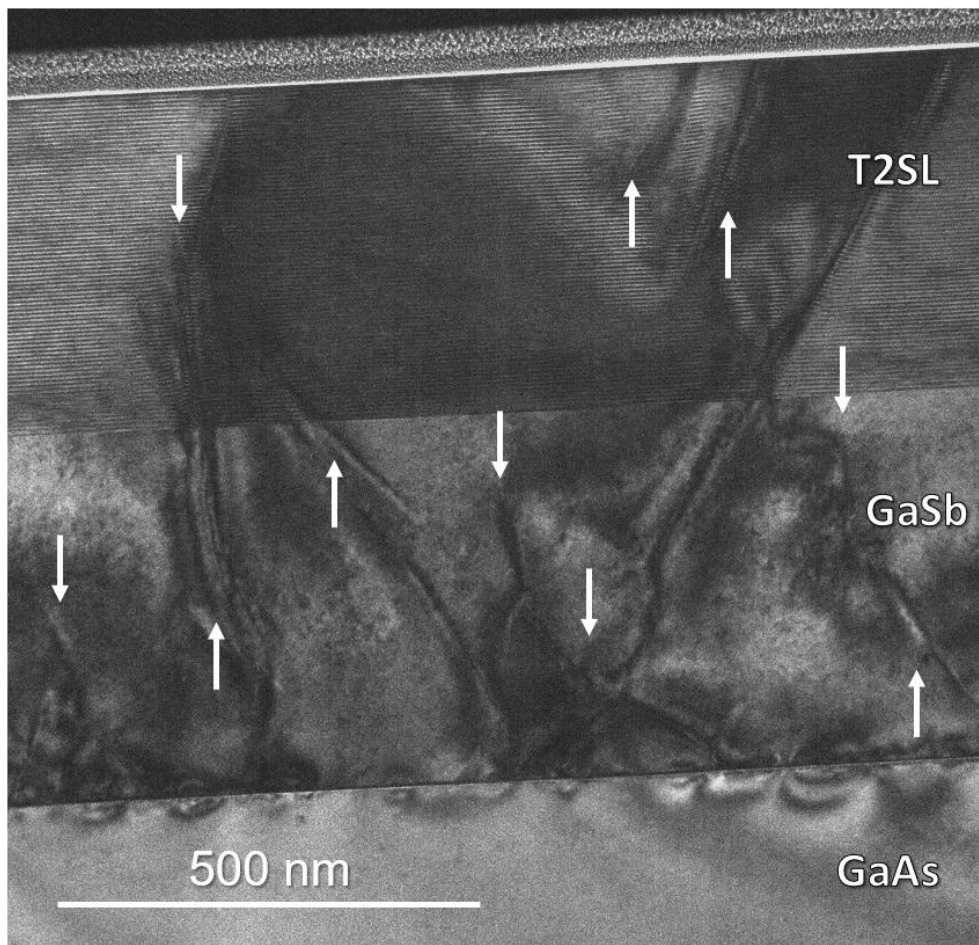


Figure 5.5: Two-beam, bright-field diffraction contrast TEM micrograph of the whole structure of Sample G. The white arrows highlight threading dislocations.

To better inspect the SL layers themselves, HRTEM was performed on each sample in regions far from any evident dislocations, as shown in Figure 5.6. These micrographs show that neither SL appears particularly rough and the transitions between InAs and GaSb regions are at least somewhat evident. The InAs and GaSb layer thicknesses are measured from each micrograph and displayed in Figure 5.6. The interfacial InSb layers were not visible in the micrographs and could not be accurately measured as their theoretical thickness (0.36 nm) is close to the resolution of the set up (0.25 nm). The InAs layer thicknesses are close to their theoretical value of about 3.6 nm for both samples but more so for Sample B. More deviation is observed for the GaSb layer thicknesses with a theoretical value of about 1.2 nm. However, it should be noted that it is difficult to identify the precise position of the IFs because the InSb layer is not well resolved spatially, and some roughness of the IFs is evident in both samples. This could possibly explain the deviation between the measured and theoretical period thickness observed with XRD measurements. Figure 5.6 also shows the SL layers of Sample G are less well defined than those of Sample B, even in regions free of evident lattice defects. This is attributed to presence of a mechanical strain, arising from the propagating defects, that leads to increased atomic intermixing¹⁹⁶.

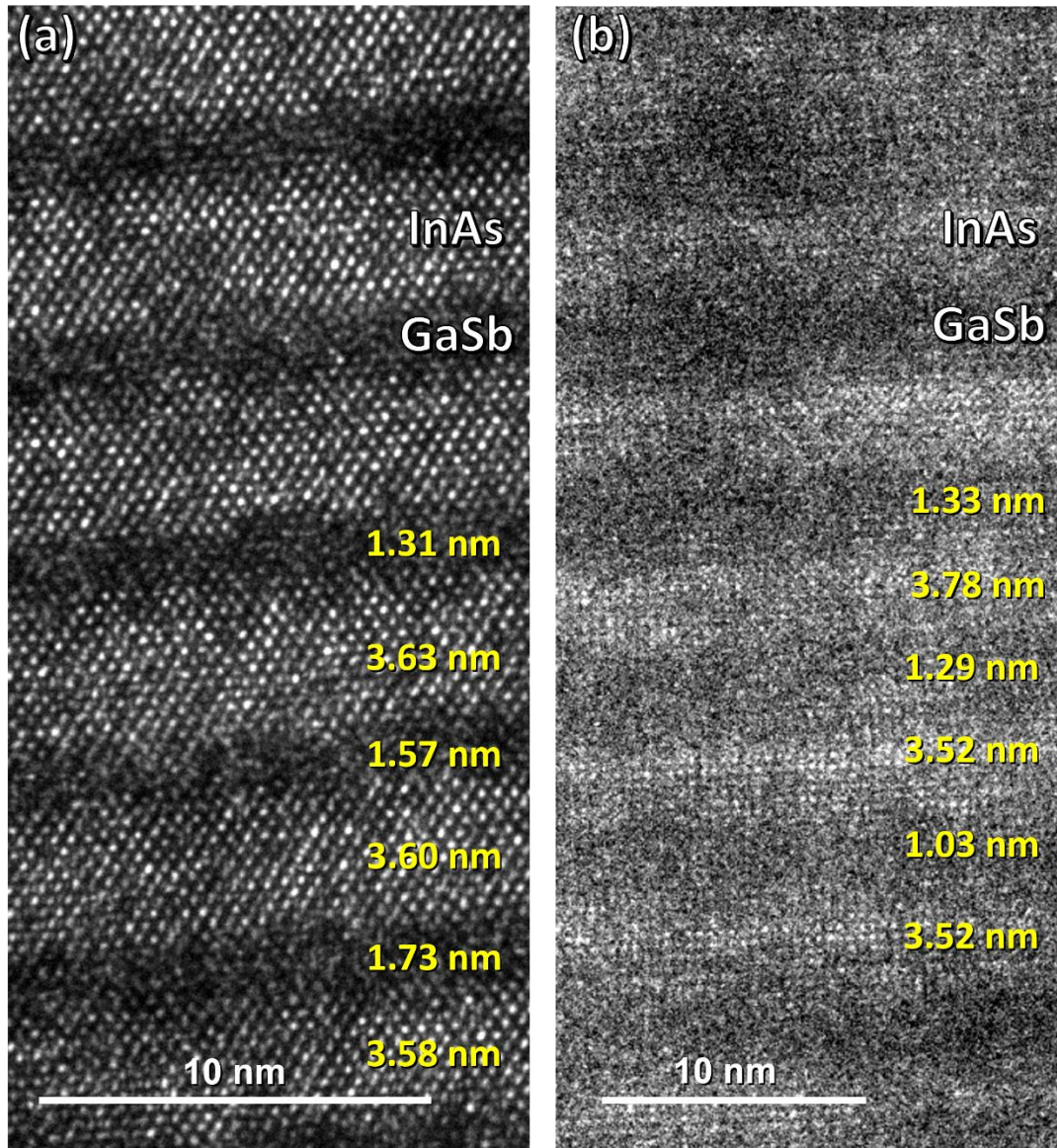


Figure 5.6: HRTEM micrographs of the T2SL layers of (a) Sample B and (b) Sample G.

To further investigate the IMF array itself, a low magnification CTEM micrograph was taken at the GaSb-on-GaAs IF, as shown in Figure 5.7a. In this micrograph, the IMF array merely appears as a dark line (labelled IF) separating the GaSb and GaAs regions. HRTEM was therefore used to obtain a higher magnification micrograph, as shown in Figure 5.7b, in which an array of dark, circular features (highlighted with red arrows) is visible along the IF. The periodicity of these features is suggestive of IMF array formation.

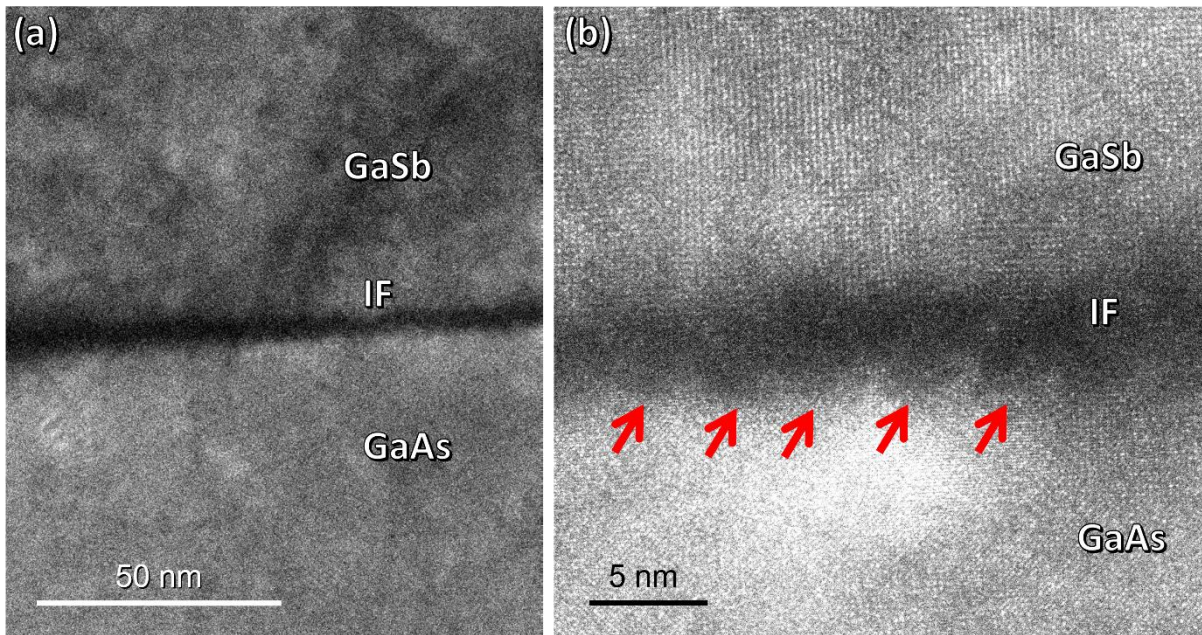


Figure 5.7: The GaSb-on-GaAs IF of Sample G as observed by (a) CTEM and (b) HRTEM. The red arrows highlight the periodic dark circles.

FFT filtering of the interfacial region shown in Figure 5.7b was performed and shown in Figure 5.8. The red arrows in Figure 5.8b-e highlight the half-planes¹⁹⁷ that are parallel to the growth direction and are mostly linearly distributed along the IF. These half planes, which can be associated with the presence of pure edge dislocations, verify the presence of the misfit dislocations that constitute the IMF array. The periodicity of these dislocations roughly agrees with the expected periodicity of the IMF array, although a statistical study has not been carried out. By considering Figures 5.7 and 5.8 together, it can be concluded that the IMF array has been successfully grown.

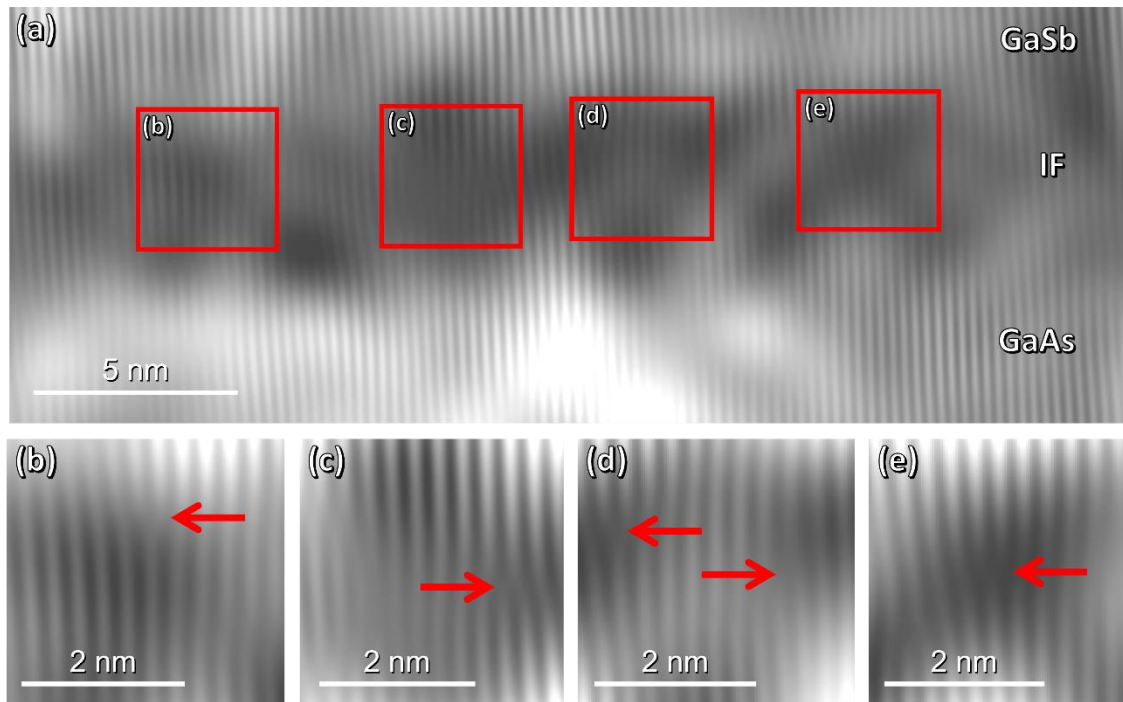


Figure 5.8: (a) FFT filtered image of Figure 5.7b and (b) – (e) enlarged images of the indicated areas. Red arrows highlight half-planes.

EDX under STEM conditions was carried out to analyse the chemical composition of the T2SLs to determine the extent of intermixing and segregation phenomena present. Figure 5.9 shows EDX maps and filtered profiles for In, As, Ga, and Sb in Samples B and G. For Sample G, EDX characterisations were performed for regions with no evident lattice defects. A prima facie examination of the EDX maps suggests that each element is predominantly present in the expected region, confirming the successful growth of InAs/GaSb T2SLs in both Samples B and G. The EDX profiles, given in Figures 5.9m and n for samples B and G respectively, shows that, though the layer thicknesses are relatively close to their expected values, the InAs and GaSb layer thicknesses are more uniform for Sample B than Sample G, as noted in Figure 5.6. This provides convincing evidence that the intermixing and segregation effects are more prevalent in Sample G, even in regions free of evident lattice defects, due to the increased defect-related strain. The presence of the intentional InSb IFs is also suggested from the overlapping signals of In and Sb, as highlighted in Figure 5.9m and n.

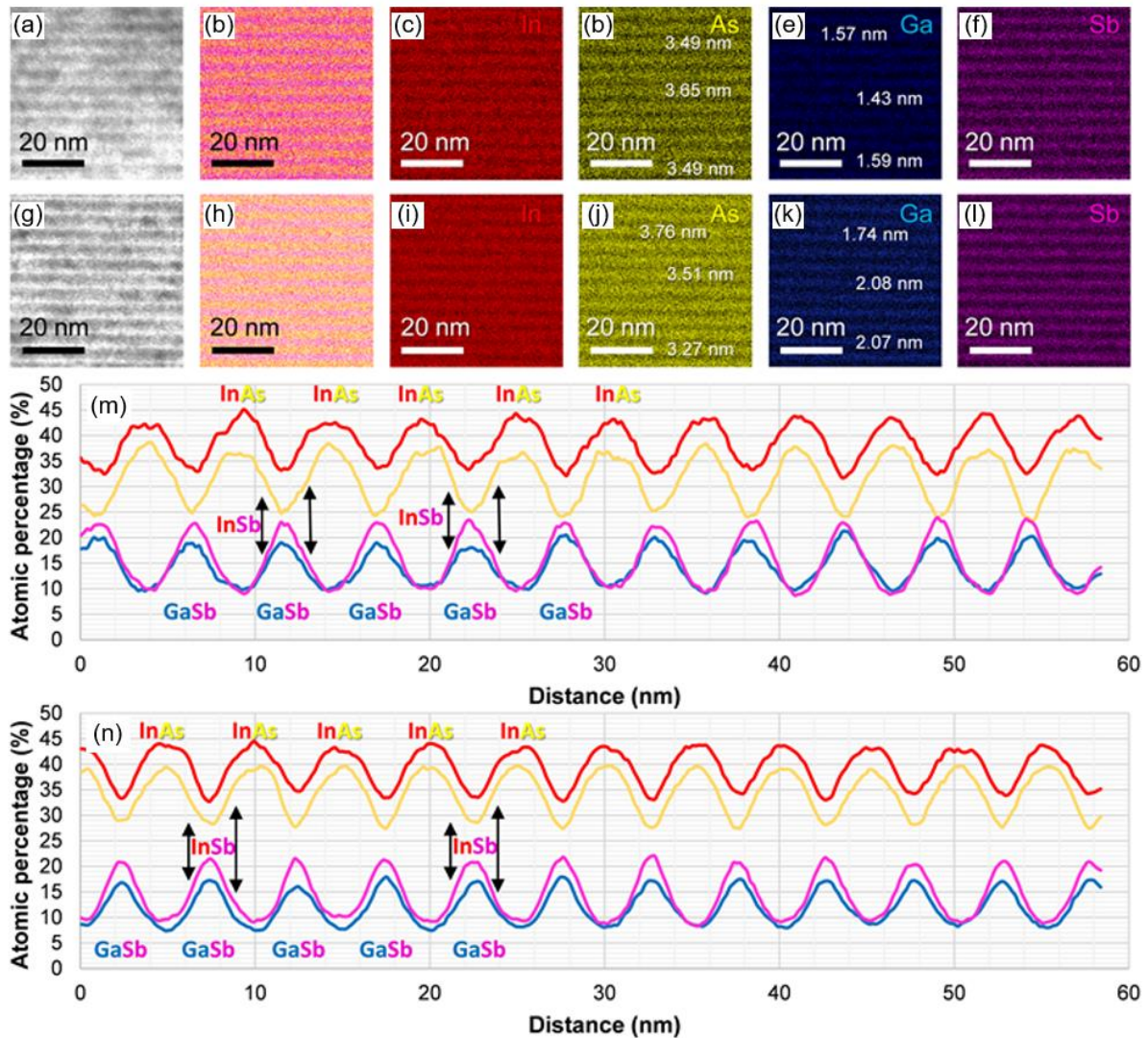


Figure 5.9: For (a) – (f) Samples B and (g) – (l) G and from left to right: STEM-HAADF image from a region around the middle layers of the T2SL, spectrum image combining atomic percentage maps by In, As, Ga, and Sb and individual maps for each element, including some thickness measurements. EDX integrated atomic percentage spectrum profiles registered from the bottom to the top of the mapped areas shown after filtering them, in (m) Sample B and (n) Sample G.

5.6. Photoluminescence

PL measurements were taken at 77 K for each sample and are shown, normalised, in Figure 5.10. The maximum intensity of Sample B (on GaSb substrate) is 8.5× greater than that of Sample G (on GaAs substrate). This likely results from the increased defect density, observed in Figure 5.4, as these defects can act as non-radiative recombination centres, provided they

are active within the energy gap. The peak energies of Samples B and G, when factoring for the thermal contribution ($k_B T/2$), are 0.128 eV and 0.119 eV respectively. This corresponds to the wavelength 10.22 μm and 11.04 μm respectively. The observed redshift in Sample G is surprising due to previous experimental studies^{198,199} which report a compressive strain-induced blue shift of the peak wavelength. The origin of this redshift is likely related to the difference in period thickness and composition, measured by XRD and TEM in Sections 5.3 and 5.5, as this can greatly affect the peak wavelength.

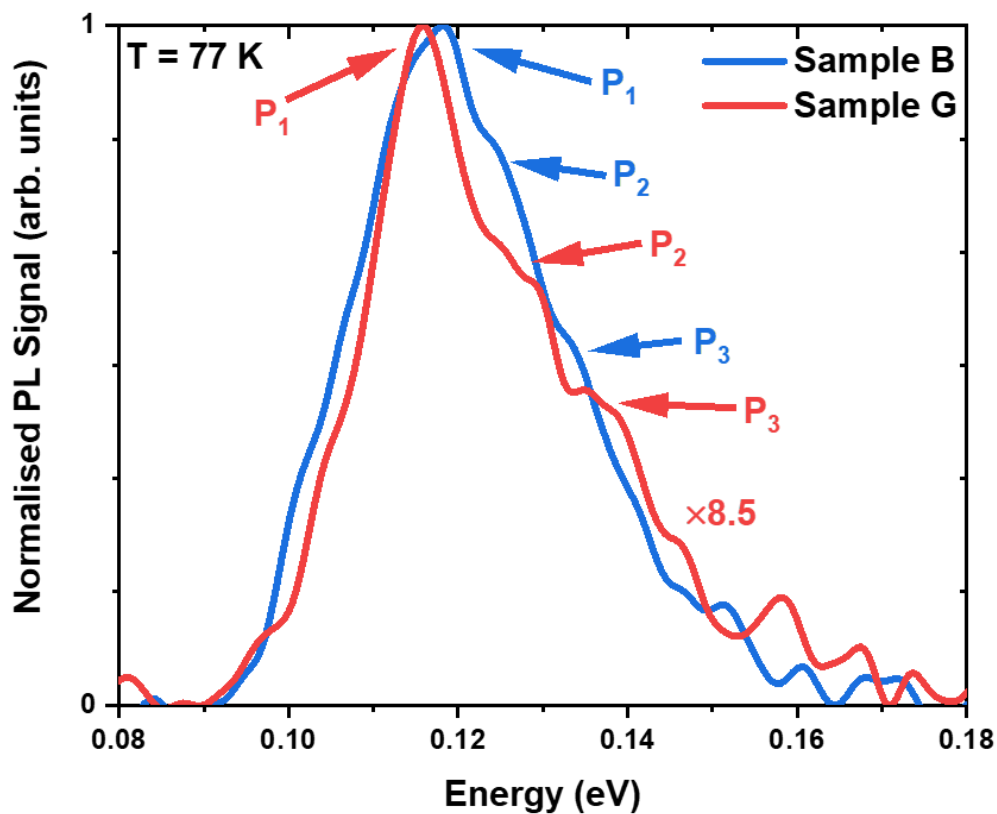


Figure 5.10: Normalised PL profiles at 77 K for Samples B and G. As indicated, the normalisation factor is around 8.5.

It is clear from Figure 5.10 that the PL profile does not consist of only one peak (e.g. Gaussian or Lorentzian) but multiple peaks. Most prominent are three peaks (P_1 , P_2 , and P_3 as labelled in Figure 5.10), evident in both samples, though the existence of further peaks is not precluded. These features were further examined using the FitYK software which was used to manually apply Gaussian approximations to fit the PL profiles as shown in Figure 5.11. It is argued that the largest peak, P_1 (related to Gauss 1 in Figure 5.11), corresponds to the primary

e_1 - hh_1 transition with an FWHM of 14 meV which is consistent with a previous report²⁰⁰. Gauss 2 and 3 were fitted to Peaks P_2 and P_3 respectively while Gauss 4 – 7 were added to ensure a good agreement between the measured profile and the resulting envelope function. The parameters used to fit Gauss 1-3 are given in Table 5.2.

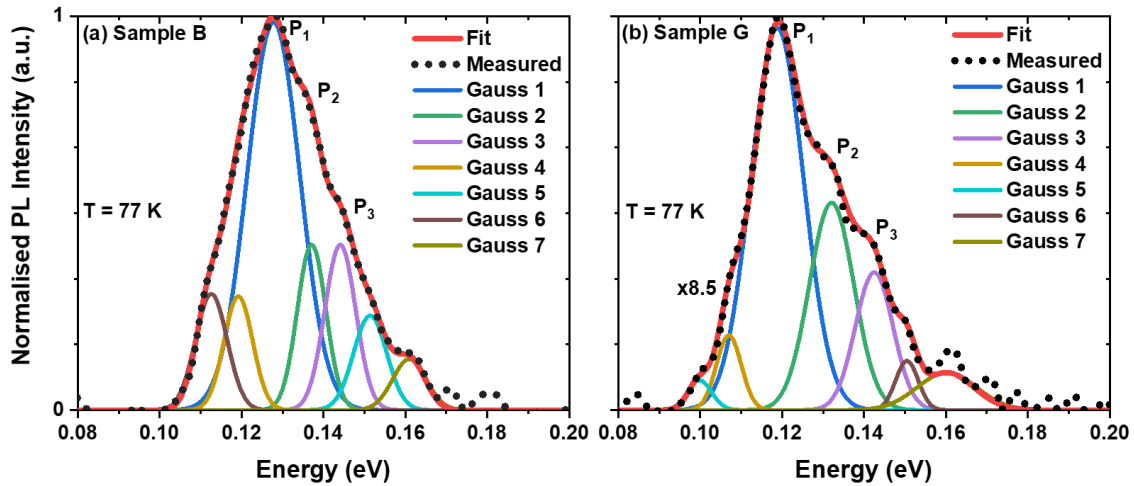


Figure 5.11: PL profiles at 77 K with fitted Gaussians and the envelope functions thereof for (a) Sample B and (b) Sample G.

Table 5.2: Parameters for peaks fitted to the PL profiles of Samples A and B.

Sample	Substrate	Peak	Centre (eV)	Height (arb. units)	FWHM (eV)
Sample B	GaSb	P_1	0.128	0.99	0.014
		P_2	0.137	0.42	0.008
		P_3	0.144	0.42	0.008
Sample G	GaAs	P_1	0.119	0.97	0.014
		P_2	0.132	0.53	0.012
		P_3	0.143	0.36	0.010

One possible explanation for the presence of peaks P₂ and P₃ is that they relate to transitions involving the second heavy hole or split-off bands. However, 8 band k.p simulation, shown in Figure 4.11, suggests that these transitions occur at energies too high to be consistent with those measured here by PL. A more likely explanation is provided by Weisbuch et al.²⁰¹ who proposed that growth islands of ~1 ML thickness can form at the interfaces of barriers and wells in multi-quantum well heterostructures. This gives rise to uncertainty in the well width which, when applied to the well-known equation for energy levels in an infinite quantum well, gives the following expression for the uncertainty:

$$\Delta E_1 = \Delta L_z \frac{h^2}{4m^*L_z^3}, \quad (5.1)$$

where ΔE_1 is the energy uncertainty, ΔL_z is the well width uncertainty, h is the Planck's constant, m^* is the effective mass and L_z is the well width. By taking the uncertainty in well width to be half the lattice constant and the effective mass to be a weighted average of the InAs and GaSb effective masses, the energy uncertainty can be calculated to be around 0.01 eV. This is in good agreement with the variation between Gauss 1, 2, and 3 (Table 5.2). The distance between successive peaks is larger for Sample G, suggesting the energy uncertainty is larger for this sample. This is in agreement with XRD and TEM measurements which indicate the period thickness, and therefore well width, is smaller for this sample which will increase the energy uncertainty. This result is supported by the findings of Kim et al.²⁰² who report a high level of intermixing at the IFs of Ga-containing T2SLs, particularly when an intentional InSb IF is grown, using APT and high-resolution (scanning) transmission electron microscopy (HR(S)TEM).

A possible explanation for the presence of Gauss 4-7 is the formation of sub-monolayer quantum dots (QDs) at the IFs as InGaSb QDs have been reported to emit in the LWIR.^{203,204} Furthermore, the growth kinetics are favourable for the preferential formation of InGaSb QDs due to the respective diffusion lengths of Ga and In. This may be the cause of the interfacial features observed by TEM in Figure 5.6, but this cannot be confirmed without higher resolution TEM.

The normalised PL spectra for each sample over the temperature range 77 K – 240 K is shown in Figure 5.12, where the normalisation factor is shown above each PL profile. The redshift in

the measured band gap energy observable in both samples is attributed to the thermal expansion of the lattice¹⁸².

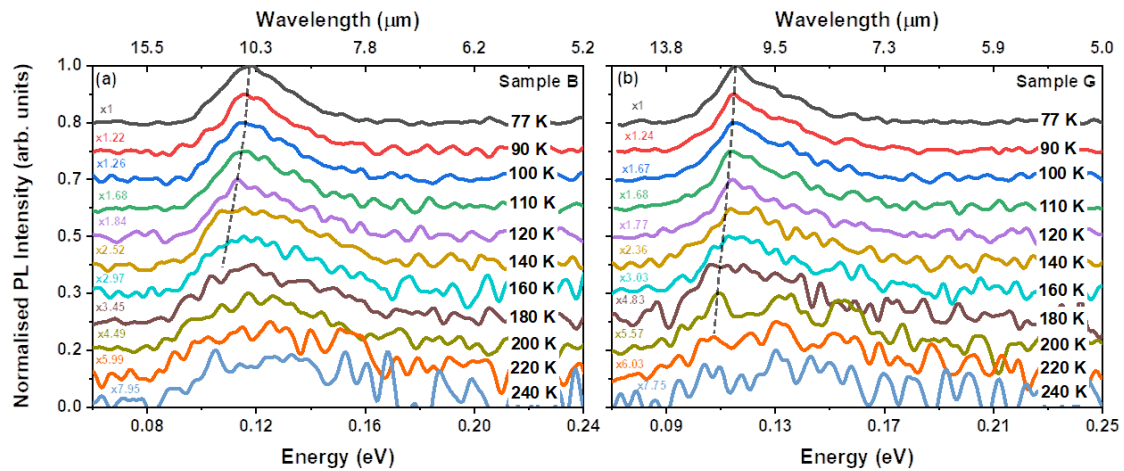


Figure 5.12: The normalised PL spectra for (a) Sample B and (b) Sample G from 77 K – 240 K.

The temperature dependant behaviour of the peak PL energy is examined further through use of Varshni analysis, shown in Figure 5.13. Equation (4.1) was used, as described in Section 4.2.3, and the Debye temperature, β , was again fixed at 270 K¹⁸². Here, the energy gap of the sample is usually taken at the point of maximum PL intensity but, in cases where multiple local maxima were present near the global maximum, the band gap energy was taken to be the average of these peaks on the assumption that these peaks are noise related. Due to the thermal noise present at high temperatures, shown in Figure 5.12, only the data from 77 K – 140 K was considered. It is clear from Figure 5.13 that the data from Sample B matches the fit much better than Sample G. This can be quantified by comparing the reduced chi squared values for each fit which are 7.93×10^{-9} and 1.98×10^{-7} for Samples B and G respectively. This can be attributed to the reduced PL intensity of Sample G which increases the difficulty with which important features can be distinguished from the noise. The energy band gap at $T = 0$ K was projected to be 0.118 eV and 0.115 eV for Samples B and G respectively. The damping constant, α , was measured to be 0.018 meV and 0.015 meV, respectively showing Sample B is slightly more sensitive to changes in temperature.

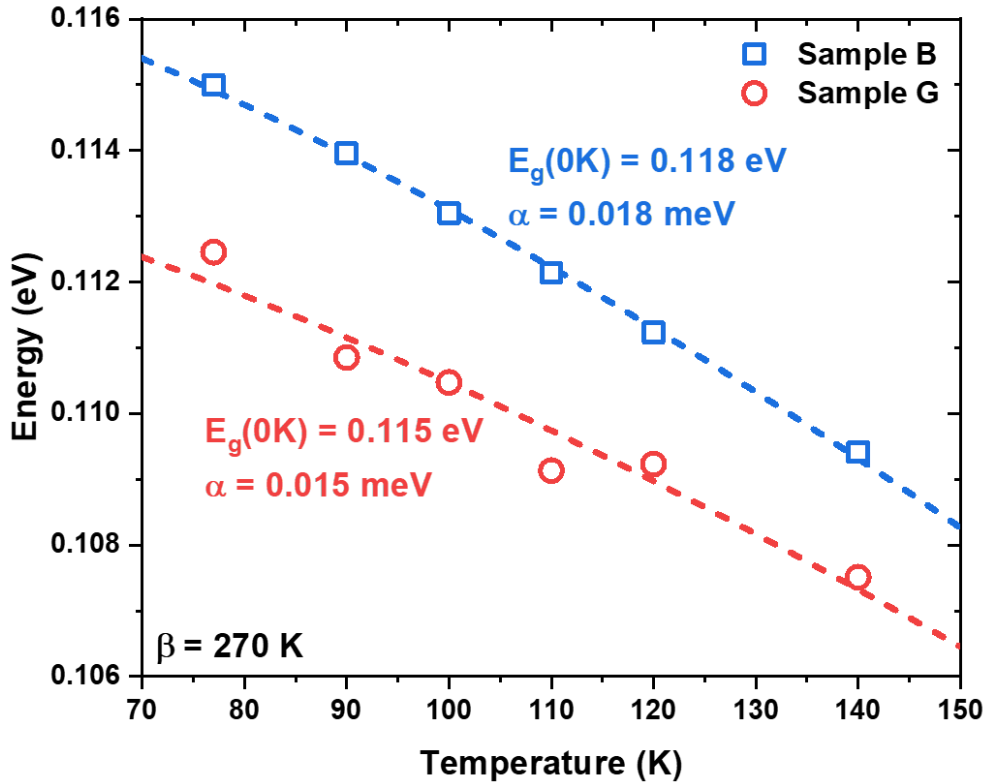


Figure 5.13: Measured energy band gap as a function of temperature and fitted Varshni equation for both samples.

The temperature dependence of the integrated PL intensity for both samples is shown in Figure 5.14. Due to the prominence of thermal noise at high temperatures, the gaussian approximation technique, shown in Figure 5.11, cannot be applied here. Only the integrated PL is considered on the assumption that secondary peaks and thermal noise will not greatly obscure the results. Consequently, these measurements should only be considered as useful for discerning trends and not for extracting parameters. The rate of thermal quenching was largest for Sample G. The cause of the thermal quenching may be related to material defects in the SL, as suggested by TEM measurements, or thermal escape of excitons from the electron miniband to the conduction band of InSb which then recombine non-radiatively¹⁸³. Further PL investigations at lower temperatures, in combination with Gaussian approximation, could be used for reliable extraction of the activation energies of the non-radiative recombination mechanism.

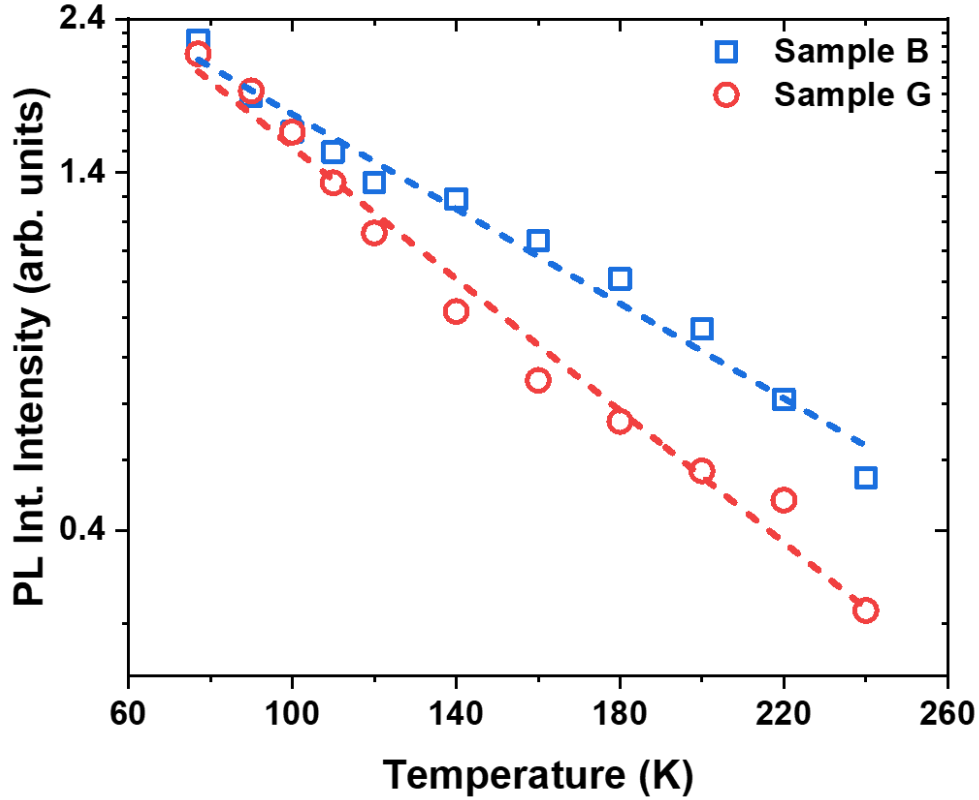


Figure 5.14: Integrated PL intensity as a function of temperature for Samples B and G.

The FWHMs of both SL samples are shown, as a function of temperature, in Figure 5.15. In Figure 5.15a, no fitting technique is used such that both noise and secondary PL peaks will influence the data. In Figure 5.15b, a Voigt fitting technique is used which will mitigate the influence of noise but not additional peaks. Unfortunately, as discussed above, Gaussian approximation is not possible due to the prevalence of thermal noise at higher temperatures. As described in Section 4.2.3, Equation 4.4 was used to model the inhomogeneous and temperature-dependant homogeneous broadening. The extracted parameters are given in Table 5.3. The data collected using the Voigt fitting appears in much better agreement with the fit than that collected without any fitting and is therefore considered here. Table 5.3 shows a considerable difference in the E_{LO} which may be attributed to the difference in composition between the two samples suggested by Figure 5.9. The larger exciton-phonon coupling, Γ_c , in Sample G supports this explanation as this interaction is centred around the IFs of the SL. Sample G shows the largest inhomogeneous broadening, Γ_i , which, as this broadening is related to fluctuations in well width¹⁸³, corroborates XRD and TEM measurements suggesting reduced material homogeneity in this sample. However, due to the

considerable uncertainty involved with measuring the FWHM of both samples, the parameters extracted by these measurements should only be considered as a corroboration to other techniques.

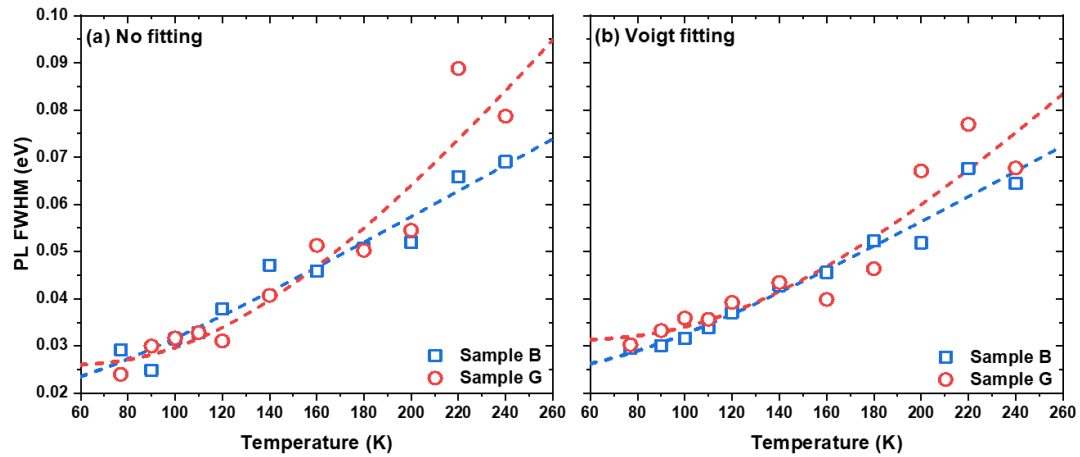


Figure 5.15: PL FWHM vs temperature for Samples B and G as determined by (a) no fitting and (b) Voigt fitting.

Table 5.3: Parameters extracted from PL FWHM analysis for both samples.

Samples	Substrate	No fitting			Voigt fitting		
		Γ_i	Γ_c	E_{Lo} (meV)	Γ_i	Γ_c	E_{Lo} (meV)
Sample B	GaSb	0.0202	0.0464	0.0140	0.0246	0.0636	19.0
Sample G	GaAs	0.0258	0.303	0.0377	0.0312	0.236	38.2

Figure 5.16 shows the integrated PL intensity of both T2SL samples as a function of laser power. The peak fitting method, described above, was used to consider only the e_1-hh_1 peak. Equation 5.2 was used to determine the dominant recombination mechanism in each sample:

$$P_{PL} = A_{PL}(L_{PL})^{1/2} + B_{PL} \cdot L_{PL} + C_{PL}(L_{PL})^{3/2}, \quad (5.2)$$

where P_{PL} is the pump power, L_{PL} is the integrated signal over energy, and A_{PL} , B_{PL} , and C_{PL} are fitting parameters. The first, second, and third terms in Equation 5.2 correspond to the SRH, radiative, and Auger processes respectively. From the powers in Equation 5.2 and the linear dependence on pump power in Figure 5.16, it can be seen that both T2SL samples are dominated by radiative recombination. Due to the level of noise associated with these PL measurements, the SRH and Auger coefficients cannot be calculated here with a sufficient degree of certainty. An informative future study would be to perform these measurements at lower temperature for reliable extraction of these coefficients. Furthermore, the doping concentration, δ_p , has a significant effect on the radiative ($\sim\delta_p$) and Auger ($\sim\delta_p^2$) recombination mechanisms^{72,76}. The doping calibration of the MBE reactor was performed prior to the growth of all samples. In Chapter 4, the doping concentration of a similar 12/4 SL sample on GaSb (Sample F) was measured, through C-V, to be $1.3 \times 10^{15} \text{ cm}^{-3}$. As this sample was grown under the same growth conditions as the T2SLs in the present study, a similar doping concentration is assumed here. However, direct measurement of the doping concentration, for example through Hall measurements, would be informative for a future study.

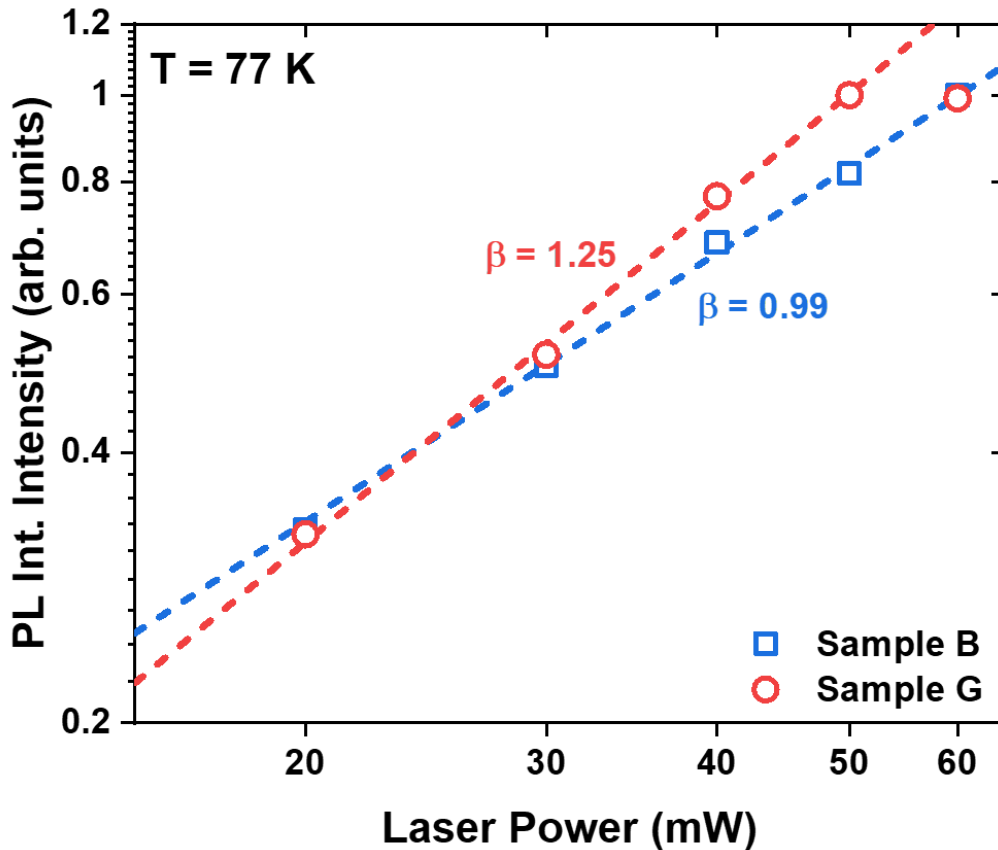


Figure 5.16: Integrated PL intensity as a function of the power of the pump laser for Samples B and G.

The influence of PL spot position along the sample surface on the extracted PL profiles was examined to measure the optical uniformity of each sample. 77 K PL mapping was performed at different points along the sample surface of each sample as shown in Figure 5.17. Sample B is an approximately 10 mm × 10 mm square while the straight edges of Sample G measure approximately 15 mm by 10 mm. Figure 5.17 shows that the optical behaviour of Sample B is largely independent of position, but Sample G shows a considerable variation in both the shape of the PL profile and the maximum intensity. The apparent optical nonuniformity of the T2SL is attributed to the increased defect density or reduced material homogeneity noted previously. It is also possible this arises from the disparity in thermal expansion of the GaSb and GaAs substrates²⁰⁵. Interestingly however, peaks P_1 , P_2 , and P_3 of both samples are still observable at positions which closely correlate with those observed in Figure 5.11.

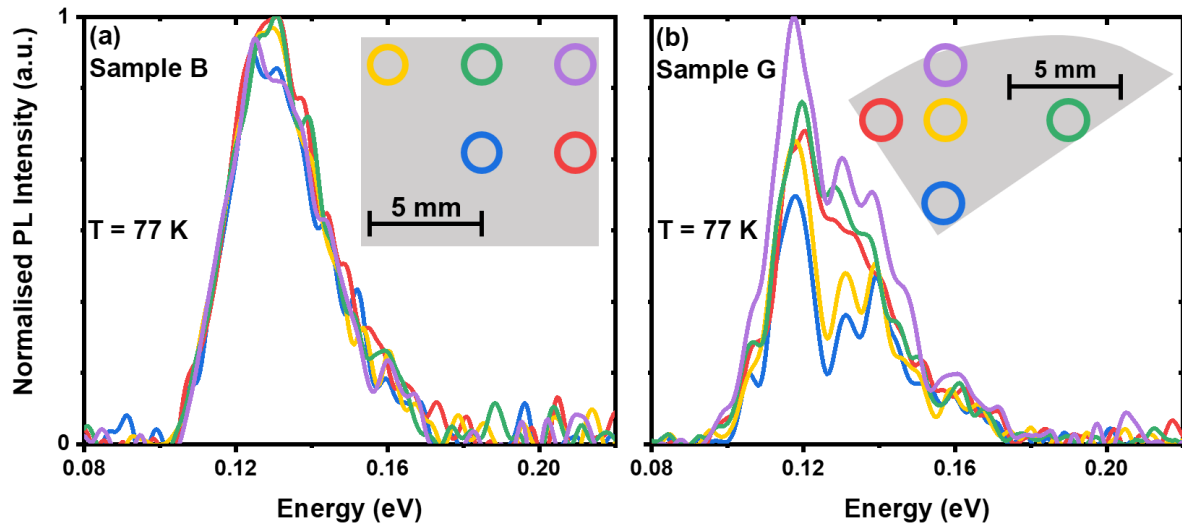


Figure 5.17: PL mapping for selected spots on (a) Sample B and (b) Sample G.

5.7. A PIN Diodes on GaAs

Following the growth of 12/4 PIN diodes on GaSb (Sample F) and GaAs (Sample H) substrates, XRD and PL characterisations were performed to determine whether the introduction of doping significantly alters the material and optical quality of the samples. This will also allow us to infer the extent to which observations made on the reference samples can be applied to the diodes.

Figure 5.18 shows the XRD rocking curves for Samples F and H with the extracted parameters in Table 5.4, in which the rocking curve for the sample on GaAs is offset by a factor of 10^3 for clarity. For comparison, the XRD parameters for Samples A and B are also given. The period thickness was extracted using the method described in Section 3.4.3.

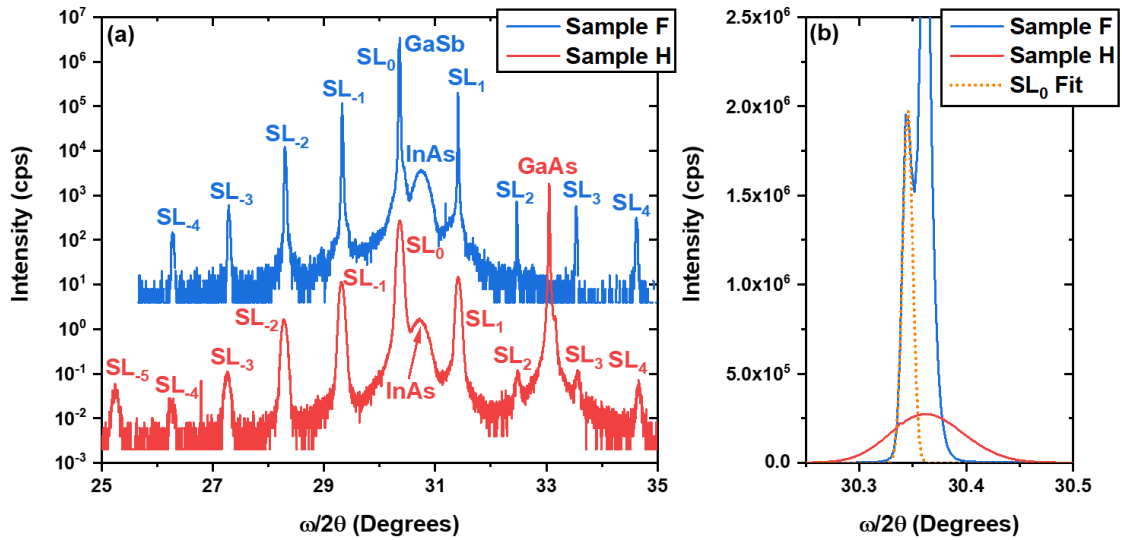


Figure 5.18: (a) XRD rocking curves and (b) an enhanced view of the SL_0 peak for both Samples F and H.

Table 5.4: Parameters extracted from XRD measurements for Samples A, B, C, and D.

Sample	Structure	Substrate	FWHM SL_{-1} (arcsec)	Period Thickness (nm)	Lattice mismatch (%)
Sample B	Reference	GaSb	60	5.17	-0.05
Sample G	Reference	GaAs	301	4.86	7.90
Sample F	PIN Diode	GaSb	53	4.91	0.05
Sample H	PIN Diode	GaAs	301	4.87	7.89

Table 5.4 shows the SL_{-1} FWHM, which represents the material homogeneity, of the diode samples has not been substantially altered by the addition of dopants in that the SL_{-1} FWHM of the T2SL on GaAs remains roughly a factor of five larger than that on GaSb. The period thickness and doping are both also largely unchanged. However, a slight change in the period thickness between Samples B and F appears to give rise to a slight change in the lattice

mismatch which is sufficient to change the strain from compressive to tensile. This may be attributed to the change in composition introduced by the doping impurities.

The PL profiles at 77 K of Samples F and H are shown in Figure 5.19. As was the case for the reference T2SLs, Figure 5.19 shows a notable reduction in PL intensity when compared to the sample grown on GaSb. By comparing Figures 5.19 and 5.10, it appears that the introduction of doping impurities is detrimental to the PL intensity of each sample. This is most clear by comparing Samples G and H because, while Sample G shows a clear PL peak at the correct wavelength (Figure 5.10), it is difficult to distinguish between the PL signal and the noise in the case of Sample H (Figure 5.19). A *prima facie* comparison of the PL profiles of Samples B and F appears to suggest this is also the case for the samples on GaSb. Unfortunately, however, a reliable quantitative comparison is not possible due to some minor modifications to the PL set up made between these measurements.

The XRD and PL comparisons presented above suggest that the effect of the GaAs substrate on the material and optical properties is the same for doped and undoped samples. It can therefore be argued that the phenomena observed in Sections 5.3 – 5.6 are applicable to the observations of the diode performance characterisation performed in this section.

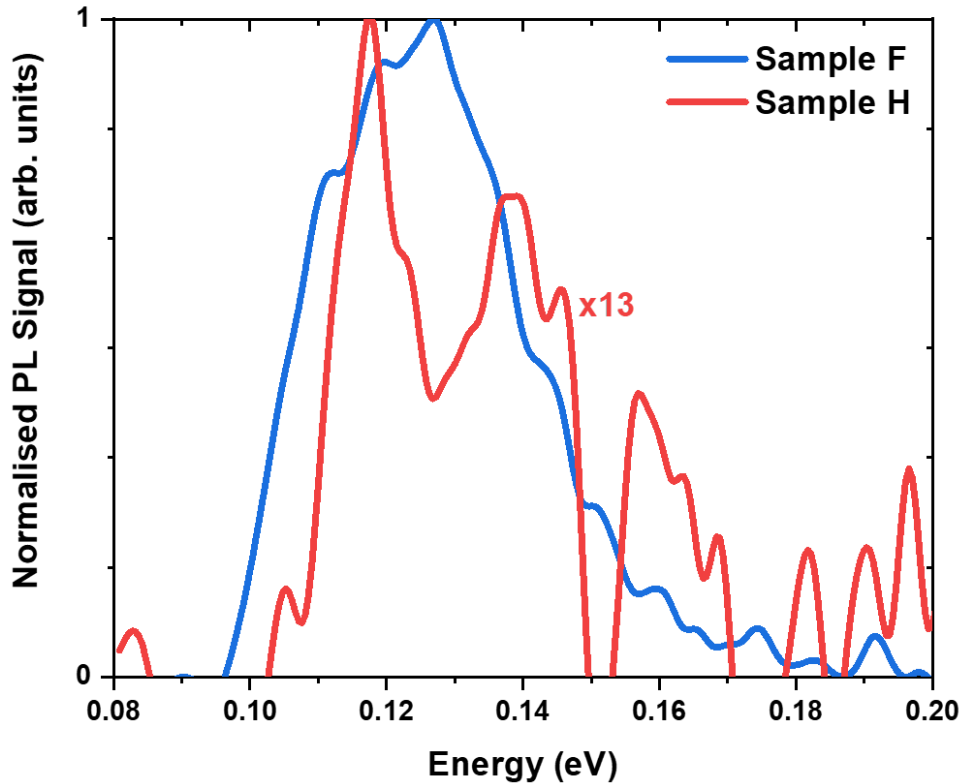


Figure 5.19: Normalised PL signal for Samples F and H. As indicated, the normalisation factor is around 13.

The temperature dependant I-V behaviour of Samples F and H (Figures 5.20a and b respectively) was performed to measure the device performance and determine limiting dark current mechanisms. As discussed in Section 4.3.5, the I-V profile of Sample F (the 12/4 diode on GaSb) shows the characteristic diode shape. Furthermore, as shown by the Arrhenius plot in Figure 5.20c, Sample F is dominated by diffusion currents at high temperature and G-R currents at lower temperature. As Figure 5.20b shows, the I-V profile of Sample H appears to be completely symmetrical. This suggests that the I-V profile simply represents some path of least resistance, described by Ohm's law, rather than a diode. Accordingly, the Arrhenius behaviour is not consistent with either diffusion or G-R dominant trends. Repeating the fabrication of these samples would have been informative for ruling out a fabrication error as the cause of the degradation in device performance. Unfortunately, due to the complete cancelation or slow pace of cleanroom operations due to various Covid-19 measures, this was not deemed a high priority use of resources.

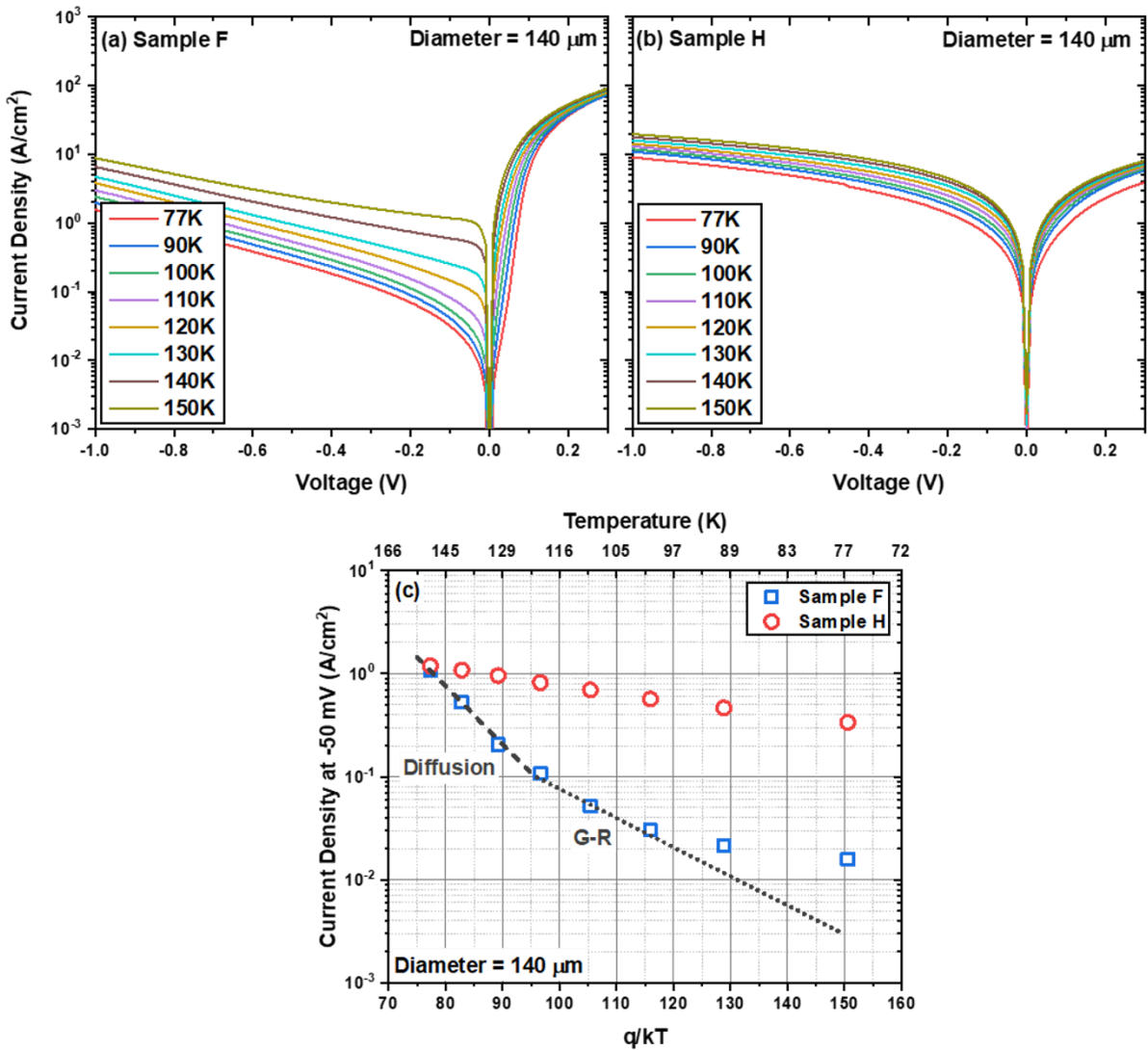


Figure 5.20: The I-V profiles for the temperature range 77 K – 150 K of a 140 μm diameter diode for (a) Sample F and (b) Sample H. (c) The corresponding Arrhenius for Samples F and H.

To further investigate the dark current in each device, the I-V fitting, described in Section 4.3.5, was carried out for Samples F and H (Figure 5.21). The analysis of Sample F, given in Section 4.3.5, is not repeated in detail here. Figure 5.21b shows that Sample H is almost entirely dominated by the shunt current, as suggested by Figure 5.20b and c. This suggests the reason the diode appears non-functioning is because the shunt current is sufficiently high to short the junction. At higher reverse bias, there appears to be an additional contribution from the TAT current. By comparing Figure 5.21a and b it can be seen the TAT current in Sample H is roughly a factor of four higher than in Sample F. This can be attributed to the

increased defect density in Sample H, observed by XRD, Nomarski, and TEM, as the TAT process occurs via mid-gap states arising from defects.

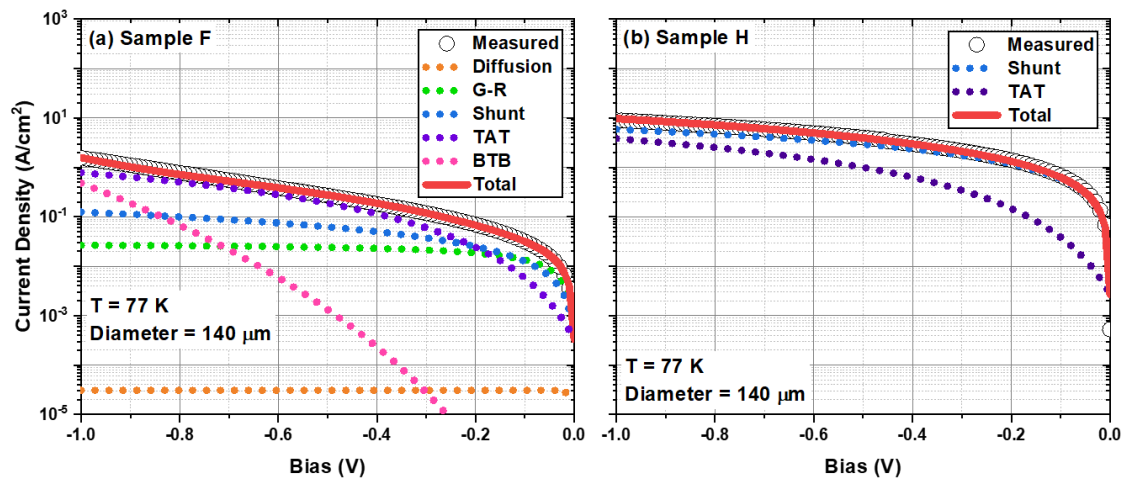


Figure 5.21: I-V profiles and fitting for a (a) Sample F and (b) Sample H for a 140 μm diameter diode at 77 K.

By only considering the reverse bias of Sample H, it is difficult to determine whether the diode is non-functioning or simply has a high shunt current. As Figure 5.22 shows, the forward bias of each sample was therefore analysed through fitting of the diode equation:

$$I = I_0 \left(e^{\frac{qV}{\eta kT}} - 1 \right), \quad (5.3)$$

where I is the net current flowing through the diode, I_0 is the saturation current, V is the applied bias, q is the electron charge, and η is the ideality factor. Here, the ideality factor takes a value between 1 and 2 and is a fitting parameter. The saturation current, I_0 , was also a fitting parameter. Figure 5.22a shows that, over the range of -0.1 V - 0 V, the ideality factor takes a constant value of around 1.82, within the expected range. By plotting the diode equation for $\eta = 1$ and $\eta = 2$ over the forward bias for Sample H, it can be seen that there is no agreement between the I-V profile and the diode equation. This suggests that the diodes from Sample H are indeed non-functioning and do not simply have a high shunt current.

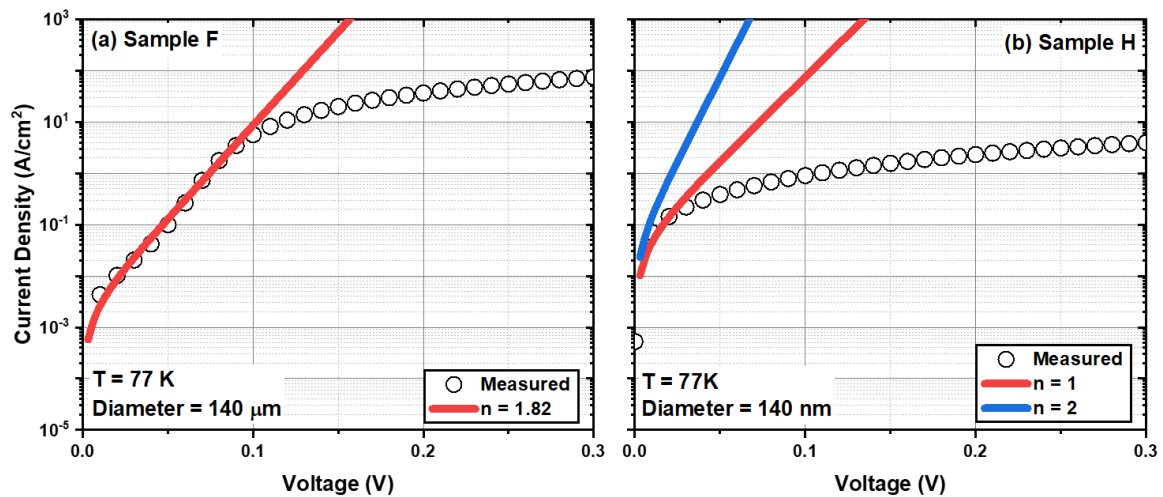


Figure 5.22: The forward bias and fitted diode equation for (a) Sample F and (b) Sample H.

As discussed above, the degradation in device performance can be attributed to the degradation in material quality revealed by XRD, Nomarski microscopy, and TEM. The degradation can greatly affect the bulk performance of our devices due to, for example, a reduction in the minority carrier lifetime or increase in defects contributing to SRH or TAT currents. However, this can also affect the surface currents due to the response of the altered material to the citric acid based wet etch. To determine whether this was the case, SEM micrographs of the etched mesa sidewalls are compared in Figure 5.23.

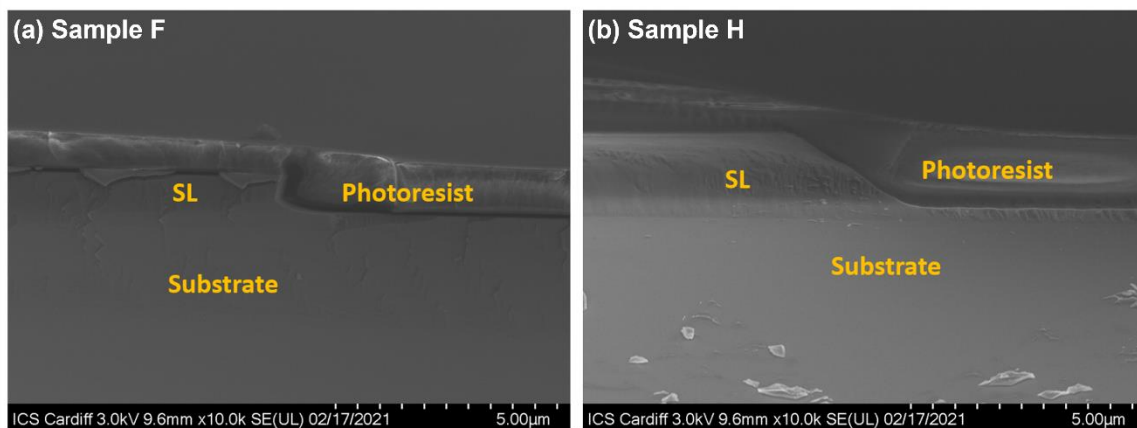


Figure 5.23: SEM micrographs of the mesa sidewalls of (a) Sample F and (b) Sample H.

The micrographs in Figure 5.23 were obtained by cleaving each sample to bisect one row of mesas. The samples were then mounted in the SEM with the cleaved edge facing the detector. The micrographs chosen are representative of those measured. However, only one cleave

plane was considered, which, due to the crystallographic nature of wet etches, may mean the sidewall profiles shown here are not representative of the whole of the mesa. Figure 5.23 shows that, for Sample F, the wet etch produces a near vertical sidewall but with a foot near the base of the sidewall. However, the sidewall of Sample H is roughly 45° and, if representative of the mesa, will have a much larger surface than that of Sample F. Given the identical design of SL region of each structure, it is surprising that the same etch should produce such drastically different etch profiles. This may be attributed to the composition and uniformity differences between T2SLs on GaSb and GaAs substrates noted in Chapter 5. In the presence of a strongly crystallographic etch, these differences can be expected to produce notably different etch profiles. Regardless, this may result in a larger surface-related contribution to the total dark current and further highlights the need for a dry etch, as discussed in Chapter 6.

5.8. Comparison of 12/4 and 14/7 T2SLs on GaAs

In Chapter 4, it was noted that the 12/4 SL was especially suited to HET applications due to increased absorption and lower effective masses. This section aims to determine whether these advantages are maintained when the structures are grown on GaAs substrates by growth and characterisation of 12/4 (Sample H) and 14/7 (Sample I) SL diodes on GaAs substrates.

Figure 5.24 shows the XRD rocking curves for Samples H and I with the extracted parameters shown in Table 5.5, in which the rocking curve for the sample on GaAs is offset by a factor of 10^3 for clarity.

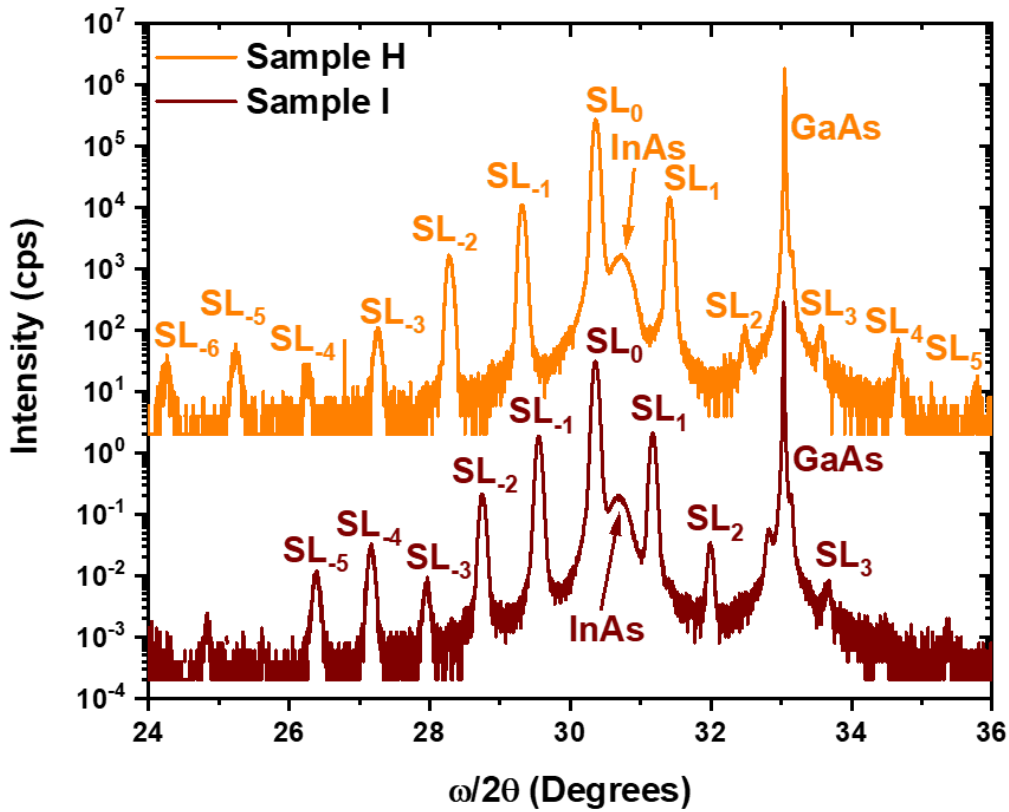


Figure 5.24: XRD rocking curves for Samples H and I.

Table 5.5: Parameters extracted from XRD measurements for Samples H and I.

Sample	SL Structure	FWHM SL ₁ (arcsec)	Period Thickness (nm)			Lattice mismatch (%)
			Expected	Measured	Error	
Sample H	12/4 SL	301	4.85	4.87	0.02	7.89
Sample I	14/7 SL	296	6.37	6.31	-0.06	7.88

Table 5.5 shows that Sample I has a slightly lower SL₁ FWHM than Sample H. It was also noted, in Section 4.2.2, that the 14/7 SL diode on GaSb (Sample E) had a lower SL₁ FWHM than the equivalent 12/4 structure (Sample F). These results suggest that the 14/7 SL has a slightly better material homogeneity than the 12/4 SL, regardless of whether the SL is grown on GaSb or GaAs. One possible explanation relates to the larger period thickness of the 14/7 SL which,

proportionately, will be less affected by fluctuations in composition or layer thickness. The period thickness and lattice mismatch are close to the expected values for both Samples D and E, as was the case for diodes on GaSb.

PL measurements at 77 K, shown in Figure 5.25, were performed for both Samples H and I. No normalisation was used such that the relative magnitudes of the PL peaks can be accurately compared. The maximum PL intensity for Samples H and I was 0.109 arb. units and 0.104 arb. units respectively. This corroborates the findings of Chapter 4 in which the 12/4 SL was found to have superior optical properties compared to the 14/7 SL due to the increased wavefunction overlap. However, as the peak intensities of Samples H and I are very similar, it is unclear if this trend is continued in T2SL diodes on GaAs. Furthermore, the evident noise in PL profiles of both samples, particularly Sample H, is too large to draw a firm conclusion on the max PL intensity. The extracted peak wavelengths of Samples H and I are 10.84 μm and 10.76 μm respectively, both of which are close to both the intended 10 μm and simulated wavelengths. However, it can be noted that, for the T2SLs on GaAs, the 12/4 SL has the higher cut-off wavelength whereas the opposite is the case for the T2SLs on GaSb (see Table 4.6). This can be attributed to a slight change in growth rates and layer thicknesses.

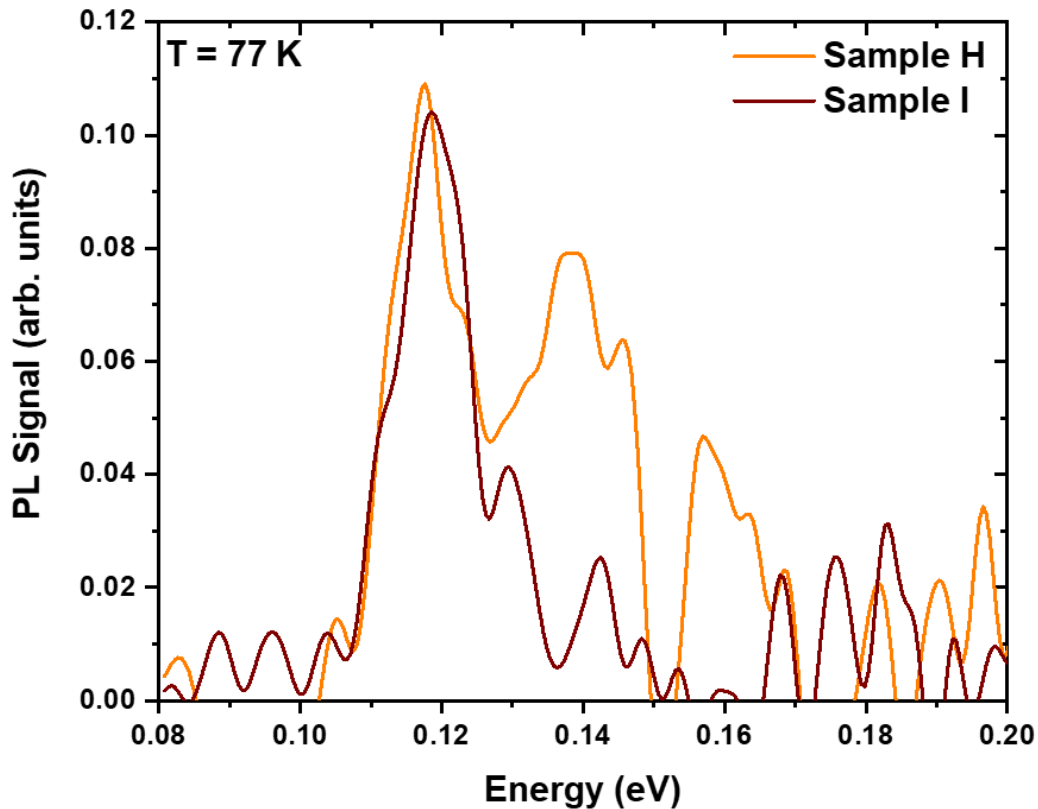


Figure 5.25: PL spectra at 77 K for Samples D and E.

I-V measurements were performed for Samples H and I over the temperature range 77 K – 150 K for circular diodes of 440 μm , 240 μm , 140 μm diameters. The I-V profiles and corresponding Arrhenius plots are shown in Figure 5.26. The temperature dependence trends, shown by the Arrhenius plots, is different for each sample and mesa diameter. This behaviour can be explained by assuming the shunt current is dominant at all temperatures, as is the case in Figure 5.21b. The shunt current arises due to both surface leakage currents and the dislocations in the material^{206,207} and therefore depends on many parameters such as band structure, resistivity, and the concentration and position of trap levels. It is therefore difficult to predict the how the relative magnitudes of the different shunt processes will change with temperature, as shown in Figures 5.26c, f, and i. Furthermore, the significant inhomogeneity of the samples on GaAs, as noted above, may mean the disparity is due to the position of the device rather than its diameter. However, this was mitigated through choosing to measure devices next to one another.

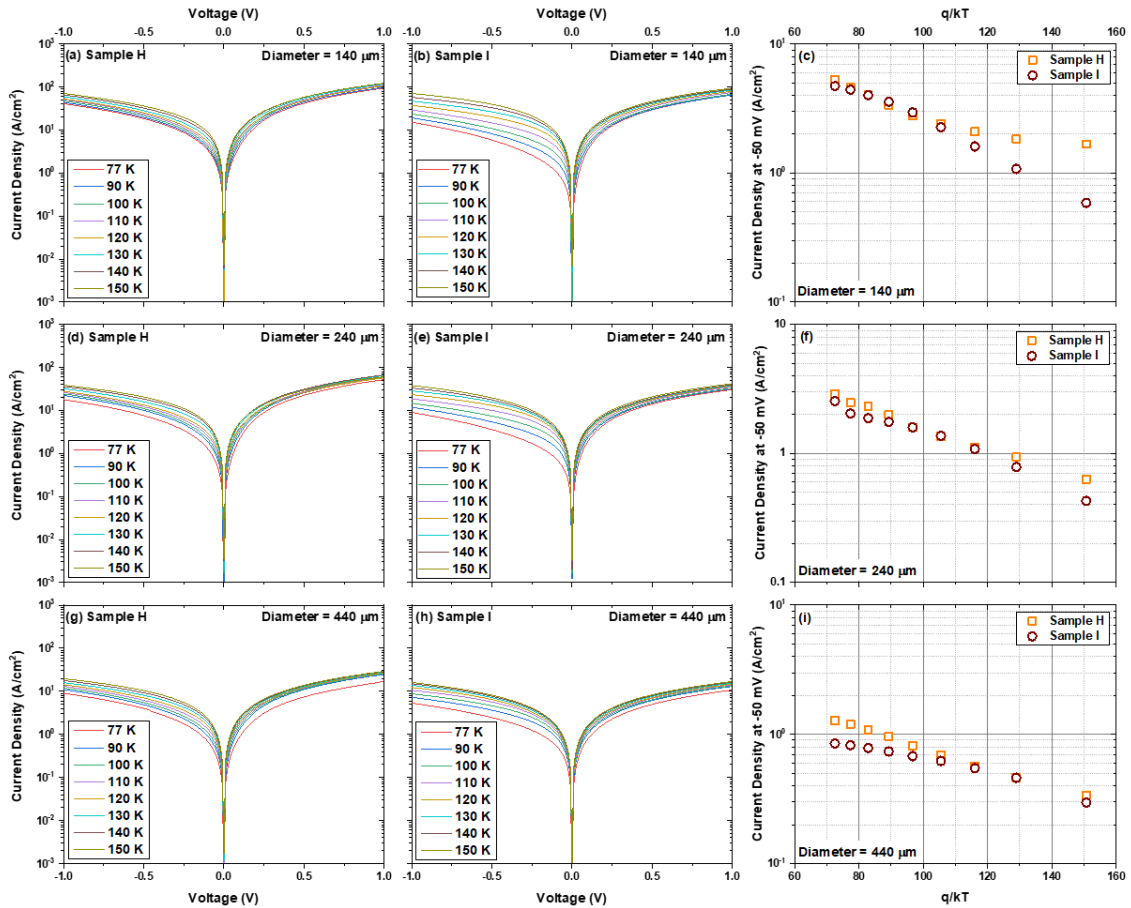


Figure 5.26: The I-V profile over the temperature range 77 K – 150 K for (a) a 440 μm 12/4 T2SL diode, (b) a 440 μm 14/7 T2SL diode, (d) a 240 μm 12/4 T2SL diode, (e) a 240 μm 14/7 T2SL diode, (g) a 140 μm 12/4 T2SL diode, and (h) a 140 μm 14/7 T2SL diode. Figures (c), (f), and (i) show the Arrhenius plots of 440 μm , 240 μm , and 140 μm diameter diodes respectively.

By plotting the current density at -50 mV against the mesa diameter for both samples (Figure 5.27), it is clear that the devices with larger mesa diameters have lower dark currents. As shunt currents dominate in both devices, this behaviour can be explained by the presence of surface-related currents which have a greater effect on smaller diode due to their proportionally larger surface. This can be checked by plotting the current density as a function of the perimeter/area for many devices on each sample (Figure 5.28). Figure 5.28 shows only a moderate dependence of the current density on the perimeter/area of the diodes which is attributed to the inhomogeneity of the samples obscuring the trend. This inhomogeneity can

be seen by noting the variation in current density at -50 mV for devices of the same diameter on the same sample, though this is more pronounced in Sample H.

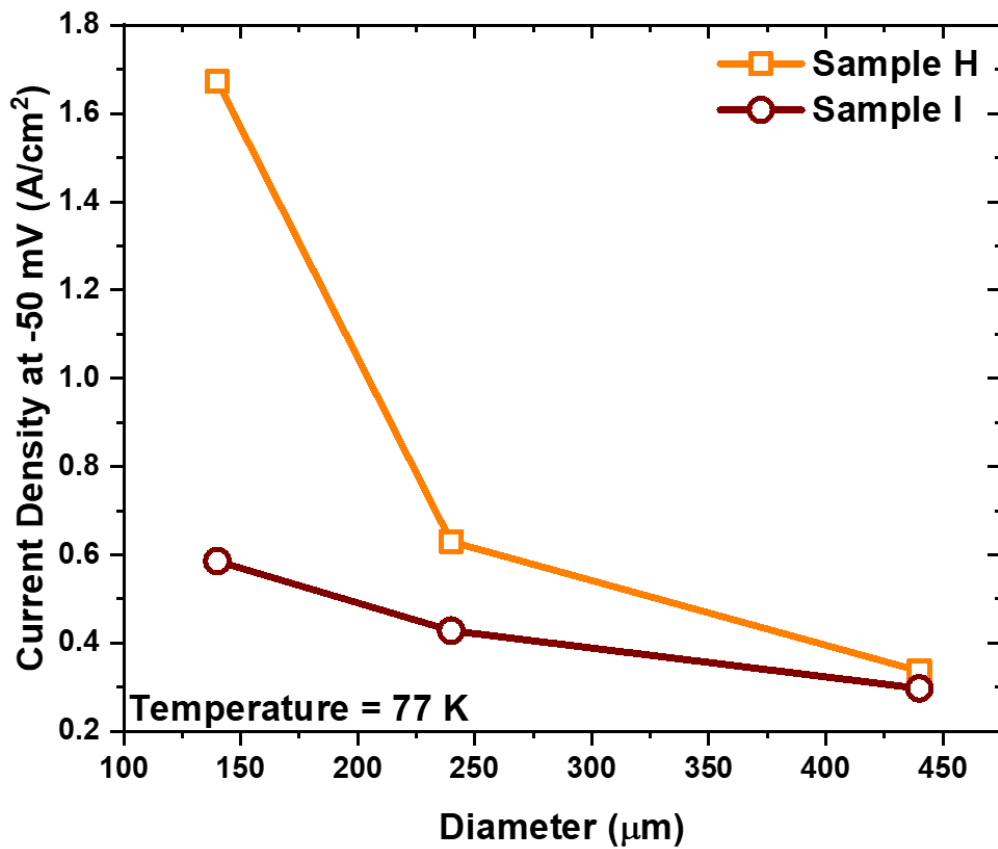


Figure 5.27: Dark current density at -50 mV as a function of device diameter for Samples H and I.

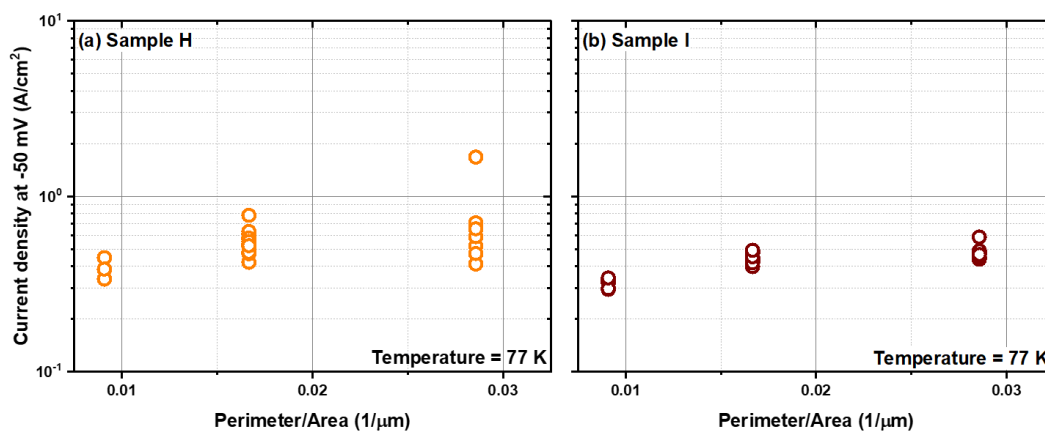


Figure 5.28: The measured current density at -50 mV at 77 K as a function of the Perimeter/Area for (a) Sample H and (b) Sample I.

Figure 5.27 also shows that Sample I has a superior dark current to Sample H which becomes more pronounced as the device diameter decreases. This corroborates I-V measurements on T2SL diodes on GaSb, discussed in Section 4.3.5, which show the low temperature performance of the 12/4 SL diode was worse than that of the 14/7 SL. By considering the Arrhenius plots (Figure 4.22) and I-V fitting (Figure 4.24) it was argued that this was due to higher shunt currents. This corroboration of results on GaSb and GaAs suggests there is an intrinsic property of the 12/4 SL that increases prominence of the shunt current at low temperature. One possibility is that the 12/4 SL has a higher defect density than the 14/7 SL. This is supported by the XRD results which show that the 12/4 SL has a slightly larger SL_{-1} FWHM on both GaSb (Tables 4.2 and 4.6) and GaAs substrates (Tables 5.4 and 5.5). However, the difference in SL_{-1} FWHM is likely to be too marginal to wholly explain this trend. A more likely explanation relates to the different band structure of the 12/4 SL. As Table 4.4 shows, the conduction and valence bands of the 12/4 SL sit higher than those of the 14/7 SL. This may result in a larger proportion of the trap states in the 12/4 SL lying in the band gap and therefore contributing to the TAT process. Unfortunately, this hypothesis is difficult to confirm without performing a detailed study with deep level transient spectroscopy (DLTS) measurements and density functional theory (DFT) simulations. To further investigate the limiting mechanisms, I-V fitting was performed for both samples and all device diameters (Figure 5.29).

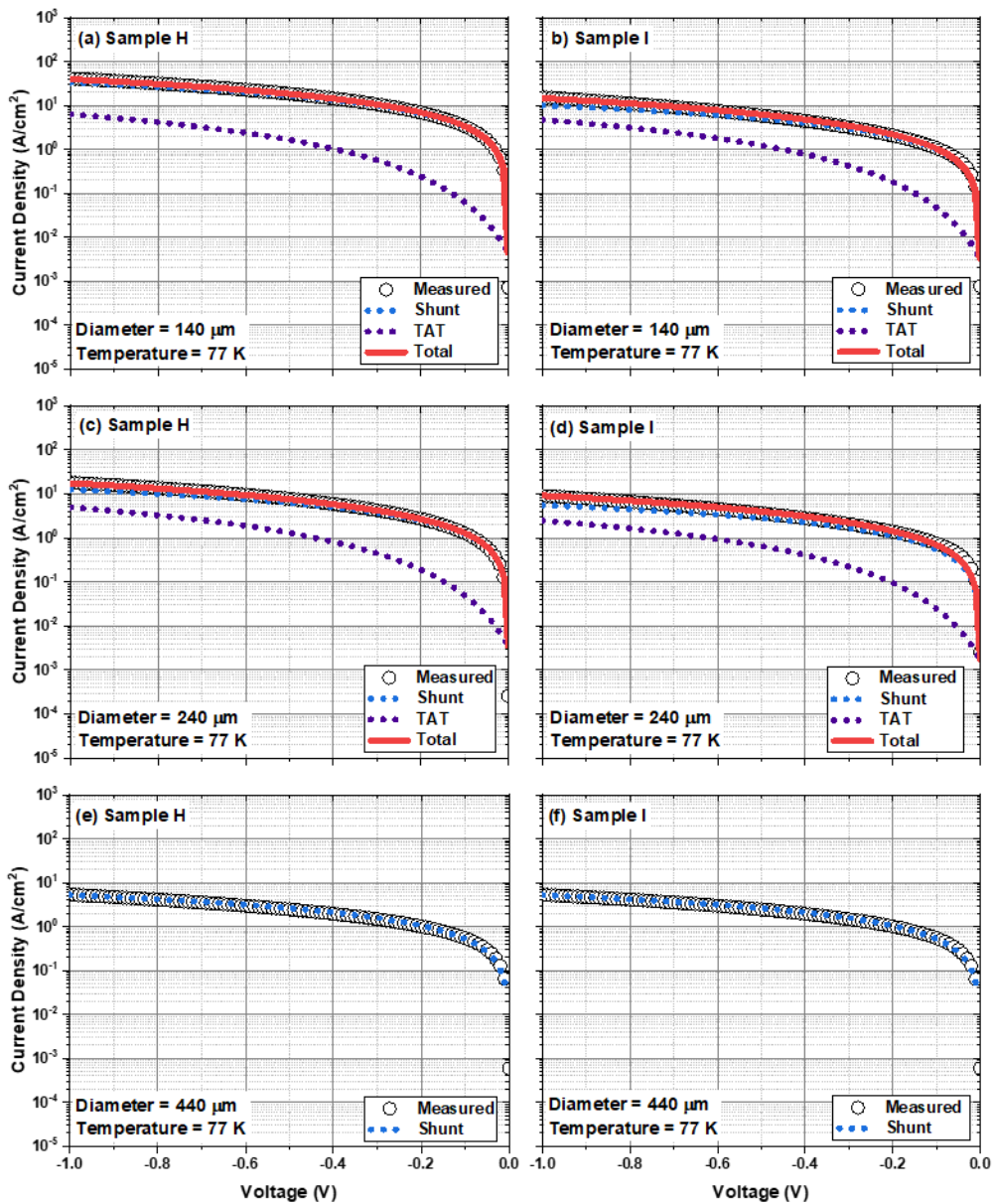


Figure 5.29: I-V profiles and fitting for a (a), (c), and (e) Sample H and (b), (d), and (f) Sample I for a 140 μm diameter diode at 77 K.

Figure 5.29 shows that both Samples H and I are dominated by shunt currents regardless of device diameter. Unfortunately, there is no measurable diffusion or G-R current in any of the devices. It is therefore difficult to determine whether the advantages of the 12/4 SL discussed previously are present when comparing devices on GaAs. However, TAT current is present for both samples for diameters of 140 μm and 240 μm though this is slightly lower in Sample I than Sample H. This is notable because, as discussed in Section 4.3.5, the lower effective

masses of Sample H (the 12/4 SL) should result in a lower TAT current. The increased TAT current is therefore attributed to a greater concentration of mid-gap trap states as described above.

To further investigate this hypothesis, Figure 5.30 plots the fitted values of the shunt and TAT currents at -50 mV as a function of device diameter. Figure 5.30a) shows the shunt current scales with increasing perimeter/area which confirms the surface related nature of the shunt current. The TAT current also appears to scale with increasing perimeter/area which suggests the TAT current is also largely surface related. This is because many trap states, used in the TAT process, arise from process contaminants or native oxides which are localised at the surface²⁰⁸.

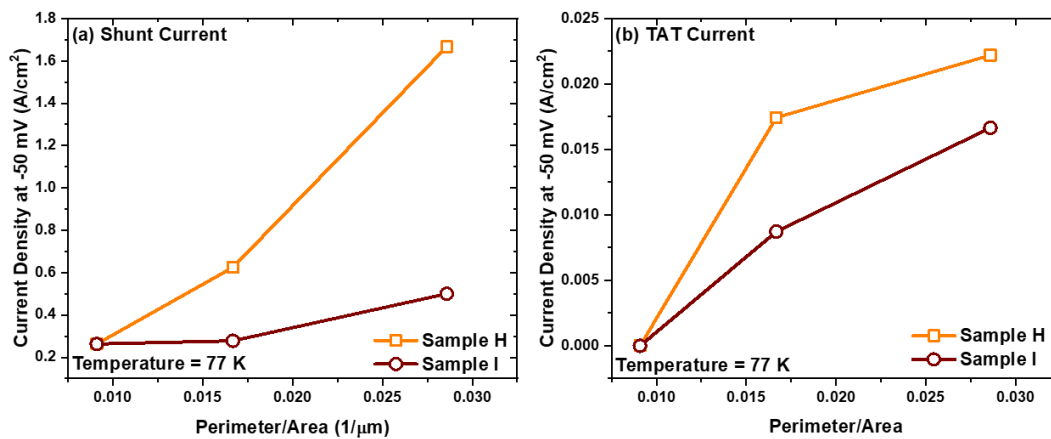


Figure 5.30: The (a) shunt and (b) TAT currents at -50 mV as a function of perimeter/area extracted from Figure 5.22 for Samples H and I.

These results suggest the 12/4 SL may be more sensitive to defects than the conventional 14/7 SL due to the position of the conduction and valence bands. The resulting increase in shunt and TAT currents would make the 12/4 SL on GaAs less suited to low temperature operation where these currents dominate. However, the 12/4 SL may still be appropriate for higher operating temperatures at which the diffusion current is dominant.

5.9. Summary

These results demonstrate the growth of 12/4 T2SLs on GaSb and GaAs substrates. In the latter case, the IMF array was used at the GaSb-on-GaAs IF to compensate for the 7.8% lattice mismatch. Material characterisations, including XRD, Nomarski microscopy, and TEM, were used to compare the structural quality of the two samples. Results suggest that the T2SL on GaAs suffers from a degraded material quality and homogeneity, despite the presence of the IMF array. TEM measurements suggest this originates from the presence of undesirable 60° dislocations at the GaSb-on-GaSb IF, in addition to the desirable 90° dislocations. These issues can be addressed through optimisation of the GaSb buffer layer growth and incorporation of additional strain compensation techniques.

PL measurements suggest the optical quality and uniformity of the T2SL on GaAs is degraded in a manner consistent with the degradation in material quality. This is attributed to the increased defect density which results in increased non-radiative recombination.

The growth, fabrication, and characterisation of 12/4 SL PIN diodes on GaSb and GaAs substrates have also been demonstrated, again using the IMF array. The I-V profile of the diode on GaAs is, unfortunately, not diode-like and this sample is therefore assumed to be non-functioning. I-V fitting suggests this is due to strong, defect related current paths on the mesa sidewalls of this device which short the junction. SEM micrographs, comparing the mesa sidewalls of both samples, suggest that this may partially be due to the effect of the citric acid based wet etch on the reduced material quality. A notable contribution from the TAT current was also observed through I-V fitting.

Following on from the results of Chapter 4, the 12/4 T2SL diode, described above, was compared to a 14/7 T2SL diode of the same design. It was found that, like the 12/4 SL diode, the 14/7 SL diode is dominated by shunt currents with some contribution from the TAT current. However, these currents were weaker in the 14/7 SL due to, it is argued, the different band structure of the 12/4 SL which makes it more sensitive to the defects that give rise to these dark current mechanisms. If this is the case, the 12/4 SL may be less appropriate for growth on GaAs substrates due to the increased defect density this incurs. However, at high

temperature, when diffusion current is dominant, the defect density and position of the trap levels is less relevant to the overall performance of the device.

6. Fabrication

As discussed in Section 2.2.3., the incorporation of dry etch and chemical passivation processes into the T2SL fabrication process is vital for the development of high-performance FPAs. Prior to this project, neither of these processes were developed for T2SLs in Cardiff. Instead, the more accessible processes of wet etching and photoresist protection were used. This chapter therefore details the development and characterisation of a dry etch process that will be effective for the fabrication LWIR T2SL detectors. A brief summary of the ongoing chemical passivation work is also provided.

6.1. Dry etching

This section firstly describes the development of the etch mask fabrication process and dry etch recipe. As these two elements were developed simultaneously, this account will be roughly chronological to best describe the reasons behind each development. Unfortunately, a design of experiments approach, in which one parameter at a time is varied until an optimum recipe is reached, could not be followed when developing the dry etch recipe due to the limited availability of SL samples. Instead, as described below, educated guesses were used to correct deficiencies at each stage. For clarity, the development of this process is summarised in Table 6.1.

Table 6.1: Summary of dry etching processes, recipes, and results.

Recipe	Process	Change compared to previous run	Reasons for changes	Results	
				Successes	Shortcomings
Recipe 1	Process 1			- Successful formation of micro trenches	- Rough floor and sidewalls - Significant undercut - Damage to Ni mask
Recipe 1	Process 3c	Used SiO ₂ mask instead of Ni	Reduce SiO ₂ damage by etching	- Much less damage to etch mask - Smoother sidewalls and floor	- Curved sidewall profile - Some roughness / striations on sidewalls - Inhomogeneity of sidewall profiles - Some damage to SiO ₂ etch mask
Recipe 3	Process 3c	Increase BCl ₃ /Ar ratio	Use more chemical etch to improve sidewall morphology	- Improved sidewall verticality - More homogeneous sidewall profiles	- Sidewall roughness/striations remain - Etch mask damage remains
Recipe 4	Process 3c	Reduce ICP power	Reduce damage to SiO ₂ etch mask	- Little or no change	- Little or no change
Recipe 5	Process 3c	Increase Ar flow rate	Encourage desorption of etch by products	- Slight improvement in morphology	- Striations and etch mask damage persist
Recipe 5	Process 3d	Used SiN etch mask instead of SiO ₂	Reduce etch mask damage with better quality material	- Less visible damage to etch mask - Fewer visible striations - Preserved good sidewall verticality	- Some sidewall roughness evident

6.1.1. Process and Recipe development

The first process (Process 1), shown schematically in Figure 6.1, involves the deposition of a Ni etch mask using the bilayer photoresist recipe described in Section 3.3. The thickness of the Ni layer was chosen to be 150 nm but this could be increased if necessary. After etching, the Ni etch mask was removed using a nitric acid based wet etch.

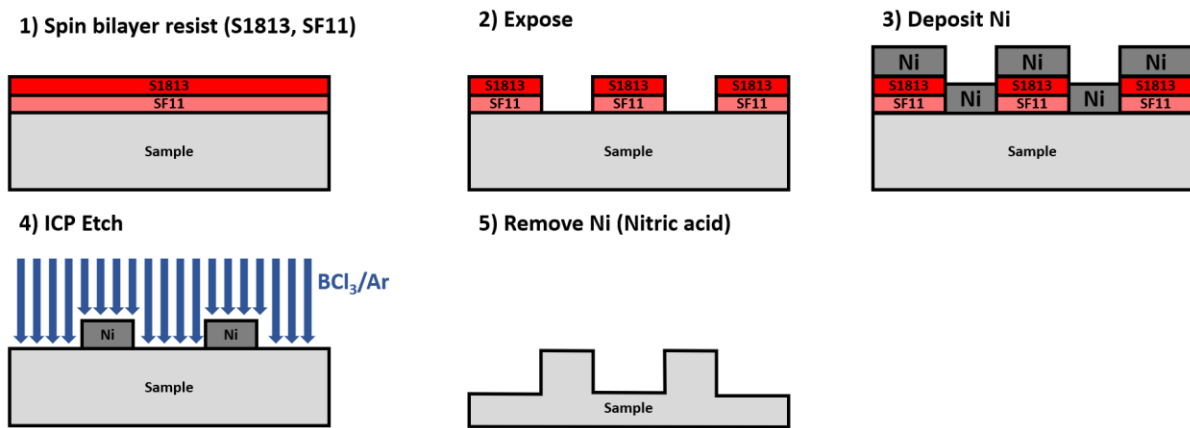


Figure 6.1: Schematic of the Ni etch mask process (Process 1).

The advantage of this process is its simplicity as it contains very few steps and can be completed in the ICS cleanroom. Metal etch masks have also been shown to be resistant to erosion during etching²⁰⁹. Ni stripes, of 50 nm thickness, were deposited on a InAs/GaSb SL using the above process. To conserve high quality SL samples, a T2SL on GaAs was used for the initial run. An initial recipe (Etch 1) was chosen by liaising with Oxford Instruments (the manufacturer of the ICP system).

The popular etchant gasses for InAs/GaSb T2SLs are BCl₃, Cl₂, Ar, N₂, CH₄, and H₂^{210–218}. The Cl-based precursors, BCl₃ and Cl₂, are used for the high volatility of gallium, antimony, and arsenic chlorides. Unfortunately, however, the volatility of indium chlorides is relatively low (boiling point of >560°C). The inert gasses, Ar and N₂, are used to encourage desorption of the etch by-products. CH₄ and H₂ have a passivating effect which protects the sidewalls and improves verticality²¹⁰. Recently, this property has also been attributed to N₂ for ICP etching of InAs/GaSb T2SLs²¹⁷. For the initial recipe, recipes involving three or more etchants were excluded for simplicity which leaves BCl₃/Ar and Cl₂/Ar chemistries as the most viable starting points. For bulk GaSb, BCl₃/Ar has been shown to produce vertical sidewalls and smoother surfaces compared to Cl₂/Ar^{219–221}. This is attributed to the dominant role of physical sputtering desorption in the BCl₃/Ar etch which is more effective for the removal of etch by-products than the chemical reaction which dominates in the Cl₂/Ar etch. Due to the limited number of reactive Cl in BCl₃/Ar plasma, the etch rate is lower compared to Cl₂/Ar which is advantages for achieving the high degree of control desirable for device fabrication. Therefore, BCl₃/Ar was chosen to maximise verticality and smoothness of the sidewalls.

Lee et al.²²² studied the effect of the BCl_3/Ar ratio on the rms roughness in GaSb and found that a smooth morphology could only be obtained when the percentage of BCl_3 was below 50%. Furthermore, Hong et al.²²³ observed a low percentage of BCl_3 reduces the overall etch rate in GaSb. This corroborates the findings of Lee et al. as processes with high etch rates can more easily break through the surface native oxide layer causing the surface morphology to become rough²²⁴. Therefore, a low BCl_3 concentration ($\text{BCl}_3:6 \text{ sccm}/\text{Ar}:23\text{sccm}$) was chosen. The RIE power and ICP power were set to 150 W and 1000 W respectively in accordance with Lee et al.²²². The chamber temperature was maintained at 60°C . This was done to limit any fluctuations in temperature rather than for its effect on the etch chemistry. A laser trace system was used to monitor the progress of the etch and was used to stop the etch when the GaSb substrate was reached such that the total etch time was 4 minute 27 seconds. Figure 6.2 shows representative SEM micrographs of the resulting mesa sidewalls, obtained by cleaving the sample.

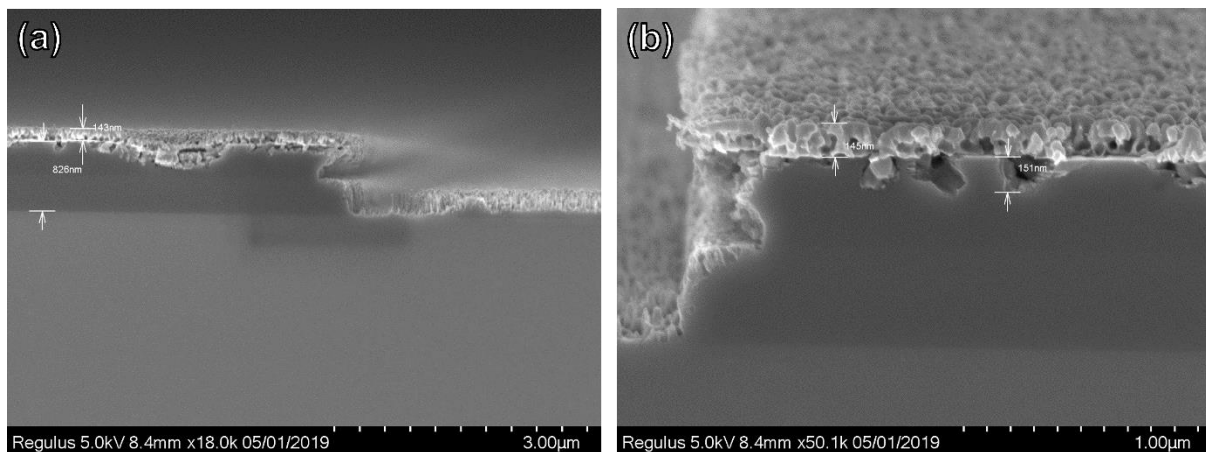


Figure 6.2: SEM micrographs of different mesa sidewalls etched using Etch 1.

Figure 6.2 shows that both the mesa sidewalls and the etched surface appear very rough. This can be partially attributed to the low quality of the T2SL on GaAs. It was therefore decided that higher quality SLs on GaSb would be used for future etches. However, the evident damage to the Ni mask suggests the power of the etch was sufficient to sputter the Ni mask onto the surface of the sample. This may have had a micromasking effect that added to the surface roughness. The damage to the Ni mask also appears to have allowed some of the etchant gasses to penetrate through the mask to damage the mesa itself. The last notable

feature is the significant undercut in the sidewalls of each stripe. This suggests the chemical component of the etch is too dominant.

To determine whether the Ni etch mask is viable for etching T2SL, Process 1 was used to deposit a Ni mask on a GaSb substrate sample. Due to the reduced material quality of the T2SL samples on GaAs, GaSb was chosen as the test sample. For etch 2, the ICP power was reduced from 1000 W to 700 W to reduce the sputtering of the Ni mask observed in Figure 6.2. The flow rates of the BCl_3/Ar gasses were reduced to 12 sccm and 8 sccm respectively to reduce the chemical component of the etch and thereby the undercut observed in Figure 6.2. The total flow rate of the gasses was also decreased to reduce the aggressiveness of the etch. SEM micrographs of Etch 2 are shown in Figure 6.3.

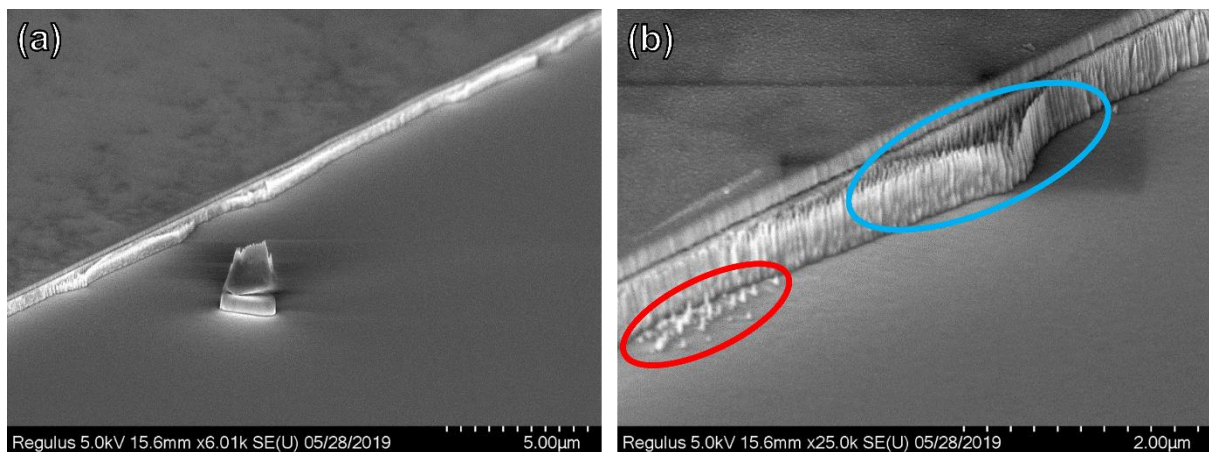


Figure 6.3: SEM micrographs of mesa sidewalls etched using Etch 2. The red oval highlights suspected micromasking and the blue oval highlights a shelf.

By comparing Figures 6.2 and 6.3, it can be seen that the Ni etch mask is significantly less damaged under Etch 2 than Etch 1. The etched floor of the sample also appears much smoother than under Etch 1, possibly due to reduced Ni sputtering. However, the red circle in Figure 6.3b highlights a possible micromasking or sputtering but, unlike in Figure 6.2, this is localised within a small region. The undercut observed following Etch 1 is not visible following Etch 2, possible due to the reduced chemical component of the etch. However, both the smoothness of the etch floor and the profile of the sidewalls may, to some extent, be attributed to the change in sample from T2SL to GaSb. Despite this progress, Etch 2 exhibits two concerning features. First, the mesa sidewalls still appear rough which, based on the

apparent roughness of the Ni mask, may be attributed to features of the mask being projected onto the mesa sidewalls. The second concerning feature is the visible “shelves” on the edges of each stripe whereby certain portions of the GaSb substrate remain unetched despite not being protected by the Ni mask. As Figure 6.3a shows, this feature extends across large portions of each stripe. One possible cause for this is the presence of some kind of residue or contaminant that accumulates on the side of the Ni mask, though this cannot be seen in any optical micrographs taken prior to the etch (not shown). In light of the aforementioned concerns and the possibility of sputtering the Ni mask under a high intensity etch, a process for fabricating a dielectric hard mask was developed.

This process (Process 2) is shown schematically in Figure 6.4. First, a 300 nm layer of SiO₂ was deposited on the sample by e-beam evaporation. Unfortunately, the quality of SiO₂ deposited by this process is relatively low but, at the time of development, this was the only method of dielectric deposition available in the ICS cleanroom. A Ni mask was then deposited on the SiO₂ surface using the bilayer lift-off technique. The SiO₂ was then etched into stripes using a CHF₃/Ar RIE process. Finally, the Ni was removed using a nitric acid based wet etch. Process 2 could be simplified by use of a photoresist etch mask instead of Ni but this process was chosen as it was already being used by other ICS cleanroom users.

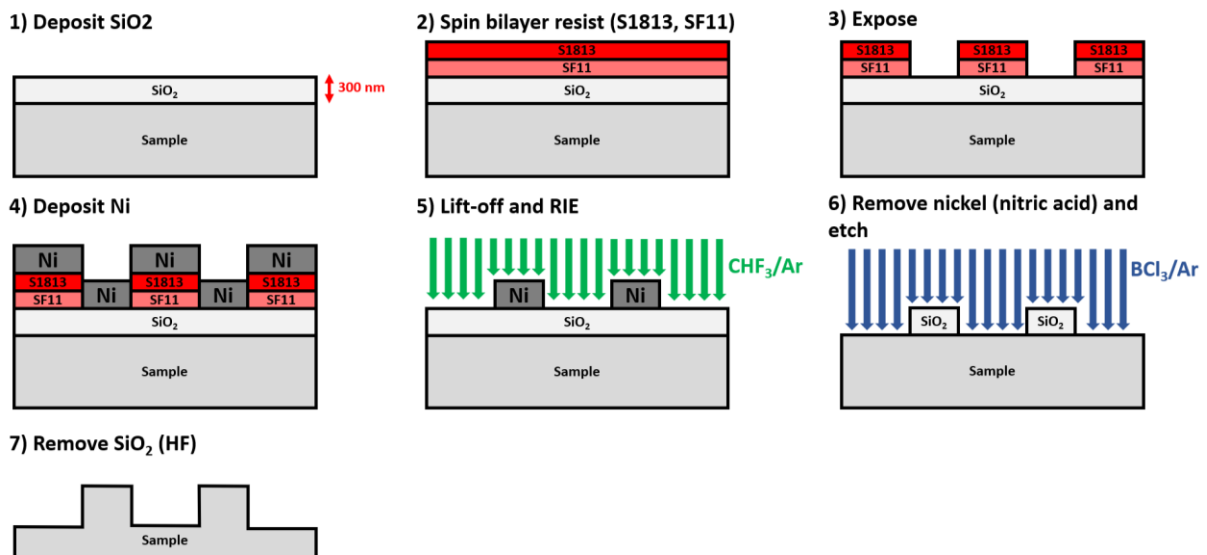


Figure 6.4: Schematic of an SiO₂ etch mask process (Process 2).

Unfortunately, some issues were encountered with this process as highlighted by the optical micrographs given in Figure 6.5. Following the SiO_2 etch, some residue was apparent on one edge of the Ni stripes, as shown in Figure 6.5a. This residue may be related to the “shelves” observed in Figure 6.3. Furthermore, following the removal of the Ni with the nitric acid based wet etch, the optical micrograph, shown in Figure 6.5b, shows that this etch removed both the Ni and the SiO_2 with some small pieces of SiO_2 visible, albeit displaced, on the sample surface. As the etch mask was removed, no etch was attempted on this sample.

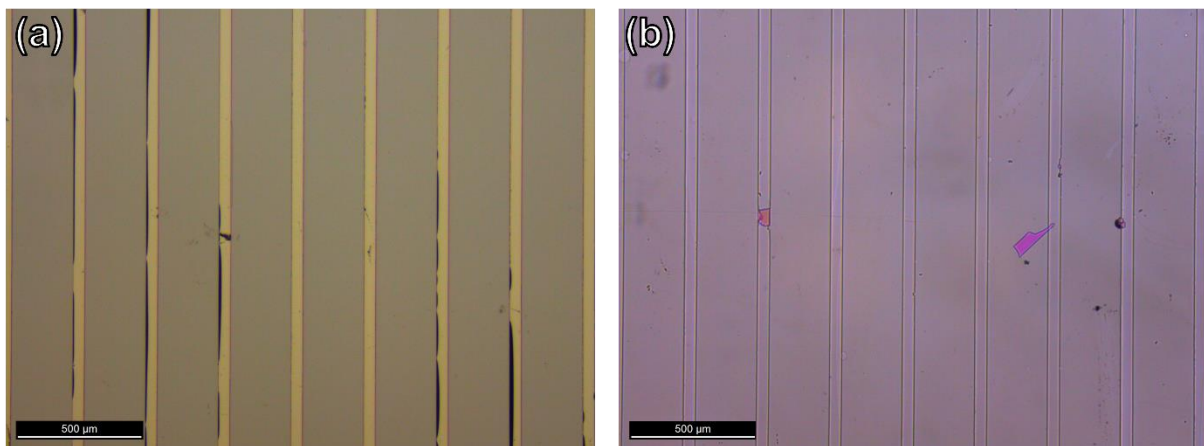


Figure 6.5: Optical micrographs of the Sample fabricated under Process 2 (a) after the RIE etch of SiO_2 (Step 5) and (b) after the removal of the Ni mask (Step 6).

Due to the issues encountered with Ni in Processes 1 and 2, a process (Process 3a) was developed that replaced the Ni mask with a durable photoresist (AZ9260). Process 3a is shown schematically in Figure 6.6.

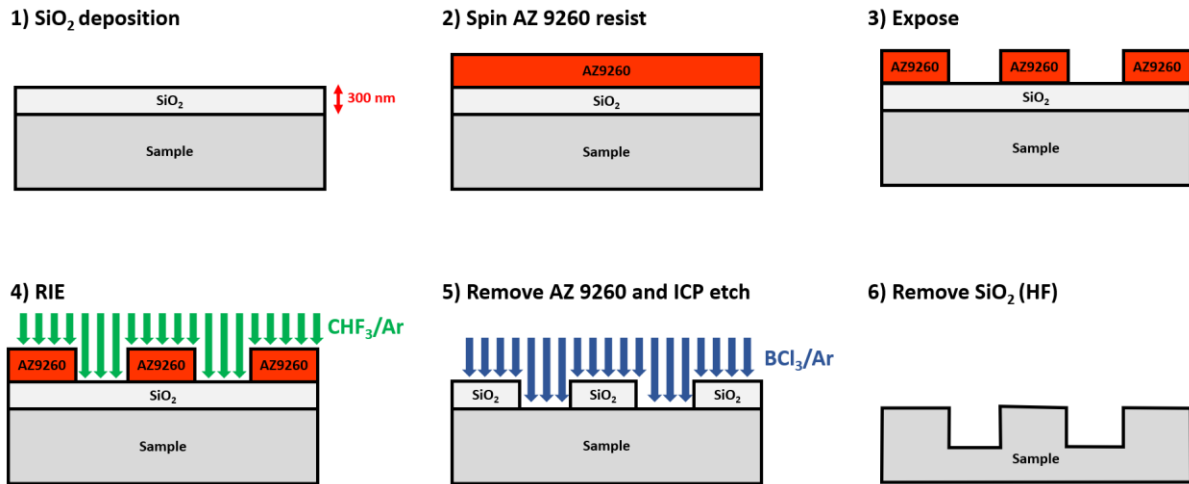


Figure 6.6: Schematic of an updated SiO₂ etch mask process (Process 3a).

Initially, Process 3a was tested on a dummy Si sample. This method also presented some challenges as shown in the optical micrographs in Figure 6.7, which shows the sidewalls of the photoresist are very poorly defined. This could result in a poorly defined etch mask and, eventually, low quality mesas.

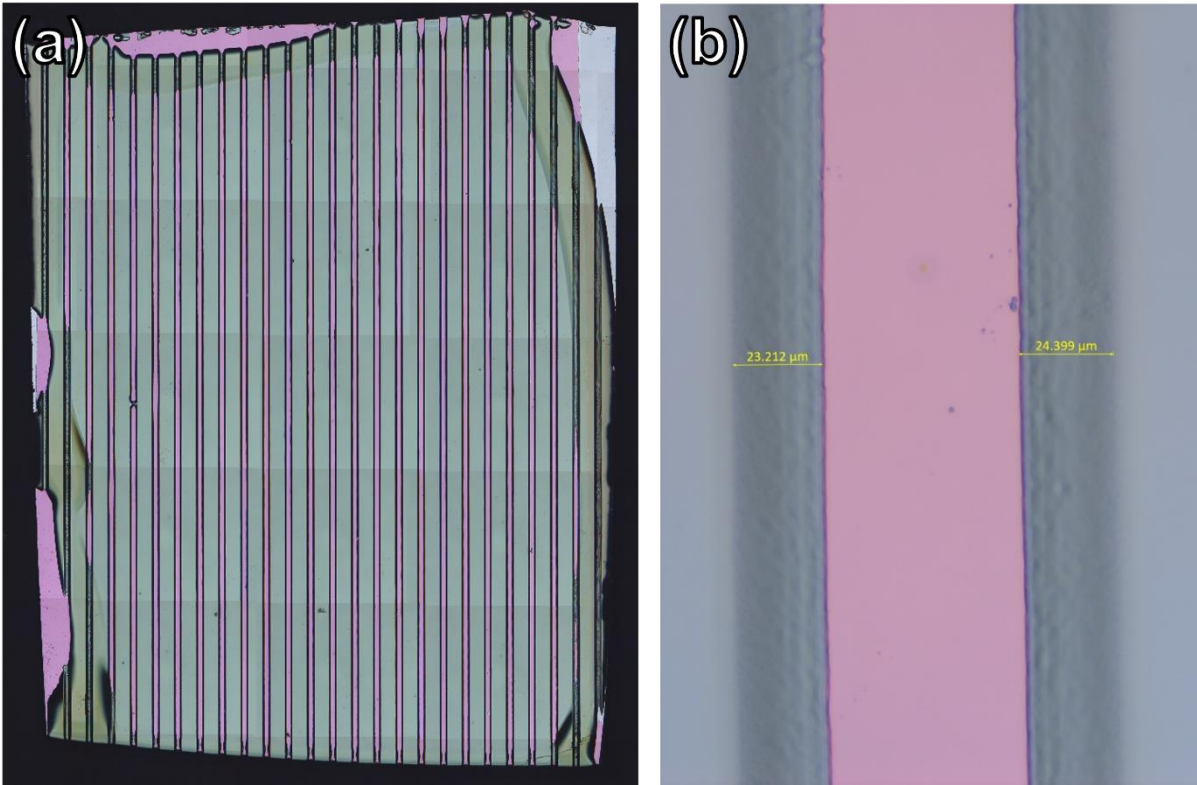


Figure 6.7: Optical micrographs of the Si test sample undergoing Process 3a following photolithography (Step 3). (a) shows a stitched image of the whole sample and (b) shows a close-up of one strip.

The poorly defined sidewalls, shown in Figure 6.7, are attributed to the loss of adhesion between the SiO_2 and AZ9260. This was therefore addressed by spinning of an adhesion promoter, TI Prime, onto the SiO_2 surface prior to spinning the AZ9260 (Process 3b). As shown in Figure 6.8, this greatly improves the sidewall quality of the AZ9260.

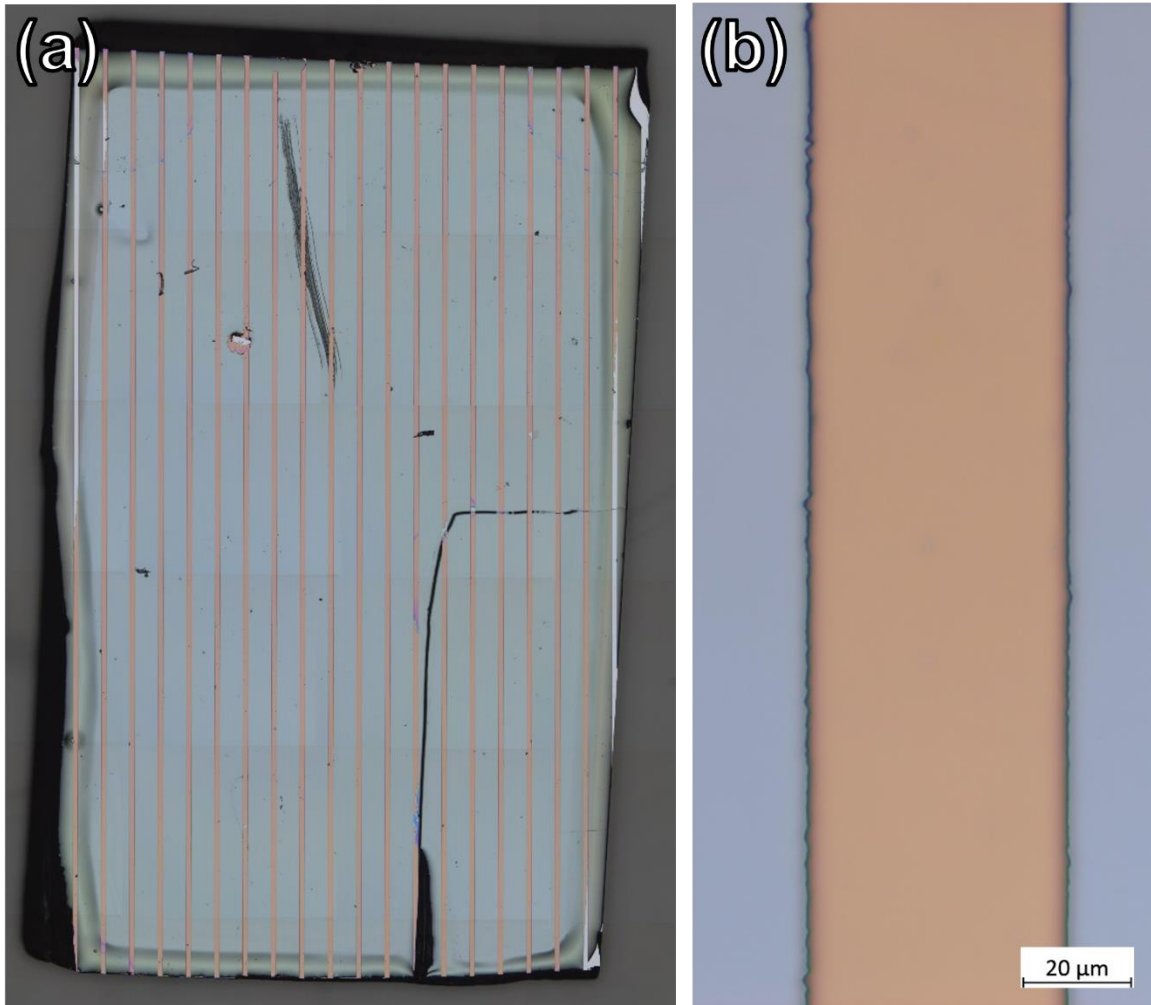


Figure 6.8: Optical micrographs of the Si test sample undergoing Process 3b following photolithography (Step 3). (a) shows a stitched image of the whole sample and (b) shows a close-up of one strip.

Figure 6.8 shows that the addition of TI Prime successfully enhances the verticality of the mesa sidewalls. However, Figure 6.8b shows that, once the quality of the sidewalls is improved, it becomes evident that the photoresist stripes have very jagged edges. Two possible causes for this were identified. Firstly, the stripe mask that was used to this point was relatively old and therefore may be dirty or deformed. If this was case, the defects on the mask would translate onto the profile of the photoresist itself. This was addressed by replacing the mask with a newer, cleaner alternative. Secondly, as Figure 6.8a shows, there is a build-up of photoresist on the edges of the sample, known as edge beads, caused by the spinning process. These edge beads increase the separation between the photomask and photoresist which causes the UV radiation to diffract before exposing the photoresist, leading

to the jagged edges observed in Figure 6.8b. This can be mitigated through use of a process known as edge bead removal (EBR). Here, the edge beads are photolithographically removed prior to exposure with the stripe mask. These alterations were then implemented (Process 3c) and shown in optical micrographs in Figure 6.9.

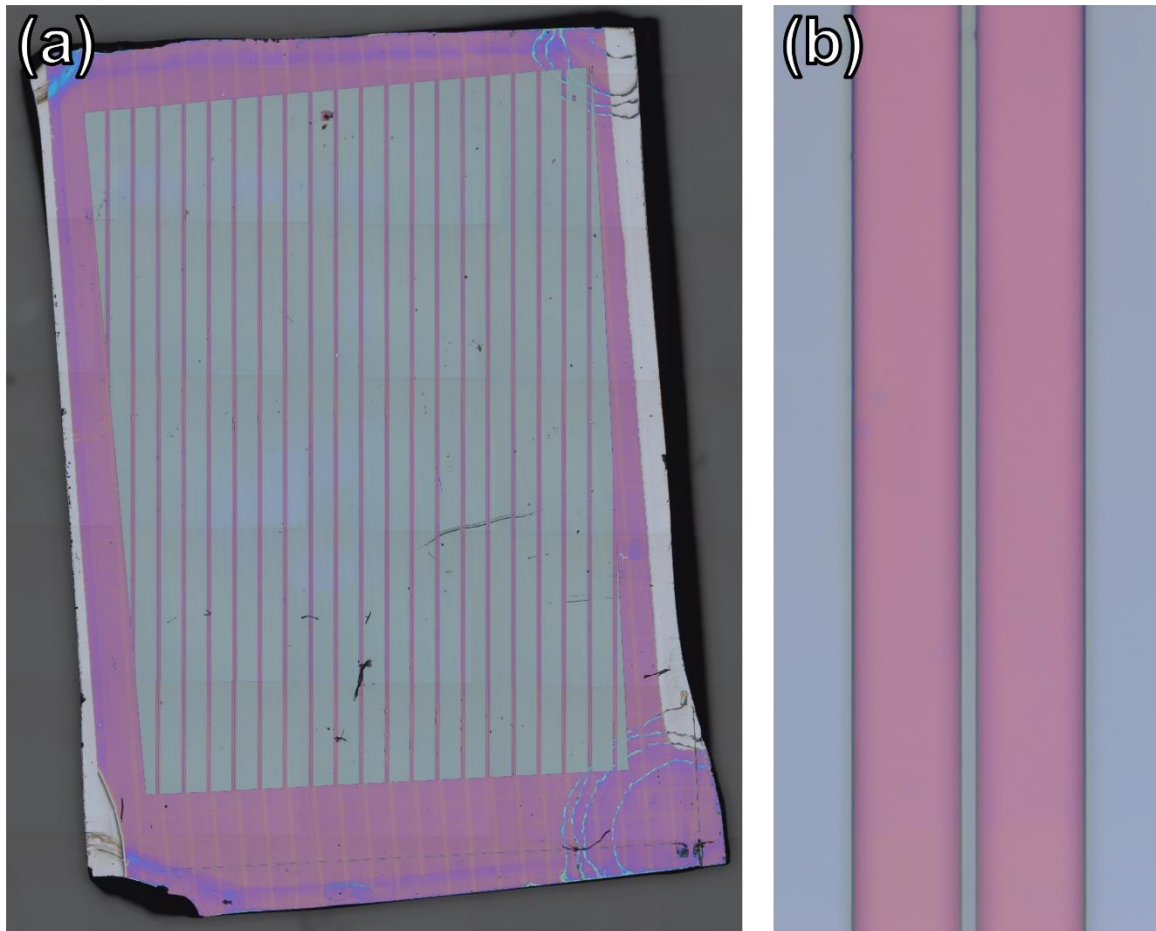


Figure 6.9: Optical micrographs of the Si test sample undergoing Process 3c following photolithography (Step 3). (a) shows a stitched image of the whole sample and (b) shows a close-up of one strip.

Figure 6.9 shows that Process 3c can be used to deposit very well-defined layers of AZ9260 onto SiO_2 . After this process was completed on the dummy Si sample, SEM and optical micrographs (Figure 6.10a and b) show that the resulting SiO_2 mask is well defined. The SEM micrograph shows a slight over etch of the SiO_2 which was intentionally added to ensure there was no unwanted SiO_2 on the sample surface. DEKTAK profilometry (Figure 6.10c) confirms the presence of strips roughly 300 nm in height.

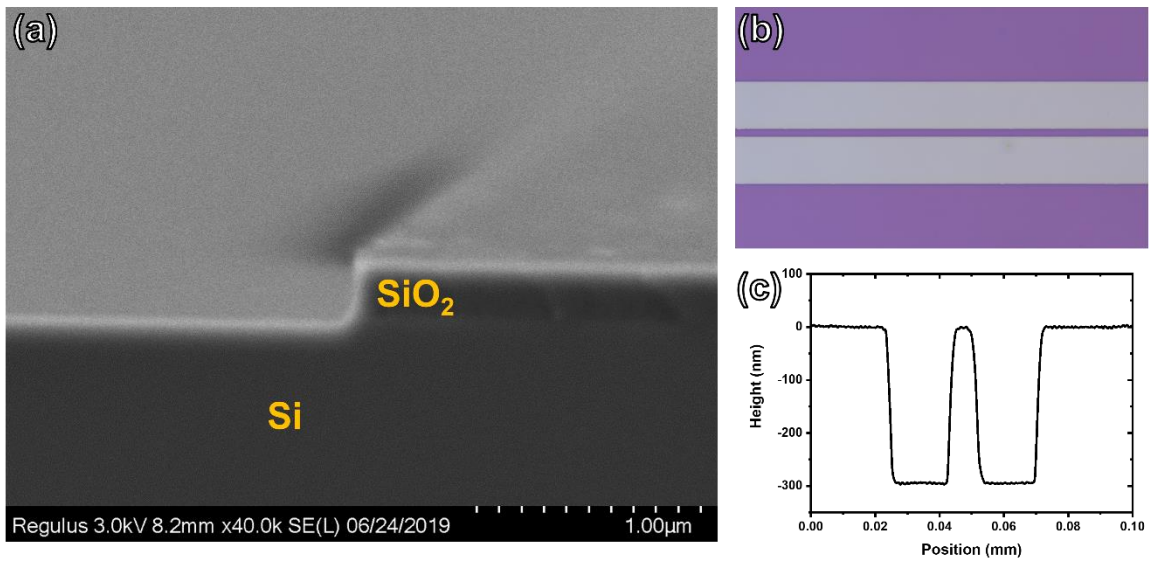


Figure 6.10: SiO₂ strips on Si, fabricated using Process 3c, measured by (a) SEM, (b) optical microscopy, and (c) DEKTAK profilometry.

Process 3c was then used to deposit SiO₂ strips on a good quality T2SL sample grown on GaSb. As Recipe 2 was developed to prevent the sputtering of the Ni mask, we reverted to Recipe 1 for the initial trial with a SiO₂ etch mask. SEM micrographs of the resulting etch are given in Figure 6.11.

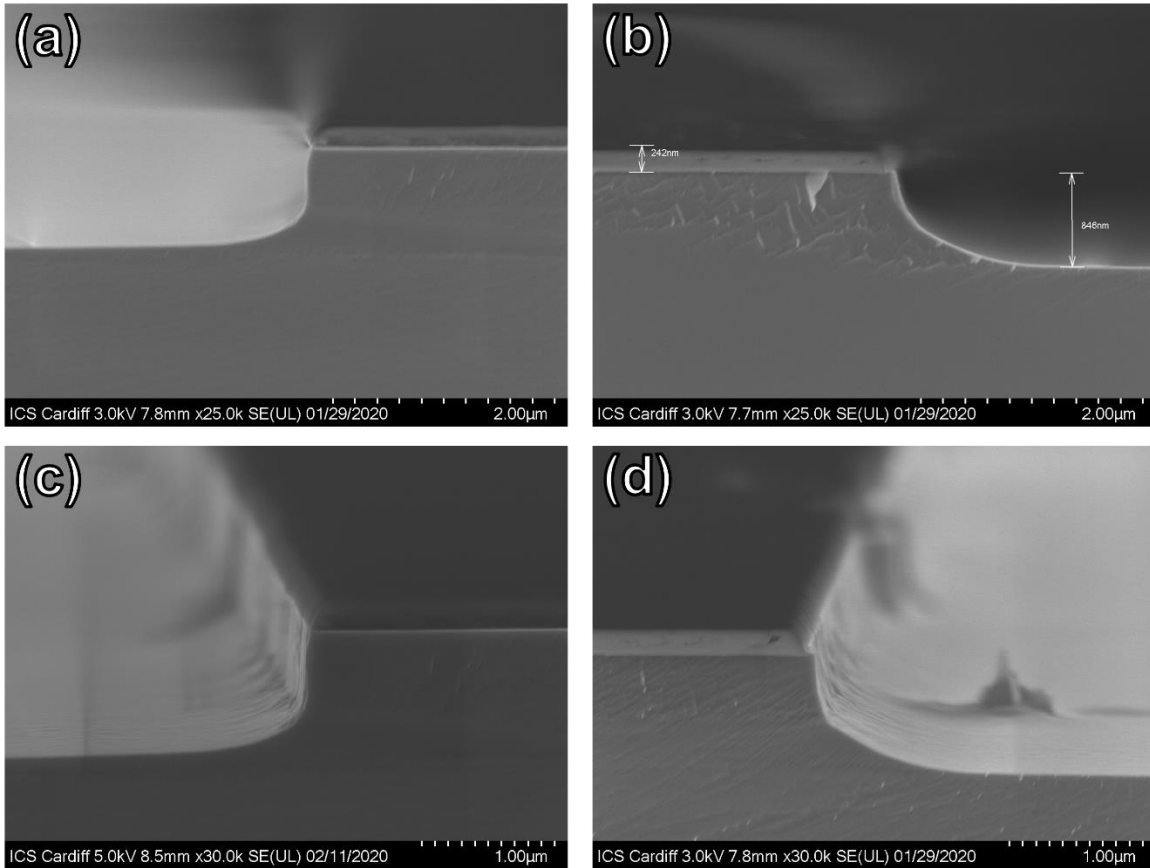


Figure 6.11: Representative SEM micrographs of the sidewalls and profiles of a T2SL sample processed using Process 3c and etched using Recipe 1.

Figure 6.11 shows that minimal damage was done to the SiO_2 etch mask such that no sputtering or micro masking phenomena were observed. Notably, as shown by Figure 6.11a and c), the left and right sidewalls have different profiles. It is possible this is due to an uneven placement of the sample or anisotropic diffusion of etchants. The left sidewalls appear close to vertical on the upper half but with a foot at the base of the etch. A similar profile is seen on the right sidewalls (Figure 6.11b) but in this case the foot is much more prominent. This profile may be related to the diffusion of ions down the surface of the sidewall. Figures 6.11c and d show the sidewall roughness is greatly improved compared to previous etches though some striations are visible. By comparing the SiO_2 mask in Figures 6.10 and 6.11, it is possible this is partly due to some damage to the edges of the SiO_2 mask that translates onto the mesa sidewalls. Jung et al.²²⁵ had previously observed that, when etching T2SLs with BCl_3/Ar , the morphology of the mesa sidewalls becomes smoother and more vertical when the proportion of BCl_3 increases, the sidewall verticality and smoothness, in addition to the overall etch rate,

increase. This finding is surprising because, as noted above, Lee et al.²²² found a low BCl_3 concentration was advantageous for surface morphology. This discrepancy may be attributed to the presence of InAs, which, due to the low volatility of InCl_x , may require a larger chemical component for etching. Furthermore, the presence of internal strain within the SL may also affect the etch chemistry. Therefore, an updated recipe (Recipe 3) was developed to increase the BCl_3/Ar ratio (12 sccm/23 sccm). The other parameters of Recipe 3 were the same as Recipe 1. Representative SEM micrographs of the resulting mesa sidewalls are shown in Figure 6.12.

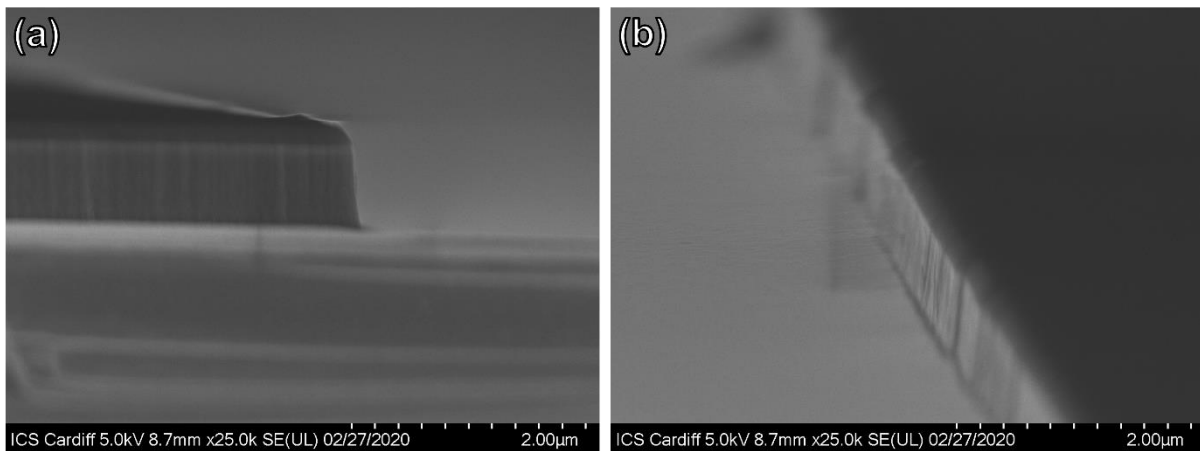


Figure 6.12: Representative SEM micrographs of the sidewalls and profiles of a T2SL sample processed using Process 3c and etched using Recipe 3.

Figure 6.12a shows that the sidewall verticality produced by Etch 3 is notably greater than that of Etch 1. Furthermore, unlike Etch 1, the left and right sidewalls show very similar profiles. This is attributed to the increased chemical component in the etch recipe which attacks the sidewalls more aggressively. However, contrary to Jung et al.²²⁵, we did not observe an attendant increase in the etch rate. One possible explanation for this is that here, the additional BCl_3 ions are consumed removing the foot observed in Figure 6.11 rather than increasing the overall etch rate. Unfortunately, the deformation of the SiO_2 etch mask and the striations in the mesa sidewalls remain. This was addressed by reducing the ICP power to 800 W (Recipe 4) while keeping all other parameters from Recipe 3 unchanged. This was intended to reduce the damage to the etch mask and thereby reduce the formation of striations in the mesa sidewalls. Representative SEM micrographs are shown in Figure 6.13.

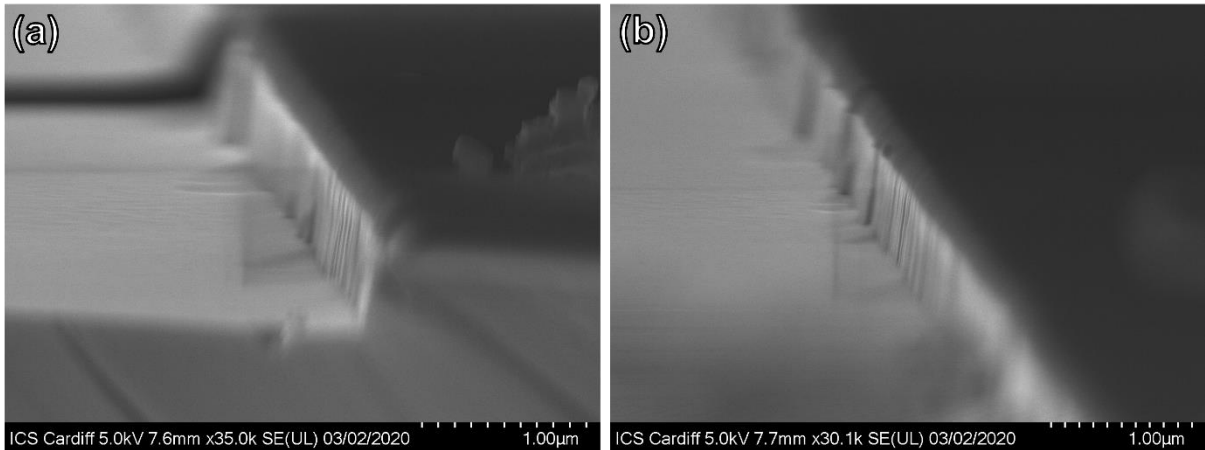


Figure 6.13: Representative SEM micrographs of the sidewalls and profiles of a T2SL sample processed using Process 3c and etched using Recipe 4.

Figure 6.13 shows that the verticality of sidewalls observed previously is maintained. However, there is still some evident damage to the SiO_2 etch mask and striations in the sidewalls. Unfortunately, further reductions of the ICP power to limit the damage to the etch mask compromised the stability of the plasma. Instead, the Ar flow rate was increased from 23 sccm to 46 sccm (Recipe 5) to encourage desorption of the etch by products from the sidewalls. All other parameters were kept constant. Representative SEM micrographs are shown in Figure 6.14.

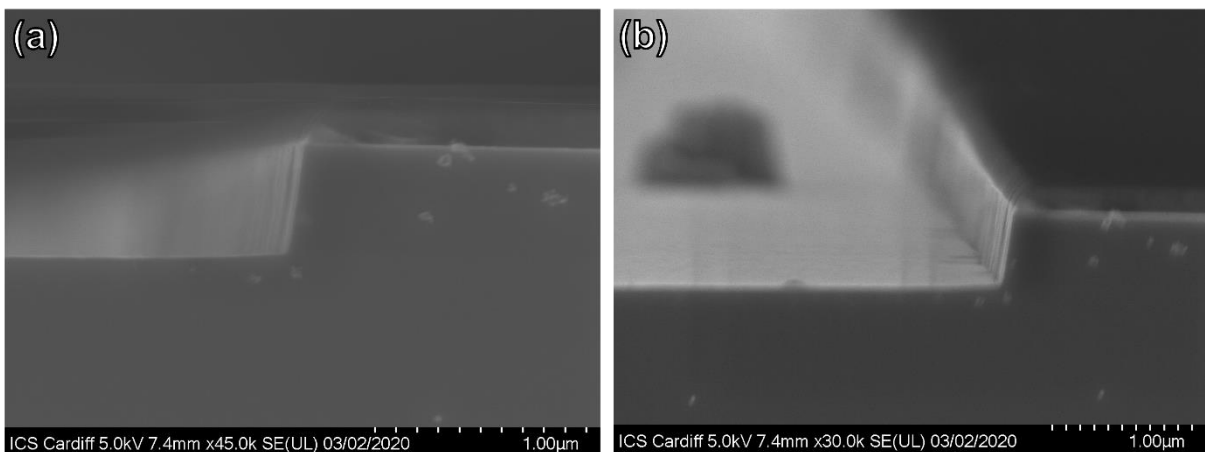


Figure 6.14: Representative SEM micrographs of the sidewalls and profiles of a T2SL sample processed using Process 3c and etched using Recipe 5.

Figure 6.14 shows that Recipe 5 again produces good sidewall quality. Furthermore, the sidewall morphology appears slightly superior to that of previous etches though damage to

the etch mask and some striations are still visible. This was addressed by replacing the e-beam evaporation of a SiO₂ etch mask with the plasma-enhanced chemical vapour deposition (PECVD) of a SiN etch mask (Process 3d). It should be noted that, at this point in the development, the ICS cleanroom replaced the AZ9260 with AZ10XT but the two resists are very similar. Figure 6.15 presents optical and SEM micrographs of the SiN etch mask on a T2SL sample prior to ICP definition.

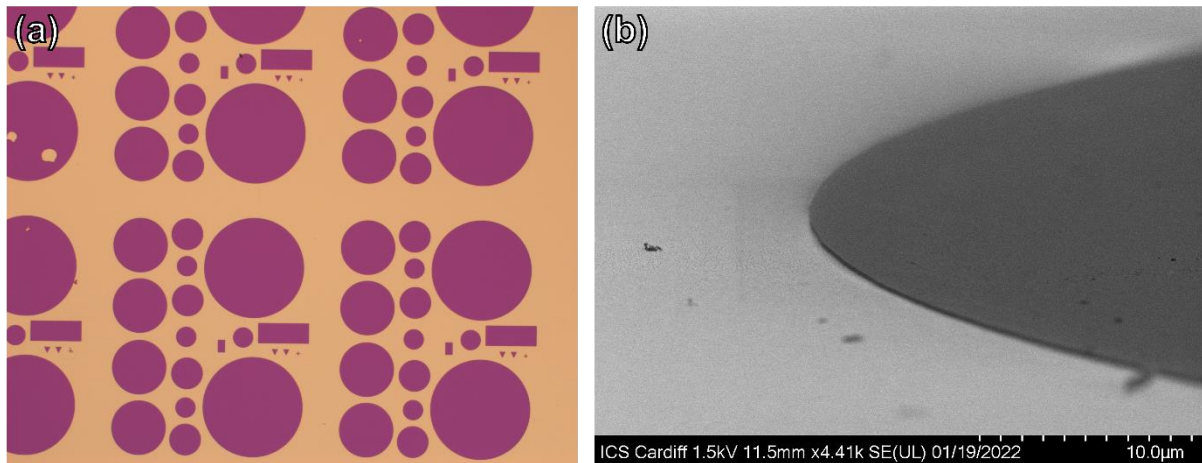


Figure 6.15: An (a) optical and (b) SEM micrograph of the SiN etch mask deposited on a T2SL sample using Process 3d.

Figure 6.15 shows that Process 3d can be used to deposit well defined SiN mesas with good sidewall verticality. This was then used to deposit a SiN etch mask on a T2SL sample for etching using Recipe 5. Representative SEM micrographs are given in Figure 6.16.

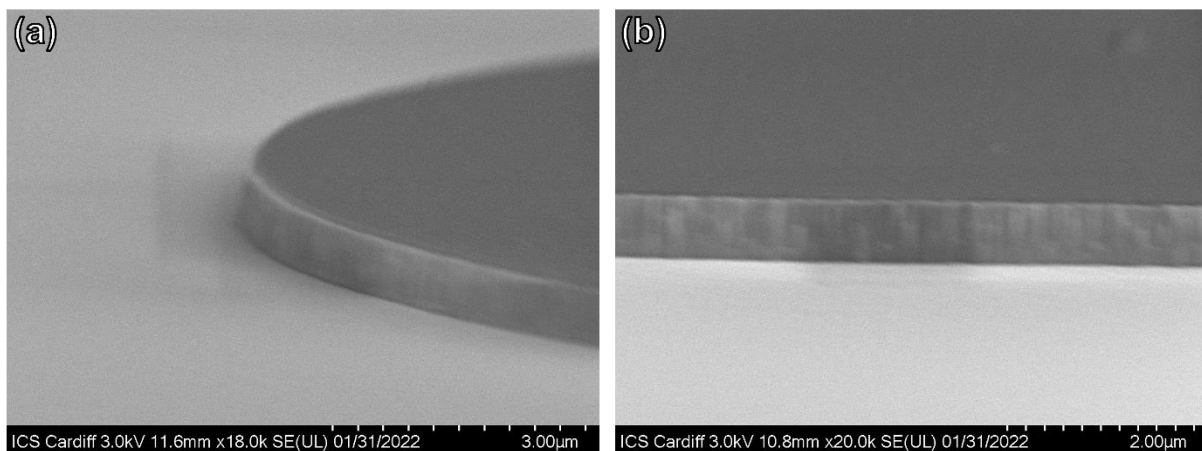


Figure 6.16: Representative SEM micrographs of the sidewalls and profiles of a T2SL sample processed using Process 3d and etched using Recipe 5.

Due to the change in photomask, a direct comparison between Figures 6.14 and 6.16 is difficult. However, Figure 6.16a confirms the good verticality of the etch is preserved. Furthermore, there is less evident damage to the SiN etch mask compared to the SiO₂ and possibly fewer striations on the sidewalls as a result although this is difficult to confirm. Further improvement of the etch recipe is possible through optimisation of the chemistry. In particular, increasing the temperature to around 200°C would encourage the desorption of InCl_x etch by-products and is a promising route to improving sidewall morphology. The use of a wet etch following the dry etch is also a popular means of removing sidewall damage. However, at this intermediate stage in development, Process 3d and Recipe 5 were used to fabricate and test a dry etched PIN diode.

6.1.2. Device fabrication

First, mesa definition was achieved through Process 3d and Recipe 5 in the manner described above. The SiN etch mask was removed using the same RIE process used above. Contact deposition was then performed using the processes described in Section 3.3. A H₂SO₄, H₂O₂, and H₂O (1:8:80) wet etch was used to clean the sidewalls of the samples to remove the damage of the dry etch followed by immediate protection with a photoresist, as in Section 3.3. The finished device is shown in Figure 6.17.

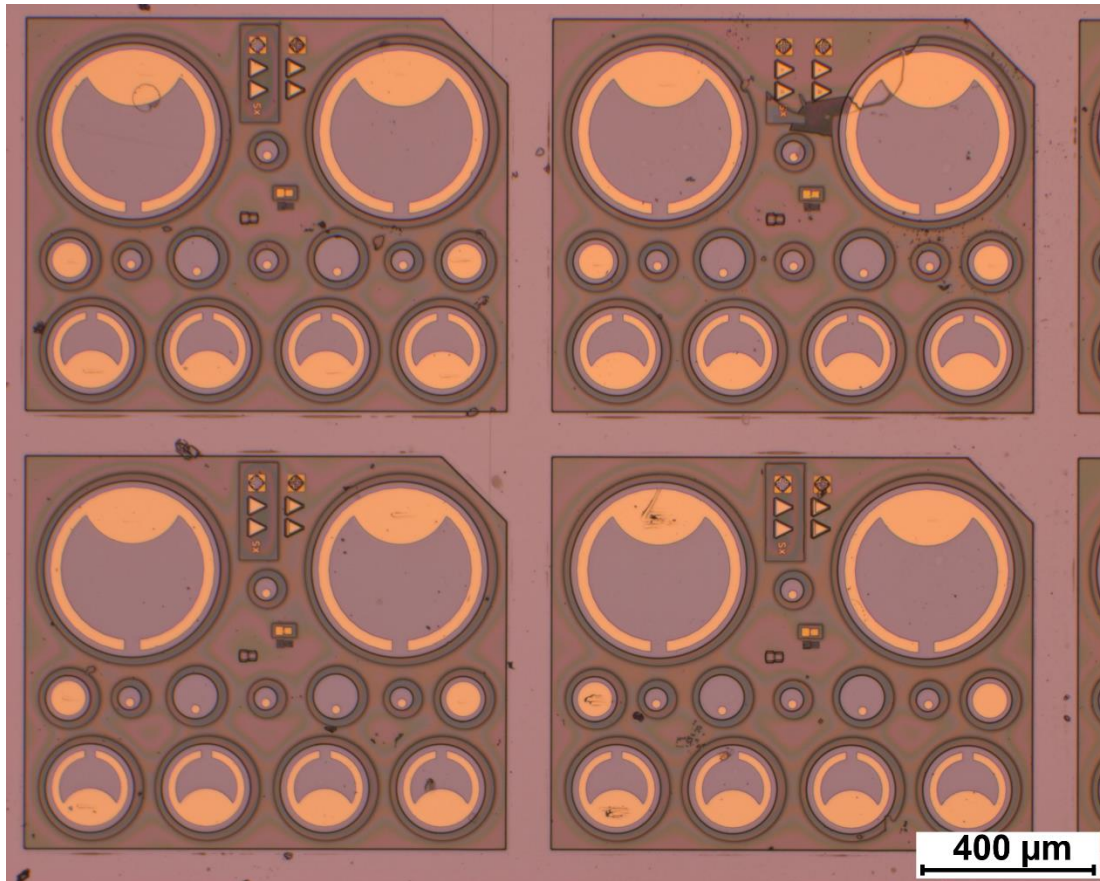


Figure 6.17: Optical micrograph of a LWIR T2SL fabricated using the dry etch.

A cryogenic probe station was used to compare the I-V profiles of the dry etched device with that of the wet etch, reported in Section 4.3.5. The dry etched device was also measured prior to cleaning and photoresist protection to determine the efficacy of these measures. The results are shown in Figure 6.18.

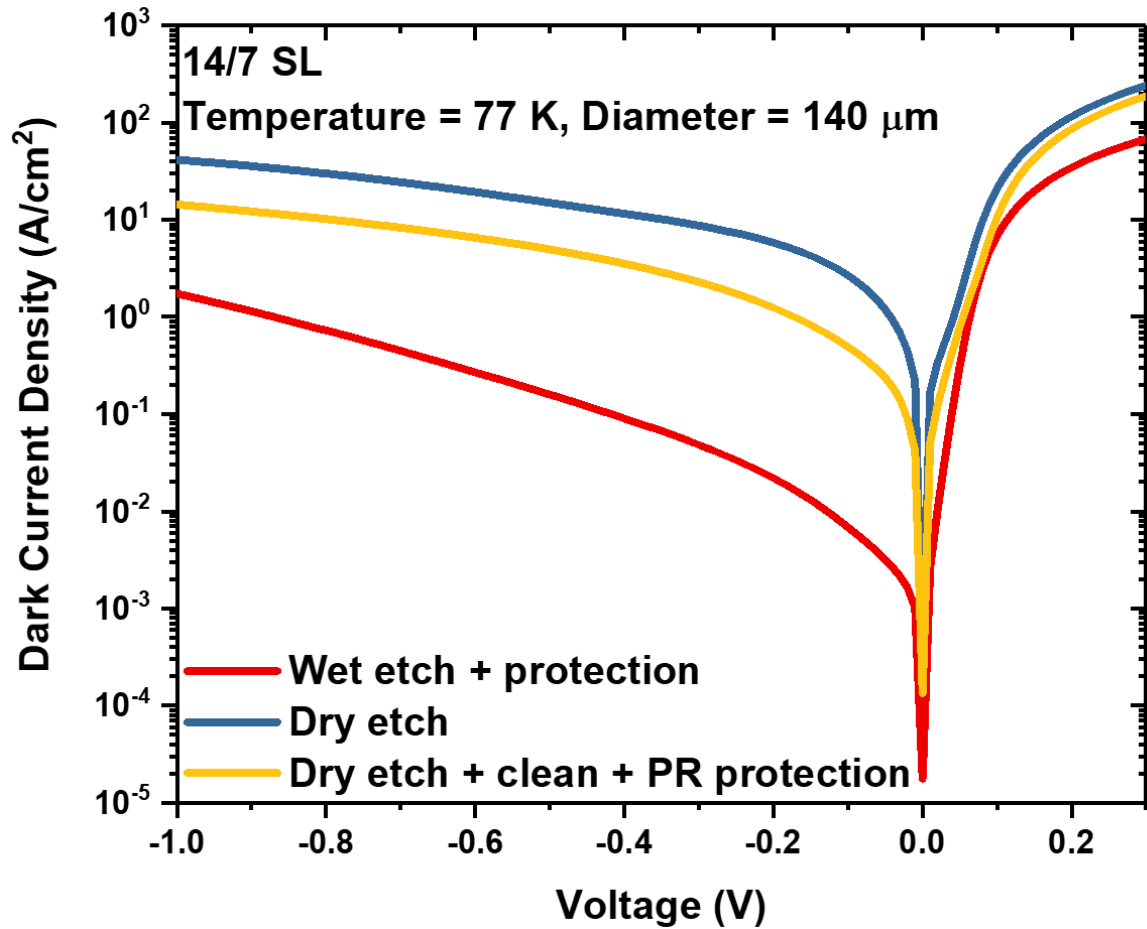


Figure 6.18: I-V profiles at 77 K for a 140 μm diameter device fabricated using the wet etch and dry etch approaches.

Figure 6.18 shows that the I-V profiles of each diode appear diode-like, being roughly linear under forward bias and increasing gradually with increasing reverse bias. After dry etching alone, the dark current density at low reverse bias is almost 3 orders of magnitude larger than the reference wet etch sample. However, the dark current of the dry etched sample was reduced by a factor of ~ 5 following the clean and photoresist protection, suggesting that a notable proportion of the increased dark current is surface related. To verify that the I-V profiles are indeed diode-like, the forward bias of each sample was plotted against the diode equation as shown in Figure 6.19.

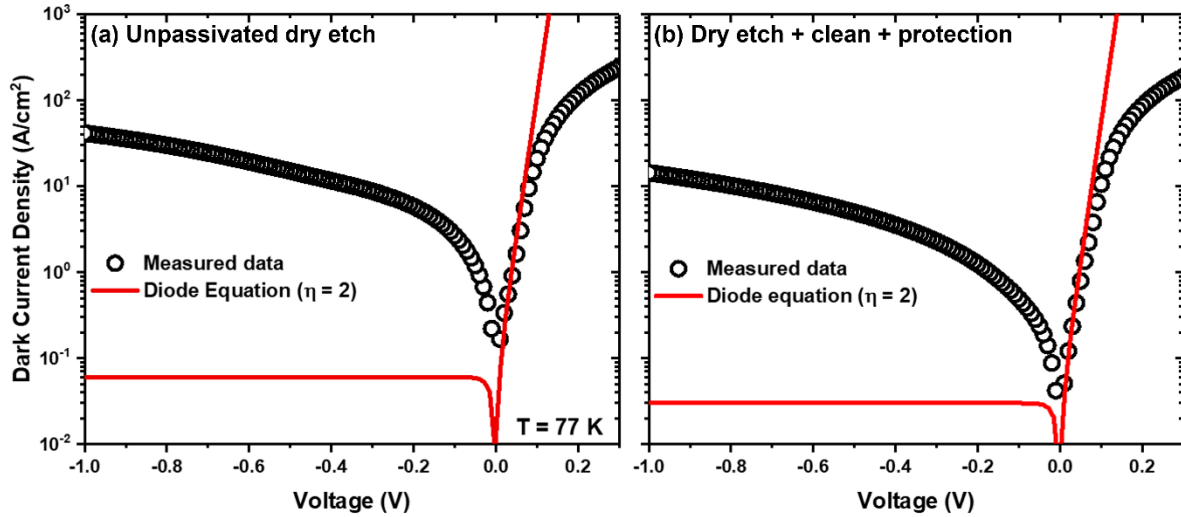


Figure 6.19: The measured I-V profile and diode equation fit for the dry etched sample (a) before and (b) after cleaning of photoresist protection.

Figure 6.19 shows a close agreement between the measured data for both samples and the diode equation with a maximum ideality factor of 2. However, some deviation is evident in both samples, possibly due to significant shunt current as discussed below. Overall, the forward I-V is close to the expected behaviour of a functioning diode. Figure 6.20 shows I-V measurements over the temperature range 77 K – 200 K, taken for a 140 μm diameter device from each sample, compared to that of the wet etch (reproduced from Figure 4.21). These data were used to construct an Arrhenius plot, shown in Figure 6.21.

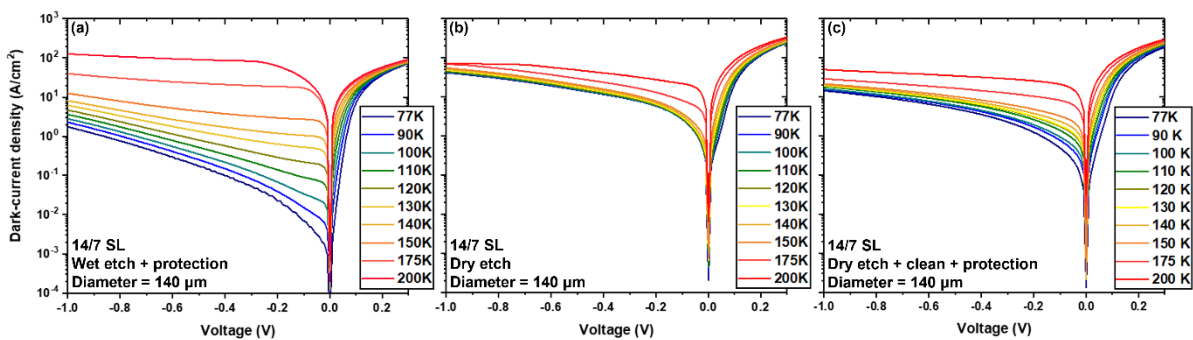


Figure 6.20: Temperature dependant I-V profiles for (a) the wet etched reference sample, (b) the dry etched sample before cleaning, and (c) the dry etched sample after cleaning and photoresist protection.

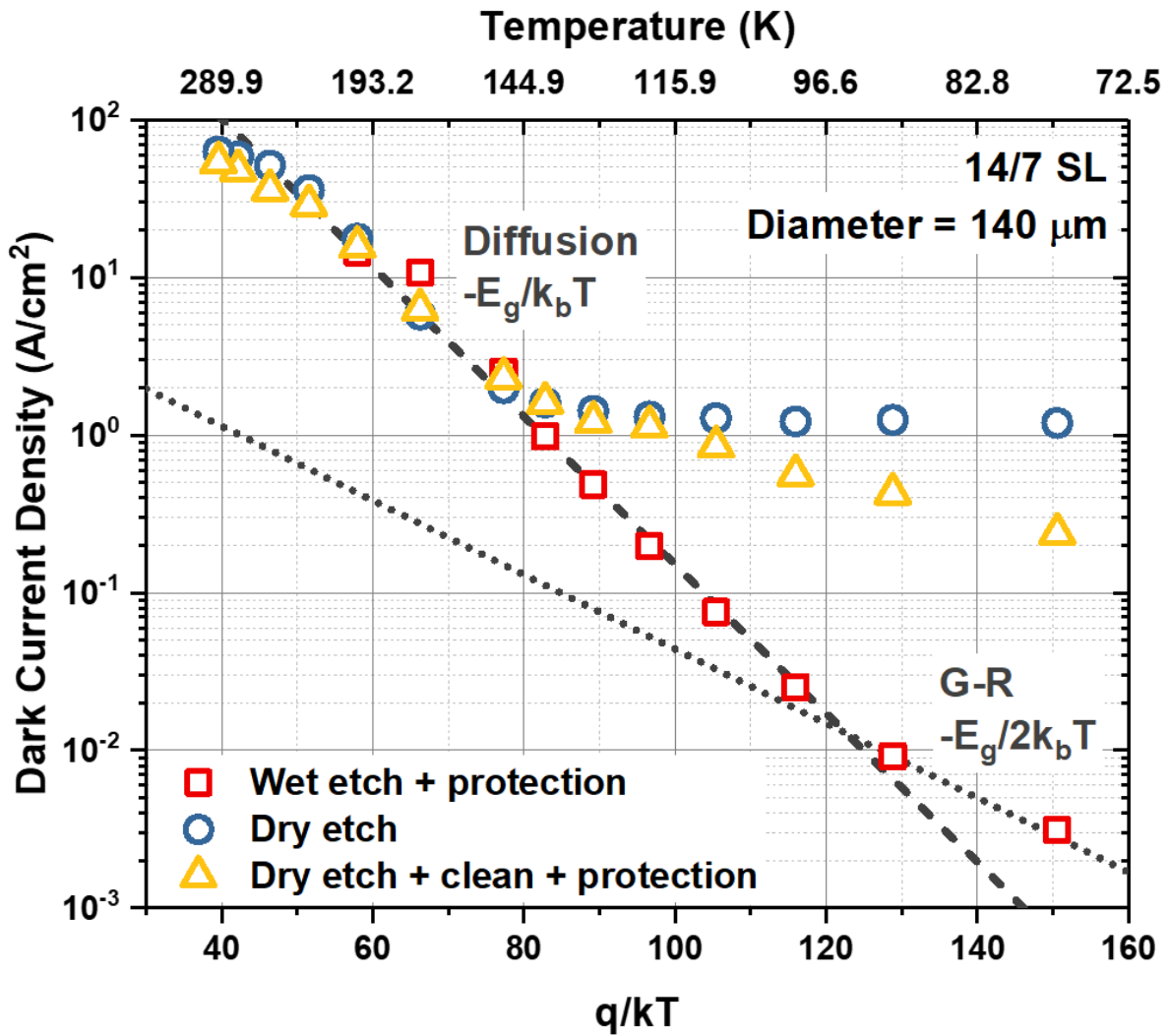


Figure 6.21: The Arrhenius plot for the wet etched reference sample, the dry etched sample before cleaning, and the dry etched sample after cleaning and photoresist protection.

Figure 6.21 shows that the wet etched reference sample behaves as expected in that it is dominated by the diffusion current at high temperature and G-R current at low temperature with an inflection point around 100 K. Both dry etched samples are also dominated by diffusion current above a temperature of around 140 K but then show behaviour consistent with neither diffusion nor G-R currents. This suggests that there is no reduction in device performance arising from the dry etch if the intended operating temperature of the device is above 140 K, as is often the case in modern applications. Below 140 K, the dark current density at -50 mV is lower for the dry etched sample with the clean and photoresist protection and decreases more sharply with decreasing temperature. To determine the origin of this dark

current at low temperature, the I-V profiles at 77 K were fitted using the manner described in Section 4.3.5., the results of which are shown in Figure 6.22.

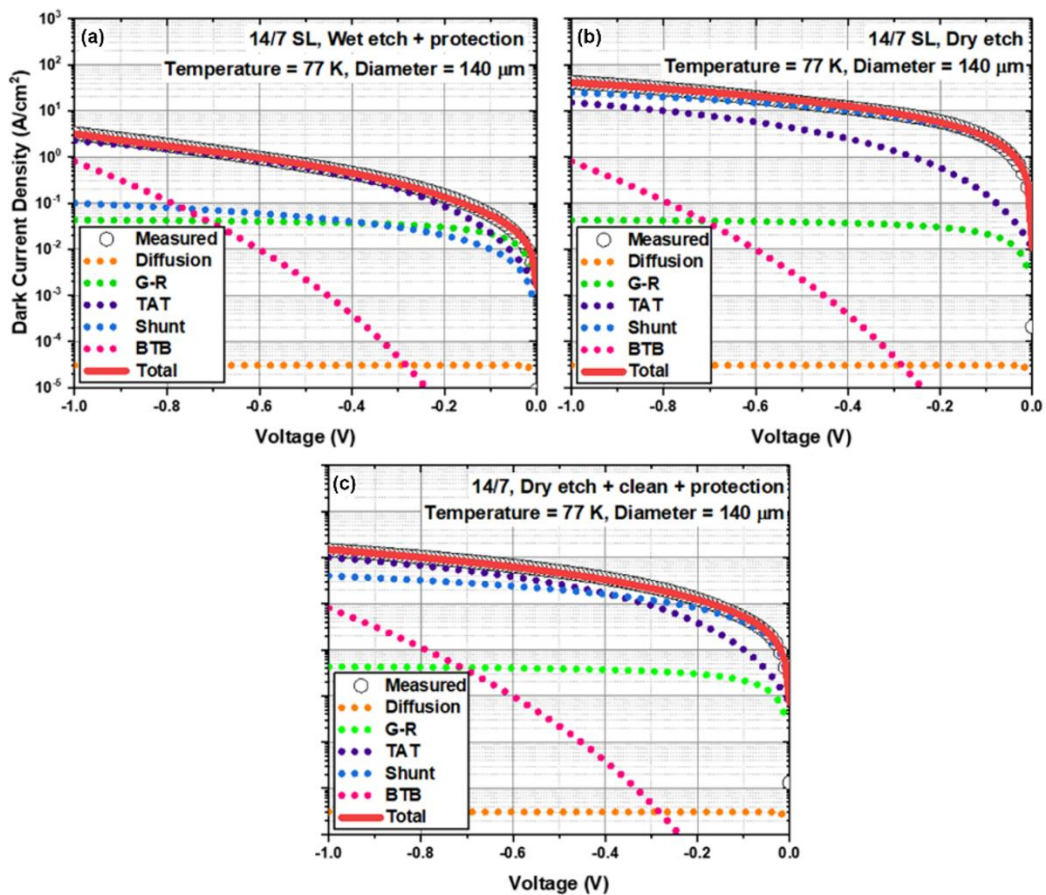


Figure 6.22: I-V fitting at 77 K for (a) the wet etched reference sample, (b) the dry etched sample before cleaning, and (c) the dry etched sample after cleaning and photoresist protection.

The I-V fitting of the wet etched reference sample has been discussed extensively in Section 4.3.5. For the dry etched samples, it was hypothesised that only the dark current sources that have a significant surface dependant component (such as shunt and TAT currents) would increase as a result of the dry etch process. This appears to be confirmed by Figure 6.22b and c, which show good agreement between the measured and fitted data when only these dark current sources are increased compared to Figure 6.22a. It can therefore be seen that the deviation from diffusion- and G-R-limited behaviour for the dry etched samples, observed in Figure 6.21, is due to the presence of significant shunt and TAT currents. The increased presence of these currents may also explain the deviation from the diode equation observed

in Figure 6.19. Interestingly, Figure 6.22b and c show that the clean and protection, applied to the dry etch sample, are effective for suppressing shunt current but not TAT current. This suggests that the clean and photoresist protection is effective at mitigating the surface leakage current but not the dislocations at the surface which correspond to the trap states. This can be attributed to the presence of a physical barrier to ambient air that prevents oxidation, but absence of chemical passivation. The continued presence of these surface defects explains why the shunt current in Figure 6.22c remains higher than in Figure 6.22a. This may be mitigated through use of a chemical passivation such as SiN or optimisation of the dry etch to minimise the damage to the surface. In the latter case, the incorporation of additional precursors which can passivate the sample such as CH₄, H₂, or N₂ is an avenue of particular interest. Furthermore, the wet etch cleaning could be improved as the processes used here was not thoroughly optimised for use following a dry etch. The different ratio of shunt and TAT currents before and after the clean and photoresist protection also explains the different temperature dependence of these samples below 140 K, observed in Figure 6.21.

To further study the surface currents, I-V measurements from all devices on each sample were taken, though this was not performed extensively for the dry etch sample prior to cleaning and photoresist protection. The dark current density at -50 mV was then plotted against the perimeter/area ratio for each sample, as shown in Figure 6.23.

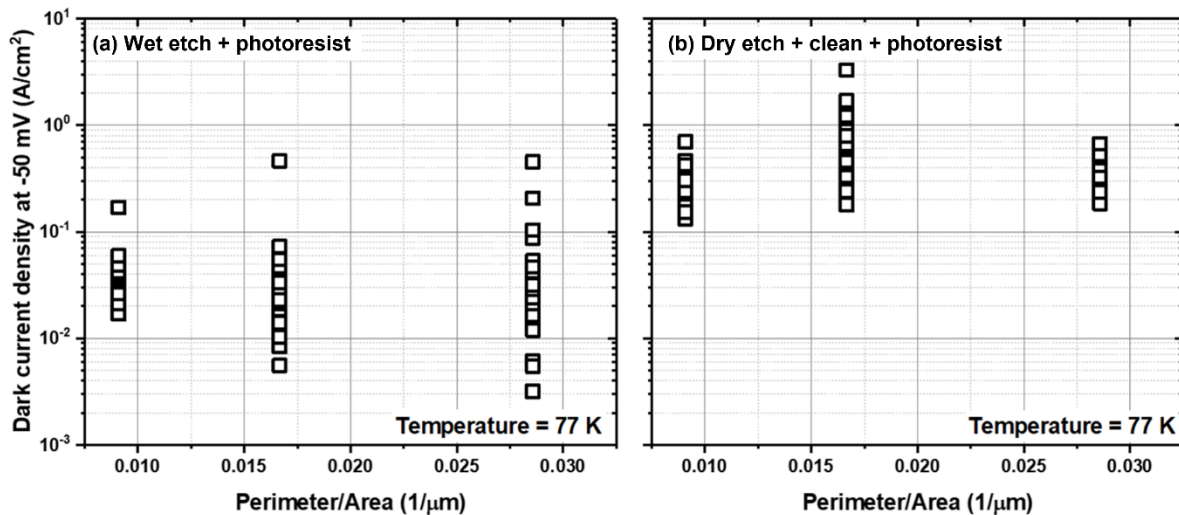


Figure 6.23: Dark current density at -50 mV as a function of the perimeter/area ratio for (a) the wet etched sample and (b) the dry etched sample after cleaning and photoresist protection.

Figure 6.23 shows a considerable inhomogeneity in the dark current of both samples such that, in each case, no particular trend is discernible. It could be argued that the dry etching process appears to reduce the inhomogeneity of the dark current but, as two different dark current mechanisms are dominant in each case, this is not a fair comparison. Comparing Figure 6.23a and b also suggests that the average reduction in dark current density resulting from the dry etch is only one order of magnitude, lower than that suggested by Figure 6.18. The difference in dark current density between the two samples is smallest for the largest devices (smallest perimeter/area ratio), which supports the hypothesis that increased dark current is surface related.

6.2. Passivation

As mentioned in Section 2.2.3., the suppression of surface related sources of dark current is of great importance for improving the device performance of T2SLs. This is further highlighted by the prevalence of the shunt and TAT currents observed in Figures 4.24, 5.21, and 6.22. One approach that I have explored during the course of this project is to block the exposed mesa sidewalls to ambient air using SU8 photoresist. This hinders the formation of native oxides on the mesa sidewalls which act as good conductors for shunt currents. I have also explored an alternative approach in which SiN or Al₂O₃ are used to chemically

passivate the dangling bonds exposed on the mesa sidewalls. Due to favourable Gibbs free energies, these passivation schemes are more likely to form oxides that do not contribute to surface leakage currents, unlike Ga, As, and Sb oxides.

6.3. Summary

An effective dry etching process for LWIR T2SLs has been developed and tested for the fabrication of dry etched T2SLs. I-V measurements indicate the use of this dry etch introduces a surface-related dark current that dominates at temperatures below 140 K. However, no reduction in device performance is observed when operated above this temperature, suggesting the dry etched T2SLs are suitable for the high operating temperatures demanded by modern military and space applications. Even at the low temperature of 77 K, the device performance was within roughly one order of magnitude of the wet etched reference samples. Due to the many avenues for optimisation such as incorporation of passivating precursors, optimisation of the wet etch cleaning process, and use of chemical passivation to suppress surface currents, these results represent a promising proof of concept for T2SL dry etch development at Cardiff.

7. Conclusion

The InAs/GaSb T2SL has increasingly been viewed as a promising competitor to state-of-the-art MCT for LWIR detector applications due to higher theoretical performance limits, better uniformity, ease of fabrication, and less restrictive regulations. However, MCT continues to outperform T2SLs in the key areas of dark current density and quantum efficiency. The aim of the present work is therefore to develop novel methods of improving the performance of T2SLs to achieve their theoretically predicted levels. In Section 2.2, three objectives were identified to pursue this aim:

1. Optimise the InAs and GaSb layer thicknesses through development of a band structure simulation tool and growth, fabrication, and characterisation of novel SL designs (see Section 2.2.2).
2. Determine the mechanisms through which performance degradation occurs in LWIR InAs/GaSb T2SLs grown on GaAs substrates using the IMF array (see Section 2.2.1).
3. Develop dry etching and passivation processes and evaluate the resultant products (see Section 2.2.3.).

7.1. T2SL layer thicknesses

The minimal lattice mismatch between InAs and GaSb affords T2SL device designers a great deal of flexibility for performance optimisation. However, the conventional 14/7 SL, used for most LWIR applications, has not demonstrated a clear superiority over alternative designs. An objective of this project was therefore to demonstrate a novel T2SL design more optimal for LWIR applications than the conventional 14/7 SL. This would be partially achieved through the development of a simulation tool capable of predicting the band parameters of any given T2SL structure. This tool would firstly allow for identification of a range of candidate SL designs to target the 10 μm cut-off wavelength. It is then possible to choose, from the identified structures, the SL that is best suited to a predetermined set of performance criteria

that can be based on the intended application. The tool can also be used for analysis of existing T2SL samples.

The simulation tool was developed through implementation of an 8 band k·p solver in Nextnano³ software. Due to the sparsity of available data on InAs/GaSb T2SLs, the accuracy of the simulation tool was firstly verified through comparison with other structures in the literature. InAs/InAsSb T2SLs, M-structure SLs, W-structure SLs, and an InAsSb/InGaAsSb T2SL were all examined. In each case, the simulation tool was able to accurately reproduce the results of the literature.

Four T2SL samples, three novel designs and one conventional 14/7 SL, were then grown by MBE. The material quality and accuracy of the growth of these samples were firstly verified by XRD measurements. PL measurements then showed that T2SLs with thinner period thicknesses demonstrated better absorption albeit with an altered peak wavelength. However, the 12/4 SL was identified as a structure with better absorption than the conventional 14/7 SL but with a comparable (10 μm) peak wavelength. The optical data collected by PL were also used to verify the simulation tool for InAs/GaSb T2SLs. This allowed for the identification of multiple T2SL structures appropriate for LWIR applications. Two PIN diodes, using the 14/7 and 12/4 SL structures, were then grown, fabricated, and characterised. The 12/4 SL was found to have a lower diffusion current than the conventional 14/7 SL at high temperature (>100 K) but higher dark current at low temperature (<100 K), likely due to shunt currents. The reduced diffusion current of the 12/4 SL is attributed to its reduced effective mass, as calculated by the simulation tool while the increased shunt currents may be related to the difference in the band structure, leading to more energetically active traps. However, it is argued that the 12/4 SL represents a demonstrable improvement over the conventional 14/7 SL due to improved absorption and lower diffusion currents. Furthermore, the dominance of diffusion current under high temperature operation and the industry driven demand for low SWaP devices serve to enhance the advantage of the 12/4 SL for the next generation of IR detectors. This, in combination with the development of an accurate band structure simulation tool, fulfils the requirements of the first objective. Figure 7.1 shows that these diodes have dark current densities roughly two orders of magnitude higher than Rule 07 and one order of magnitude higher than the best performing T2SL device of comparable wavelength. However, it should be noted that, unlike the diodes reported in

Figure 2.1, these diodes were designed without performance-enhancing barrier layers. This allows better study of the dominant dark current mechanisms and thereby provides more information on the relative merits of each T2SL layer thickness design. Furthermore, the 12/4 SL (the diode with higher dark current) was optimised for higher operating temperature, where diffusion current dominates, making the comparison at 77 K unfavourable.

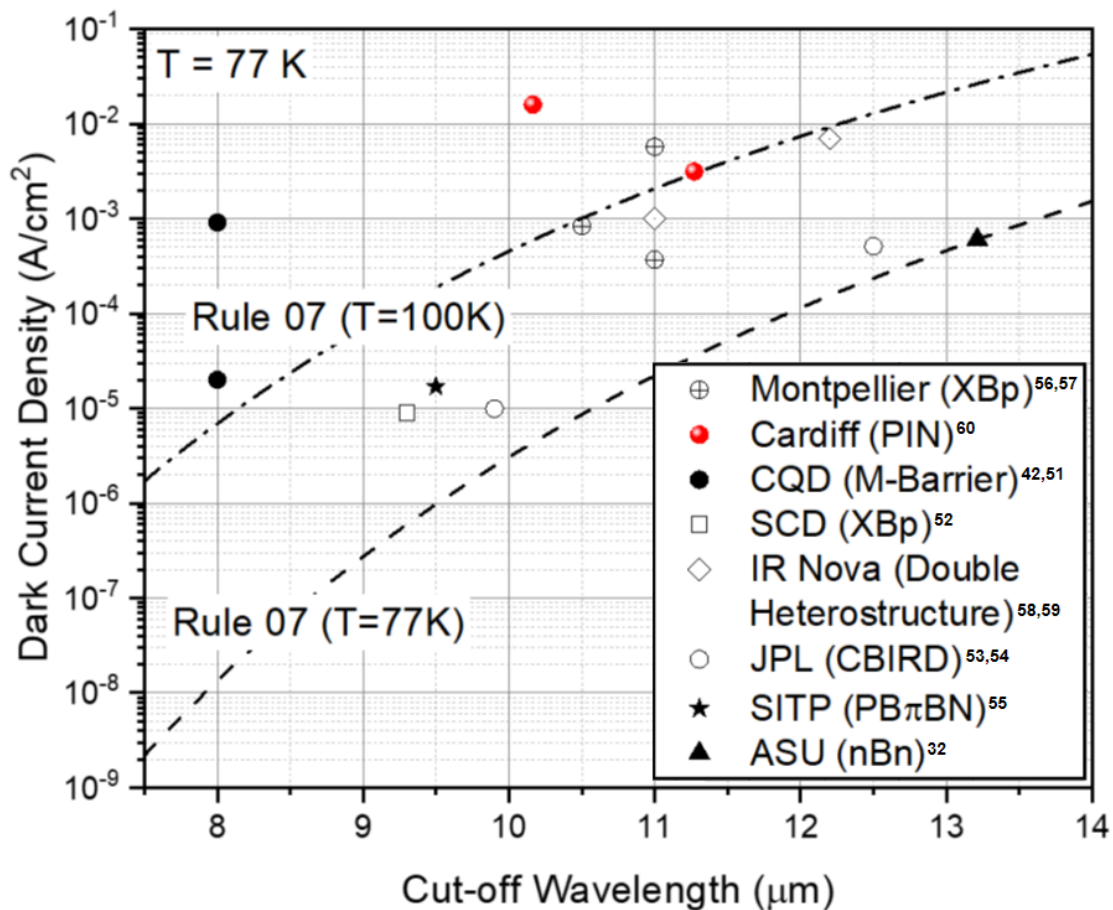


Figure 7.1: The dark current density of the diodes reported in Chapter 4 of this work compared with T2SLs and Rule 07 as reported in Figure 2.1.

7.2. InAs/GaSb T2SLs on GaAs

T2SLs on GaAs substrates have demonstrated considerable cost, manufacturing, and performance advantages but are hindered by reduced material quality arising from the 7.8% lattice mismatch between GaAs and GaSb. However, this issue has now been addressed through use of the IMF array at the GaSb-on-GaAs IF which prevents the propagation of threading dislocations into the device active region. Unfortunately, recent results either show

that T2SLs on GaAs, grown using the IMF array, continue to show degraded performance compared to those grown on conventional GaSb substrates²² or else are vague on traditional performance metrics^{93,94}. The second objective of this project was therefore to determine the mechanisms through which this performance degradation occurs using a detailed comparative characterisation study.

Two 12/4 SL samples were grown on GaSb and GaAs substrates. In the latter case, an IMF array was used to mitigate the strain at the GaSb-on-GaAs IF. Material characterisations, including XRD, Nomarski microscopy, and TEM, were used to compare the structural quality of the two samples. Results suggest that the T2SL on GaAs suffers from a degraded material quality and homogeneity, despite the presence of the IMF array. TEM measurements suggest this originates from the presence of undesirable 60° dislocations at the GaSb-on-GaSb IF, in addition to the desirable 90° dislocations. These issues can be addressed through optimisation of the GaSb buffer layer growth and incorporation of additional strain compensation techniques. PL measurements suggest the optical quality and uniformity of the T2SL on GaAs is degraded in a manner consistent with the degradation in material quality. This is attributed to the increased defect density which results in increased non-radiative recombination.

Two analogous 12/4 SL PIN diodes on GaSb and GaAs substrates were also grown, fabricated, and characterised. The I-V profile of the diode on GaAs is, unfortunately, not diode-like and this sample is therefore assumed to be non-functioning. I-V fitting suggests this is due to strong, defect related current paths on the mesa sidewalls of this device which short the junction. SEM micrographs, comparing the mesa sidewalls of both samples, suggest that this may partially be due to the effect of the citric acid based wet etch on the reduced material quality. A notable contribution from the TAT current was also observed through I-V fitting.

These results show that the performance degradation of T2SLs on GaAs that make use of the IMF array is likely a result of defect-related shunt and TAT currents, originating from the threading dislocations induced by the 60° misfits at the GaSb-on-GaAs IF. This conclusion, supported by both material and device characterisation and analysis, fulfils the requirements of the second objective.

7.3. Dry etching and passivation

Due to the need for high fill factor etches with low leakage currents, there is considerable research into dry etching processes for T2SLs^{221,223-225}. Development of an effective dry etching process was therefore the third objective of this project.

A dry etching process, effective for InAs/GaSb T2SLs, has been demonstrated and tested for fabrication of dry etched T2SLs. SEM micrographs show this process produces relatively smooth sidewalls with good verticality. I-V measurements indicate the use of this dry etch introduces a surface-related dark current that dominates at temperatures below 140 K. However, no reduction in device performance is observed when operated above this temperature, suggesting the dry etched T2SLs are suitable for the high operating temperatures demanded by modern military and space applications. Even at the low temperature of 77 K, the device performance was within roughly two orders of magnitude of the wet etched reference samples. The improvement in etch profiles and comparable HOT dark current achieved by the dry etching process represent a partial fulfilment of the third objective.

7.4. Future work

The results of this project highlight many promising avenues for future study. These are summarised below:

1. The simulation tool demonstrated in Chapters 3 and 4 represents a potential for device design beyond what has been covered in this project. The tool has predicted many T2SL structures suitable for LWIR applications that have yet to be tested experimentally. An informative future study would be to grow, fabricate, and characterise these structures to get a broader understanding of how the T2SL period affects key parameters such as band gap energy, effective mass, and wavefunction overlap. This may allow prediction and demonstration of T2SL structures even more optimal than the 12/4 SL.
2. The superior absorption (Sections 4.1.3 and 4.1.4) and HOT dark current (Section 4.2.5) of the 12/4 SL warrants further demonstration with more sophisticated

characterisation techniques. In particular, the increased detectivity of a 12/4 SL detector, suggested by increased PL peak intensity, should be verified through spectral response measurements. FPA fabrication and characterisation would also be informative to verify the predicted advantages are retained in this context. Implementation of the 12/4 SL within a barrier infrared detector such as the nBn would be informative as, in this case, the diffusion current will, theoretically, dominate at every temperature. This would be useful for verifying whether the 12/4 SL demonstrates a lower total dark current density compared to the conventional 14/7 SL at every temperature or if other sources of dark current undermine its advantages.

3. It is clear from the results of the study of T2SLs on GaAs substrates (Chapter 5) that further optimisation of the growth of the IMF array and GaSb buffer layer should be conducted to reduce the prevalence of 60° misfits and, thereby, threading dislocations. This can be done through optimisation of the growth parameters, particularly growth temperature. Further optimisation can be achieved through incorporation of additional strain compensation measures such as thicker buffer layers, dislocation filters, and growth islands. The efficacy of these measures can be appraised through the characterisation techniques described in Chapter 5.
4. The dry etch process described in Chapter 6 requires further optimisation to minimise the surface leakage induced by the etch. Firstly, increasing the temperature at which the etch is conducted, to around 200°C may assist in the desorption of the InCl_x by-products which have low volatility at the 60°C chamber temperature used in Chapter 6. Secondly, incorporation of passivating etchants such as CH_4 and H_2 into the existing recipe may be effective in reducing surface leakage. Thirdly, optimisation of the wet etch used to remove the dry etch damage should be undertaken as the present recipe was not developed for cleaning purposes. Once each of these optimisations has been implemented, the uniformity of the etch should be verified and, eventually, used to fabricate T2SL-based FPAs.

If the above four future works are achieved, it may be possible to demonstrate a LWIR T2SL with lower dark current, better absorption, enhanced detectivity through use of GaAs substrates, and optimised fabrication. Such a device may be preferable to MCT in certain applications or even be able to surpass the current performance benchmark set by MCT.

Finally, it is argued that the stated aim of finding novel methods of improving the performance levels of T2SLs has been achieved through the three objectives outlined in Section 2.2. Firstly, in fulfilment of the objective set out in Section 2.2.2, a band-structure simulation tool for T2SLs has been developed and utilised in the demonstration of a novel LWIR T2SL design with better absorption and lower HOT dark current density compared to a conventional design. Secondly, in fulfilment of the objective set out in Section 2.2.1, T2SLs have been grown fabricated and characterised on GaAs substrates and the mechanisms giving rise to performance degradation identified. Thirdly, in fulfilment of the objective, an effective dry etch process has been developed with no detriment to HOT dark current. With the fulfilment of these objectives, the overall aim of the project, stated above, has been achieved.

References

1. IR (Infrared) Camera Market 2023 | Industry Size, Share & Growth Analysis.
<http://www.sbwire.com/press-releases/ir-infrared-camera-market-size-to-exceed-usd-68-billion-by-2023-top-key-players-are-axis-communications-flir-systems-fluke-corporation-l3-technologies-pelco-by-schneider-electric-raytheon-1082141.htm>.
2. Tidrow, M. Z. & Reago, D. A. VISTA video and overview. In: Fulop, G. F., Hanson, C. M., Norton, P. R., Andresen, B. F. & Miller, J. L. editors. *Infrared Technology and Applications XLIII* **10177 21** (2017).
3. C5ISR Center U.S.ARMY CCDC | NVESD.
https://c5isr.ccdc.army.mil/inside_c5isr_center/nvesd/.
4. Rogalski, A., Martyniuk, P. & Kopytko, M. Type-II superlattice photodetectors versus HgCdTe photodiodes. *Progress in Quantum Electronics* **68** 100228 (2019).
5. Sai-Halasz, G. A., Tsu, R. & Esaki, L. A new semiconductor superlattice. *Appl Phys Lett* **30**, 651–653 (1977).
6. Plis, E. A. InAs/GaSb Type-II Superlattice Detectors. *Advances in Electronics* **2014**, 1–12 (2014).
7. Kwan, D., Kesaria, M., Anyebe, E. A. & Huffaker, D. Recent trends in 8–14 μm type-II superlattice infrared detectors. *Infrared Physics and Technology* **116** 103756 (2021).
8. Sapritsky, V, & Prokhorov, A. Blackbody Radiometry. Volume 1, Fundamentals (Springer Switzerland, 2020).
9. Plis, E. A. Mid-IR type-II InAs/GaSb nanoscale superlattice sensors. (University of New Mexico, 2007).
10. Razeghi, M. & Nguyen, B. M. Band gap tunability of Type II Antimonide-based superlattices. *Phys Procedia* **3**, 1207–1212 (2010).
11. Smith, D. L. & Mailhot, C. Proposal for strained type II superlattice infrared detectors. *J Appl Phys* **62**, 2545–2548 (1987).

12. Youngdale, E. R. *et al.* Auger lifetime enhancement in InAs-Ga_{1-x}In_xSb superlattices. *Appl Phys Lett* **64**, 3160–3162 (1994).
13. Grein, C. H., Young, P. M., Flatté, M. E. & Ehrenreich, H. Long wavelength InAs/InGaSb infrared detectors: Optimization of carrier lifetimes. *J Appl Phys* **78**, 7143–7152 (1995).
14. Sai-Halasz, G. A., Esaki, L. & Harrison, W. A. InAs-GaSb superlattice energy structure and its semiconductor-semimetal transition. *Phys Rev B* **18**, 2812–2818 (1978).
15. Nucho, R. N. & Madhukar, A. Tight-binding study of the electronic structure of the InAs-GaSb (001) superlattice. *J Vac Sci Technol* **15**, 1530–1534 (1978).
16. Johnson, J. L. *et al.* Electrical and optical properties of infrared photodiodes using the InAs/Ga_{1-x}In_xSb superlattice in heterojunctions with GaSb. *J Appl Phys* **80**, 1116–1127 (1996).
17. Mohseni, H. *et al.* Growth and characterization of InAs/GaSb photoconductors for long wavelength infrared range. *Appl Phys Lett* **71**, 1403 (1998).
18. Fuchs, F. *et al.* High performance InAs/Ga_{1-x}In_xSb superlattice infrared photodiodes. *Appl Phys Lett* **71**, 3251–3253 (1997).
19. Cabanski, W. A. *et al.* Third-generation focal plane array IR detection modules and applications. In: Andresen, B. F. & Fulop, G. F. editors. *Infrared Technology and Applications* **5406** 184 (2004).
20. Osbourn, G. C. InAsSb strained-layer superlattices for long wavelength detectors applications. *Journal of Vacuum Science & Technology B: Microelectronics Processing and Phenomena* **2**, 176–178 (1983).
21. Knox, C. S. *et al.* Partial hybridisation of electron-hole states in an InAs/GaSb double quantum well heterostructure. *Semicond Sci Technol* **32**, 104002 (2017).
22. Korkmaz, M., Arıkan, B., Suyolcu, Y. E., Aslan, B. & Serincan, U. Performance evaluation of InAs/GaSb superlattice photodetector grown on GaAs substrate using AlSb interfacial misfit array. *Semicond Sci Technol* **33**, 035002 (2018).
23. Ciesla, C. M. *et al.* Suppression of Auger recombination in arsenic-rich InAs_{1-x}Sb_x strained layer super-lattices. *J Appl Phys* **80**, 2994–2997 (1996).

24. Pullin, M. J. *et al.* Room-temperature InAsSb strained-layer superlattice light-emitting diodes at $\lambda=4.2 \mu\text{m}$ with AlSb barriers for improved carrier confinement. *Appl Phys Lett* **74**, 2384–2386 (1999).
25. Wilk, A. *et al.* Type-II InAsSb/InAs strained quantum-well laser diodes emitting at $3.5 \mu\text{m}$. *Appl Phys Lett* **77**, 2298–2300 (2000).
26. Zhang, Y. H. Continuous wave operation of InAs/InAs_xSb_{1-x} midinfrared lasers. *Appl Phys Lett* **66**, 118 (1995).
27. Lackner, D. *et al.* Strain balanced InAs/InAsSb superlattice structures with optical emission to $10 \mu\text{m}$. *Appl Phys Lett* **95**, 081906 (2009).
28. Steenbergen, E. H. *et al.* Significantly improved minority carrier lifetime observed in a long-wavelength infrared III-V type-II superlattice comprised of InAs/InAsSb. *Appl Phys Lett* **99**, 251110 (2011).
29. Steenbergen, E. H. *et al.* Structural and optical characterization of type-II InAs/InAs_{1-x}Sb_x superlattices grown by metalorganic chemical vapor deposition. *Appl Phys Lett* **99**, 071111 (2011).
30. Huang, Y. *et al.* Epitaxial growth and characterization of InAs/GaSb and InAs/InAsSb type-II superlattices on GaSb substrates by metalorganic chemical vapor deposition for long wavelength infrared photodetectors. *J Cryst Growth* **314**, 92–96 (2011).
31. Zuo, D. *et al.* Direct minority carrier transport characterization of InAs/InAsSb superlattice nBn photodetectors. *Appl Phys Lett* **106**, 071107 (2015).
32. Prins, A. D. *et al.* Evidence for a defect level above the conduction band edge of InAs/InAsSb type-II superlattices for applications in efficient infrared photodetectors. *Appl Phys Lett* **106**, 171111 (2015).
33. Kim, H. S. *et al.* Long-wave infrared nBn photodetectors based on InAs/InAsSb type-II superlattices. *Appl Phys Lett* **101**, 161114 (2012).
34. Haddadi, A., Chen, G., Chevallier, R., Hoang, A. M. & Razeghi, M. InAs/InAs_{1-x}Sb_x type-II superlattices for high performance long wavelength infrared detection. *Appl Phys Lett* **105**, 121104 (2014).

35. Haddadi, A., Dehzangi, A., Adhikary, S., Chevallier, R. & Razeghi, M. Background-limited long wavelength infrared InAs/InAs_{1-x}Sb_x type-II superlattice-based photodetectors operating at 110 K. *APL Mater* **5**, 035502 (2017).
36. Hoang, A. M., Chen, G., Chevallier, R., Haddadi, A. & Razeghi, M. High performance photodiodes based on InAs/InAsSb type-II superlattices for very long wavelength infrared detection. *Appl Phys Lett* **104**, 251105 (2014).
37. Ting, D. Z., Soibel, A. & Gunapala, S. D. Hole effective masses and subband splitting in type-II superlattice infrared detectors. *Appl Phys Lett* **108**, 183504 (2016).
38. Gunapala, S. *et al.* Antimonides Type-II superlattice digital focal plane arrays for Space remote sensing instruments. In: Karafolas, N., Sodnik, Z. & Cugny, B. editors. *International Conference on Space Optics — ICSO 2018* **11180** 136 (2019).
39. Ting, D. Z. *et al.* InAs/InAsSb Type-II Strained Layer Superlattice Barrier Infrared Detectors. In: *2019 IEEE Photonics Conference* (2019).
40. Tang, P. *et al.* 4-11 μm infrared emission and 300 K light emitting diodes from arsenic-rich InAs_{1-x}Sb_x strained layer superlattices. *Semicond Sci Technol* **10**, 1177–1180 (1995).
41. Michalczewski, K. *et al.* Demonstration of HOT LWIR T2SLs InAs/InAsSb photodetectors grown on GaAs substrate. *Infrared Phys Technol* **95**, 222–226 (2018).
42. Sidor, D. E., Savich, G. R. & Wicks, G. W. Surface Leakage Mechanisms in III–V Infrared Barrier Detectors. *J Electron Mater* **45**, 4663–4667 (2016).
43. Wu, D. H., Dehzangi, A., Zhang, Y. Y. & Razeghi, M. Demonstration of long wavelength infrared type-II InAs/InAs_{1-x}Sb_x superlattices photodiodes on GaSb substrate grown by metalorganic chemical vapor deposition. *Appl Phys Lett* **112**, 241103 (2018).
44. Ting, D. Z., Soibel, A. & Gunapala, S. D. Hole effective masses and subband splitting in type-II superlattice infrared detectors. *Appl Phys Lett* **108**, 183504 (2016).
45. Rogalski, A., Kopytko, & M., Martyniuk, P. Antimonide-based infrared detectors : a new perspective. SPIE (2018).
46. Gopal, V. *et al.* Modelling of dark characteristics of mercury cadmium telluride n +-p junctions. *Infrared Phys Technol* **44**, 143–152 (2003).

47. Gopal, V. *et al.* Modelling of electrical characteristics of midwave type II InAs/GaSb strain layer superlattice diodes. *J Appl Phys* **104**, 124506 (2008).
48. Gopal, V., Gautam, N., Plis, E. & Krishna, S. Modelling of current-voltage characteristics of infrared photo-detectors based on type - II InAs/GaSb super-lattice diodes with unipolar blocking layers. *AIP Adv* **5**, 097132 (2015).
49. Holst, G. C. *The Infrared & Electro-Optical Systems Handbook*. SPIE Optical Engineering Press (1993).
50. Kinch, M. A. *State-of-the-Art Infrared Detector Technology*. SPIE Press (2014).
51. Tennant, W. E. ‘Rule 07’ revisited: Still a good heuristic predictor of p/n HgCdTe photodiode performance? *Journal of Electronic Materials* **39** 1030–1035 (2010).
52. Nguyen, B. M., Hoffman, D., Huang, E. K. W., Delaunay, P. Y. & Razeghi, M. Background limited long wavelength infrared type-II InAs/GaSb superlattice photodiodes operating at 110 K. *Appl Phys Lett* **93**, 123502 (2008).
53. Klipstein, P. C. *et al.* Type II superlattice technology for LWIR detectors. In: Andresen, B. F., Fulop, G. F., Hanson, C. M. & Norton, P. R. editors. *Infrared Technology and Applications XLII* **9819**, 216–225 (2016).
54. Ting, D. Z. Y. *et al.* A high-performance long wavelength superlattice complementary barrier infrared detector. *Appl Phys Lett* **95**, 023508 (2009).
55. Gunapala, S. D. *et al.* Type-II strained-layer superlattice digital focal plane arrays for earth remote sensing instruments. In: Neeck, S. P., Kimura, T. & Martimort, P. editors. *Sensors, Systems, and Next-Generation Satellites XXIII* **11151** 36 (2019).
56. Huang, M. *et al.* InAs/GaAsSb Type-II Superlattice LWIR Focal Plane Arrays Detectors Grown on InAs Substrates. *IEEE Photonics Technology Letters* **32**, 453–456 (2020).
57. Christol, P. *et al.* InAs/GaSb Type-II superlattice (T2SL) photodetector operating in the very-long wavelength infrared (VLWIR) spectral domain. In: Sodnik, Z., Karafolas, N., and Cugny, B. editors. *International Conference on Space Optics* **11180**, 2394–2400 (2019).

58. Alchaar, R., Rodriguez, J. B., Höglund, L., Naureen, S. & Christol, P. Characterization of an InAs/GaSb type-II superlattice barrier photodetector operating in the LWIR domain. *AIP Adv* **9**, 055012 (2019).
59. Höglund, L. *et al.* Advantages of T2SL: results from production and new development at IRnova. In: Andresen, B. F., Gabor, F. F., Hanson, C. M., & Norton P. R. editors. *Infrared technology and applications XLII* **9819**, 250–259 (2016).
60. Ivanov, R. *et al.* T2SL development for space at IRnova: from eSWIR to VLWIR. In: Neeck, S. P., Matrimort, P., Kimura, T. editors. *Sensors, Systems, and Next-Generation Satellites XXIII* **11151**, 194–202 (2019).
61. Delmas, M., Kwan, D. C. M., Debnath, M. C., Liang, B. L. & Huffaker, D. L. Flexibility of Ga-containing Type-II superlattice for long-wavelength infrared detection. *J Phys D Appl Phys* **52**, 475102 (2019).
62. Klipstein, P. C. *et al.* Minority carrier lifetime and diffusion length in type II superlattice barrier devices. *Infrared Phys Technol* **96**, 155–162 (2019).
63. Matthews, J. W. & Blakeslee, A. E. Defects in epitaxial multilayers: I. Misfit dislocations. *J Cryst Growth* **27**, 118–125 (1974).
64. Höglund, L. *et al.* Influence of shallow versus deep etching on dark current and quantum efficiency in InAs/GaSb superlattice photodetectors and focal plane arrays for long wavelength infrared detection. *Infrared Phys Technol* **95**, 158–163 (2018).
65. Klipstein, P. C. *et al.* Type II Superlattice Infrared Detector Technology at SCD. *Journal of Electronic Materials* **47**, 5725–5729 (2018).
66. Hanna, S. *et al.* Space Application Requirement Breakdown and Sensor Concept Implementation for MCT-Based LWIR and VLWIR 2D High-Performance Focal Plane Detector Arrays at AIM. *Journal of Electronic Materials* **49**, 6946–6956 (2020).
67. Haiml, M., Eich, D., Fick, W. & Figgemeier, H. Below Rule'07 low dark current LWIR and VLWIR MCT 2D focal plane detector arrays from AIM. In: Cugny, B., Karafolas, N., & Sodnik, Z. editors. *International Conference on Space Optics* **10562**, 1759–1766 (2019).

68. Lutz, H., Breiter, R., Eich, D., Figgemeier, H. & Hanna, S. Improved high performance MCT MWIR and LWIR modules. In: Andresen, B. F., Gabor, F. F., & Hanson, C. M. editors. *Infrared technology and applications XLV* **11002**, 249–261 (2019).
69. Asici, B. *et al.* The status of LWIR MCT detector development at ASELSAN. In: Andresen, B. F., Gabor, F. F., & Hanson, C. M. editors. *Infrared technology and applications XLV* **11002**, 290–298 (2019).
70. Rogalski, A., Martyniuk, P. & Kopytko, M. InAs/GaSb type-II superlattice infrared detectors: Future prospect. *Applied Physics Reviews* **4** 031304 (2017).
71. Taghipour, Z. *et al.* Temperature-Dependent Minority-Carrier Mobility in p-Type InAs/GaSb Type-II-Superlattice Photodetectors. *Phys Rev Appl* **11**, 024047 (2019).
72. Connelly, B. C. *et al.* Investigation of trap states in mid-wavelength infrared type II superlattices using time-resolved photoluminescence. *J Electron Mater* **42**, 3203–3210 (2013).
73. Donetsky, D., Svensson, S. P., Vorobjev, L. E. & Belenky, G. Carrier lifetime measurements in short-period InAs/GaSb strained-layer superlattice structures. *Appl Phys Lett* **95**, 212104 (2009).
74. Donetsky, D., Belenky, G., Svensson, S. & Suchalkin, S. Minority carrier lifetime in type-2 InAs–GaSb strained-layer superlattices and bulk HgCdTe materials. *Appl Phys Lett* **97**, 052108 (2010).
75. Belenky, G. *et al.* Effects of carrier concentration and phonon energy on carrier lifetime in type-2 SLS and properties of InAs_{1-x}Sb_x alloys. In: Andresen, B. F., Gabor, F. F., & Hanson, C. M. editors. *Infrared technology and applications XXXVII* **8012**, 318–327 (2011).
76. Connelly, B. C., Metcalfe, G. D., Shen, H. & Wraback, M. Direct minority carrier lifetime measurements and recombination mechanisms in long-wave infrared type II superlattices using time-resolved photoluminescence. *Appl Phys Lett* **97**, 251117 (2010).
77. Höglund, L. *et al.* Minority carrier lifetime and photoluminescence studies of antimony-based superlattices. In: Strojnik, M. & Paez, G. editors. *Infrared Remote Sensing and Instrumentation XX* **8511**, 47–53 (2013).

78. Höglund, L. *et al.* Influence of radiative and non-radiative recombination on the minority carrier lifetime in midwave infrared InAs/InAsSb superlattices. *Appl Phys Lett* **103**, 221908 (2013).
79. Olson, B. V. *et al.* Auger recombination in long-wave infrared InAs/InAsSb type-II superlattices. *Appl Phys Lett* **107**, 261104 (2015).
80. Aytac, Y. *et al.* Effects of layer thickness and alloy composition on carrier lifetimes in mid-wave infrared InAs/InAsSb superlattices. *Appl Phys Lett* **105**, 022107 (2014).
81. Pellegrino, J. & DeWames, R. Minority carrier lifetime characteristics in type II InAs/GaSb LWIR superlattice $n^+p^+p^+$ photodiodes. In: Andresen, B. F., Fulop, G. F., & Norton, P. R. editors. *Infrared Technology and Application XXXV* **7298**, 646–655 (2009).
82. Kinch, M. A. *et al.* Minority carrier lifetime in p-HgCdTe. *Journal of Electronic Materials* **34**, 880–884 (2005).
83. Krishnamurthy, S. & Casselman, T. N. A detailed calculation of the auger lifetime in p-type HgCdTe. *Journal of Electronic Materials* **29**, 828–831 (2000).
84. Youngdale, E. R. *et al.* Auger lifetime enhancement in InAs-Ga_{1-x}In_xSb superlattices. *Appl Phys Lett* **64**, 3160–3162 (1994).
85. Rogalski, A., Martyniuk, P. & Kopytko, M. InAs/GaSb type-II superlattice infrared detectors: Future prospect. *Appl Phys Rev* **4**, 031304 (2017).
86. Klipstein, P. C. *et al.* Performance Limits of III–V Barrier Detectors. *J Electron Mater* **49** 6893–6899 (2020).
87. Aytac, Y. *et al.* Temperature-dependent optical measurements of the dominant recombination mechanisms in InAs/InAsSb type-2 superlattices. *J Appl Phys* **118**, 125701 (2015).
88. Herres, N. *et al.* Effect of interfacial bonding on the structural and vibrational properties of InAs/GaSb superlattices. *Phys Rev B* **53**, 15688 (1996).
89. Mohseni, H., Wojkowski, J., Razeghi, M., Brown, G. & Mitchel, W. Uncooled InAs-GaSb type-II infrared detectors grown on GaAs substrates for the 8-12- μ m atmospheric window. *IEEE J Quantum Electron* **35**, 1041–1044 (1999).

90. Mohseni, H. *et al.* Growth and characterization of InAs/GaSb photoconductors for long wavelength infrared range. *Appl Phys Lett* **71**, 1403–1405 (1997).
91. Benyahia, D. *et al.* Electrical Properties of Midwave and Longwave InAs/GaSb Superlattices Grown on GaAs Substrates by Molecular Beam Epitaxy. *Nanoscale Res Lett* **13**, 196 (2018).
92. Pour, S. A., Nguyen, B. M., Bogdanov, S., Huang, E. K. & Razeghi, M. Demonstration of high performance long wavelength infrared type II InAs/GaSb superlattice photodiode grown on GaAs substrate. *Appl Phys Lett* **95**, 173505 (2009).
93. Michalczewski, K., Tsai, T. Y., Martyniuk, P. & Wu, C. H. Demonstration of HOT photoresponse of MWIR T2SLs InAs/InAsSb photoresistors. *Bulletin of the Polish Academy of Sciences: Technical Sciences* **67**, 141–145 (2019).
94. Müller, R. *et al.* High operating temperature InAs/GaSb type-II superlattice detectors on GaAs substrate for the long wavelength infrared. *Infrared Phys Technol* **96**, 141–144 (2019).
95. Müller, R. *et al.* Thermoelectrically-Cooled InAs/GaSb Type-II Superlattice Detectors as an Alternative to HgCdTe in a Real-Time Mid-Infrared Backscattering Spectroscopy System. *Micromachines (Basel)* **11**, 1124 (2020).
96. Michalczewski, K. *et al.* Demonstration of the Very Long Wavelength Infrared Type-II Superlattice InAs/InAsSb GaAs Immersed Photodetector Operating at Thermoelectric Cooling. *IEEE Electron Device Letters* **40**, 1396–1398 (2019).
97. Benyahia, D. *et al.* Optimization of the interfacial misfit array growth mode of GaSb epilayers on GaAs substrate. *J Cryst Growth* **483**, 26–30 (2018).
98. Taylor, P. J. *et al.* Optoelectronic device performance on reduced threading dislocation density GaAs/Si. *J Appl Phys* **89**, 4365 (2001).
99. Huang, S. H. *et al.* Strain relief by periodic misfit arrays for low defect density GaSb on GaAs. *Appl Phys Lett* **88**, 131911 (2006).
100. Huffaker, D., Dawson, L. & Balakrishnan, G. US20070160100A1 - Misfit dislocation forming interfacial self-assembly for growth of highly-mismatched III-Sb alloys - Google Patents. (2007).

101. Qian, W., Skowronski, M., Kaspi, R., De Graef, M. & Dravid, V. P. Nucleation of misfit and threading dislocations during epitaxial growth of GaSb on GaAs(001) substrates. *J Appl Phys* **81**, 7268 (1998).
102. Kim, J. H., Seong, T. Y., Mason, N. J. & Walker, P. J. Morphology and defect structures of GaSb islands on GaAs grown by metalorganic vapor phase epitaxy. *Journal of Electronic Materials* **27**, 466–471 (1998).
103. Qian, W., Skowronski, M. & Kaspi, R. Dislocation Density Reduction in GaSb Films Grown on GaAs Substrates by Molecular Beam Epitaxy. *J Electrochem Soc* **144**, 1430–1434 (1997).
104. Huang, S., Balakrishnan, G. & Huffaker, D. L. Interfacial misfit array formation for GaSb growth on GaAs. *J Appl Phys* **105**, 103104 (2009).
105. Löwdin, P. A Note on the Quantum-Mechanical Perturbation Theory. *J Chem Phys* **19**, 1396 (2004).
106. Martyniuk, P. *et al.* Demonstration of the long wavelength InAs/InAsSb type-II superlattice based methane sensor. *Sens Actuators A Phys* **332**, 113107 (2021).
107. Kwan, D. C. M. *et al.* Optical and structural investigation of a 10 μm InAs/GaSb type-II superlattice on GaAs. *Appl Phys Lett* **118**, 203102 (2021).
108. Khoshakhlagh, A. *et al.* Background carrier concentration in midwave and longwave InAs/GaSb type II superlattices on GaAs substrate. *Appl Phys Lett* **97**, 051109 (2010).
109. Abrahams, M. S., Weisberg, L. R., Buiocchi, C. J. & Blanc, J. Dislocation morphology in graded heterojunctions: GaAs $_{1-x}$ P $_x$. *Journal of Materials Science* **4**, 223–235 (1969).
110. Grider, D. E. *et al.* Metamorphic In $_y$ Ga $_{1-y}$ As/In $_z$ Al $_{1-z}$ As heterostructure field effect transistors grown on GaAs(001) substrates using molecular-beam epitaxy. *Journal of Vacuum Science & Technology B: Microelectronics Processing and Phenomena* **8**, 301 (1998).
111. Inoue, K., Harmand, J. C. & Matsuno, T. High-quality In $_x$ Ga $_{1-x}$ As/InAlAs modulation-doped heterostructures grown lattice-mismatched on GaAs substrates. *J Cryst Growth* **111**, 313–317 (1991).

112. Shen, L., Wieder, H. H. & Chang, W. S. C. Low Temperature Grown Thin InAlAs Step Graded Buffers for Application on Optical Modulator at 1.3 μm . *MRS Online Proceedings Library (OPL)* **379**, 297–301 (1995).
113. Wakita, A. *et al.* Low-noise bias reliability of AlInAs/GaInAs modulation-doped field effect transistors with linearly graded low-temperature buffer layers grown on GaAs substrates. *Japanese Journal of Applied Physics, Part 1: Regular Papers and Short Notes and Review Papers* **38**, 1186–1189 (1999).
114. Shang, X. Z. *et al.* Low temperature step-graded InAlAs/GaAs metamorphic buffer layers grown by molecular beam epitaxy. *J Phys D Appl Phys* **39**, 1800 (2006).
115. Lee, B. *et al.* Optical properties of InGaAs linear graded buffer layers on GaAs grown by metalorganic chemical vapor deposition. *Appl Phys Lett* **68**, 2973 (1998).
116. Ćngring, I. *et al.* 1.58 μm InGaAs quantum well laser on GaAs. *Appl Phys Lett* **91**, 221101 (2007).
117. Ji-Fang, H. *et al.* GaAs-based long-wavelength InAs quantum dots on multi-step-graded InGaAs metamorphic buffer grown by molecular beam epitaxy. *JPhD* **44**, 335102 (2011).
118. Wong, L. H. *et al.* Thermal stability of a reverse-graded SiGe buffer layer for growth of relaxed SiGe epitaxy. *Electrochemical and Solid-State Letters* **9**, G114 (2006).
119. Aifer, E. H. *et al.* Shallow-etch mesa isolation of graded-bandgap ‘W’-structured type II superlattice photodiodes. *J Electron Mater* **39**, 1070–1079 (2010).
120. Aifer, E. H. *et al.* W-structured type-II superlattice-based long- and very long wavelength infrared photodiodes. In: Razeghi, M. & Brown, G. J editors. *Quantum Sensing and Nanophotonic Devices II* **5732** 259 (2005).
121. Aifer, E. H. *et al.* Recent progress in W- structured type-II superlattice photodiodes. In: Razeghi, M. & Brown, G. J editors. *Quantum Sensing and Nanophotonic Devices IV* **6479** 64790Y (2007).
122. Vurgaftman, I. *et al.* Graded band gap for dark-current suppression in long-wave infrared W-structured type-II superlattice photodiodes. *Appl Phys Lett* **89**, 121114 (2006).

123. Nguyen, B.-M., Razeghi, M., Nathan, V. & Brown, G. J. Type-II M structure photodiodes: an alternative material design for mid-wave to long wavelength infrared regimes. In: Razeghi, M. & Brown, G. J. editors. *Quantum Sensing and Nanophotonic Devices IV* **6497** 64790S (2007).
124. Salihoglu, O., Muti, A. & Aydinli, A. A Comparative Passivation Study for InAs/GaSb Pin Superlattice Photodetectors. *IEEE J Quantum Electron* **49**, 661–666 (2013).
125. Salihoglu, O. *et al.* Electronic and optical properties of 4.2 μm "N" structured superlattice MWIR photodetectors. *Infrared Phys Technol* **59**, 36–40 (2013).
126. Salihoglu, O., Muti, A., Turan, R., Ergun, Y. & Aydinli, A. Low dark current N structure superlattice MWIR photodetectors. In: Andresen B. F., Fulop, F. F., Hanson, C. M., & Norton, P. R. editors. *Infrared Technology and Applications XL* **9070** 907012 (2014).
127. Wu, D., Dehzangi, A., Li, J. & Razeghi, M. High performance Zn-diffused planar mid-wavelength infrared type-II InAs/InAs_{1-x}Sb_x superlattice photodetector by MOCVD. *Appl Phys Lett* **116**, 161108 (2020).
128. Dehzangi, A., Wu, D., McClintock, R., Li, J. & Razeghi, M. Planar nBn type-II superlattice mid-wavelength infrared photodetectors using zinc ion-implantation. *Appl Phys Lett* **116**, 221103 (2020).
129. Dehzangi, A. *et al.* Demonstration of Planar Type-II Superlattice-Based Photodetectors Using Silicon Ion-Implantation. *Photonics* **7**, 68 (2020).
130. Rajavel, R. *et al.* Fabrication of InAs/GaSb type-II superlattice LWIR planar photodiodes. In: Andresen, B. F., Fulop, G. F., & Norton, P. R. editors. *Infrared Technology and Applications XXXV* **7298**, 72981S (2009).
131. Huang, E. K. W., Hoffman, D., Nguyen, B. M., Delaunay, P. Y. & Razeghi, M. Surface leakage reduction in narrow band gap type-II antimonide-based superlattice photodiodes. *Appl Phys Lett* **94**, 053506 (2009).
132. Kim, H. S. *et al.* Reduction of surface leakage current in InAs/GaSb strained layer long wavelength superlattice detectors using SU-8 passivation. *Appl Phys Lett* **97**, 143512 (2010).

133. Specht, T. *et al.* Side wall passivation of LWIR P-type superlattice detectors using atomic layer deposition. In: *RAPID 2018 - 2018 IEEE Research and Applications of Photonics In Defense Conference* 31–34 (2018).
134. Salihoglu, O. *et al.* Atomic layer deposited Al₂O₃ passivation of type II InAs/GaSb superlattice photodetectors. *Journal of Applied Physics* **111** 074509 (2012).
135. Rehm, R., Walther, M., Fuchs, F., Schmitz, J. & Fleissner, J. Passivation of InAs/(GaIn) Sb short-period superlattice photodiodes with 10 μm cutoff wavelength by epitaxial overgrowth with Al_xGa_{1-x}As_ySb_{1-y}. *Appl Phys Lett* **86**, 1–3 (2005).
136. Plis, E. *et al.* Passivation of long-wave infrared InAs/GaSb superlattice detectors with epitaxially grown ZnTe. In: Andresen, B. F., Fulop, G. F., Hanson, C. M. & Norton, P. R. editors. *Infrared Technology and Applications XL* **9070** 907010 (2014).
137. Henry, N. C. *et al.* Surface conductivity of InAs/GaSb superlattice infrared detectors treated with thiolated self assembled monolayers. *Appl Phys Lett* **108**, 011606 (2016).
138. Nolde, J. A. *et al.* Reticulated shallow etch mesa isolation for controlling surface leakage in GaSb-based infrared detectors. *Appl Phys Lett* **111**, 051102 (2017).
139. Chen, G. *et al.* Elimination of surface leakage in gate controlled type-II InAs/GaSb mid-infrared photodetectors. *Appl Phys Lett* **99**, 183503 (2011).
140. Chen, G. *et al.* Surface leakage investigation via gated type-II InAs/GaSb long-wavelength infrared photodetectors. *Appl Phys Lett* **101**, 213501 (2012).
141. Chen, G. *et al.* Effect of sidewall surface recombination on the quantum efficiency in a Y₂O₃ passivated gated type-II InAs/GaSb long-infrared photodetector array. *Appl Phys Lett* **103**, 223501 (2013).
142. Chen, G., Hoang, A. M. & Razeghi, M. Evaluating the size-dependent quantum efficiency loss in a SiO₂-Y₂O₃ hybrid gated type-II InAs/GaSb long-infrared photodetector array. *Appl Phys Lett* **104**, 103509 (2014).
143. Kim, H. S. *et al.* Dark current improvement of the type-II InAs / GaSb superlattice photodetectors by using a gate bias control. *Journal of the Korean Physical Society* **66**, 535–538 (2015).

144. Akel, K., Hoştut, M., Akin, T. & Ergün, Y. Interband optical absorption obtained by pseudopotential method for type-II InAs/GaSb SL photodetectors. *J Phys D Appl Phys* **54**, 195103 (2021).
145. Dente, G. C. & Tilton, M. L. Comparing pseudopotential predictions for InAs/GaSb superlattices. *Phys Rev B* **66**, 165307 (2002).
146. Wei, Y. & Razeghi, M. Modeling of type-II InAs/GaSb superlattices using an empirical tight-binding method and interface engineering. *Phys Rev B* **69**, 085316 (2004).
147. Cardona, M. & Pollak, F. H. Energy-Band Structure of Germanium and Silicon: The $k \cdot p$ Method, *Phys. Rev.* **2**, 530–543 (1966).
148. Boyer-Richard, S. et al. 30-band $k \cdot p$ method for quantum semiconductor heterostructures, *Appl. Phys. Lett.* **25**, 251913 (2011).
149. Chao, C. Y.-P. & Chuang, S. L. Spin-orbit-coupling effects on the valence-band structure of strained semiconductor quantum wells, *Phys. Rev. B* **7**, 4110–4122 (1992).
150. T. B. Bahder, Eight-band $k \cdot p$ model of strained zinc-blende crystals, *Phys. Rev. B* **17**, 11992–12001 (1990).
151. Andlauer, T. Optoelectronic and spin-related properties of semiconductor nanostructures in magnetic fields. (Technische Universität München, 2009).
152. Birner, S. Modeling of semiconductor nanostructures and semiconductor-electrolyte interfaces. (Technische Universität München, 2011).
153. Foreman, B. A. Elimination of spurious solutions from eight-band $k \cdot p$ theory, *Phys. Rev. B* **56**, R12748 (1997).
154. Hestenes, M. R. & Stiefel, E. Methods of Conjugate Gradients for Solving Linear Systems, *J. Res. Nat. Bur. Stand.* **49**, 409 (1952).
155. Chan, T. F. & Szeto, T. Composite step product methods for solving nonsymmetric linear systems SIAM, *J. Sci. Comput.* **17**, 1491 (1996).

156. Lanczos, C. J. Solution of Systems of Linear Equations by Minimized Iterations, Res. Nat. Bur. Stand. 49, 33 (1952).
157. nextnano3 - next generation 3D nano device simulator.
<https://www.nextnano.de/nextnano3/>.
158. Livneh, Y. *et al.* K \cdot p model for the energy dispersions and absorption spectra of InAs/GaSb type-II superlattices. *Phys Rev B* **86**, 235311 (2012).
159. Vurgaftman, I., Meyer, J. R. & Ram-Mohan, L. R. Band parameters for III-V compound semiconductors and their alloys. *J Appl Phys* **89**, 5815–5875 (2001).
160. Halvorsen, E., Galperin, Y. & Chao, K. A. Optical transitions in broken gap heterostructures. *Phys Rev B* **61**, 16743 (2000).
161. Wei, S.-H. & Zunger, A. Predicted band-gap pressure coefficients of all diamond and zinc-blende semiconductors: Chemical trends. *Phys Rev B* **60**, 5404 (1999).
162. Wei, S. H. & Zunger, A. Calculated natural band offsets of all II-VI and III-V semiconductors: Chemical trends and the role of cation d orbitals. *Appl Phys Lett* **72**, 2011–2013 (1998).
163. Klipstein, P. C. Operator ordering and interface-band mixing in the Kane-like Hamiltonian of lattice-matched semiconductor superlattices with abrupt interfaces. *Phys Rev B Condens Matter Mater Phys* **81**, 235314 (2010).
164. Kim, H. *et al.* Atomic resolution mapping of interfacial intermixing and segregation in InAs/GaSb superlattices: A correlative study. *J Appl Phys* **113**, 103511 (2013).
165. Kotulak, N. A. *et al.* Three-dimensional visualization of Sb segregation in InAs/InAsSb superlattices using atom probe tomography. *J Appl Phys* **128**, 15302 (2020).
166. Keen, J. A., Lane, D., Kesaria, M., Marshall, A. R. J. & Krier, A. InAs/InAsSb type-II strained-layer superlattices for mid-infrared LEDs. *J Phys D Appl Phys* **51**, 075103 (2018).
167. Liu, P. W. *et al.* Photoluminescence and bowing parameters of InAsSbInAs multiple quantum wells grown by molecular beam epitaxy. *Appl Phys Lett* **89**, 201115 (2006).
168. Nguyen, B.-M., Razeghi, M., Nathan, V. & Brown, G. J. Type-II M structure photodiodes: an alternative material design for mid-wave to long wavelength infrared regimes. In: Razeghi,

- M. & Brown, G. J. editors. *Quantum Sensing and Nanophotonic Devices IV* **6479** 64790S (2007).
169. Nguyen, B. M., Hoffman, D., Delaunay, P. Y. & Razeghi, M. Dark current suppression in type II InAsGaSb superlattice long wavelength infrared photodiodes with M-structure barrier. *Appl Phys Lett* **91**, 163511 (2007).
 170. Du, P. *et al.* Fabrication and Characterization of an InAs(Sb)/In_xGa_{1-x}As_ySb_{1-y} Type-II Superlattice. *Physica Status Solidi - Rapid Research Letters* **13**, 1900474 (2019).
 171. Du, P. *et al.* Mid- and long-infrared emission properties of In_xGa_{1-x}As_ySb_{1-y} quaternary alloy with Type-II InAs/GaSb superlattice distribution. *J Alloys Compd* **847**, 156390 (2020).
 172. Wu, D., Durlin, Q., Dehzangi, A., Zhang, Y. & Razeghi, M. High quantum efficiency mid-wavelength infrared type-II InAs/InAs_{1-x}Sb_x superlattice photodiodes grown by metal-organic chemical vapor deposition. *Appl Phys Lett* **114**, 011104 (2019).
 173. Huang, Y. *et al.* Strain-balanced InAs/GaSb type-II superlattice structures and photodiodes grown on InAs substrates by metalorganic chemical vapor deposition. *Appl Phys Lett* **99**, 011109 (2011).
 174. Haugan, H. J. *et al.* Post growth annealing study on long wavelength infrared InAs/GaSb superlattices. *J Appl Phys* **111**, 053113 (2012).
 175. Chen, X. *et al.* Evolution of interfacial properties with annealing in InAs/GaSb superlattice probed by infrared photoluminescence. *Jpn J Appl Phys* **53**, 082201 (2014).
 176. Delmas, M. *et al.* Radiometric characterization of type-II InAs/GaSb superlattice (t2sl) midwave infrared photodetectors and focal plane arrays. In: Karafolas, N., Cugny, B. & Sodnik, Z. editors. *International Conference on Space Optics — ICSO 2016* **10562** 105623Y (2017).
 177. Herman, M. A. & Sitter, H. *Molecular Beam Epitaxy*. **7** (Springer Berlin Heidelberg, 1996).
 178. Seta, M., Asahi, H., Kim, S. G., Asami, K. & Gonda, S. I. Gas source molecular beam epitaxy/migration enhanced epitaxy growth of InAs/AlSb superlattices. *J Appl Phys* **74**, 5033–5037 (1993).

179. Inoue, M., Yano, M., Furuse, H., Nasu, N. & Iwai, Y. Optical analysis of InAs heterostructures grown by migration-enhanced epitaxy. *Semicond Sci Technol* **8**, S121 (1993).
180. Xu, Z. *et al.* Interface design and properties in InAs/GaSb type-II superlattices grown by molecular beam epitaxy. In: Gong, H., Shi, Z., Chen, Q. & Lu, J. editors. *International Symposium on Photoelectronic Detection and Imaging 2013: Infrared Imaging and Applications* **8907** 89073J (2013).
181. Li, J. H. *et al.* Effect of strain on the growth of InAs/GaSb superlattices: An x-ray diffraction study. *J Appl Phys* **107**, 123504 (2010).
182. Klein B *et al.* Varshni parameters for InAs/GaSb strained layer superlattice infrared photodetectors. *Journal of Physics D* **44**, 075102 (2011).
183. Wu, J., Xu, Z., Chen, J. & He, L. Temperature-dependent photoluminescence of the InAs-based and GaSb-based type-II superlattices. *Infrared Phys Technol* **92**, 18–23 (2018).
184. Fasolino, A., Molinari, E. & Maan, J. C. Calculated superlattice and interface phonons of InAs/GaSb superlattices. *Phys Rev B* **33**, 8889–8891 (1986).
185. Rehm, R. *et al.* InAs/GaSb superlattice focal plane arrays for high-resolution thermal imaging. In: Rogalski, A., Dereniak, E. L. & Sizov, F. F. editors. *Infrared Photoelectronics* **5957** 595707 (2005).
186. Oguz, F., Arslan, Y., Ulker, E., Bek, A. & Ozbay, E. Fabrication of 15- μ m Pitch 640 \times 512 InAs/GaSb Type-II Superlattice Focal Plane Arrays. *IEEE J Quantum Electron* **55**, 161–164 (2019).
187. Hood, A. D., Evans, A. J., Ikhlassi, A., Lee, D. L. & Tennant, W. E. LWIR strained-layer superlattice materials and devices at teledyne imaging sensors. *Journal of Electronic Materials* **39** 1001–1006 (2010).
188. Hao, H.-Y. *et al.* Wet Chemical Etching of Antimonide-Based Infrared Materials. *Chinese Physics Letters* **32**, 107302 (2015).
189. Sze, S. M. & Ng, K. K. *Physics of Semiconductor Devices: Third Edition. Physics of Semiconductor Devices: Third Edition* John Wiley and Sons (2006).

190. Taghipour, Z. *et al.* Temperature-Dependent Minority-Carrier Mobility in p-Type InAs/GaSb Type-II-Superlattice Photodetectors. *Phys Rev Appl* **11**, 024047 (2019).
191. Gutiérrez, M., Araujo, D., Jurczak, P., Wu, J. & Liu, H. Solid solution strengthening in GaSb/GaAs: A mode to reduce the TD density through Be-doping. *Appl Phys Lett* **110**, 092103 (2017).
192. Wang, Y. *et al.* The source of the threading dislocation in GaSb/GaAs hetero-structures and their propagation mechanism. *Appl Phys Lett* **102**, 052102 (2013).
193. Hopkins, P. E. *et al.* Effect of dislocation density on thermal boundary conductance across GaSb/GaAs interfaces. *Appl Phys Lett* **98**, 161913 (2011).
194. Wang, Y., Ruterana, P., Desplanque, L., el Kazzi, S. & Wallart, X. Strain relief at the GaSb/GaAs interface versus substrate surface treatment and AlSb interlayers thickness. *J Appl Phys* **109**, 023509 (2011).
195. Kang, J. M., Nouaoura, M., Lassabatère, L. & Rocher, A. Accommodation of lattice mismatch and threading of dislocations in GaSb films grown at different temperatures on GaAs (001). *J Cryst Growth* **143**, 115–123 (1994).
196. Ouyang, L. *et al.* Structural properties of InAs/InAs_{1-x}Sb_x type-II superlattices grown by molecular beam epitaxy. *Journal of Vacuum Science & Technology B, Nanotechnology and Microelectronics: Materials, Processing, Measurement, and Phenomena* **30**, 02B106 (2011).
197. Lozano, J. G. *et al.* Evaluation of the influence of GaN and AlN as pseudosubstrates on the crystalline quality of InN layers. *physica status solidi c* **4**, 1454–1457 (2007).
198. Korkmaz, M., Arikan, B., Suyolcu, Y. E., Aslan, B. & Serincan, U. Performance evaluation of InAs/GaSb superlattice photodetector grown on GaAs substrate using AlSb interfacial misfit array. *Semicond Sci Technol* **33**, 035002 (2018).
199. Kuo, C. P., Vong, S. K., Cohen, R. M. & Stringfellow, G. B. Effect of mismatch strain on band gap in III-V semiconductors. *J Appl Phys* **57**, 5428–5432 (1985).
200. Suchalkin, S. *et al.* In-plane and growth direction electron cyclotron effective mass in short period InAsGaSb semiconductor superlattices. *J Appl Phys* **110**, 043720 (2011).

201. Weisbuch, C., Dingle, R., Gossard, A. C. & Wiegmann, W. Optical characterization of interface disorder in GaAs-Ga_{1-x}Al_xAs multi-quantum well structures. *Solid State Commun* **38**, 709–712 (1981).
202. Kim, H. *et al.* Atomic resolution mapping of interfacial intermixing and segregation in InAs/GaSb superlattices: A correlative study. *J Appl Phys* **113**, 103511 (2013).
203. Gustafsson, O. *et al.* Long-wavelength infrared photoluminescence from InGaSb/InAs quantum dots. *Infrared Phys Technol* **59**, 89–92 (2013).
204. Liu, R. *et al.* Mid-infrared emission from In(Ga)Sb layers on InAs(Sb). *Opt Express* **22**, 24466 (2014).
205. Detz, H. Thermal expansion of III-V materials in atomistic models using empirical Tersoff potentials. *Electron Lett* **51**, 1455–1457 (2015).
206. Johnson, S. M. *et al.* Effect of dislocations on the electrical and optical properties of long-wavelength infrared HgCdTe photovoltaic detectors. *Journal of Vacuum Science & Technology B: Microelectronics and Nanometer Structures Processing, Measurement, and Phenomena* **10**, 1499 (1998).
207. Gopal, V. & Gupta, S. Effect of dislocations on the zero-bias resistance-area product, quantum efficiency, and spectral response of LWIR HgCdTe photovoltaic detectors. *IEEE Trans Electron Devices* **50**, 1220–1226 (2003).
208. Delaunay, P. Y. *et al.* Passivation of type-II InAs/GaSb double heterostructure. *Appl Phys Lett* **91**, 091112 (2007).
209. Lothian, J. R., Ren, F. & Pearton, S. J. Mask erosion during dry etching of deep features in III-V semiconductor structures. *Semicond Sci Technol* **7**, 1199 (1992).
210. Gunapala, S. D. *et al.* Demonstration of a 1024 × 1024 Pixel InAsGaSb superlattice focal plane array. *IEEE Photonics Technology Letters* **22**, 1856–1858 (2010).
211. Huang, E. *et al.* Inductively coupled plasma etching and processing techniques for type-II InAs/GaSb superlattices infrared detectors toward high fill factor focal plane arrays. In: Rezeghi, M., Sudharsanan, R., Brown, G. J. editors. *Quantum Sensing and Nanophotonic Devices VI* **7222**, 72220Z (2009).

212. Binh-Minh Nguyen, M., Chen, G., Hoang, M.-A. & Razeghi, M. Growth and characterization of long wavelength infrared type II superlattice photodiodes on a 3" GaSb wafer. *IEEE Journal of Quantum Electronics* **7945**, 441–449 (2011).
213. Jean Nguyen, al *et al.* Inductively coupled plasma etching for delineation of InAs/GaSb pixels. In: Strojnik, M. & Paez, G. editors. *Infrared Remote Sensing and Instrumentation* **8511**, 851103 (2012).
214. Li, S. *et al.* Dry etching and surface passivation techniques for type-II InAs/GaSb superlattice infrared detectors. In: Lewis, C., Burgess, D., Zamboni, Kajzar, F., & Heckman, E. M. editors. *Optics and Photonics for Counterterrorism and Crime Fighting VI and Optical Materials in Defence Systems Technology VII* **7838**, 318–325 (2010).
215. Xiangfeng Zhang, al *et al.* Study on ICP dry etching of GaSb and InAs/GaSb super lattices. In: Jiang, Y., Yu, J., & Wang, Z. editors. *6th International Symposium on Advanced Optical Manufacturing and Testing Technologies: Optoelectronic Materials and Devices for Sensing, Imaging, and Solar Energy* **8419**, 274–281 (2012).
216. Nguyen, J. *et al.* Low dark current long-wave infrared InAs/GaSb superlattice detectors. *Appl Phys Lett* **97**, 051108 (2010).
217. Xu, J. *et al.* Effects of etching processes on surface dark current of long-wave infrared InAs/GaSb superlattice detectors. *Infrared Phys Technol* **107**, 103277 (2020).
218. Kutty, M. N. *et al.* Study of Surface Treatments on InAs/GaSb Superlattice LWIR Detectors. *Journal of Electronic Materials* **39**, 2203–2209 (2010).
219. Zhang, L., Lester, L. F., Shul, R. J., Willison, C. G. & Leavitt, R. P. Inductively coupled plasma etching of III–V antimonides in BCl₃/Ar and Cl₂/Ar. *Journal of Vacuum Science & Technology B: Microelectronics and Nanometer Structures Processing, Measurement, and Phenomena* **17**, 965 (1999).
220. Swaminathan, K., Janardhanan, P. E. & Sulima, O. V. Inductively coupled plasma etching of III–V antimonides in BCl₃/SiCl₄ etch chemistry. *Thin Solid Films* **516**, 8712–8716 (2008).
221. Nilsen, T. A. *et al.* High aspect ratio etching of GaSb/AlGaAsSb for photonic crystals. *MRS Online Proceedings Library* **891**, 1–6 (2006).

222. Lee, J. W. *et al.* Plasma etching of III–V semiconductors in BCl₃ chemistries: Part I: GaAs and related compounds. *Plasma Chemistry and Plasma Processing* **17**, 155–167 (1997).
223. Hong, T., Zhang, Y. G., Liu, T. D. & Zheng, Y. L. BCl₃/Ar ICP Etching of GaSb and Related Materials for Quaternary Antimonide Laser Diodes. *J Electrochem Soc* **152**, G372 (2005).
224. Lee, J. W. *et al.* Inductively coupled plasma etching of III–V semiconductors in Cl₂-based chemistries. *Mater Sci Semicond Process* **1**, 65–73 (1998).
225. Jung, H. C. *et al.* Investigation of ICP dry etching of InAs/GaSb type-II superlattice LWIR photodetector. In: Andresen B. F., Fulop, G. F., & Zheng, L. editors. *Infrared Technology and Applications* **11741**, 377–381 (2021).